Structural geology of the Kinsevere Copper Deposit, DRC

By

KAZADI BANZA Samuel-Barry

Submitted in partial fulfilment of the requirements for the degree

M. Sc. Geology

In the Faculty of Natural and Agricultural Sciences,

University of Pretoria

PRETORIA

November 2012

Structural geology of the Kinsevere Copper Deposit, DRC.

By KAZADI BANZA Samuel-Barry

Supervisor : Prof. Adam J. Bumby (University of Pretoria, South Africa)

Advisor : Dr. Damien Delvaux (Royal Museum for Central Africa in Tervuren, Belgium)

Department : Geology

University : University of Pretoria

Degree : M. Sc. Geology

ABSTRACT

The Kinsevere mine is a copper deposit located in the Democratic Republic of Congo (DRC), within the Central African Copperbelt. This area is situated in the Katangan basin within the SE portion of the Lufilian Arc, which is a large, arcuate structure that extends from SE Angola, across the DRC, and into NW Zambia. The purpose of this study is to characterise the brittle deformation observed around the Kinsevere copper deposit to lead to an understanding of the deformation history of the area. This is accomplished by analysing fault-slip and fold data to help understand the relationship between regional palaeostress, faulting and folding present in the mine vicinity. This study also attempts to characterise fracture-controlled copper mineralisation within the interpreted geodynamic context of the area. The broader objective of this study is to relate the structural observations from Kinsevere to the deformation history of the Lufilian Arc.

This study uses the right dihedral method to analyse four categories of brittle structures. The structural types analysed include slickensided faults, mineralised joints, and unmineralised joints and shear fractures. The data suggests that the palaeostress associated with the formation of brittle structures in the Kinsevere area occurred during three deformation events. The first event is characterised by a compressional stress regime which occurred during the early stage of the Kolwezian phase (D_1). The second event is characterised by a strike-slip stress regime that formed as the result of clockwise rotation of the earlier (D_1) compressional regime. Two fault-slip vectors were observed on the strike-slip fault planes, indicating that a reactivation occurred during the Monwezian phase (D_2). The final structural event was characterised by the development of an extensional stress regime. This was associated with North-South oriented extension and is related to the East African Rift System (D_3). These interpreted events correlate well with the geodynamic context related to the Lufilian orogeny.

Another line of evidence that supports this structural interpretation is the presence of evaporitic minerals observed in the stratigraphic units surrounding the brecciated zones such

as the RAT and the CMN. The structural association of these evaporitic minerals may be related to pre-existing, salt-bearing units, which were dissolved during an early compressive (D_1) phase of the Lufilian orogeny. However, the contact between the Grey RAT and the Red RAT (distal from the breccia zones) does not show any evidence of faulting, and in the Kinsevere area the Grey RAT is always observed above the Red RAT. This suggests that the Grey RAT may be the uppermost stratigraphic unit of the RAT subgroup, which contradicts some previously published interpretations. Thus, the current structural architecture was probably formed from a combination of two separate mechanisms, including compression-related salt extrusion and the development of thrust faults and folding resulting from the shortening of the Katangan basin.

Based on an analysis of the fracture-controlled mineralisation in the study area, it is shown here that most of the stress tensors indicate that these fractures were induced within the compressional stress regime generated by the Lufilian orogeny. This conclusion supports studies which suggest a multiphase origin for the mineralizing fluids active in the Katangan basin. Thus, the age of the copper mineralisation associated with fractures is interpreted to correlate with the timing of the folding event that occurred during the Lufilian orogeny between 540-550Ma.

Keywords: brittle deformation, faults and faulting, kinematic, salt extrusion, folding, clockwise rotation, mineralisation, Lufilian orogeny, Kinsevere.

I hereby declare that this thesis is my own unaided work except where referenced otherwise. It is being submitted for the degree M.Sc. Geology at the University of Pretoria, Pretoria, South Africa. It has not been submitted before any degree or examination in any other University.

_____ Signature of author

Date _27th November 2012_____

TABLE OF CONTENTS

ABSTRACT i

TABLE OF CONTENTS iv

LIST OF ABBREVIATIONS xvii

Stress symbols: explanation of WinTensor figures xvii

Chapter 1 1

INTRODUCTION 1

1.1 Location of study area 3

1.2 Regional geology 8

1.2.1 Pre-Kibaran Basement 8

1.2.2 Kibaran Supergroup 8

1.2.3 Katangan Supergroup 8

1.3 Metamorphism 9

1.4 Previous works (tectonic setting) 13

1.4.1 Kolwezian Event (Phase 1) 16

1.4.2 Monwezian Event (Phase 2) 16

1.4.3 Chilatembo Event (Phase 3) 16

1.5 Aims 21

1.6 Methodology 21

1.6.1 Fieldwork 21

1.6.2 Structural analysis 22

Chapter 2 23

KINSEVERE GEOLOGY 23

2.1 Background 23

2.2 Local geology 24

2.2.1 RAT Subgroup (R1) 30

2.2.2 Mines Subgroup (R2) 34

2.2.3 Breccia 47

2.2.4 The Footwall and Hanging wall 52

Chapter 3 54
STRUCTURAL GEOLOGY DATA 54
3.1 General concepts of crustal stress analysis 55
3.2. Right dihedral method (RDM) 58
3.2.1 Rotational optimisation procedure (ROP) 59
3.2.2 Data filtering 60
3.2.3 Stress field characterisation 60
3.3 Field results 60
3.3.1 Tshifufiamashi fragment 61
3.3.2 Tshifufia fragment 82
3.3.3 Kinsevere Hill fragment 107
3.4. Synthesis of results 119
Chapter 4 121
INTERPRETATIONS AND DISCUSSIONS 121
4.1 Folding analysis 121
4.1.1 F_1 folding events. 121
4.2 Fracturing analysis 124
4.2.1 Analysis of the mineralised joints. 124
4.2.2 Analysis of the unmineralised joints 127
4.3 Faulting analysis 128
4.3.1 Compressive stress regime 128
4.3.2 Strike-slip stress regime 129
4.3.3 Extensional stress regime 129
4.4 Thrusting analysis 130
4.5 Partial conclusions. 130
4.6 Discussions 136
Chapter 5 146
CONCLUSIONS 146

5.1 Suggestions for further study 149

Acknowledgements 150

REFERENCES 151

APPENDIX 1 165

FIELD DATA (WINTENSOR FORMAT) 165

APPENDIX 2 195

STRESS TENSOR LOCATION MAPS 195

LIST OF FIGURES

Figure 1: Geological map of the southern part of the Katangan Province with the Congolese Copper Belt (CCB) of the Lufilian Arc highlighted with yellow dash lines. 1

Figure 2: Location of the Lufilian Arc (red rectangle) in southern Africa (Cailteux *et al*. 2005) 2

Figure 3: Location map of the Kinsevere copper deposit. 4

Figure 4: The Katangan belt with main localities (modified from François, 1974; Cailteux, 1994; Broughton and Rogers, 2010) 5

Figure 5: Geological map of Kinsevere copper deposit (produced by Anvil exploration team under the supervision of B. Houda, 2008). 7

Figure 6: Collision between the Congo and Kalahari cratons (John *et al.,* 2004). 14

Figure 7: Tectonic setting and structural architecture of the Lufilian fold belt 15

Figure 8: Google Earth image of the Kinsevere area. 21

Figure 9: Geological map of the Kinsevere Copper Deposit. (Compiled under the supervison of B. Houda, Anvil Exploration, 2008). 25

Figure 10: Section A-A' along the central part of the Tshifufiamashi fragment. E-W steeply dipping cross-section showing a duplication of R2 Mines Subgroup rocks with the Roan Breccia. All strata are dipping West and show a faulted contact with the Kundelungu. 26

Figure 11: Section B-B' along the central part of the Tshifufia fragment. 27

Figure 12: Section C-C' along the south part of the Tshifufia fragment. The known Roan breccias have outcropped in the eastern side of the mine. Small-scale folds are observed in the CMN strata. (Anvil Exploration, Houda B., 2008) 28

Figure 13: Section E-E' along the Kinsevere Hill fragment. 29

Figure 14: Sub-unit lithologies of the R1.3 at Kinsevere-TCDH027 31

Figure 15: Heterogeneous breccia occurring copper oxides, mostly malachite mixed with red iron oxides (limonite and hematite)-TCDH032-Tshifufia fragment. 32

Figure 16: Pinkish-white massive talceous siltstone affected by banded fabric, RAT-R.1.3 overlain by the heterogeneous breccia through a shear contact down to 268.80m (TCDH012-Tshifufia). 32

Figure 17: Greenish-pink diffusely laminated fresh dolomitic siltstone - Undifferentiated RAT (TCDH012-Tshifufia fragment) 33

Figure 18: Open pit outcrop of pink massive talceous siltstone showing a slicken surface (Central Pit-Tshifufia). 33

Figure 19: Transitional contact of RSF with SDB-Tshifufia fragment (absence of RSC). 36

Figure 20: Proximal facies of GRAT showing erratic siliceous bedding and evaporitic textures and occurring fine grained replacement chalcopyrite. TCRD003-Tshifufia fragment. 37

Figure 21: Distal facies of GRAT underlying the proximal facies of GRAT. TCRD003-Tshifufia fragment. 37

Figure 22: Yellowish-grey massive fractured dolomitic siltstone (Grey RAT) with hematite staining and malachite, heterogenite and manganese oxides in fractures (TCDH027-Tshifufia fragment). 38

Figure 23: Spherical nodule comprising silica-dolomite rimmed by chalcocite-TCRD003-Tshifufia fragment. 39

Figure 24: D.Strat and RSF (a) Fresh rocks Tshifufiamashi fragment-TFDH004 and (b) Weathered facies-Tshifufia fragment-TCDH 027 40

Figure 25: Dolomite with pseudomorphs (nodules) replaced by chalcopyrite in carbonaceous shale-TFDH004-Tshifufiamashi fragment 41

Figure 26: Dark grey bedded dolomitic shale with stratiform nodular (TCHD001-Tshifufia fragment-HQ size). 42

Figure 27: Open pit outcrop showing fractured SD with mineralised joint, Qtz-malachite veins and reactivated bedding planes - Tshifufia Fragment 42

Figure 28: Dark coloured dolomite with bedded chalcopyrite and quartz-chalcopyrite veins, lower CMN-Tshifufia Fragment 44

Figure 29: Grey well laminated dolomite with bedded chalcocite-KPDH002 - Kinsevere Hill fragment. 44

Figure 30: Light grey bedded dolomite with intercalated “collapse breccia” and calcite-dolomite veins, Uppermost CMN unit - Tshifufia fragment. 45

Figures 31 a) and b): Open pit outcrop showing mineralised joints and fractures, and affected by small-scale folding - Tshifufia Fragment. 46

Figure 32: Dark grey laminated coarse-grained dolomite with replacement chalcopyrite-dolomite in stratiform evaporitic band-lower CMN - Tshifufia Fragment. 46

Figure 33: Brecciated well-bedded dolomite constituting the CMN monolithic breccias - KPDH002 . 47

Figure 34: Heterogeneous breccia with RAT and Mines Subgroup clasts 48

Figure 35: Highly fractured RAT breccia showing banded fabrics. 48

Figure 36: RAT breccia showing dolomite veins (hydro-fractures), TCDH010 - Tshifufia fragment. ... 49

Figure 37: The contact between the crackle breccia and the heterogeneous breccia (RAT breccia). .. 49

Figure 38: The contact between the Mines Series rocks (CMN) and the RAT Subgroup rocks (R1.3) -TCDH010 Tshifufia fragment. 51

Figure 39: W-E section showing normal sequence from the Red RAT overlain by Grey RAT that shows a transitional contact with the overlain formation D.Strat-RSF (a). Proximal facies indicated by evaporitic texture within the Grey RAT. Tshifufia fragment. Looking North. 52

Figure 40: The normal σ_n and shear stress σ_s acting on a fault plane 55

Figure 41: The stress ellipsoid showing the three principal stress axes σ_1, σ_2, and σ_3. 56

Figure 42: The three types of faults as defined by Anderson (1942): (a) Normal fault, (b) Thrust fault or reverse fault and (c) Strike-slip fault 57

Figure 43: The principle of the improved right dihedral method 58

Figure 44: Geological map of the Tshifufiamashi fragment. Cross section A-A' refers to Fig. 10. 62

Figure 45: Rose diagram of strike plane (a) and dip (b) of the major phase of the mineralised joints in the Tshifufiamashi fragment. 63

Figure 46: Stereonet of the rotational optimisation results of mineralised joints related to the first stress tensor obtained at Tshifufiamashi. 63

Figure 47: Rose diagram of strike plane (a) and dip plane (b) of the intermediated phase of the mineralised joints in the Tshifufiamashi fragment. 64

Figure 48: Stereonet of the rotational optimisation results of mineralised tension joints related to the second stress tensor obtained at Tshifufiamashi. 64

Figure 49: Rose diagram of strike plane (a) and dip plane (b) of the minor phase of the mineralised joints in the Tshifufiamashi fragment. 65

Figure 50: Stereonet of the rotational optimisation results of mineralised joints related to the third stress tensor obtained at Tshifufiamashi. 65

Figure 51: Rose diagram of strike plane (a) and dip plane (b) of the first phase of the unmineralised joints observed at Tshifufiamashi 66

Figure 52: Stereonet showing the principal stress axis (σ_1, σ_2, σ_3) obtained with the improved right dihedral method combined with the rotational optimisation procedure of the unmineralised joints related to the stress tensor obtained at Tshifufiamashi. 67

Figure 53: Rose diagrams of the strike plane (a) and dip plane (b), trend of fault slip (c) and plunge angle and (d) of slickensided faults observed at Tshifufiamashi of the first stress tensor. 68

Figure 54: Stereonet showing the principal stress axis (σ_1, σ_2 and σ_3) obtained with the improved right dihedral method combined with the rotational optimisation procedure of the slickensided faults observed at Tshifufiamashi. Faults are displayed as the large circle and the slip striae are represented with an arrow indicating the slip sense. 69

Figure 55: Stereonet using tangent-lineation with pole to plane displays with the corresponding slip direction of slickensided faults observed in Tshifufiamashi..... 69

Figure 56: Stereonet showing tangent-lineation data with fault slip acting on fault planes. Stereonet (a) shows the first group related to a SE-NE radial compressional regime and (b) shows the second is related to a pure compression regime oriented SE-NW. 70

Figure 57: Rose diagrams of the strike plane (a) and dip plane (b), azimuth of fault slip (c) and plunge angle (d) of slickensided faults observed in Tshifufiamashi induced by the second stress tensor. 71

Figure 58: Stereonet obtained from dip and dip direction, azimuth and plunge angle of the fault observed on the open pit outcrop of the Tshifufiamashi fragment..... 72

Figure 59: Stereonet showing tangent-lineation data obtained from fault-slip acting on the fault planes of the intermediate phase observed in Tshifufiamashi. 72

Figure 60: Rose diagrams of the strike plane (a) and dip plane (b), azimuth of fault slip (c) and plunge angle (d) of slickensided faults observed in Tshifufiamashi belonging to the third stress tensor. 73

Figure 61: Stereonet showing the principal stress axis obtained with the improved dihedral method combined with the rotational optimisation procedure of the fault-slip data collected from the open pit outcrop at the Tshifufiamashi fragment. 74

Figure 62: Stereonet with tangent-lineation data of fault slip acting on the fault planes belonging to the third stress tensor observed at Tshifufiamashi..... 74

Figure 63: Rose diagram of strike planes (a) and dip planes (b) obtained from the fault plane of the observed reverse fault in the Tshifufiamashi open pit..... 75

Figure 64: Stereonet showing the principal stress axis obtained with the improved dihedral method combined with the rotational optimisation procedure of the reserve shear fracture observed at the Tshifufiamashi fragment..... 76

Figure 65: Rose diagram of strike planes (a) and dip planes (b) obtained from the fault plane of the observed normal fault in the Tshifufiamashi open pit. 76

Figure 66: Stereonet showing the principal stress axis obtained with the improved dihedral method combined with the rotational optimisation procedure of the normal shear fracture observed at the Tshifufiamashi fragment..... 77

Figure 67: π diagram indicating the fold axis of the Tshifufiamashi fragment. 78

Figure 68: π diagram indicating the fold axis obtained from the bedding plane observed in Tshifufiamashi. 78

Figure 69: Stereonet showing the hinge lines data collected from the Tshifufiamashi fragment. 79

Figure 70 (a): Tight micro-folds in the CMN strata showing NE vergence in the Tshifufiamashi open pit. Looking South. 79

Figure 70 (b): Stereonet showing the hinge lines data collected from the Tshifufiamashi fragment.....80

Figure 71: NE-SW section along the Tshifufiamashi open pit showing faulted-fold thrusting toward the NE. Looking South. 81

Figure 72: Geological map of the Tshifufia fragment. B-B' and C-C' cross-sections refer to Figs. 11 and 12. (Anvil Mining-Exploration, Houda, B., 2008). 83

Figure 73: Mineralised joints in outcrop of the Central pit. (a) Acute angle between set of mineralised joint, looking East; (b) Mineralised joint cutting bedding planes, looking NW; (c) E-W section showing D.Strat + RSF strata affected by mineralised joints, looking South. 84

Figure 74: Rose diagram of strike plane (a) and Dip plane (b) obtained from the mineralised joints observed in the Tshifufia open pit and related to the first stress tensor. 84

Figure 75: Stereonet showing the principal stress axis obtained with the improved dihedral method combined with the rotational optimisation procedure of the mineralised joints observed in the Tshifufia open pit. 85

Figure 76: Rose diagram of strike plane (a) and dip plane (b) obtained from the mineralised joints observed in the Tshifufia open pit and related to the second stress tensor 85

Figure 77: Stereonet showing the principal stress axis obtained with the improved dihedral method combined with the rotational optimisation procedure of the mineralised joints related to the second stress tensor at the Tshifufia open pit..... 86

Figure 78: Diagram of strike plane (a) and dip plane (b) obtained from the mineralised joints observed in the Tshifufia open pit and related to the third stress tensor. 86

Figure 79: Stereonet showing the principal stress axis obtained with the improved dihedral method combined with the rotational optimisation procedure of the mineralised joints related to the third stress tensor at the Tshifufia open pit. 87

Figure 80: Rose diagram of strike plane (a) and dip plane (b) obtained from the mineralised joints observed in the Tshifufia open pit and related to the fourth stress tensor..... 87

Figure 81: Stereonet showing the principal stress axis obtained with the improved dihedral method combined with the rotational optimisation procedure of the mineralised joints related to the fourth stress tensor at Tshifufia open pit. 88

Figure 82: Rose diagram of strike of planes (a) and dip planes (b) obtained from the unmineralised joints observed in the Tshifufia open pit. 89

Figure 83: Stereonet showing the principal stress axis obtained with the improved right dihedral method combined with the rotational optimisation of the unmineralised tension joint related to the second stress tensor encountered in the Central open pit. 89

Figure 84: Rose diagram of strike plane (a) and dip plane (b) obtained from the unmineralised tension joint of the second stress tensor observed at the Tshifufia open pit. 90

Figure 85: Stereonet showing the principal stress axis obtained with the improved right dihedral method combined with the rotational optimisation of the unmineralised tension joint related to the second stress tensor encountered in the Central open pit. 90

Figure 86: Fault plane containing strike-slip slicken lines well marked by clayey mineral (a) and calcite (b); (a) looking South-East and (b) looking South. 91

Figure 87: Rose diagrams of the strike plane (a) and dip plane (b), azimuth of fault slip (c) and plunge angle (d) of the first stress tensor deduced from the observed slickensided faults at Tshifufia. 92

Figure 88: Stereonet showing the principal stress axis obtained with the improved right dihedral method combined with the rotational optimisation of the slickensided faults related to the first stress tensor encountered at the Tshifufia open pit. 93

Figure 89: Stereonet showing tangent-lineation data obtained from fault-slip acting on the fault planes of the first stress tensor deduced from the fault-slip observed at the Tshifufia fragment 93

Figure 90: Rose diagrams of the strike plane (a) and dip plane (b), azimuth of fault slip (c) and plunge angle (d) of slickensided faults observed in Tshifufia induced during the second phase. 94

Figure 91: Stereonet showing the principal stress axis obtained with the Improved right dihedral method combined with the rotational optimisation of the slickensided faults related to the second stress tensor obtained at the Tshifufia open pit. 95

Figure 92: Stereonet showing tangent-lineation data obtained from fault-slip acting on the fault planes of the second stress tensor deduced from the fault-slip observed at the Tshifufia. 95

Figure 93: Rose diagrams of the strike plane (a) and dip plane (b), azimuth of fault-slip (c) and plunge angle (d) of slickenside observed in Tshifufia belonging to the third stress tensor. 96

Figure 94: Stereonet showing the principal stress axis obtained with the improved right dihedral method combined with the rotational optimisation of the slickensided faults related to the third stress tensor obtained at the Tshifufia open pit. 97

Figure 95: Stereonet showing tangent-lineation data obtained from fault-slip acting on the fault planes of the third stress tensor deduced from the fault-slip observed at the Tshifufia. 97

Figure 96: Rose diagram of strike plane (a) and dip plane (b) obtained from the fault plane of faults observed in the Tshifufia open pit 98

Figure 97: Stereonet showing the principal stress axis obtained with the improved right dihedral method combined with the rotational optimisation of the shear fracture related to the first stress tensor obtained at the Tshifufia open pit. 99

Figure 98: Rose diagram of strike plane (a) and dip plane (b) obtained from the shear fractures observed in the Tshifufia open pit 99

Figure 99: Stereonet showing the principal stress axis obtained with the improved right dihedral method combined with the rotational optimisation of the shear fracture related to the second stress tensor obtained at the Tshifufia open pit..... 100

Figure 100: π diagram of poles to bedding indicating the fold axis obtained from bedding observed at Tshifufia. 101

Figure 101: πi diagram plotting pole to bedding planes and indicating the fold axis obtained from the bedding planes of the tight micro-folds observed in the CMN strata at Tshifufia. 102

Figure 102: Stereographic projection showing fold axial planes of the tight micro-folds observed in the CMN strata of the Tshifufia fragment where the black crosses represent the poles and the blue star represents the great circle. 102

Figure 103 (a): Stereographic projection of raw data collected from the hinge line observed in the Tshifufia fragment. 103

Figure 103 (b): Stereographic projection showing contour of the hinge lines data collected from the Tshifufia fragment.....103

Figure 104: Kink band fold affecting the SD strata and indicating a thrust movement towards the North-Tshifufia Central open pit Kinsevere Copper Deposit. Looking North. 105

Figure 105: E-W section along the Central open pit showing an overturned limb of R2 Mines Subgroup strata and two types of thrust faults. The first type (in red) affects the CMN strata along a thrust oriented SSW-NNE (56/278) and the second type of fault (in blue) shows a fault plane oriented SW-NE (30/115) with heterogeneous breccias between these R2 Mines Subgroups strata. Looking South. 106

Figure 106: Geological map of the Kinsevere Hill fragment. Cross-section E-E' refers to Fig.13. 108

Figure 107: Rose diagram of strike plane (a) and dip plane (b) obtained from the mineralised joints induced during the first stress tensor observed at Kinsevere Hill. 109

Figure 108: Stereonet showing the principal stress axis obtained with the improved right dihedral method combined with the rotational optimisation of the mineralised joints related to the first stress tensor obtained at Kinsevere Hill. 109

Figure 109: Rose diagram of strike plane (a) and dip plane (b) obtained from the mineralised joints formed related to the second stress tensor observed at Kinsevere Hill. 110

Figure 110: Stereonet showing the principal stress axis obtained with the improved right dihedral method combined with the rotational optimisation of the mineralised joints related to the second stress tensor obtained at Kinsevere Hill. 110

Figure 111: Rose diagram of strike planes (a) and dip planes (b) obtained from the unmineralised joints at Kinsevere Hill 111

Figure 112: Stereonet showing the principal stress axis obtained with the improved right dihedral method combined with the rotational optimisation of the unmineralised joints observed at Kinsevere Hill. 112

Figure 113: Rose diagrams of the strike plane (a) and dip plane (b), azimuth of fault-slip (c) and plunge angle (d) of slickensided faults observed at Kinsevere hill. 113

Figure 114: Stereonet showing the principal stress axis of the first tensor obtained with the improved right dihedral method combined with the rotational optimisation of the slickensided faults observed at Kinsevere Hill. 113

Figure 115: Stereonet showing tangent-lineation data obtained from lineation acting on the fault planes and belonging to the stress tensor deduced from the faults observed at Kinsevere Hill. 114

Figure 116: Stereonet showing the principal stress axis of the second tensor obtained with the improved right dihedral method combined with the rotational optimisation of the slickensided faults observed at Kinsevere Hill 114

Figure 117: Stereonet showing the principal stress axis of the second tensor obtained with the improved right dihedral method combined with the rotational optimisation of the slickensided faults observed at Kinsevere Hill. 115

Figure 118: Stereonet showing tangent-lineation data obtained from fault slip acting on the fault planes of the stress tensor deduced from the fault-slip observed at Kinsevere Hill. 116

Figure 119: π diagram indicating the fold axis obtained from the bedding planes observed at Kinsevere Hill. 117

Figure 120: π diagram indicating the fold axis obtained from the bedding planes collected from the isoclinal fold observed in the CMN strata at Kinsevere Hill. 117

Figure 121: Stereographic projection showing the fold axial plane contour of the Kinsevere Hill fragment where the black crosses represent the fold axial plane poles. The blue triangle represents the average pole and the large black circle represents the average plane. 118

Figure 122: Stereographic projection of raw data collected from the hinge line observed in the Kinsevere Hill fragment. 118

Figure 123: Summary of Phi diagrams and fold axial planes for F1a and F1b folding in the study area. Lower R2 = RAT+D.STRAT+RSF. Green bullet = Fold axial planes and Black cross = Pole to bedding of tight/isoclinal folds. 123

Figure 124: Simplistic overturned folding (B) (generation of NE-vergent fold) cannot account for the overturned, westward-younging strata observed in Tshifufia (A) 131

Figure 125: 3D model illustrating the history of the structural deformation in the Kinsevere area (B). (A) Indentor model of the tectonic deformation developed (modified after Kampunzu and Cailteux, 1999). K.C: Kalahari craton, C.C: Congo craton, K: Kinsevere. Blue plane: fold axial plane 1b, Green plane: fold axial plane 1c; Grey plane: strike-slip fault plane. 132

Figure 126: Sharp-related subdivision of the Lufilian Arc generated two arcs, a large arc situated in the southwest and a small arc developed to the NE. These arcs are separated by the tectonic lineament along which the Kinsevere Copper deposit is situated. Tenke F. Fungurume area (circled in red) and Domes region (circled in purple) (modified after Cailteux *et al.,* 1994; Broughton and Rogers, 2010). 133

Figure 127: Tectonic setting and structural architecture of the Lufilian fold belt, S (A)-N (A') schematic cross-section of the central part of the Lufilian fold belt, highlighting the variation in structural style between tectonic zones (modified from Porada, 1989; Selley *et al.,* 2005) 139

Figure 128: Cartoon showing type of salt structure associated with passive margin building out over a salt layer (Vendeville and Jackson, 1992)..... 140

Figure 129: Restoration of the regional section of the western part of the Lufilian fold belt using GeoSec2D restoration software. Bedding lengths were maintained by flexural slip during unfolding. The cross-sectional area of Roan evaporite-gigabreccia, which is highly speculative, was decreased forward through time to allow dissolution of evaporites. The restoration omits progressive erosion during deformation. No vertical exaggeration (Jackson *et al.,* 2003) 141

Figure 130: (a) Map showing the importance of strike-slip faults in the evolution of the Lufilian fold belt. DSMT: "Deep-seated magnetic throw" marker; Mu: Musoshi, Ki: Kinsenda, Ma: Mabaya, Mf: Mwanfwe, Lo: Lupoto, Ls: Luishia, Lw: Luiswishi, Sh: Shinkolobwe, Me: Menda, Mi: Mindingi; Ka: Kakanda, Kv: Kambove, Ke: Kela, Kf: Kinsanfu fault zone, Kt: Kitongwe, Ti: Tilwezembe, K-M: Kalumbe-Myunga, Lu: Luankoko, To: Tombolo Kilppe, Gt: Gule-Tondo Klippe, Fu: Fungurume Kilppe and Kb: Kabwe in Zambia. The numbers given are ages dating D2 diachronous movements in Ma, while arrows with numbers represent qualitatively major block motions and numbers refer to succession of extrusion phases. Probable age sequence: arrow 1: ca. 690Ma; arrow 2: ca. 660 Ma and arrow 3: ca.600 Ma; (b); Fault observed in unilaterally confined indentation experiments and related successive extrusions of blocks 1 and 2 (after Peltzer *et al.,* 1982; Kampunzu and Cailteux, 1999). . 144

Figure 131: Location map of the stress tensor obtained from the mineralised joints in the Kinsevere area belonging to the stress compressive regime..... 196

Figure 132: Location map of the stress tensor obtained from the mineralised joints in the Kinsevere area belonging to the strike-slip regime. 197

Figure 133: Location map of the stress tensor obtained from the mineralised joints in the Kinsevere area belonging to the extensive stress regime. 198

Figure 134: Location map of the stress tensor obtained from the unmineralised joints in the Kinsevere area belonging to the extensive stress regime. 199

Figure 135: Location map of the stress tensor obtained from the slickensided faults (reverses) in the Kinsevere area belonging to the compressive stress regime. 200

Figure 136: Location map of the stress tensor obtained from the strike-slip faults in the Kinsevere area belonging to the strike-slip stress regime. 201

Figure 137: Location map of the stress tensor obtained from the slickensided faults in the Kinsevere area belonging to the extensive stress regime. 202

Figure 138: Location map of the stress tensor obtained from the shear fractures observed in the Kinsevere area belonging to the compressive stress regime. 203

Figure 139: Location map of the stress tensor obtained from the shear fractures indicating normal faults observed in the Kinsevere area and belonging to the extensive stress regime. 204

LIST OF TABLES

Table 1: Lithostratigraphy of the Katangan Supergroup (Cailteux, 1994)..... 12

Table 2: Summary of the timing and Deformation Events within the Lufilian Arc..... 18

Table 3: Katangan stratigraphy column and dates of major tectonism in southern Katanga (Jackson *et al.,* 2003)..... 19

Table 4: Lithostratigraphy of the Katangan Supergroup and Mines Subgroup at Kinsevere..... 35

Table 5: Proposed lithostratigraphic table of the RAT group in Kolwezi (Hitzman, 2008)..... 50

Table 6: Summary of all stress tensors (σ_1, σ_2 and σ_3), stress ratio (R) and the tectonic stress regime of the mineralised joint in the Tshifufiamashi open pit. 66

Table 7: Summary of all stress tensors (σ_1, σ_2 and σ_3), stress ratio (R) and the tectonic stress regime of the unmineralised joint in the Tshifufiamashi open pit. 67

Table 8: Summary of all stress tensors (σ_1, σ_2 and σ_3), stress ratio and the stress regime of the slickensides at the Tshifufiamashi fragment. 75

Table 9: Summary of all stress tensors (σ_1, σ_2 and σ_3), stress ratio (R) and the stress regime of the shear fracture observed at the Tshifufiamashi fragment. 77

Table 10: Showing the dip/plunging angle, dip-dip direction/azimuth orientation and vergence of the folding event obtained at the Tshifufiamashi open pit. 80

Table 11: Summary of the principal stress axis (σ_1, σ_2 and σ_3), and stress ratio (R) of the palaeostress tensor of the mineralised joints in the Tshifufia fragment. 88

Table 12: Summary of the principal stress axes (σ_1, σ_2 and σ_3), and stress ratio (R) of the palaeostress tensor of the unmineralised tension joints in the Tshifufia fragment. 91

Table 13: Summary of the principal stress axes (σ_1, σ_2 and σ_3) and stress ratio (R) of the palaeostress tensor of the slickensided faults encountered at the Tshifufia fragment..... 98

Table 14: Summary of the principal stress axis (σ_1, σ_2 and σ_3), stress ratio (R) and the friction angle obtained from the shear fractures data collected at the Tshifufia pit..... 100

Table 15: Showing the dip/plunging angle, dip-dip direction/azimuth orientation and vergence of the folding event obtained in Tshifufia open pit. 104

Table 16: Summary of the principal stress axis (σ_1, σ_2 and σ_3), stress ratio (R) and the friction angle obtained from the mineralised joints data collected at Kinsevere Hill..... 111

Table 17: Summary of the principal stress axis (σ_1, σ_2 and σ_3), stress ratio (R) and the friction angle obtained from the mineralised joints data collected at the Kinsevere Hill..... 116

Table 18: Showing the dip/plunging angle, dip-dip direction/azimuth orientation and vergence of the folding event obtained in the Kinsevere Hill fragment. 119

Table 19: Results of the reduced palaeostress tensors obtained from the mineralised and unmineralised joints (MJ and UMJ), slickensided faults (fault-slip) and shear fractures data. 120

LIST OF ABBREVIATIONS

CCB : Congolese Copperbelt
CMN : Calcaire à Minéraux Noirs
D.STRAT : Dolomie Stratifiée
DRC : Democratic Republic of Congo
DSI : Direct Stress Inversion
EARS : East African Rift System
EXACO : Exploitation Artisanale du Congo
FAP : Fold Axial Plane
GRAT : Roche Argilo-Talqueuse Grises (Grey RAT)
HBX : Heterogeneous breccia
HL : Hinge Line
Ind. Breccia : Undifferentiated Breccia
INF : Lower Mines Series / Kamoto Dolomites
Ku : Kundelungu
LOB : Lower Ore Body
MCK : Mining Company Katanga
MJ : Mineralised Joints
Ng : Nguba
RAT : Roche Argilo-Talqueuse
RDM : Right dihedral method
ROP : Rotational Optimisation Procedure
RRAT : Roche Argilo-Talqueuse Rouge (Red RAT)
RSC : Roche Siliceuse Cellulaire
RSF : Roche Siliceuse Feuilletée
SD : Shale Dolomitique
SDB : Shale Dolomitique de Base
TOB : Third Ore Body
UMHK : Union Minière du Haut-Katanga
UMJ : Unmineralised Joints
UOB : Upper Ore Body
ZCB : Zambian Copperbelt

Stress symbols: explanation of WinTensor figures

Stress symbols show the horizontal stress axes (S_{Hmax} and S_{hmin}) as a function of the stress ratio R. Their length and colour represent the horizontal deviatoric stress magnitude, relative to the isotropic stress (σi). White outward arrows: σ_3 stress axis, green arrows: σ_2 stress axis (outward when extensional ($\sigma_2 > \sigma_i$) and inward when compressional ($\sigma_2 > \sigma_i$)), red inwards arrows: σ_1 axis). The vertical stress (σ_v) is represented by a solid circle for extensional regimes ($\sigma_1=\sigma_v$), a dot for strike-slip regimes ($\sigma_2=\sigma_v$) or an open circle for compressional regimes ($\sigma_3=\sigma_v$). The bars outside the stereograms represent the orientation of the SHmax (black) and Shmin (white) axes associated with the individual fault data. The histogram represents the distribution of the misfit function F5, weighted arithmetically according to the magnitude.

Chapter 1

INTRODUCTION

The Neoproterozoic Katangan Supergroup contains major stratiform sediment-hosted Cu-Co deposits, as well as numerous others deposits including Cu, Pb, Zn, U, Au and Fe, which constitute the Central African Copperbelt in Zambia and the Democratic Republic of Congo (DRC) (Mendelson, 1961; François 1973; Kampunzu and Cailteux, 1999). The Central African Copperbelt forms a northward convex structure, straddling the Congo-Zambia border called the "Lufilian Arc" formed during the Lufilian orogeny (c. 620-570 Ma). It stretches over an area 700 km long and 50 km wide from the Mwinilunga district in North-West Zambia (Brock, 1961; Steven, 2000) and East-North-Eastwards to Bwana Mkubwa (Zambia) and Lonshi. The central section of the arc is located in the Democratic Republic of Congo (DRC) (Fig. 1).

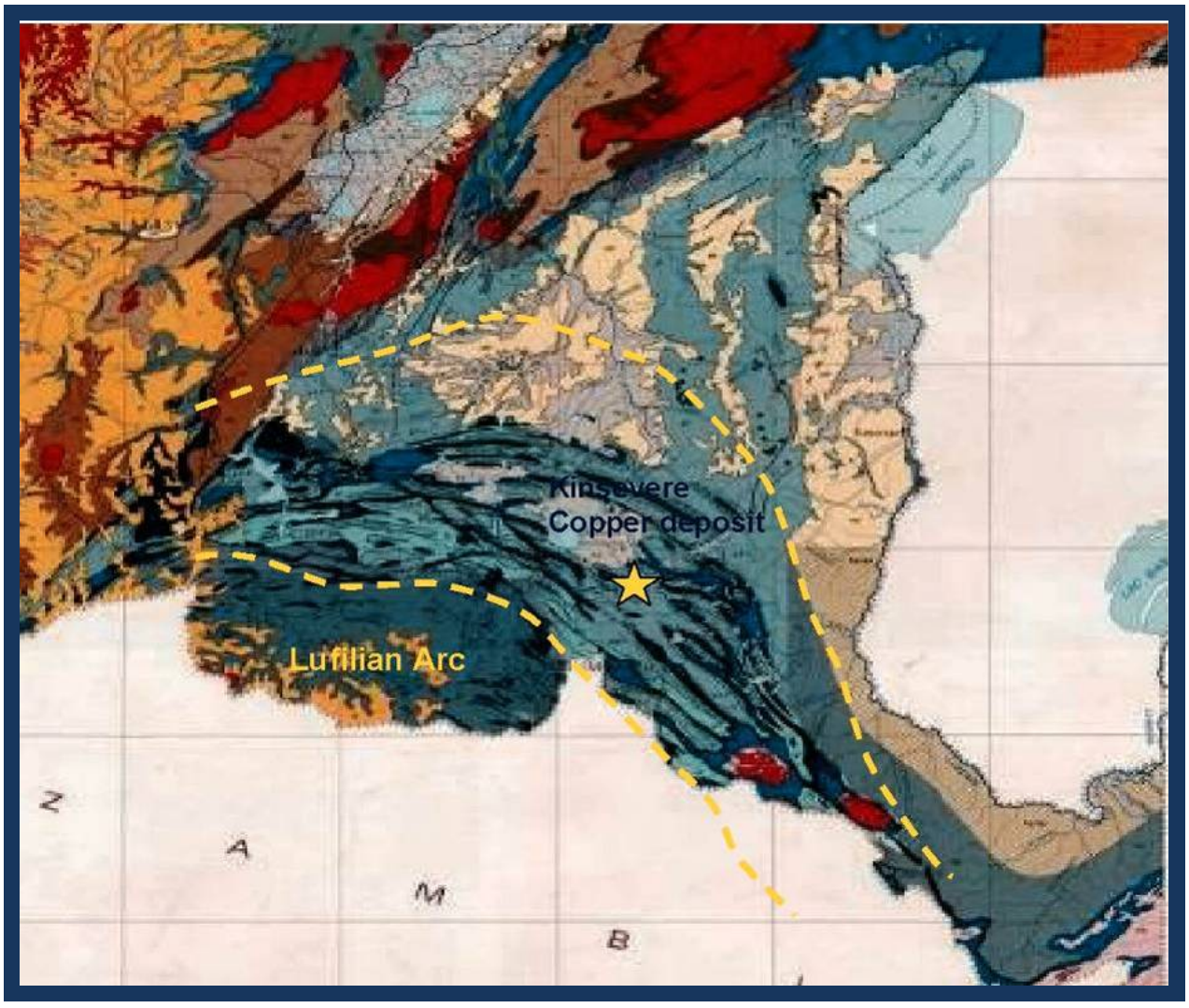

Figure 1: Geological map of the southern part of the Katangan Province with the Congolese Copper Belt (CCB) of the Lufilian Arc highlighted with yellow dash lines.

The Lufilian Arc is part of a network of Neoproterozoic-Early Paleozoic (Pan-African) orogenic belts that surround and separate the Congo and Kalahari cratons in southern Africa. It

represents the northern segment of a transcontinental orogenic system that includes the Zambezi and the Damara belt (Fig. 2).

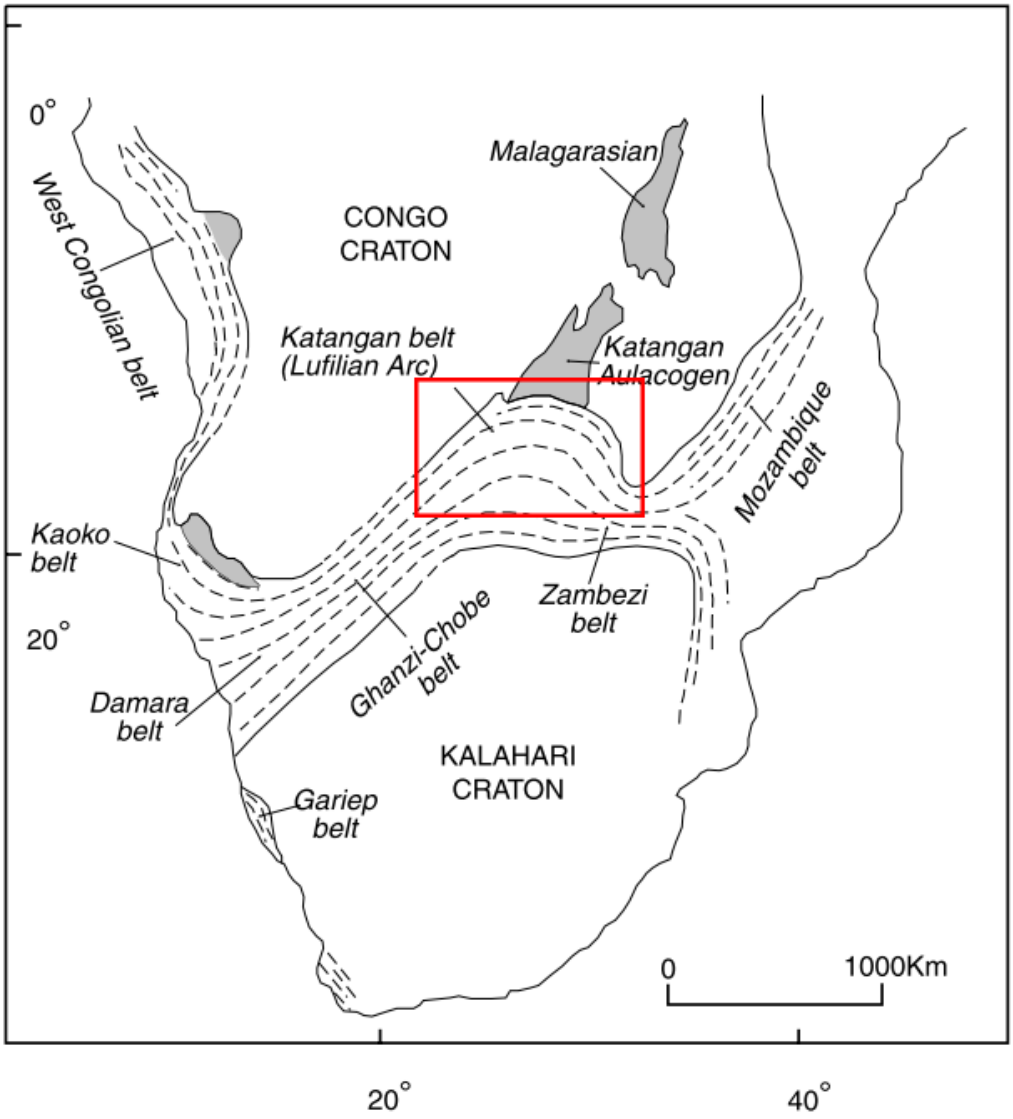

Figure 2: Location of the Lufilian Arc (red rectangle) in southern Africa (Cailteux *et al*. 2005)

The Pan-African orogeny in Central Africa evolved from an extensive system marked by an open-type rift sedimentation at the end of the Kibaran orogeny between 1300 and 1000 Ma to a compressive system related to the collision of the Kalahari and the Congo cratons (750-550 Ma) (Kroner, 1977; Unrug, 1983; Okitaudji, 1989; Kampunzu *et al*., 2000; Bumby and Giraud, 2005).

The Katangan Supergroup totals 5-10 km in thickness and is subdivided into three major lithostratigraphical units (François, 1974, 1995; Cailteux *et al*., 2003) that were deposited from 880 Ma to 500 Ma (Master *et al*., 2002; Jackson *et al*., 2003; Cailteux *et al*., 2005; Batumike *et al.,* 2007).

From the bottom to top, these units are the Roan (R), Nguba (Ng, formerly Lower Kundelungu) and Kundelungu (Ku, formerly Upper Kundelungu) groups. Roan Group

sediments were deposited in a basin that evolved from a continental rift through a proto-oceanic rift (Kampunzu *et al.,* 1993, 2000; Okitaudji, 2001). Upper Roan Group and Mwashya Subgroup sediments and the overlying Nguba sediments were deposited in a wider basin corresponding to a major phase of extensional tectonics (Buffard, 1988; Kampunzu *et al.,* 2003).

Most of the Cu-Co deposits of the Lufilian Arc have already been subject to mineralogical, geochemical and petrological studies and a few radiometrical, geophysical and structural studies in recent decades. The few structural studies already conducted were based on the general geodynamic aspect of the deformation (François, 1973; Cahen *et al.,* 1984; Daly, 1986; Buffard, 1988; Unrug, 1988; Cosi *et al.,* 1992; Cailteux and Kampunzu, 1995; Kampunzu and Cailteux, 1999; Key *et al.,* 2001; Jackson *et al.,* 2003). Consequently, the kinematic of the Lufilian Arc is not well understood at present. In an effort to remedy this deficiency, this study, which is intended to help to characterise the deformation and structural evolution of the Lufilian orogeny, was conducted on the Kinsevere area located in the SE of the Lufilian Arc.

1.1 Location of study area

The Kinsevere Copper deposit is located in the Kipushi territory in the Katanga Province of the Democratic Republic of Congo (DRC). The Kinsevere copper deposit consists of the Kinsevere exploitation permit (PE 528) and parts of the exploration permit PR 2350 (20km^2) held by Anvil Mining Limited sprl. The deposit is located about 30km NNE of Lubumbashi, the provincial capital of Katanga Province (Fig. 3), at 11°20’ South latitude and 27°34’ East longitude.

Figure 3: Location map of the Kinsevere copper deposit.

Geologically, the Kinsevere copper deposit is located in the SE part of the Lufilian Arc along a SE-NW trending tectonic lineament which can be traced from the Domes region (Zambia) up to the Fungurume mining district through Kalasa, Kamuse, Kitundu and other copper occurrences. This lineament is located north of and parallel to the lineament containing deposits such as Luiswishi, Lukuni, Etoile, Ruashi, Kakanda and Kambove (Fig. 4).

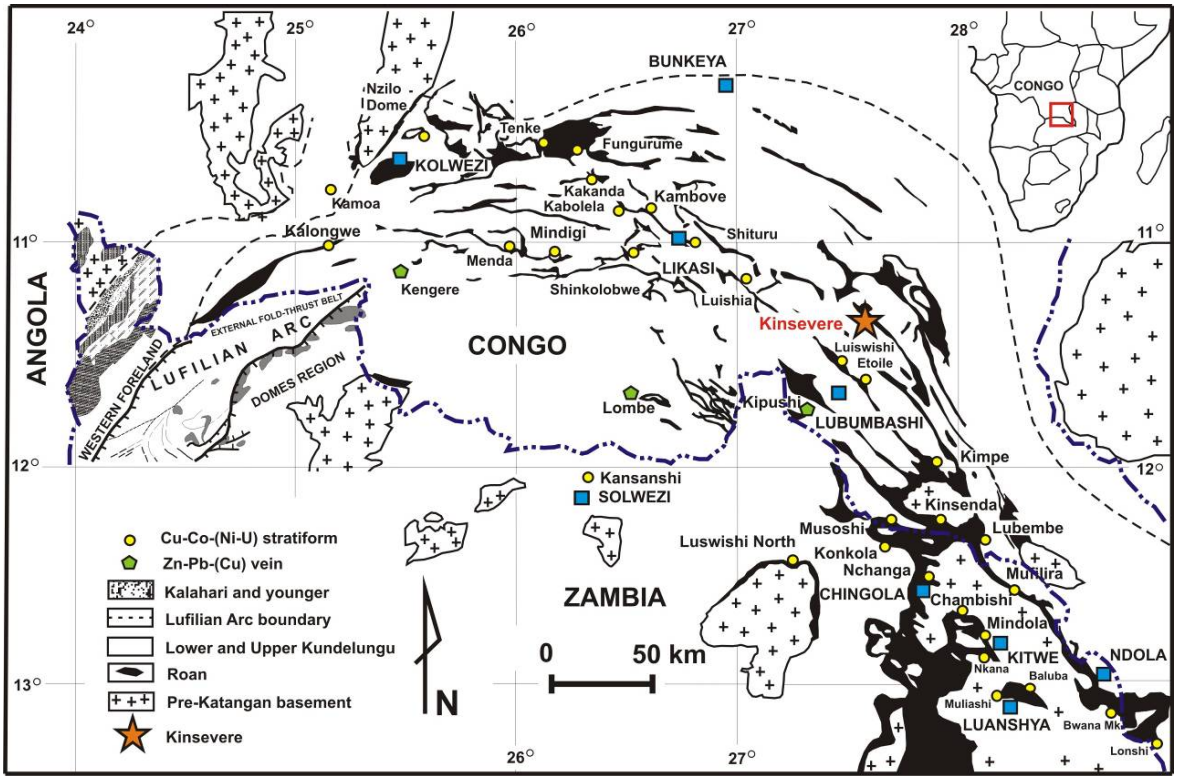

Figure 4: The Katangan belt with main localities (modified from François, 1974; Cailteux, 1994; Broughton and Rogers, 2010)

The Kinsevere deposit lies in rocks of the Neoproterozoic Roan Group, a succession of predominantly shallow-marine and terrestrial metasediments up to 1,000 metres thick, that accumulated after the break-up of the Rodinia supercontinent (1050 to 950 Ma) (Kampunzu *et al.,*1993; Meert and Van der Voo, 1996; Tembo *et al.,* 1999 and Kampunzu *et al.,* 2000).

The Kinsevere copper deposit lies mainly in rocks of the Mines Series Subgroup (R2) overlying the RAT (R1) Formation. This sequence is overlain by the Dipeta (R3) and Mwashya (R4) Subgroups (Table 1) and consists of four Mines Series (R2) fragments. The Tshifufiamashi and Tshifufya fragments are situated along a major N-S oriented fracture and are separated by a sinistral strike-slip fault. The Kilongo and Kinsevere Hill fragments are situated along a major NW-SE fracture and are separated from the other fragments by another sinistral strike-slip fault (Houda, 2008). All these fragments are affected by fractures and breccias (Fig. 5).

This study will focus on three of these fragments: Tshifufiamashi situated to the NE, Tshifufia which hosts the "Central Pit" and Kinsevere Hill located to the SE. All these fragments are underlain by siliciclastic and carbonate Mines Series rocks which are the typical hosts to Katangan Copper Belt Mineralisation.

The current geometric position of these fragments (Tshifufiamashi, Tshifufia and Kinsevere Hill) resulted from a kinematic evolution in which some secondary structures were active. These have been examined in this structural study and are summarised as: (i) folding which has been scrutinized through a detailed analysis of structural elements including bedding plane orientations, the orientation of hinge lines, and the orientation of fold axial planes; (ii)

analysis of fractures represented by mineralised and unmineralised joints; (iii) analysis of faults.

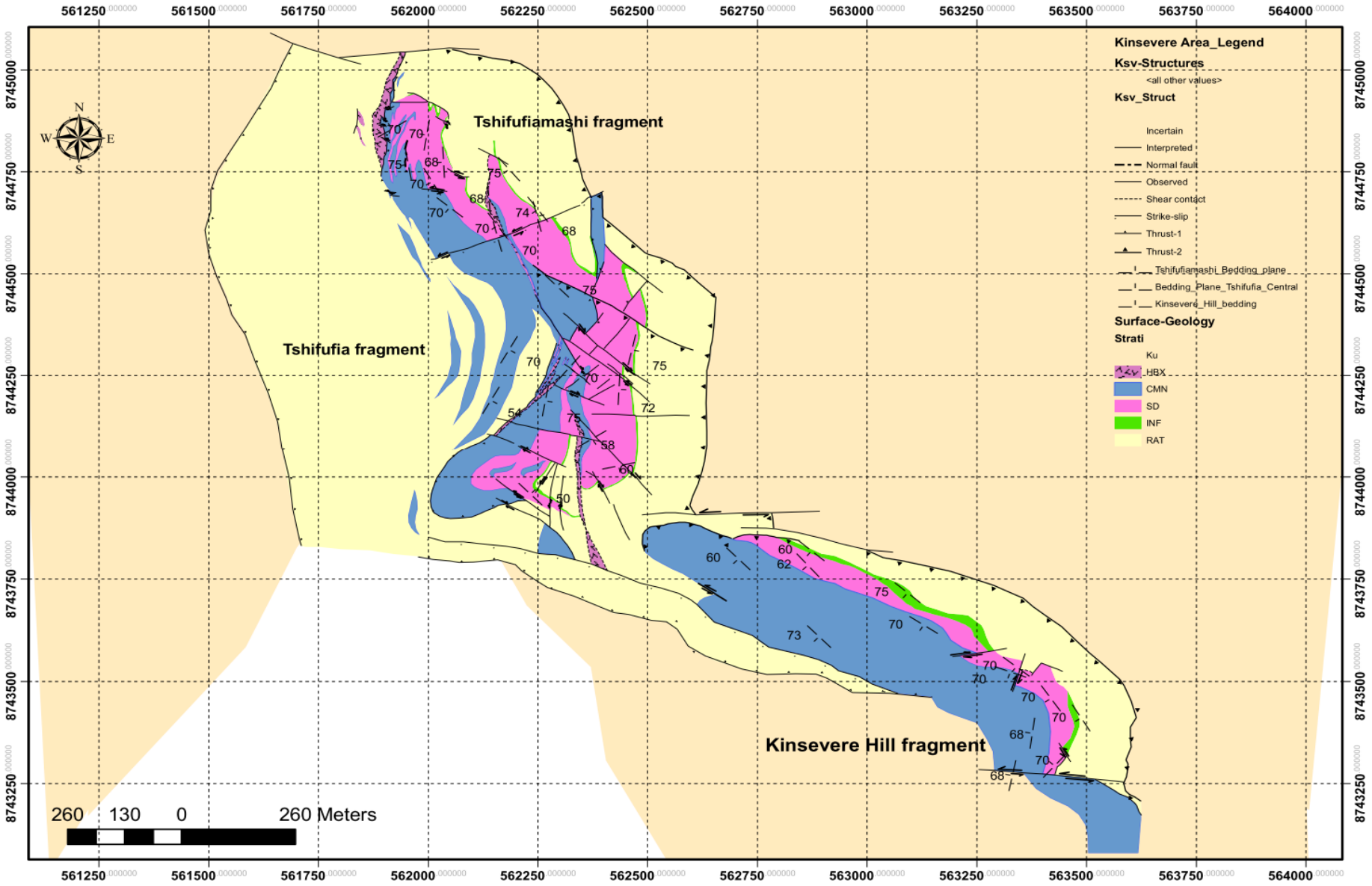

Figure 5: Geological map of Kinsevere copper deposit (produced by Anvil exploration team under the supervision of B. Houda, 2008).

1.2 Regional geology

Workers in the Congolese Copper Belt including Groseman (1948), Aderca (1950), Cahen (1954; 1970); Cahen *et al.,* (1961; 1970; 1971; 1984), Mendelsohn (1961) and Drysdall *et al.,* (1972) have identified the following three main geological events in southern Katanga which are, from top to bottom:

1. Katangan (<880 Ma to 600 Ma) which resulted from the Lufilian orogeny (620±20 Ma);
2. Kibaran (> 1320 Ma) affected by the Kibaran orogeny (1320±40 Ma) and
3. Pre-Kibaran (± 2000 Ma) affected by the pre-Kibaran orogeny (1850±20 Ma)

1.2.1 Pre-Kibaran Basement

Studies by Garlick (1961), Mendelsohn (1961), Drysdall *et al.,* (1972) described pre-Kibaran outcrops in Zambia and around the Luina and Mokambo domes, both located to the South of Katangan province (Congolese Copperbelt) (Gysin, 1934; Ngoy, 1992, Dejonghe, 1995). All these authors describe the pre-Kibaran as folded metamorphic gneissic granite. They subdivided the pre-Kibaran into the Muva and Lufubu systems.

According to Fleischer *et al.,* (1976), the Muva system could be the equivalent of Kibaran and would, therefore, form part of the Irumides belt.

1.2.2 Kibaran Supergroup

The Kibaran extends to the NW of the Lufilian Arc where it forms the NE-SW trending Kibaride Belt. According to Grosemans (1948), Aderca (1950) and Cahen *et al.,* (1967), the Kibaran consists of a set of thick (10,000m) low-grade sequences of slightly metamorphosed quartzitic, siliclastic and pelitic sediments, intruded by granite and associated with mineralised pegmatites (Sn-Ta-W).

1.2.3 Katangan Supergroup

The Katangan is well known for its famous Cu-Co-Pb-Zn-U mineralisation. It is composed of sedimentary rocks and volcanics deposited between 900-500 Ma (Cahen *et al.,* 1967; Kampunzu and Cailteux, 1999).

According to Buffard (1988), Okitaudji (1989) and Cailteux *et al.,* (1994), Katangan sediments were deposited in a continental rift-type basin. Several authors (Cahen *et al.,* 1967, Cahen, 1970, Kroner, 1977) attributed the Katangan deposition to the intracratonic rifting of the latest phase of the Kibaran tectogenesis. Kennedy (1964) considers the Katangan as the North-East extension of the Damarides and as a phase of the Pan-African orogeny which could be correlated with the Otavi series and/or Damara system located in the South-West of the African continent (Namibia) (Fig. 2).

Katangan sediments unconformably overlie rocks of different ages that are located to the West, on the Kibaran, to the North-East on the Ubendian and to the South-East on the Ubendian and the Kibaran (Cahen *et al.,* 1967; Ngoy, 1992; Dejonghe and Ngoy, 1995).

The lithostratigraphic subdivision of Katangan sediments is based on the presence of two glacial diamictite markers; the "Grand Conglomérat" and the "Petit Conglomérat" (François, 1973; 1974) (Table 1). It comprises, from the bottom to the top, the following groups:

1.2.3.1 Roan Group (R)

The Roan Group in Katanga consists of predominantly dolomitic rocks deposited in supratidal, intratidal and lagoonal sedimentary environments (Lefebvre, 1978; Cailteux 1978a; 1978b; 1983; 1994)

The known transgressive sequence includes supratidal and continental deposits. Within the RAT Subgroup (R1), it is characterised in Zambia by a proximal facies of coarse-grained sandstone resulting from the erosion of Kibaride basement rocks, and in Katanga, by distal finer clastics and dolostones (Cailteux *et al.,* 1994). This subgroup is overlain by a transgressive succession of supratidal sediments, intratidal and algal deposits (Mines Subgroup-R2) carrying the bulk of the stratiform copper-cobalt mineralisation. The facies changes at the top to a clayey-dolomitic confined sediment types. These are followed by a succession of similar sediments, moving from a regressive (Dipeta-R3) to a transgressive (Mwashya-R4) sequence.

Little is known about the total thickness of Roan Group sediments; the base has never been observed and tectonic discontinuities occur within the R1 and R3 subgroups.

1.2.3.2 Nguba Group (Ng)

Previously called Lower Kundelungu (Ki) (François, 1995; Cailteux *et al.,* 2005), the group consists predominantly of clastics deposited in a marine environment where different facies have been observed. It represents a major transgression over the underlying Roan. Its total thickness varies between 1000 and 3000m. The lowermost unit is the "Grand Conglomérat" which is overlain by silty shale to calcareous dolomitic formations, which locally contain Cu, Pb-Zn mineralisation (diamictite, Kakontwe limestone) notably in the Kipushi, Kengere, Lombe deposits (François 1973, 1974)

1.2.3.3 Kundelungu Group (Ku)

Formerly called the Upper Kundelungu (Ks) (François, 1995; Cailteux *et al.,* 2003), this 300m thick group comprises mainly argillaceous to sandy clastics and is floored by the "Petit Conglomérat" diamictite (François, 1973; 1974; Batumike *et al.,* 2006; 2007). The depositional environment is marine, but with a larger transgressive tract than the Nguba (Batumike *et al.,* 2006; 2007). The facies is poorly diversified and laterally homogeneous over a large area of the whole basin (Batumike *et al.,* 2006).

1.3 Metamorphism

In general, the level of regional metamorphism is relatively low-grade in the Lufilian fold-and-thrust belt. It does not exceed the stage of anchizone (Oosterbosch, 1962; François and Cailteux, 1981; Cluzel, 1986). Only sericite, chlorite and occasionally biotite are developed in the South-East part of the Lufilian Arc (Belliere, 1966; 1969; Cailteux, 1973). The low-grade

metamorphism that affected all Katangan sediments is even more attenuated from the base (Roan) to the top (Nguba and Kundelungu) (Oosterbosch 1962). The existence of North-South metamorphic zonation has been well demonstrated (Drysdall *et al.,* 1972; François and Cailteux, 1981). According to Lefebvre and Patterson (1982) and Cluzel (1986), the metamorphic grade ranges from amphibolite and locally eclogite facies in the South through greenschist facies to unmetamorphosed in the outermost sector of the belt in the North. However, in the Lufilian fold-and-thrust belt, the metamorphism can be locally distributed owing to hydrothermal activity.

CONGO			ZAMBIA				
			GROUP	SUB-GROUP	LITHOLOGIES		
			Kundelungu (prev. Upper Kundelungu. Ks) Ku	Plateaux Ku-3	Arkoses, conglomerates, sandstones, shales		
				Kiubo Ku-2	Sandstones, carbonated siltstones or shales, limestones		
				Kalule Ku-1	K-1.3 Carbonated siltstones and shales: grey to pink Oolitic limestones at base (calcaire rose oolithique)		
					K-1.2 Carbonated siltstones and shales; pink to grey dolomite at base ("calcaire rose")		
					K-1.1 "Petit Conglomérat" glacial diamictite		
			N'Guba (prev. Lower Kundelungu. Ki) G	Monwezi G-2	Dolomitic sandstones, siltstones or shales		
				Likasi G-1	G-1.3 Carbonated siltstones and shales		
					G-1.2 Dolomitic limestones, dolomitic shales and siltstones		
					G-1.1 "Grand Conglomérat": glacial diamictite		
GROUP	SUB-GROUP	FORMATION	LITHOLOGIES		LITHOLOGIES	FORMATON	SUB-GROUP	GROUP
Roan	Mwashya R-4	Upper R-4.2	Shales, carbonaceous shales or sandstones		Black shales		Mwashya	Mwashya
		Lower R-4.1	Dolomites, jasper beds, pyroclastics and hematite; local Stratiform Cu-Co mineralisation		Dolomite interbedded with dolomitic shales; gabbro bodies (volcanic intrusions in Zambia)	Kanwangungu	Bancroft RU1-RU2	Upper Roan
	Dipeta R-3	R.3.4	Dolomite interbedded with argillaceous to dolomitic siltstones and feldspathic sandstones; intrusive basic bodies and volcaniclastics					
		R-3.3			Shales with grit			
		R-3.2			Dolomites or argillaceous dolomites; local stratiform Cu mineralisation			
		R.G.S. R-3.1	Dolomitic siltstones		Arenites, argillites and dolomitic argillites; occasional Dolomites at the base; main stratiform Cu-Co Mineralisation in the lower part (ore Shale)	Kibalongo	Kitwe RL3-RL6	Lower Roan
	Mines R-2	Kambove R-2.3	Laminated, stromatolitic, talcose dolomites and dolomitic Siltstones; local stratiform Cu-Co mineralisation			Chingola		
		Dolomitic shale R-2.2	Dolomitic shales, carbonaceous shales, dolomites and occasional sandstones or arkoses			Pelito-arkosic		
			Dolomitic shales, sandy dolomite at top; stratiform Cu-Co (upper ore body)			Ore Shale		
		Kamoto R-2.1	R-2.1.3 "roches siliceuses cellulaires" : stromatolitic dolomite with interbedded siltstones; Cu-Co at top base					
			R-2.1.2: bedded dolomites with siltstones; silty dolomite in the lower part; stratiform Cu-Co (Lower Ore body)					
			R-2.1.1 "RAT grise"; dolomitic siltstone; Cu-Co at top					
<900Ma	RAT R-1	R-1.3	Pink-lilac, hematitic, chloritic-dolomitic massive siltstones		Conglomerates, coarse arkoses and argillaceous siltstones; occasional Cu-Co mineralisation	Mutonda	Mindola (Footwall) RL7	
		R-1.2	Pink to purple-grey, hematitic, chloritic siltstones; sandstones in the lower part; stromatolitic dolomite at top					
		R-1.1	Purple-red, hematitic, slightly dolomitic bedded siltstones					
	Basal conglomerate	Base of the RAT sequence unknown			Quartzites	Kafufya		
					Pebble and coble conglomerate	Chimfunsi		

Table 1: Lithostratigraphy of the Katangan Supergroup (Cailteux, 1994)

1.4 Previous works (tectonic setting)

The Lufilian Arc is reported to have formed during the collision of the Angola-Kalahari and Congo-Tanzania Plates with accompanying NE-directed thrusting between 560 and 550 Ma (Porada and Berhorst, 2000) during the assembly of the supercontinent Gondwana between 750 and 500 Ma (Condie, 2002). Although the extent of rifting between the Congo and Kalahari cratons is debatable, recent evidence (Porada and Berhorst, 2000) suggests that rifting started at 880 Ma and separated the Congo-Tanzania plate from the Angola-Kalahari plate, leading to the formation of a passive continental margin on the southern side of the Congo craton. The Lufilian Arc comprises a succession of folded, faulted and thrusted structures, which is convex northwards. This fold-and-thrust belt is part of the Pan-African orogeny which was caused by the accretion from the East to the West of Gondwana during the Neoproterozoic (Van Daornick, 1928; Robert, 1940; Demesmaeker *et al.,* 1963; François, 1973; 1974; Wilson *et al.,* 1997).

Various models for the Pan-African structural evolution of the Lufilian Arc have been proposed that involve different deformational episodes, from rifting to orogenic, creating a typical foreland fold-thrust belt terrane in the northern part of the external fold-thrust belt.

According to Oosterbosch (1962), Demesmaeker *et al.,* (1963), Cahen (1970), François (1973, 1974), Cahen *et al.,* (1984), Daly (1986), Cosi *et al.,* (1992), Kampunzu and Cailteux (1999), Key *et al.,* (2002), John *et al.,* (2004) the current tectonic architecture of the Lufilian Arc was formed under a compressive regime, during positive inversion from extensional to contractional tectonics, contemporaneous with the deposition of the Nguba (Kampunzu *et al.,* 2003, Batumike *et al.,* 2007), which is related to the collision of the Kalahari and Congo cratons (Fig. 6).

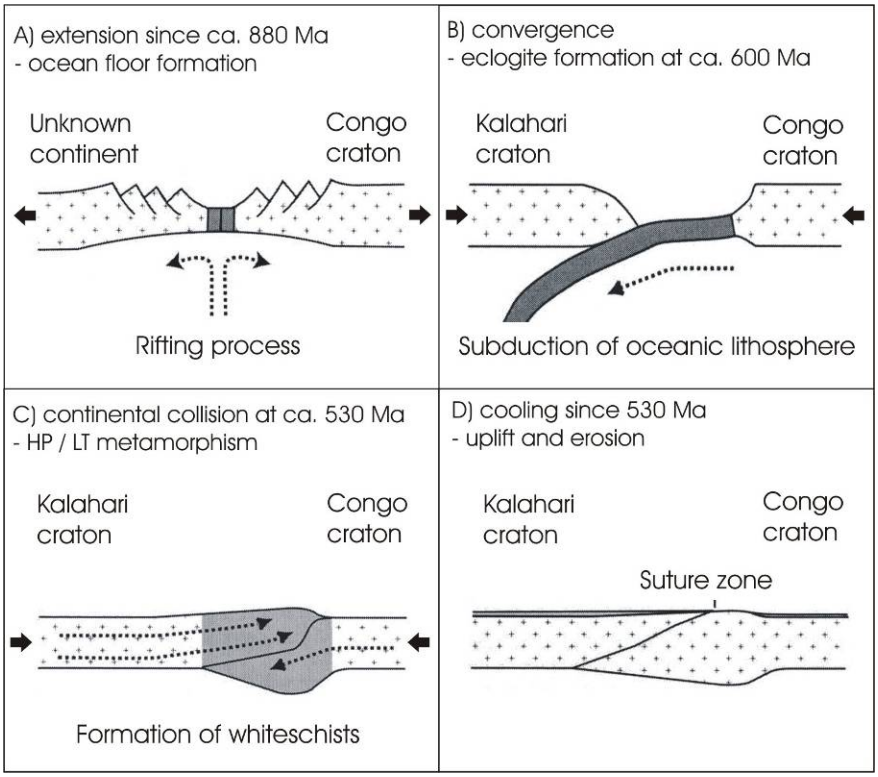

Figure 6: Collision between the Congo and Kalahari cratons (John *et al.,* 2004).

Unrug (1988) defined five tectonic domains associated with the Lufilian fold belt which are summarized by Selley *et al.,* (2005) into the following four domains, from North to South: the Extensional fold and thrust belt, the Domes regions, the Synclinorial belt and the Katangan High.

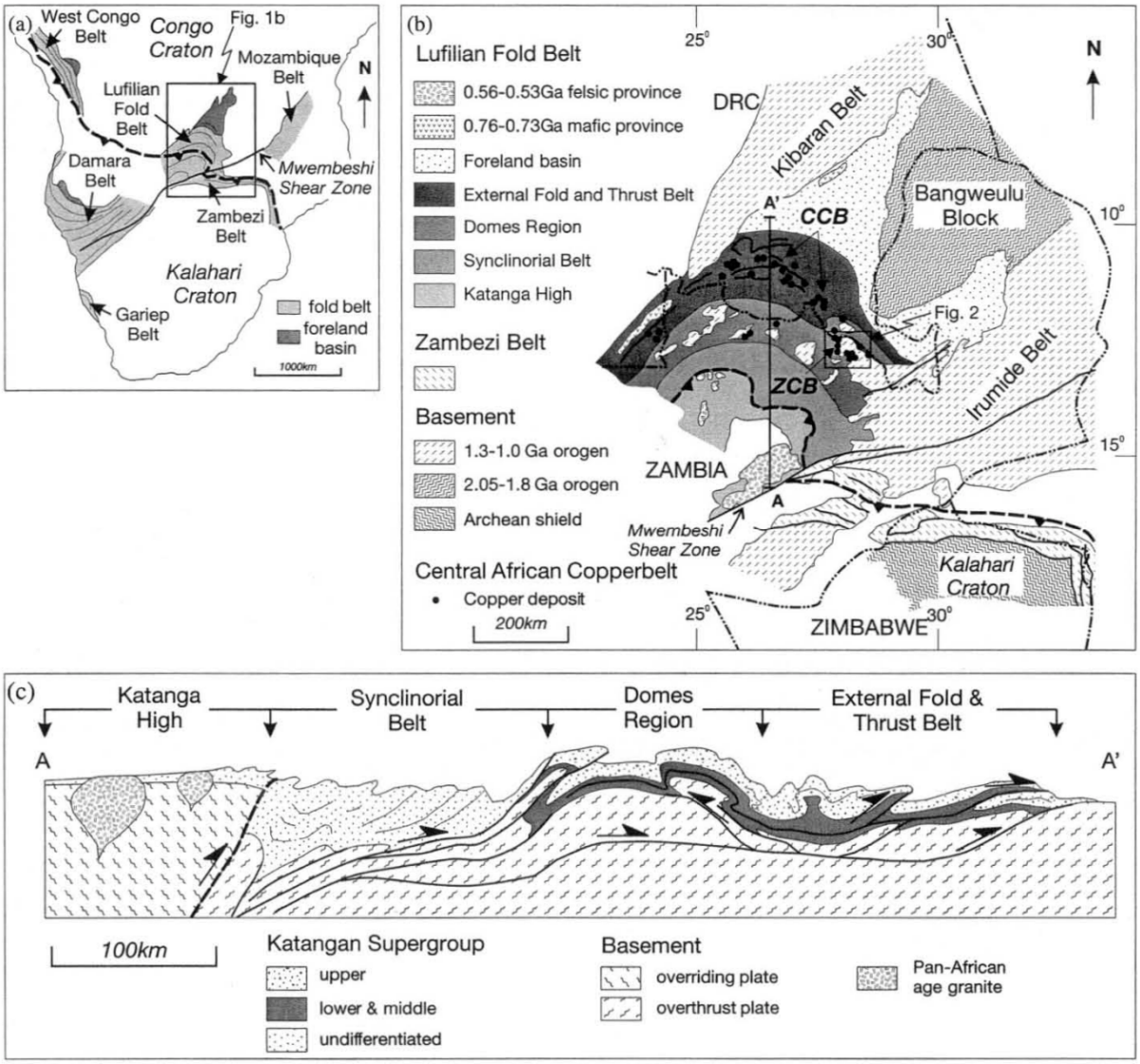

Figure 7: Tectonic setting and structural architecture of the Lufilian fold belt

Figure 7 shows: (a) the Pan-African system of central and southern Africa (modified from Kampunzu and Cailteux, 1999; Porada and Berhorst, 2000); (b) tectonic zoning in the Lufilian fold belt and distribution of copper deposits in the Zambian and Congoloese Copper Belt (ZCB and CCB respectively). This map differs from those previously published in that basement inliers of the ZCB are included within the Domes region, rather than the External fold and thrust belt (modified from Kampunzu and Cailteux, 1999); (c) schematic cross section of the Lufilian belt (S-N section line in b), highlighting variation in structural style between tectonic zones (modified from Porada, 1989)

Cahen *et al.,* (1984), following on from François (1974), established the basis of the tectonic evolution of the Lufilian Arc. They considered that five successive events (deformation phases) occurred during the Lufilian orogeny which started with E-W folding with South-dipping axial planes and northerly vergence in the Kolwezian phase. This was followed by epirogenic uplift of the Kundelungu Plateau in southern Zambia. The third Kundelungan event was characterised by E-W folds with vertical or North-dipping axial planes, locally with southerly vergence; Kampunzu and Cailteux (1999) considered this deformation as terminal to the Kolwezian event and postulated that it was the manifestation of backfolding. The

Monwezian faulting was characterised by faults with E-W trends following the Kundelungan event. François (1973) considered that the Monwezian event was mainly characterised by an E-W trending strike-slip fault associated with breccia within anticline cores. The last event was characterised by transverse folding perpendicular to the main trends of the Lufilian Arc.

Unrug (1983) regarded the first two phases identified by François (1973; 1974) as a single event, indicated by the northward folding and thrusting and followed by a back-folding and indicated a regional clockwise stress rotation from the North to the East at the end of the Kolwezian phase and based his interpretation on the geophysical observation conducted by Placet (1976) around Kolwezi. Fractures and several brittle discontinuities formed part of the Kolwezian event which took place during the deposit of Ku.2.1 sediment (François, 1973).

In a recent study based on a synthesis of observations and geological surveys carried out by several generations of geologists, Kampunzu and Cailteux (1999) proposed the following revision of the model as major events of the Lufilian orogeny:

1.4.1 Kolwezian Event (Phase 1)

The Kolwezian event represents a major deformation marked by folding and thrusting of Katangan terranes. Folds associated with this deformation are asymmetric and inclined towards the North, reflecting a northwards tectonic transport. In certain cases, the normal and reverse sides of these folds remain intact. The axial planes of anticlines are usually faulted, and the anticlines are cored by Roan megabreccia. The structures of this phase are dominated by folds verging towards the North locally, South-vergence back-folding and directed thrust sheets. This phase took place between 850 Ma and 690 Ma (François, 1973; Kampunzu and Cailteux, 1999).

1.4.2 Monwezian Event (Phase 2)

This phase is characterised by a regional strike-slip faulting with southward dipping fault planes and localized folding. The D_2 faults cut obliquely across D_1 fold axes. The strike-slip faults have sinistral movement up to 130km. This phase demonstrates sequentially activated major strike-slip faulting with horizontal displacements, generally in NW-SE directions. The dominant kinematics resulted in clockwise rotation of the fault blocks, generating the large-scale convex nature of the Lufilian Arc (Unrug, 1983). This event took place between 690 and 540 Ma (François, 1973; Kampunzu and Cailteux, 1999, Batumike *et al.,* 2007).

1.4.3 Chilatembo Event (Phase 3)

The Chilatembo event is a late transverse fold event, younger than 540 Ma and probably dating from the early Palæozoic. The NE-SW oriented Chilatembo syncline was developed during this event and represents a transversal regional structure. Similarly, several undulations of the D_2 faults with horizontal throw were caused by D_3 folding.

The folded structures are separated by cataclasites called “tectonic breccias” that occur within *écailles* (megafragments) of up to several km, forming part of the RAT (R1), Mines

(R2), Dipeta (R3) as well as Mwashya (R4) and Nguba (Ng) (Demesmaecker *et al.,* 1963; Cailteux, 1991).

Table 2 below summarises all the models supporting tectonic theories about the actual geometric structural architecture of the Lufilian arc and the related timing of events.

Based on evidence observed of evaporitic minerals in several places on both sides (Congolese and Zambian) of the Lufilian Arc (Garlick, 1972; Cailteux, 1983; Cluzel, 1985; De Magnée and François, 1988), Jackson *et al.,* (2003) proposed that during the Lufilian orogeny, the Katangan basin was radically transformed first by extrusion of allochthonous evaporites, then by orogenic shortening. Salt tectonics may explain the existence of mega-breccias which contain large fragments up to 10 km long. In addition, they suggested that salt tectonics began during the deposition of the Roan Supergroup. In the mid-Roan period, small walls and extrusions of evaporate mega-breccia began to be emplaced. In early Kundelungu time, evaporitic diapirs became enlarged. Also, they considered that Lufilian deformation began between 850-650 Ma when diapirs were laterally squeezed and formed salt welds, followed by the intrusion of a large sheet of co-mingled Roan evaporate and carbonate-dolomite sediments. Given that the extrusion so quickly blanketed uniform pre-orogenic footwall units without over-riding any synorogenic deposits, Jackson *et al.,* (2003) theorised that by the continuation of shortening, large thrust sheets were emplaced, lubricated by the pre-existing salt-sediment extrusive sheet. Jackson *et al.,* (2003) conclude that the actual shape of the Lufilian Arc may be controlled by the former northern edge of the evaporitic basin. The following Table 3 summarises the stratigraphy proposed by Jackson *et al.,* (2003) after restoring the thickness of evaporites layers.

	François (1973)	Cahen *et al.,* (1984)		Daly (1986)		Cosi *et al.,* (1992)		Kampunzu and Cailteux (1999)		Key *et al.,* (2002)
Event	**Description**	**Description**	**Age**	**Description**	**Age**	**Description**	**Age**	**Description**	**Age**	**Description**
Lufilian Orogeny	Kolwezian Event - N-vergence overthrusting of the Katangan sediments onto the Congolese craton	Phase 1: Kolwezian Folding - E-W folds with S-dipping axial planes with N-vergence	656 to 503 Ma	Northerly directed (K2) thrusting and folding of the entire Katangan Supergroup in the DRC (Roan through upper Kundelungu); produced klippes and thrusts in the DRC and recumbent, isoclinal curvilinear folds (arcuate folds axes) in NW Zambia; basement involvement in folding and thrusting produced the pattern of the "Domes" region	<850 Ma	D1-Regional recumbent, isoclinal folds (F1) with transposition of limbs associated with northwards thrusting of basement into metasedimentary pile; growth of abundant metamorphic minerals; penetrative planar metamorphic fabric parallel to bedding.	700 MA (Rb-Sr isochrons)	D1-Upright to overturned, asymmetrical, transported folds with northern vergence; faulted axial planes; northward verging imbricate thrust complex that ramps upward through stratigraphy and produced the crustal thickening in the External Fold & Thrust Belt; thrusting along reactivated extensional faults; southward verging back folding	850 to 692 Ma	D1-upright, to overturned to recumbent folds with gently plunging axes trending E-W and NE-SW; open, upright anticline-syncline pair in the Domes area with axes plunging gently 245°; overturned, tight folds overprinting an earlier N-S trending open folds in the External Fold and Thrust Belt; northward vergence, SSE dipping, thrusting of basement and cover sequence (Kakoma-Kamano Thrust); folding pre and post-dates thrusting; moderate to steeply dipping (to SE) foliation with down dip lineation
		Phase 2: Epirogenesis-Uplift of the Kundelungu Plateau in southern Zambia								
	Kundelungan Event – S-vergence folding (back-thrusting?)	Phase 3: Kundelungu Folding - E-W folds with vertical or N-dipping axial planes, locally with S-vergence				D2-Regional recumbent, tight to isoclinal folds (F2) and continued thrusting; F2 fold axes plunge 10-20 to the ENE (axial plane dips 10-20 to NNW) and plunge 10-25 to the NNE (axial plane dips 10-20 to the WNW); mineral lineations (S2) penetrative axial-planar foliation, and crenulation metamorphic fabrics; metasomatic minerals formed, scapotitization	Syn to post-metamorphic episode 490±30Ma (K-Ar/Rb-Sr on Musc.)			D2-open folds with N, NW & NE trending axial traces plunging southward; formation of an axial planar cleavage with localized crenulation of D1 foliation
	Monwezian Event-E-W trending strike-slip faults with breccia-breached anticlinal cores	Phase 4: Monwezian Faulting-faults with E-W trends						D2-Regional strike-slip faulting with southward dipping fault planes and localized folding; D2 faults cut obliquely across D1 fold axes strike-slip faults have sinistral movement up to 130km with throw of breccias of Roan stratigraphy along the faults, especially at the intersections of D1 anticlines (extrusion tectonics); synchronous with intrusion of Hook granite (ca 566Ma)	690 to 530 Ma	D3-NE and NW trending faults related to regional uplift
		Phase 5: Transverse Folding - folding perpendicular to the main trends of the Lufilian Arc				D3-Regional upright, open, conical folds producing km-scale undulation of the F2 fold axes (folds S2 mineral lineations); no metamorphic fabrics produced (no new growth of metamorphic minerals); interference folding created "domes"		D3-Regional scale, upright folds trending NNE (20) through ENE (60); both N-S trending and E-W trending faults; called the Chilatembo Event of the Lufilian Arc	< 540 Ma	

Table 2: Summary of the timing and Deformation Events within the Lufilian Arc.

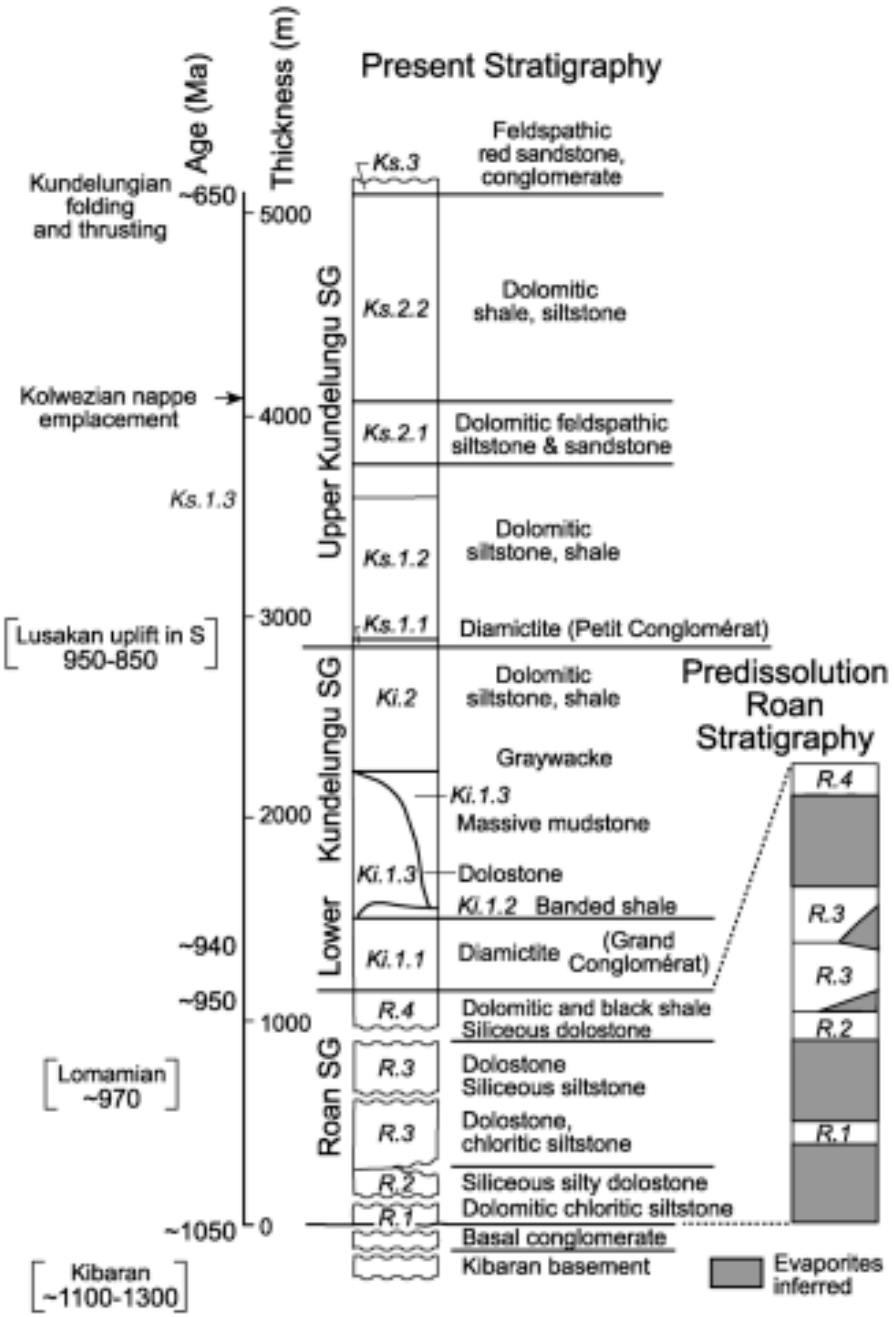

Table 3: Katangan stratigraphy column and dates of major tectonism in southern Katanga (Jackson *et al.,* 2003)

Table 3 shows stratigraphy and symbols after François (1973) and De Magnée and François (1988); ages based on Cahen *et al.,* (1984). The side column shows qualitively restored evaporite thickness inferred in the original Roan Group by De Magnée and François (1988). This restored column is similarly scaled but is twice as thick because of the inferred evaporates, whose actual thickness is conjectural. Basal units below R.1 are unknown in Katanga and are based on the Zambian Copper Belt. (All the data related to age are taken from Jackson *et al.,* 2003).

Recently, Wendorff (2000; 2003; 2005a; 2005b) offered a reinterpretation of the structural evolution of the Lufilian Arc based on field evidence from Zambia, which indicates that the

first orogenic movements marking the change from extensional to contractional regimes occurred after deposition of the "Grand Conglomérat" and prior to the "Petit Conglomérat" glaciations and resulted in the first foreland basin. His conclusion is supported by the stratigraphical association of the "Grand Conglomérat" with the youngest extension-related Katangan volcanic rocks, giving a U-Pb zircon age of c. 735 Ma (Key *et al.,* 2001). Moreover, he postulated that the mega-breccias are a syntectonic sedimentary association, deposited in response to a pronounced uplift of source regions composed of Katangan rocks. He reinterpreted the stratigraphy within the Katangan Supergroup, enabling the identification of two previously unknown basins within the Lufilian Arc, the Nguba basin and the Fungurume basin. Furthermore, Wendorff (2003) placed new constraints on the tectonic evolution of the belts. He also suggested that the continental red bed sandstones, siltstones and carbonate-clast conglomerate of the RAT Group (R1), dolomitic rocks of the Mines Series (R2) and the haematite-rich carbonate-clasts conglomerates, sandstones, siltstones and shallow marine limestones of the Dipeta (R3) constitute an intact succession unconformably overlying the Zambian Roan sediments. This is contrary to the findings of Cailteux *et al.,* (1994) and Kampunzu and Cailteux (1999) who interpreted DRC Roan as thrust sheet fragments emplaced towards the North and accompanied by breccias. These breccias are often but not always mineralised.

Several models have been proposed to explain the sediment-hosted copper-cobalt mineralisation in the Lufilian Arc. All these models fall within three majors schools which are: epigenetic-magmatic (Bateman, 1930; Davidson, 1931; Gray, 1932), syngenetic (Garlick, 1961; Fleischer *et al.,* 1976; Okitaudji, 1989; 2001) and diagenetic (Bartholomé *et al.,* 1973; Bartholomé, 1974). Recent studies in both the Zambian (Bara *et al.,* 2004; Selley *et al.,* 2005, Broughton *et al.,* 2007) and the Congolese (Cailteux *et al.,* 2005; Dewaele *et al.,* 2006; El Desouky *et al.,* 2007; Muchez *et al.,* 2007) Copper Belts emphasise a multiphase origin of copper mineralisation.

Dewaele *et al.,* (2006) suggest that the main phase of the stratiform mineralisation precedes the Lufilian orogeny and that faults and fractures formed during this event affected the pre-existing mineralisation and remobilised minor quantities of Cu-Co minerals. Supergene alteration along faults and fractures resulted in an enrichment of the mineralisation, with the formation of secondary Cu-oxides, Cu-carbonates and Cu-silicates.

In Kinsevere, both sulphides and oxides are either disseminated in sandy layers or fill bedding planes, reactivated bedding, fractures and joints. The sulphide mineralogy includes pyrite, chalcopyrite, bornite and chalcocite, although in the supergene zone, sulphides are partially or completely replaced by malachite and other copper oxides (Houda, 2008; Anvil Exploration, 2008).

Given that no agreement has yet been reached about the structural evolution of the Lufilian Arc, the simplest way to achieve consensus will be to conduct a palaeostress study within the entire Lufilian Arc (western, central and eastern parts along the SE-NW, S-N and SW-NE sections respectively) with the objective of achieving a better understanding of all aspects of

its structural evolution. Similarly, the objective of the present study, as shown below, is aligned with the reinterpretation of the entire above hypothesis.

1.5 Aims

This study investigates the structural evolution of the Kinsevere copper deposit by an analysis of the palaeo-stress tensors registered throughout the Lufilian orogeny; determines the geodynamic context in which these strains occurred and, finally, links the copper mineralisation found in fractures to tectonic events of the Lufilian orogeny.

1.6 Methodology

1.6.1 Fieldwork

Fieldwork was conducted from June to August 2009 and involved geological mapping, core logging and drill core sample collection. Additional geological mapping was done during a week's field visit in April 2010. Fieldwork focused on all three Mines Series fragments of the Kinsevere copper deposit; Tshifufiamashi to the North, Tshifufia known as the "Central Pit" and Kinsevere Hill to the SE (Fig. 8).

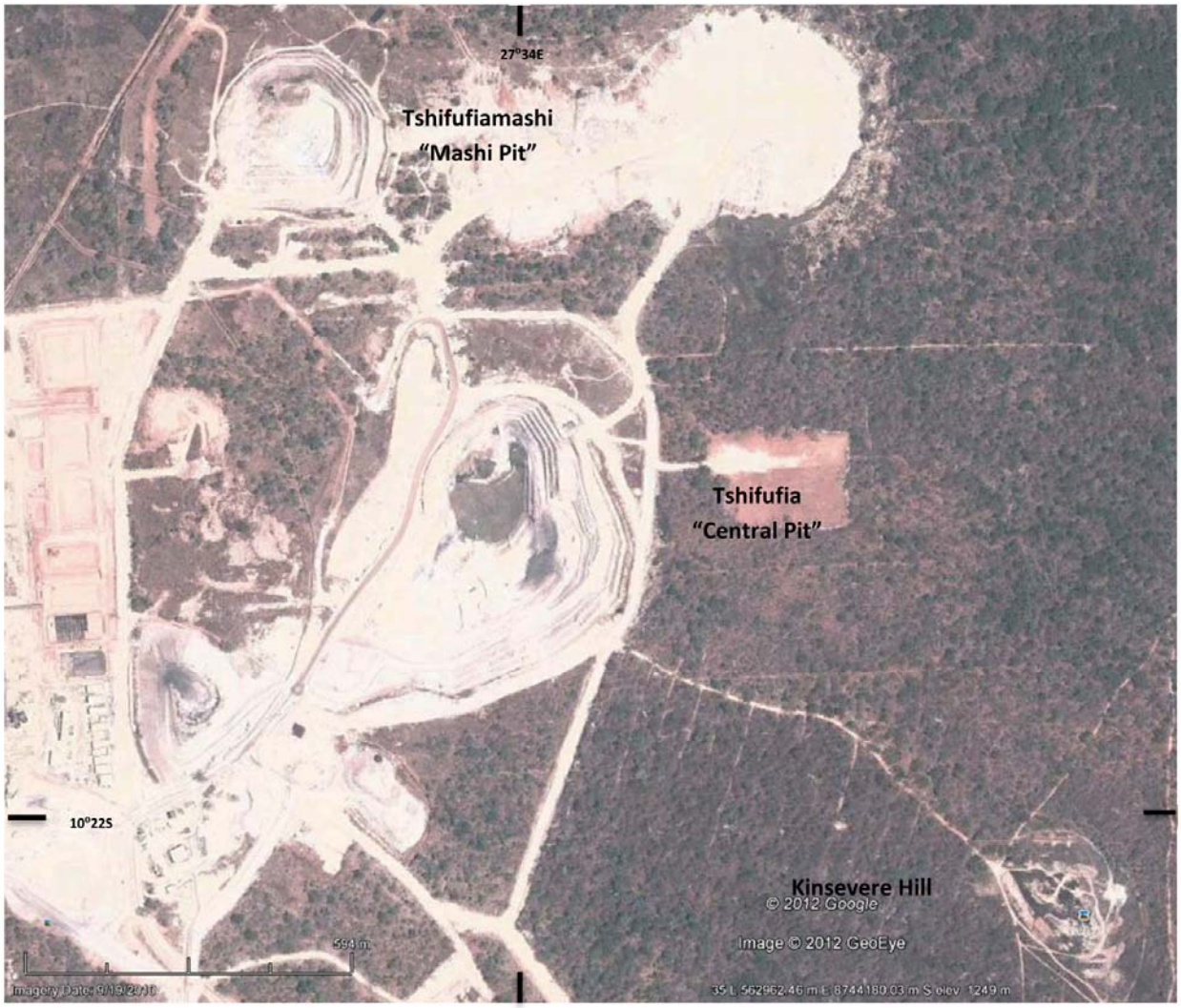

Figure 8: Google Earth image of the Kinsevere area.

1.6.2 Structural analysis

The field data measurements of the following planar and linear structures were taken:

1. For planar structures, dip and dip-direction data for bedding planes, fold axial planes, joints, fractures and slickensides planes were measured;

2. For linear structures, plunge and trend for lineations of hinge lines and slicken lines, including the sense of movement across slickensided planes, were collected throughout all three *écailles* of the Kinsevere copper deposit.

The structural analysis was undertaken using stereographic projection of field data which were regrouped by type and by fragment. The lower hemisphere of a Schmidt projection was used.

Filed data on mineralised and unmineralised joints were treated separately but regrouped into the same section; however, fault planes, slickensided fault slip data and shear fractures were treated together.

The improved right dihedral method (RDM, Angelier and Mechler, 1977; Angelier, 1994) combined with the rotational optimisation procedure (ROP, Delvaux and Sperner, 2003) were used to conduct the palaeostress analysis in the Kinsevere area.

The improved right dihedral method is based on the distinction, for each set of faults F, between two compressional right dihedrons and two extensional ones. The three orthogonal principal stresses σ_1, σ_2 and σ_3 coincide with the intersection of the dihedral planes. These principal stresses may be obtained graphically or numerically for a population of compatible fault measurements (Angelier and Mechler, 1977; Angelier, 1989; Delvaux and Sperner, 2003). This method allows the estimation of the stress ratio (R), the use of tension and compression fractures in combination with slickenside data and an initial separation of the data to be performed on the basis of the counting deviation.

The rotational optimisation procedure (ROP) is an iterative grid-search procedure using the misfit function F5 in the Tensor program and using the results (set) obtained by the RDM as the starting point for the optimisation (Delvaux and Sperner, 2003). This procedure allows simultaneous minimisations of the slip deviation angle for slickensides, the maximisation of shear stress for fault plans and shear fractures, the minimisation of normal stress for tension fractures and the maximisation of the normal stress for compression fractures.

Two structural software programs were used to complete this analysis; WinTensor which combined the two methodologies used in this work (right dihedral method and rotational optimisation procedure) and Stereo 32.

Chapter 2

KINSEVERE GEOLOGY

2.1 Background

The Kinsevere deposit was discovered around 1920 and has undergone several Cu–Co mining phases conducted by UMHK ("Union Minière du Haut Katanga"). During the 1990s the Tshifufia and Tshifufiamashi prospects were the subject of a joint venture between Gécamines and EXACO sprl, a local Congolese company interested primarily in exploiting near-surface, high-grade, cobalt oxide resources. The joint venture was restricted to cobalt resources within 30 metres of the surface and 67 holes were drilled into the Tshifufia and Tshifufiamashi deposits by EXACO, the majority of which were vertically orientated, and down the dip of the ore bodies. These boreholes were drilled to test the distribution and grade of the cobalt oxide mineralisation. Gécamines also carried out preliminary investigations and some drilling on Kinsevere Hill, Tshifufia Central, in the southern part of Tshifufia Central and at the Tshifufiamashi deposits during the early 1990s.

Subsequent to these investigations, an open pit was developed by EXACO to a depth of 30 metres on the Tshifufia South prospect. In June 2004, Anvil Mining Limited signed an agreement with MCK (Mining Company Katanga) which opened a joint venture agreement with Gécamines.

Outcrop in the vicinity of the Kinsevere deposits is limited, with less than 1% of total surface area having suitable outcrop to allow for detailed geological mapping. Therefore, regional maps have largely been generated from satellite imagery, previous work and sampling by Gécamines and data obtained from exploration drilling and from old outcrop such as Kinsevere Hill.

Kinsevere Hill is an unexploited low hillock, underlain by steeply West-South-West-dipping Mines Series (lower Roan Group) rocks, hosting predominately malachite mineralisation along its entire outcrop length. Kinsevere Hill is approximately 250m long, 110m wide and rises about 20m above the surrounding ground (Fig. 9)

The central and southern part of the Tshifufia fragment is made up of steeply East-South-East-dipping Mines Series rock formations and is mined to a depth of 58 metres. Mineralisation is made up primarily of malachite, although considerable enrichment of cuprite occurs in specific zones. All three ore bodies (the lower ore body [LOB], upper ore body [UOB] and the third ore body [TOB]) are found within the Tshifufia fragment and are intensely deformed with the bedding planes associated with mineralisation generally dipping steeply to the East at about 75° and being locally overturned, dipping West (Fig. 10).

In the Tshifufiamashi fragment, the Mines Subgroup formations outcrop over a strike length of approximately 300m and a width of approximately 200m (Fig. 9). As with the other fragments described above, a similar lithological succession is present. In contrast to the Tshifufia fragment, the beds are not overturned and dip moderately to the West. A fault is

inferred to separate the westward-dipping Tshifufiamashi strata from the generally eastward-dipping Tshifufia Central strata (section B-B').

2.2 Local geology

Broadly speaking, the following three major stratigraphic units outcrop in the Kinsevere area (Fig. 9):

1. Neoproterozoic strata of the Kundelungu Supergroup, characterised by undifferentiated dolomites, sandstones/mudstones and shale, which together with the "Petit Conglomérat" form the Kalule Subgroup, recently re-named the Gombela Subgroup (Batumike *et al.,* 2007). They outcrop in the East, South-East, South and West of the Kinsevere mine. In the Kinsevere area, these formations are represented by the Ku 1.2 (Table 6) rocks, which consist of alternating purplish and grey finer-grained sandstone, with a thick bed of dark grey dolomite-poor sandstone/schist.

2. Lower Roan Group formations (Neoproterozoic): these are represented by siliciclastic Mines Series rocks and host the Cu-Co mineralisation in the Kinsevere area. The Roan Group outcrops are bound by NNW-SSE and WNW-ESE striking, steeply-dipping faults (Fig. 9), which are interpreted as steeply-dipping reverse faults which exhumed Roan Group strata to a shallower level in the three areas. All the Kinsevere outcrops can be considered as partially preserved limbs of a large-scale fold sequence. Within these limbs, bedding planes are exploited as faults locally, suggesting layer-parallel slip to accommodate folding. As a consequence, the strata at Kinsevere are highly fractured and faulted and dip either to the East (Tshifufia) or to the West (Tshifufiamashi and Kinsevere Hill). These opposite-dipping fragments are separated by two sinistral strike-slip fault and are surrounded by heterogeneous breccias associated with undifferentiated RAT (see Map [Fig. 9] and sections B-B', C-C', E-E' and A-A' below) which lies above the Kalule strata to the East and West on a faulted contact.

3. Breccias: two types of breccia are encountered in Mines Subgroup rocks in Kinsevere; the heterogeneous breccia know as RAT breccia which contains all Mines Subgroup *écailles* and the monolithic breccia comprised mainly of angular clasts with an argillaceous matrix and hosted by the CMN.

Within the Roan Group, described above, major lithologies intersected in the drill holes and exposed in the mine are described below, from the oldest to youngest (Table 4):

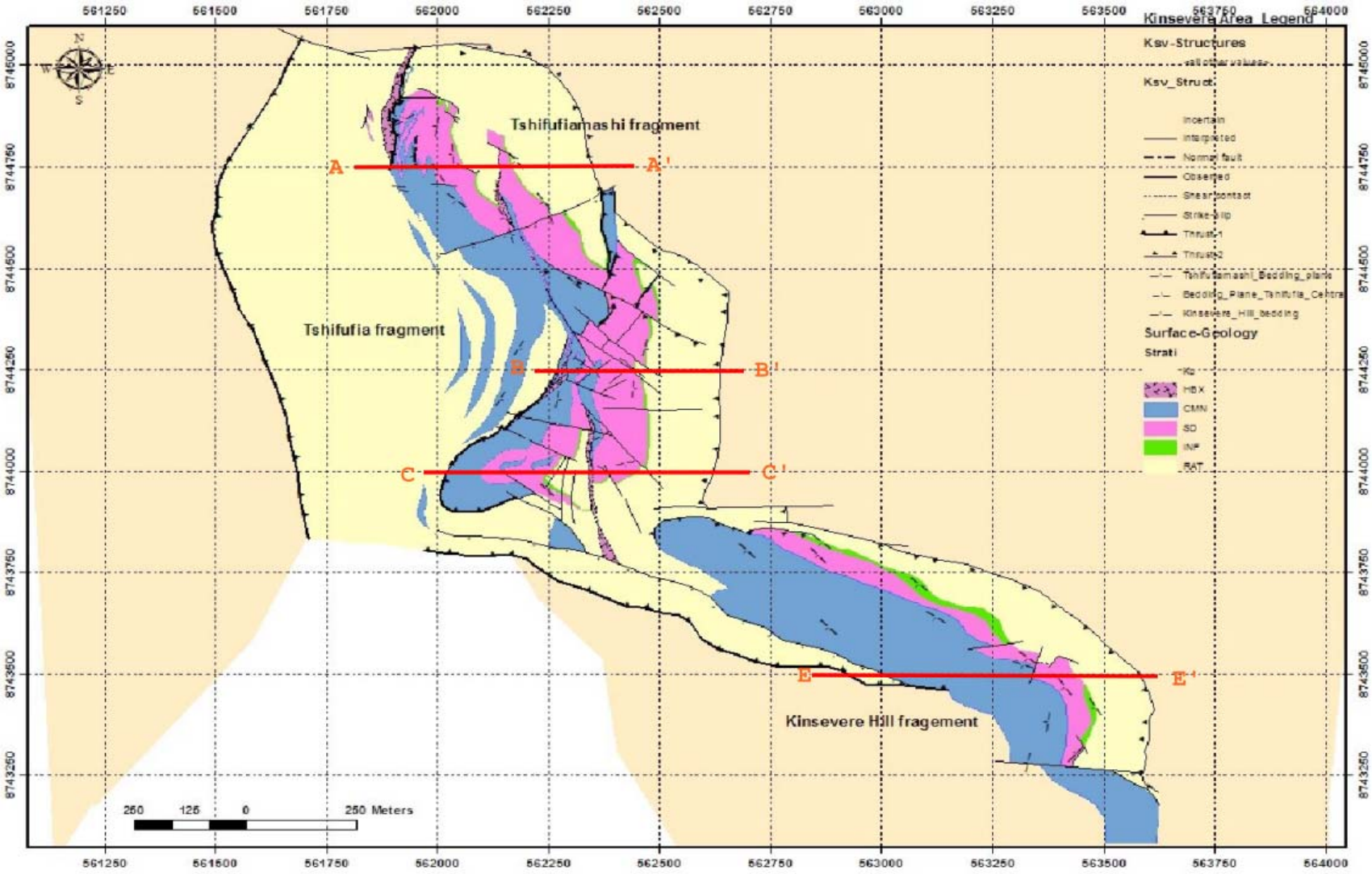

Figure 9: Geological map of the Kinsevere Copper Deposit. (Compiled under the supervison of B. Houda, Anvil Exploration, 2008).

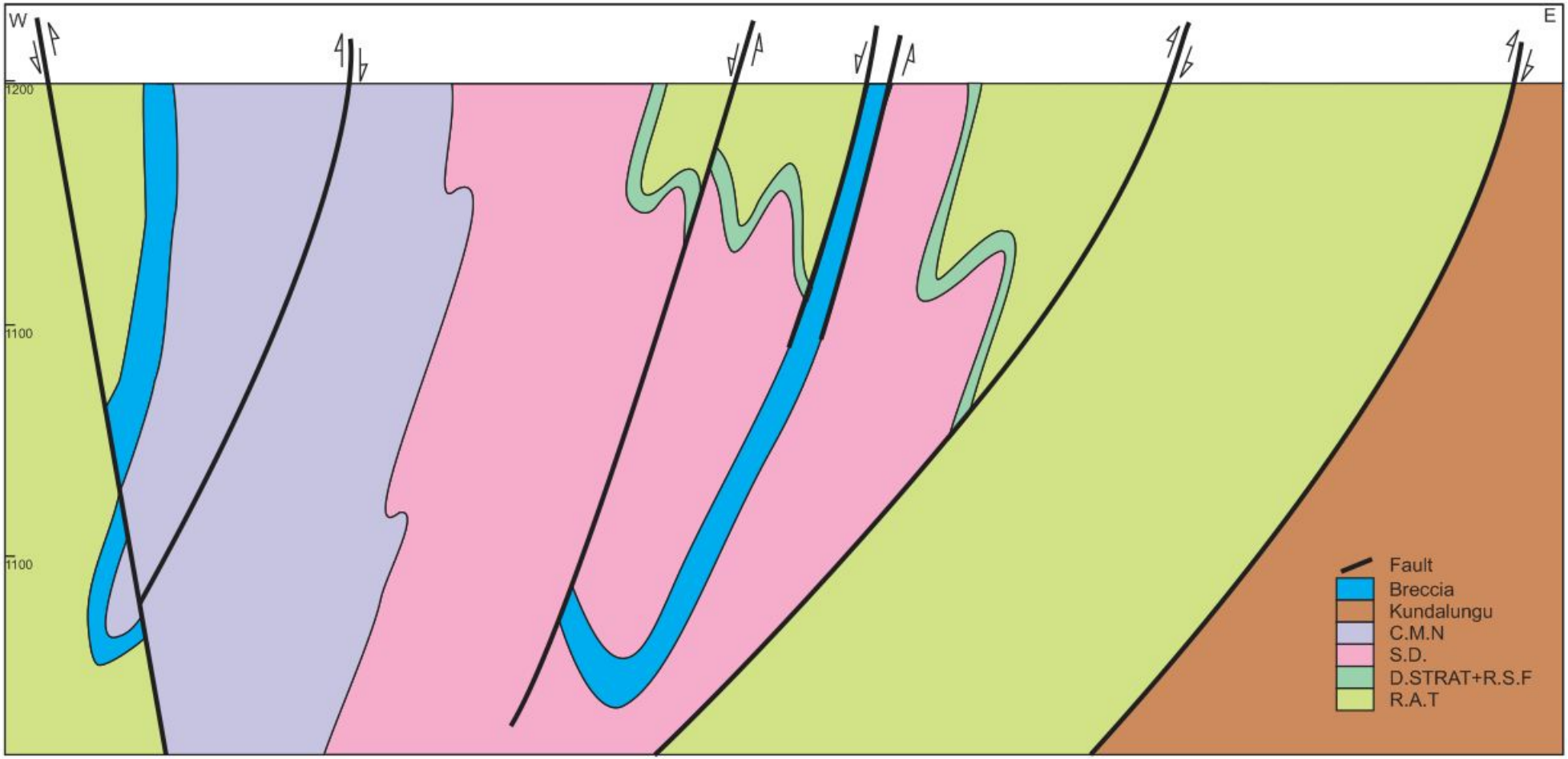

Figure 10: Section A-A' along the central part of the Tshifufiamashi fragment. E-W steeply dipping cross-section showing a duplication of R2 Mines Subgroup rocks with the Roan Breccia. All strata are dipping West and show a faulted contact with the Kundelungu.

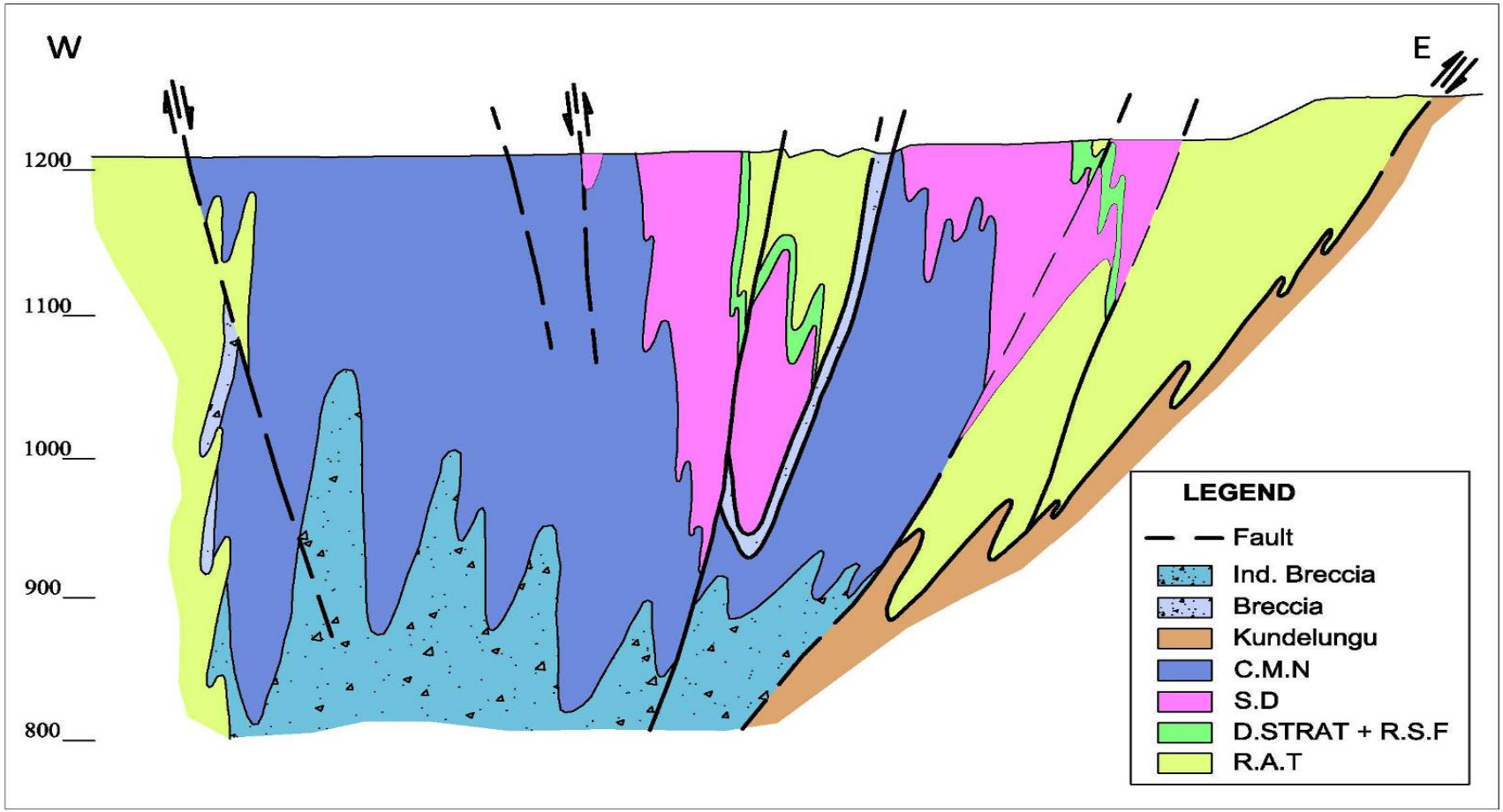

Figure 11: Section B-B' along the central part of the Tshifufia fragment.

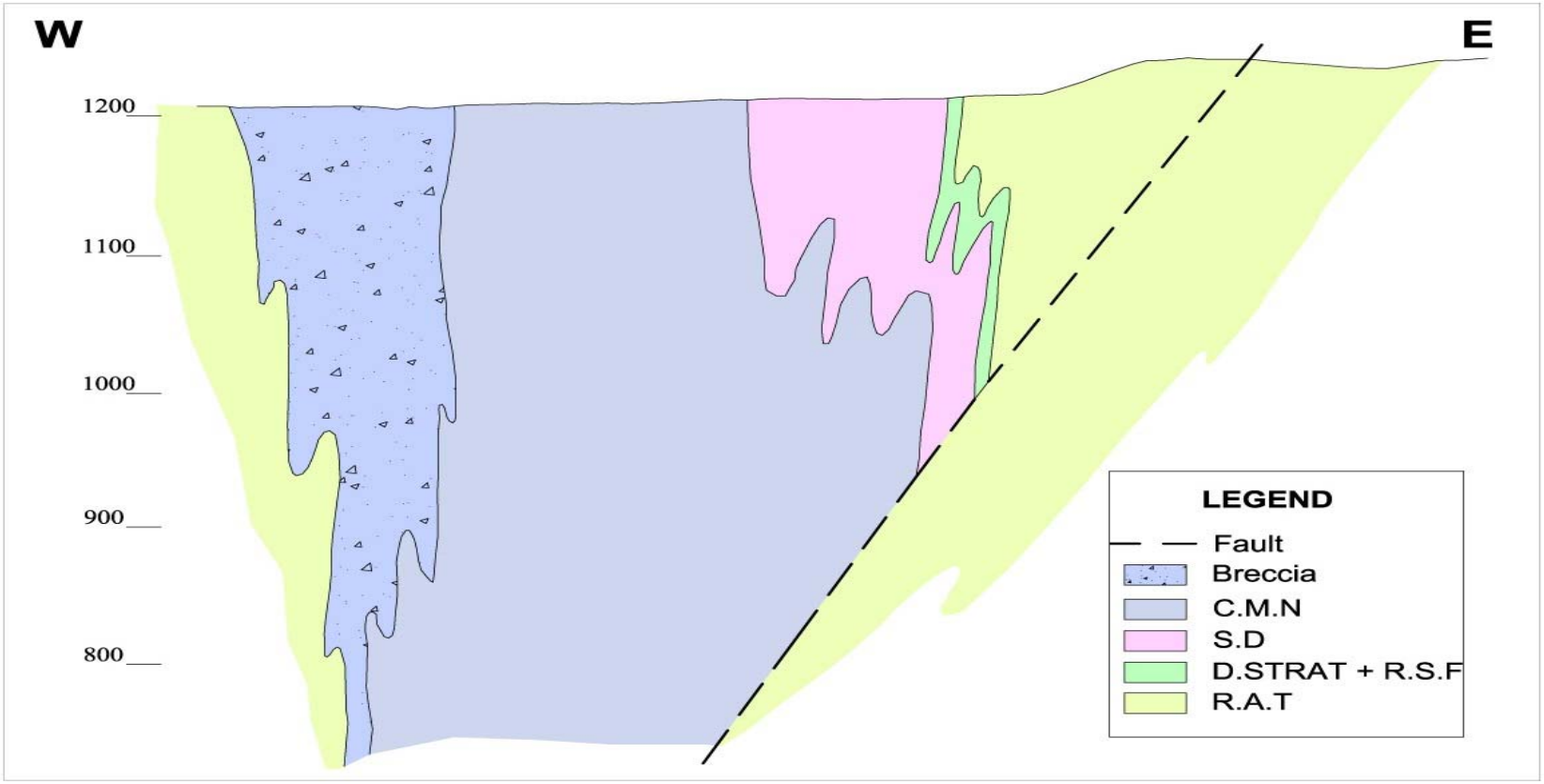

Figure 12: Section C-C' along the south part of the Tshifufia fragment. The known Roan breccias have outcropped in the eastern side of the mine. Small-scale folds are observed in the CMN strata. (Anvil Exploration, Houda B., 2008)

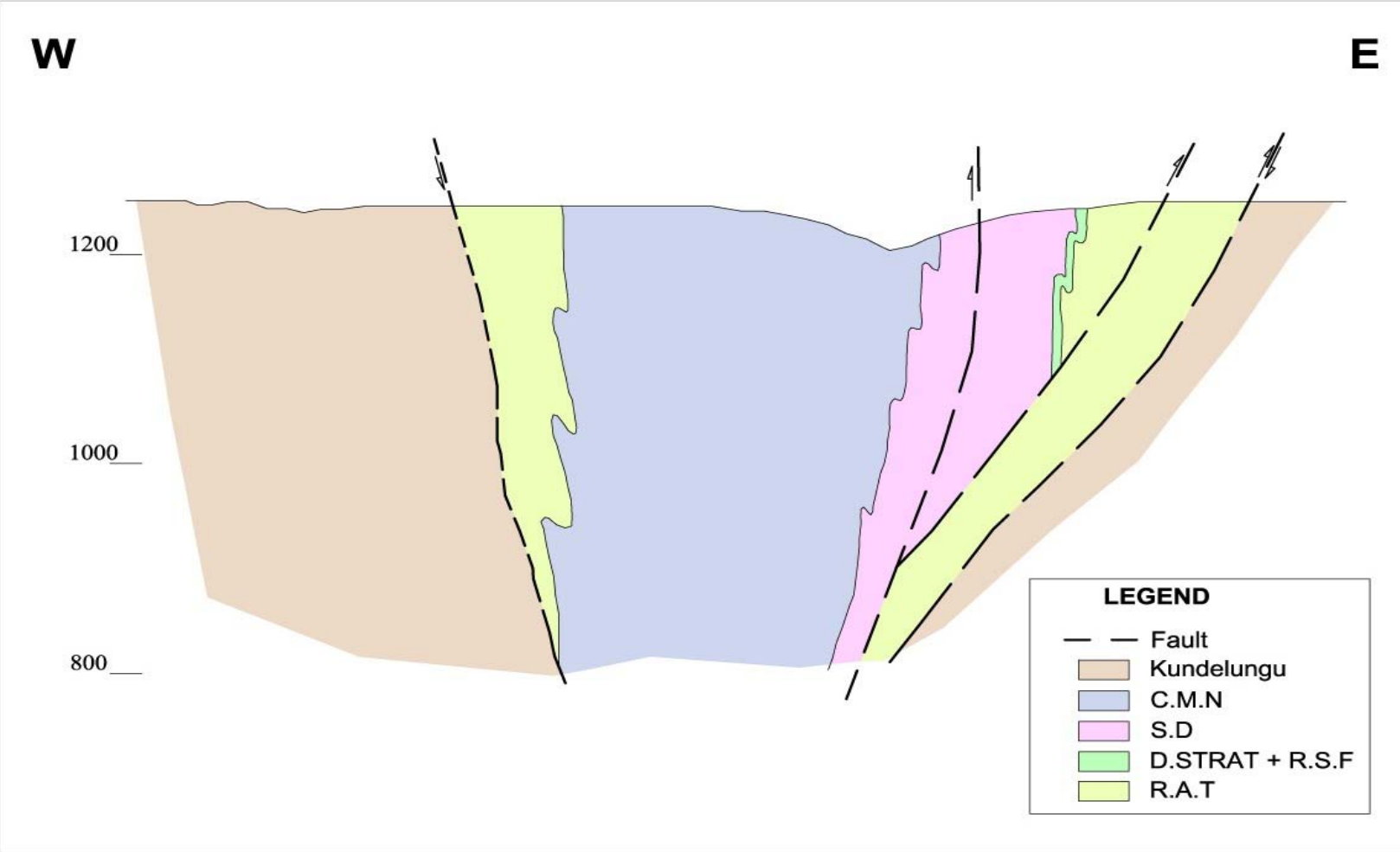

Figure 13: Section E-E' along the Kinsevere Hill fragment.

Figure 11 shows the section showing the R2 fragment affected by multiple faults that are associated with thrusted faults. Small-scale folds are observed in the eastern side of the Mine where CMN has outcropped. The known Roan breccia appears along the thrusted fault in the core of the reverse limb and undifferentiated breccia appears below the entire limb. (Anvil Exploration, Houda B., 2008)

2.2.1 RAT Subgroup (R1)

In the classic Katangan stratigraphic scheme (Cailteux, 1994), the basal unit of the system in the DRC is the RAT (Roche Argilo-Talqueuse**)** Subgroup (R1). It has been subdivided into three formations, based on drill core intersections from Kamoto in the Kolwezi region (Oosterbosch, 1962). These three formations are as follows: (i) R1.1 (40m) irregularly striped sandy purple-red pelite with minor dolomite; (ii) R1.2 (45m) pink to purple-grey argillaceous siltstone with minor dolomite; interbedded sandstones occur at the base of the unit and a pink silicified, locally stromatolitic dolomite occurs at the top; (iii) R1.3 (150m) pink-lilac chloritic dolomitic siltstone (Fig. 14).

In the Kinsevere area, the RAT Subgroup differs from that described by Oosterbosch (1963). The RAT Subgroup can be subdivided into two different sub-units: the Red RAT and the undifferentiated RAT. The Red RAT (probably the R1.3) consists of 15-20m thick of pinkish-white massive, moderately fractured sandstone with pervasive talc impregnation and manganese oxide in fractures, becoming bedded towards the top, overlain by 15-18m of a pinkish-red diffusely bedded to massive siltstone with hematite staining along bedding planes and manganese oxides in fractures. These stratified RAT rocks are generally barren or poorly mineralised in copper, though often malachite and heterogenite (Co+3O (OH)) can be found in fractures within this RAT. This copper mineralisation is found in the top 1-3 metres of the Red RAT. The Red RAT in the Kinsevere area is affected by brecciation, resulting in a 1-2m thick cross-cutting layer of monolithic crackle breccia, containing angular clasts with strong limonite staining toward the top. This breccia often hosts malachite mineralisation (Fig. 15).

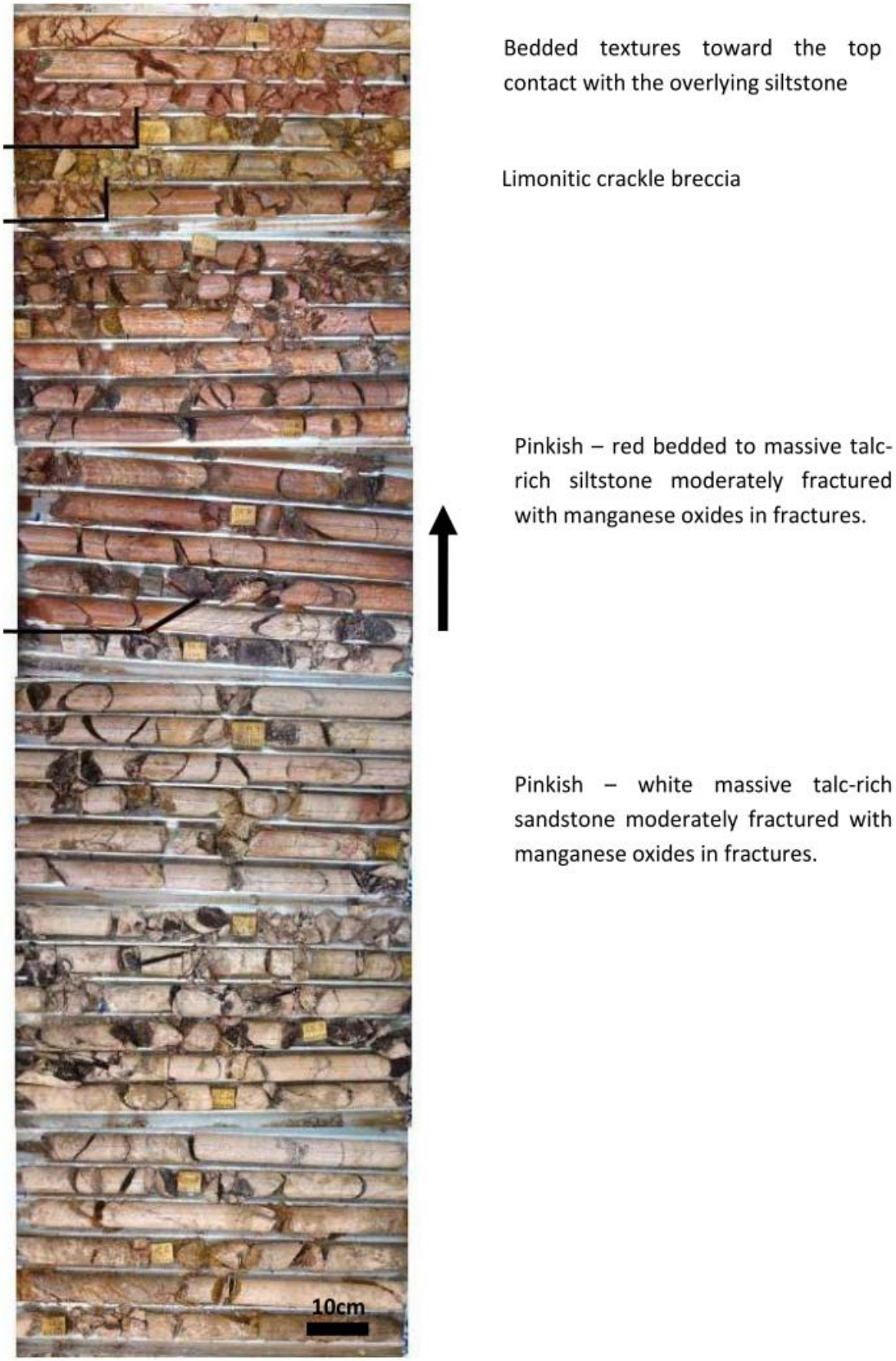

Figure 14: Sub-unit lithologies of the R1.3 at Kinsevere-TCDH027

Figure 15: Heterogeneous breccia occurring copper oxides, mostly malachite mixed with red iron oxides (limonite and hematite)-TCDH032-Tshifufia fragment.

However, the pinkish-white talc-rich and dolomitic siltstone is fractured and shows fractured fabrics at an angle of 50° to the core axis near the top contact with the breccia (Fig. 15).

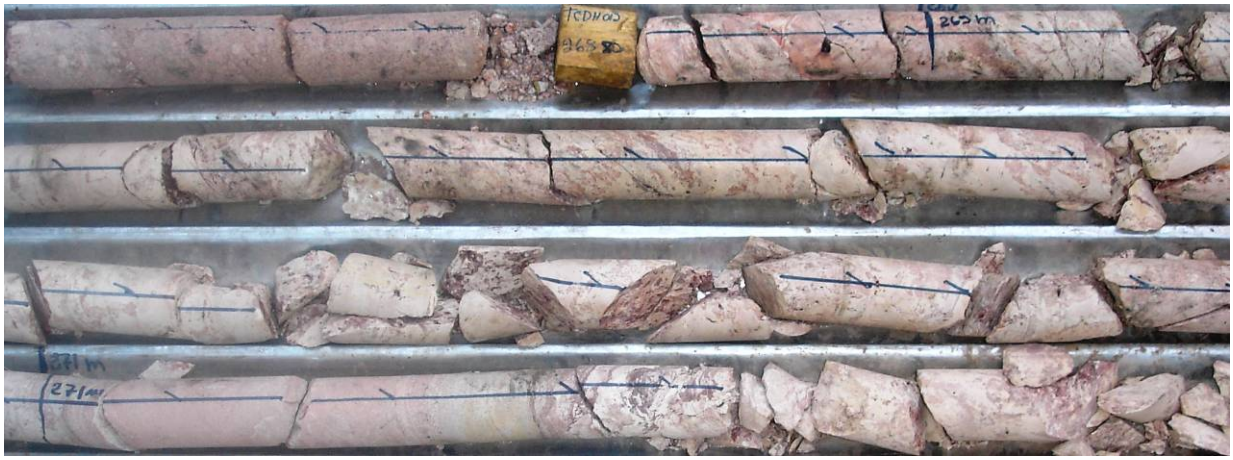

Figure 16: Pinkish-white massive talceous siltstone affected by banded fabric, RAT-R.1.3 overlain by the heterogeneous breccia through a shear contact down to 268.80m (TCDH012-Tshifufia).

The undifferentiated RAT consists of massive siltstone showing greenish-pink colouration due to a significant chlorite alteration and contains calcite veins parallel to the bedding (Fig. 17). This unit is rarely mineralised except for some malachite along a few discrete fault planes in open pit outcrops and alternating with highly tectonised zones.

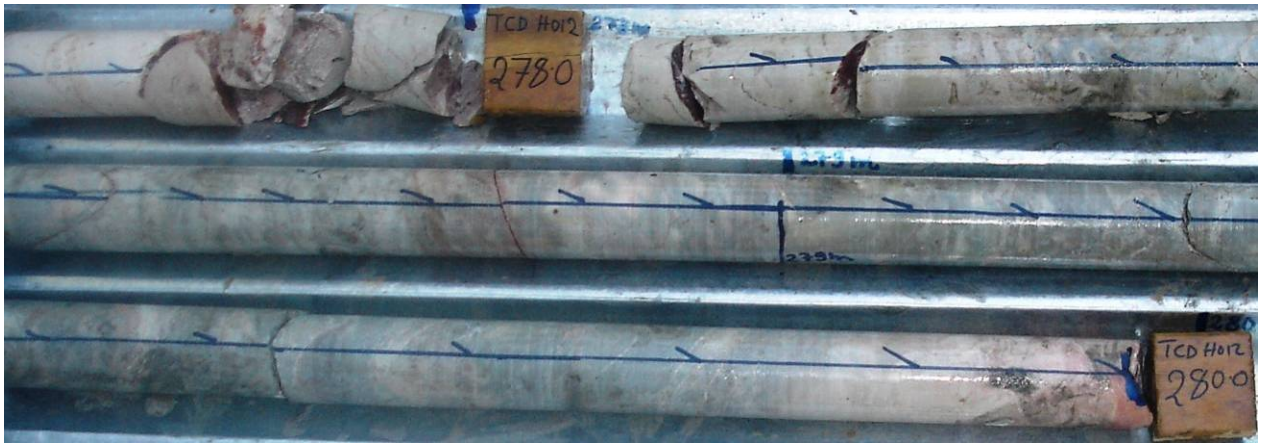

Figure 17: Greenish-pink diffusely laminated fresh dolomitic siltstone - Undifferentiated RAT (TCDH012-Tshifufia fragment)

Pinkish red-purple massive sandstone, overlying a brownish pink bedded fine grained talc-rich siltstone. Generally, deformation fabrics are not visible in weathered facies except slickenside planes (Fig. 18).

Figure 18: Open pit outcrop of pink massive talceous siltstone showing a slicken surface (Central Pit-Tshifufia).

In addition to the work described above, many geochemical and petrographical studies were conducted in several deposits within the Lufilian Arc (e.g. Luiswishi located about 26 km South of the Kinsevere copper deposit).

Petrographically, these studies reveal that in the southern part of the Congolese Copperbelt, the red RAT contains quartz (detrital and diagenetic overgrowths), chert, diagenetic Mg-chlorite and dolomite as the main rock-forming minerals (>90 vol. %). Accessory detrital and diagenetic minerals include tourmaline, green chlorite, micas, monazite, apatite, dahlite, leucoxene-rutile and sulphides. Sometimes, metamorphic minerals are included and are mainly phengitic muscovite and phlogopite (Audeoud, 1982; Okitaudji, 1989; Cailteux *et al.,* 2005).

Numerous geochemical, petrographical and fluid inclusion studies indicated that the red RAT was deposited in a confined evaporitic environment (Pirmolin, 1970; Bartholome *et al.,* 1972; Katekesha, 1975; Cailteux 1978, 1983, 1994; Audeoud, 1982; Guilloux, 1982; Cluzel, 1985, 1986; Okitaudji, 1989; Cailteux *et al.,* 1994; Tshiauka *et al.,* 1995; Loris, 1996 and Cailteux *et al.,* 2005).

2.2.2 Mines Subgroup (R2)

The Mines Subgroup, formerly called the Mines Series (François, 1973, 1974), constitutes the most significant set of host rocks of the Kinsevere copper deposit. The Mines Subgroup is the most well-known stratigraphic section of the Neoproterozoic Roan Group on account of its Cu-Co mineralisation. The Mines Group is categorised into five facies types, identified as follows by François (1973): Musonoi, Long, Kilamusembu, Kalumbwe and Menda facies.

Of these five facies, only the Menda is represented at Kinsevere. This facies is characterised by the absence of the siliceous stromatolitic dolomite (RSC) and the presence of three graphitic beds within the dolomitic shales (SD) sequence.

GROUP	SUB-GROUP
Kundelungu (Ku) (formerly Upper Kundelungu)	Plateaux (Ku3)
	Kiubo (Ku2)
	Kalule (Ku1)
Nguba (G) (formerly Lower Kundelungu)	Monwezi (G2)
	Likasi (G 1)
Roan (R)	Mwashya (R4)
	Dipeta (R3)
	Mines (R2)
	R.A.T (R1)
Base of the R.A.T sequence unknown 900 Ma	
Basal conglomerate	

FORMATION	MEMBER	Lithologies
Kambove Dolomite (R2.3) (formerly C.M.N)	Upper	Pinkish-brown to white dolomite, talceous dolomite, evaporitic breccia, red siltstone
		Dolomite, stromatolites, talceous dolomite, evaporitic breccia, grey-green siltstone
		Pinkish-brown to white massive dolomite
	Lower	Massive stromatolitic dolomites, crypto-algal & laminated talceous dolomite
		Laminated algal dolomite
		Massive dolomite, stromatolites, dolomitic shale
Dolomitic Shales (R2.2)	S.D.3b	Carbonaceous dolomitic shale
	S.D.3a	Dolomitic shale, shaly dolomites
	S.D.2d	Carbonaceous dolomitic shale
	S.D.2b+c	Dolomitic shale, shaly dolomites
	S.D.2a	Carbonaceous dolomitic shale
	B.O.M.Z	Black ore mineralised zone
	S.D.B	Basal ore mineralised zone
Kamoto Dolomite (R2.1)	R.S.C	Silicified Stromatolitic Dolomite *Not present at Kinsevere
	R.S.F	Thin laminated silicified dolomites
	D. Strat.	Stratified Dolomites
	Grey R.A.T	Grey-green dolomitic siltstone/Sandstone

Table 4: Lithostratigraphy of the Katangan Supergroup and Mines Subgroup at Kinsevere.

2.2.2.1 Kamoto Dolomite Formation (R2.1)

The Kamoto Dolomite is the lowermost formation of the Mines Subgroup and sits unconformably on a heterogeneous breccia known as the Roan Breccia (sometimes known as the RAT Breccia).

Four sub-units have been defined within the Kamoto Dolomite which are, from the oldest to the youngest: the Grey RAT, the D.Strat, the RSF and the RSC.

As shown in Table 4, the RSC, which is found elsewhere within the Lufilian Arc and is characterised by stromatolitic dolomite, is not present anywhere at Kinsevere. The upper contact of the Kamoto Dolomite Formation is therefore transitional between RSF (uppermost Kamoto) and SDB (lowermost Dolomitic Shales Formation) (Fig. 19). Each of the three units within the Kamoto Dolomite Formation will now be considered in greater detail.

Figure 19: Transitional contact of RSF with SDB-Tshifufia fragment (absence of RSC).

2.2.2.1.1 The Grey RAT

The GRAT (R2.1.1) is known as the lowermost sub-unit of the Mines Subgroup (R2) (Cailteux, 1977b, 1978, François, 1974, Cailteux *et al.,* 2005). In the Kinsevere area the GRAT presents essentially two facies. The proximal facies in the upper part, immediately below the DStrat shows a thickness of 3 to 4.5m and the distal is observed in the lower part and presents a thickness of 3 to 16m.

The proximal facies of GRAT (Fig. 20) comprises reduced pale olive to pale greyish-olive and beige argillite (when not weathered) with minor sandy component and may be partly bedded with erratic medium-grained quartz particles. This facies is not well developed and in completely absent in the Tshifufia fragment. Around 1-2m from the top contact, there is a zone of very thin (2 to 8mm) lenticular siliceous bands or short lenses, sometimes with a worm-like appearance, that follow diffuse bedding planes about 2-4cm apart. This sub-unit is well developed in the Tshifufiamashi where continuous unbroken laminae occur in a zone at least 50cm wide. These siliceous laminae are often replaced by very fine-grained pyrite and locally by chalcopyrite and, where weathered, they give rise to limonitic or hematitic layers and frequently developed, although less common, ellipsoid evaporitic nodules (<2cm long) in this zone, often replaced by chalcopyrite or pyrite, are observed. This unit shows normally sharp basal contact with an increase in reddish hematitic staining towards the base.

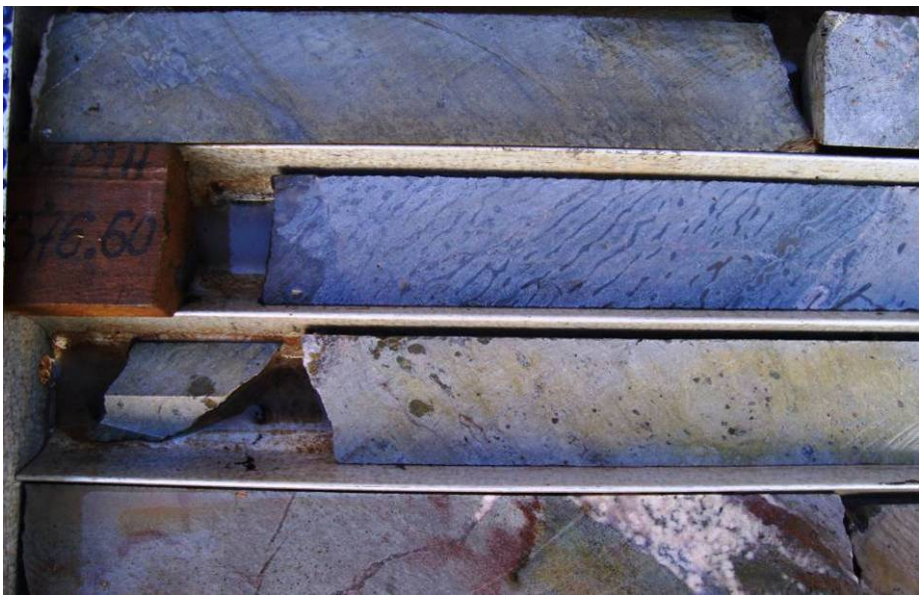

Figure 20: Proximal facies of GRAT showing erratic siliceous bedding and evaporitic textures and occurring fine grained replacement chalcopyrite. TCRD003-Tshifufia fragment.

The distal facies (Fig. 21) consists of a cream to ivory to very pale grey beige massive and homogeneous argillite, but very pale red or pinkish where weathered, with prominent hematite staining locally dominating the rock especially towards the top. In places, this facies shows rare minor, diffuse, almost anastomosing bedding texture and frequently contains >10-30% very small pseudomorphs forming tiny vugs where weathered. In proximity to well-mineralised younger sediments, this facies shows joints and veinlets of malachite increasing towards the stratigraphic top margin. This unit shows a gradational contact with the lower contact into RAT (Red RAT).

Figure 21: Distal facies of GRAT underlying the proximal facies of GRAT. TCRD003-Tshifufia fragment.

In the weathered facies the Grey RAT consists of massive, medium-grained slightly dolomitic siltstone showing a tannish-yellow to orange-grey colouration. This rock can be locally strongly deformed and fractured. Minor copper oxide mineralisations are found in these fractures. Often malachite is mixed with heterogenite and manganese oxides. In places, the Grey RAT shows a reddish colouration resulting from the staining of hematite.

In exploration drill cores, the Grey RAT shows a slightly weathered facies, highly fractured with breccia in places (Fig. 22). At the top contact, they are highly fractured with strong mineralisation by copper oxides, especially malachite, heterogenite and manganese oxides.

Figure 22: Yellowish-grey massive fractured dolomitic siltstone (Grey RAT) with hematite staining and malachite, heterogenite and manganese oxides in fractures (TCDH027-Tshifufia fragment).

As in the case of the Red RAT, in a comparative geochemical and petrographical study, the Grey RAT consists of the same main rock-forming and accessory minerals (detrital, diagenetic and metamorphic). The only difference between these rocks is their colour and the relative proportion of detrital and diagenetic minerals (Cailteux *et al.,* 2005).

2.2.2.1.2 D. Strat. (R.2.1.2) and RSF (R.2.1.3)

The D.Strat (R2.1.2: *Dolomie stratifiée*) conformably overlies the Grey RAT and comprises a relatively thin (<3m) layer of massive to crudely laminated, grey to green silicified dolomite with an algal or bacterial band in the top metre.

The D.Strat (*Dolomie stratifiée*) consists of grey to dark grey, bedded, silicified, impure dolomite with stromatolitic nodules in the top metre (Fig. 23). Moderate-to-high concentrations of sulphides are hosted in fewer dolomitic lenses and nodules. The sulphide copper mineralisation mainly takes the form of chalcocite and bornite. After weathering, it presents a coarsely-bedded siliceous dolomite, alternately clayey, grey, brownish-yellow or whitish with distinct bedding planes (Fig. 24). The D.Strat thickness varies between 2 and 3m.

Figure 23: Spherical nodule comprising silica-dolomite rimmed by chalcocite-TCRD003-Tshifufia fragment.

The RSF (*Roche Siliceuse Feuilletée*) is a thinly and regularly laminated silicified dolomite. In the unweathered facies it shows a dark grey colouration, which is due to the high concentration of copper sulphides such as chalcocite and chalcopyrite. In the weathered facies, it becomes greyish-brown thinly laminated and strongly silicified dolomite, often with high concentrations of malachite and heterogenite (Fig. 24b). In the other copper deposits of the Congolese Copper Belt, native copper and cuprite are found in this unit. The thickness varies and can exceed 3 metres.

Although the characteristics of the D.Strat and RSF are highly variable throughout the Congolese Copperbelt, within the outcrops of the Kinsevere fragments these strata have consistent characteristics and their combined thickness varies only between 5 and 6 metres. Both units are strongly fractured in places.

(a)

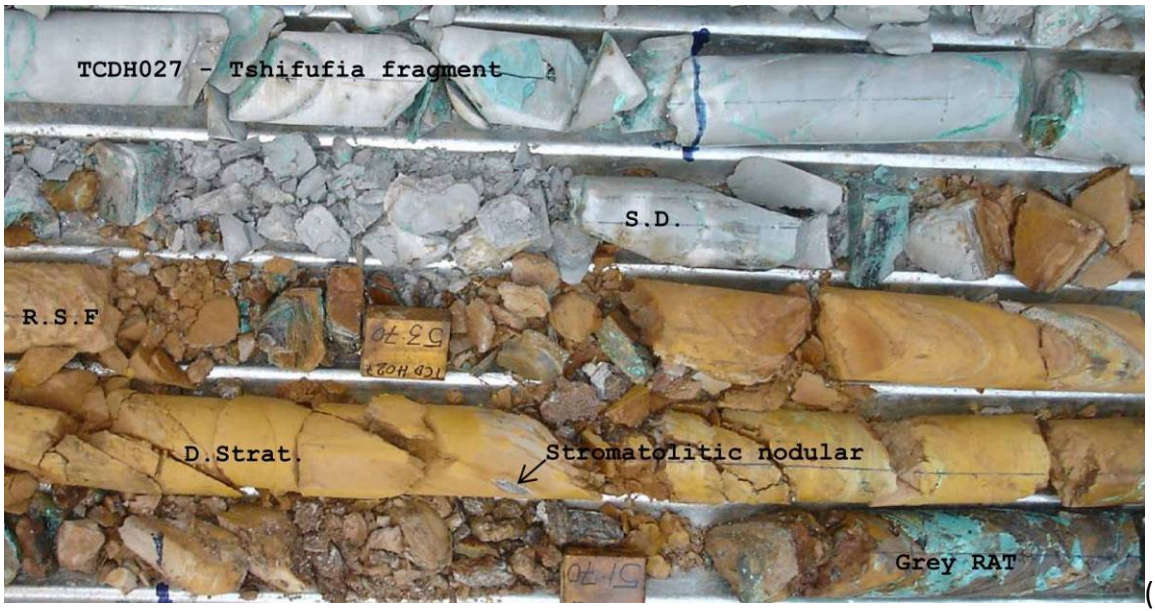

(b)

Figure 24: D.Strat and RSF (a) Fresh rocks Tshifufiamashi fragment-TFDH004 and (b) Weathered facies-Tshifufia fragment-TCDH 027.

Petrographically, both units are characterised by a high concentration of Mg-dolomite (>20%), detrital and authigenic quartz, chlorite and sericite. In particular, the RSF is characterised by the presence of muscovite (François, 1973; Cailteux, 1978, Batumike *et al.,* 2006).

2.2.2.2 Dolomitic Shale (SD)-R2.2

The SD thickness varies between 75 and 110 metres and consists of fine-grained micritic cemented clastics rocks. In Kinsevere, the SD bulk forms a succession of slightly greenish-grey dolomitic shale with finely-banded weakly carbonaceous silty dolomite alternating with

dark mostly carbonaceous shale/siltstone progressing upward into largely carbonaceous finely pyritic siltstone and shales with occasional 1-3 metres thick medium-grey diffusely bedded dolomites and dolomitic shales.

Within the carbonaceous shales and siltstone, bedding is parallel, laminated and sharp to diffuse, although the fine laminated texture is not always apparent until the framboidal pyrite within it starts to oxidise and the shale swells. Less micaceous and more dolomitic horizons show thicker, less obvious bedding with minor dolomitic pseudomorphs. The fresh non-carbonaceous dolomite shale and shaley dolomite display a weak crystalline texture, often associated with 1-3mm lath-like pseudomorphs after sulphates (Fig. 25).

At approximately 10-20 metres from the base and towards the upper margin, there are occasional narrow (<2m) zones with minor siliceous dolomite nodules (Fig. 26), normally occurring as irregular flattened elongate “blebs” parallel to the bedding (<10mm thick and 5-35mm long).

The above zone at Tshifufia fragment appears to correlate with Tshifufiamashi with a less than 3m wide zone of very abundant (<16mm) dolomite pseudomorphs (nodules) resembling porphyroblasts in carbonaceous dolomitic shale that occurs locally at approximately 10-16m above the base. At Tshifufiamashi, these are typically replaced or rimmed by pyrite with very subordinate fine chalcopyrite.

Figure 25: Dolomite with pseudomorphs (nodules) replaced by chalcopyrite in carbonaceous shale-TFDH004-Tshifufiamashi fragment.

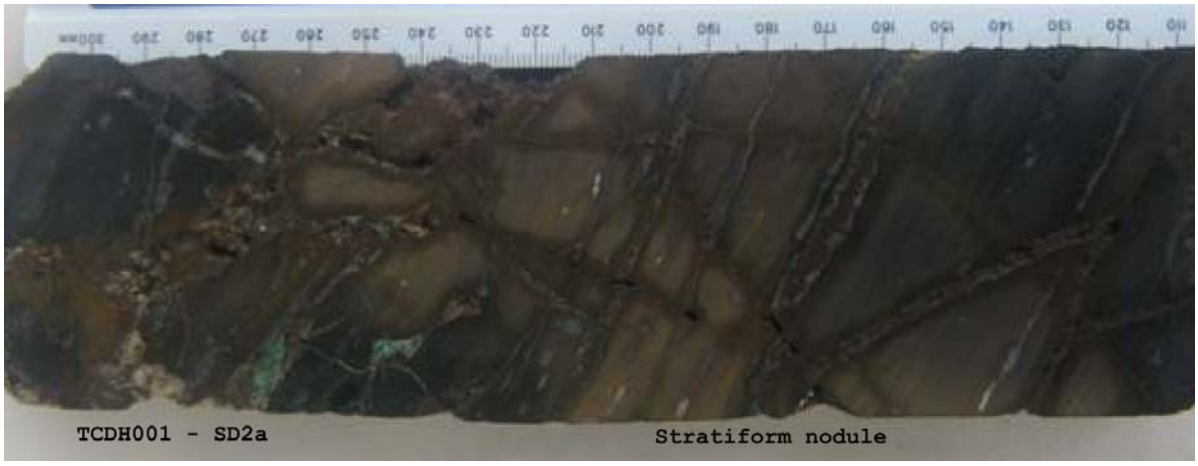

Figure 26: Dark grey bedded dolomitic shale with stratiform nodular (TCHD001-Tshifufia fragment-HQ size).

In the weathered zones, the SD generally has a light grey colour with, in places, brownish-yellow to reddish-white, well-laminated and coarser-grained dolomite bands.

In open pit outcrop, the SD comprises light grey to dark reddish regular bedded dolomitic shales packages which are strongly fractured (veins, fractures and joints). These fractures are filled by copper and manganese oxides. These are mainly malachite, heterogenite and other black iron oxides. Locally, a reddish colour due to the staining of haematite is present. The SD also contains reactivated bedding planes which are filled mainly by malachite. These reactivated planes are locally present with other fractures (Fig. 27).

Figure 27: Open pit outcrop showing fractured SD with mineralised joint, Qtz-malachite veins and reactivated bedding planes - Tshifufia Fragment.

In the unweathered zones shown from exploration drill core, fractures (tension joints and fractures) are filled by calcite (dolomite) and copper sulphides such as chalcopyrite, bornite and chalcocite. The SD hosts the Mines Series Upper Ore Body (UOB).

François (1973, 1974), Cailteux (1977a; 1977b) and Cailteux *et al.,* (1994) conducted a petrographical and geochemical study in the Kolwezi, Kambove areas respectively and also elsewhere in the Lufilian Arc. They noted that this formation (SD) contains a siliciclastic part consisting of detrital quartz and also contains muscovite flake along bedding planes and blue to green tourmaline as metamorphic minerals. The diagenetic crystallisation surrounds the quartz within dolomite-tourmaline overgrowths. Metamorphic phengite and chlorite are also well represented. Rare authigenic apatite associated with dahllite represents growth zoning. Eeuhedral neoformed Monazite is present (Cailteux, 1977a; 1977b)

2.2.2.3 Kambove Dolomites-R2.3

The CMN is the uppermost unit of the Mines Subgroup and has been subdivided into two units (Oosterbosch, 1962); a lower interval of dark-coloured organic dolostones (Fig. 28); and an upper unit of clean dolomites interbedded with chloritic siltstones. More detailed internal subdivisions have recently been proposed by Cailteux (1977a; 1977b; 1994) based on cores drilled in Kambove area. In this subdivision (Table 4), the basal unit (R2.3.1) has been divided into three sub-units, comprising mixtures of stromatolitic and laminated dolostones (including RSF and RSC-type facies) and dolomitic shales. The upper unit (R2.3.2) comprises similar facies but has interbedded chloritic siltstones and “collapse breccias” and is capped by clean pink-white dolomite (Bull and Selley, 2005).

In the Kinsevere area, the CMN unit is thick, locally exceeding 160 metres and can be sub-divided into three sub-units:

1. A lower 40-80m thick section of homogeneous, parallel diffuse to sharply laminated crystalline dolomite and dark carbonaceous finely laminated shaley dolomite with alternating subsidiary black shale bands (Fig. 26).

2. A 25-35m intermediate zone commencing with 3-6m of weakly carbonaceous banded to irregularly finely-bedded dolomite with much bed-parallel dolomite veining/alteration. This gives way to a cyclic unit consisting of well-defined dark to medium grey well-bedded dolomites (Fig. 29), (becoming less carbonaceous upwards) alternating with very pale olive massive shales. Each lithological unit is from <2 to 5m thick with a gradual increase in the proportion of shale upwards. The shales are poorly bedded (rarely anastomosing and diffuse irregular) with poorly sorted medium grained sand to coarse gritty (+ rare fine pebbles) layers less than 1-4cm thick, at the base of many of the units. Contacts are mostly sharp.

3. The youngest member consists of white to cream, variably bedded dolomites with occasional very pale olive dolomitic shales. Within the lower to central sections are zones with very pale lilac beds less than 2-3cm thick, or large, ill-defined crystals resembling anhydrite. Occasional small stromatolites, possible evaporite collapse

breccias (Fig. 30) and pseudomorphs testify to the shallow water environment. Monotonous sharp to diffusely and thickly bedded dolomites with minor chert lenses along the bedding (as flattened bed-parallel nodules) dominate much of this division.

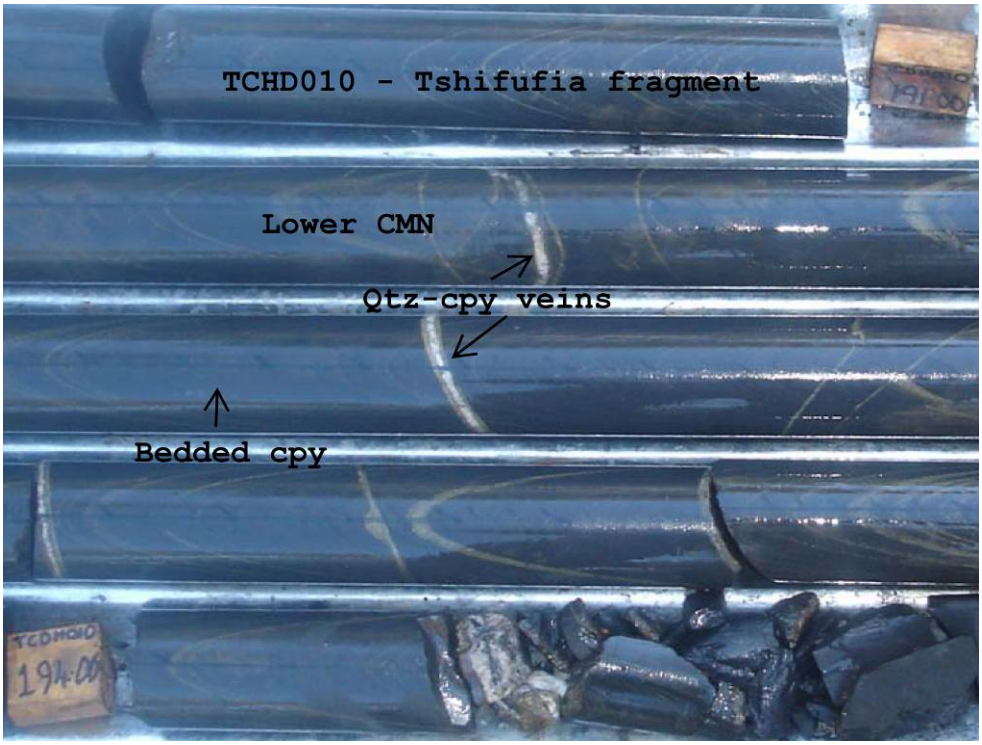

Figure 28: Dark coloured dolomite with bedded chalcopyrite and quartz-chalcopyrite veins, lower CMN-Tshifufia Fragment

Figure 29: Grey well laminated dolomite with bedded chalcocite-KPDH002 - Kinsevere Hill fragment.

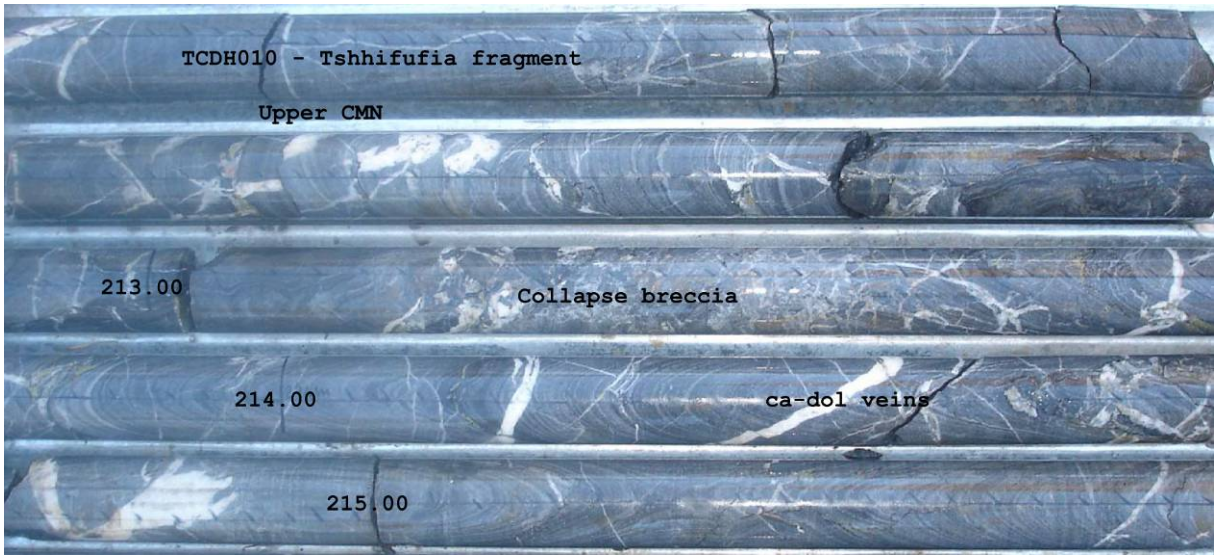

Figure 30: Light grey bedded dolomite with intercalated "collapse breccia" and calcite-dolomite veins, Uppermost CMN unit - Tshifufia fragment.

In the weathered zone the lower CMN consists of yellowish-brown to grey siliceous dolomite with dark purplish vuggy shale, while the upper CMN shows a yellowish to reddish-brown siliceous dolomite with patches of green-grey chloritic conglomeratic sandstone (greywacke).

In all three areas of the Kinsevere copper deposit, the CMN outcrops in the eastern part of Tshifufiamashi and Tshifufia open pit. At the Kinsevere hillock, the CMN is well exposed in an artisanal excavation pit.

Isoclinal micro-folds with axial planes dipping 10° to the SW and W respectively in the Tshifufiamashi and Tshifufia open pits and at Kinsevere Hill affect the CMN (Fig. 31a and b). The CMN is also affected by fractures (joints and veins, Fig. 29a) which are filled with copper oxides (malachite and heterogenite), manganese oxides and black iron oxides.

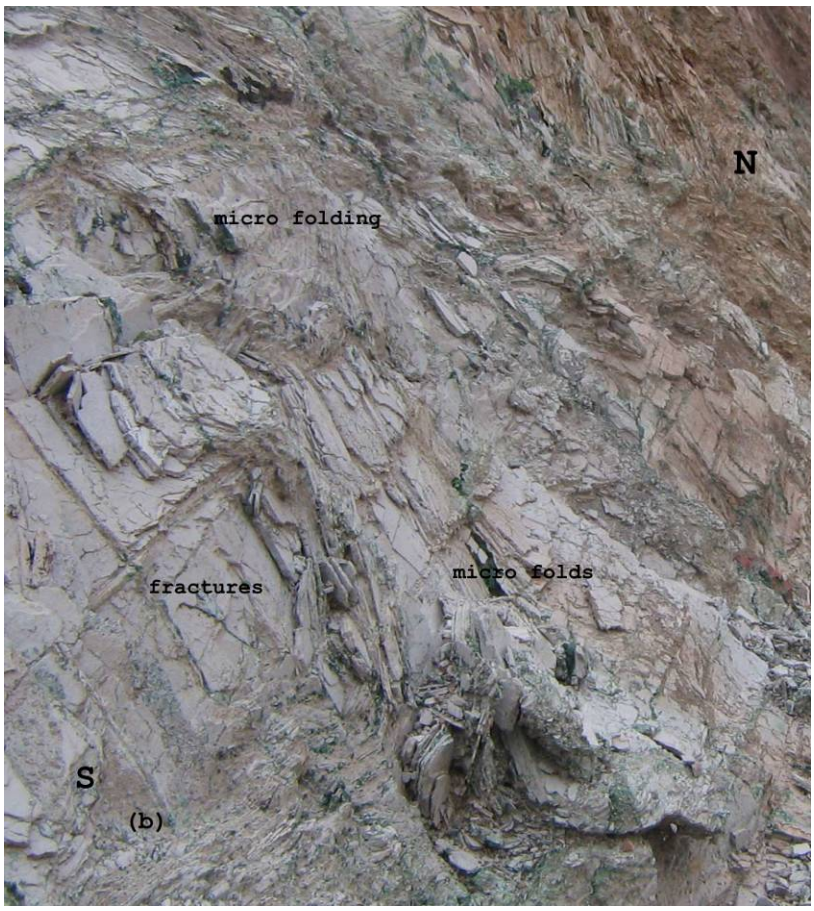

Figures 31 a) and b): Open pit outcrop showing mineralised joints and fractures, and affected by small-scale folding - Tshifufia Fragment.

In the unweathered zone, the exploration drill cores reveal that the fractures are filled by dolomite-calcite veins and associated with copper sulphides (chalcocite, bornite, chalcopyrite and occasionally pyrite). With the exception of mineralisation within fractures, the copper sulphides can also occur along bedding planes and as disseminated and replaced dolomite in stratiform evaporitic nodules in dark grey laminated, coarse-grained dolomite (lower CMN) (Fig. 32).

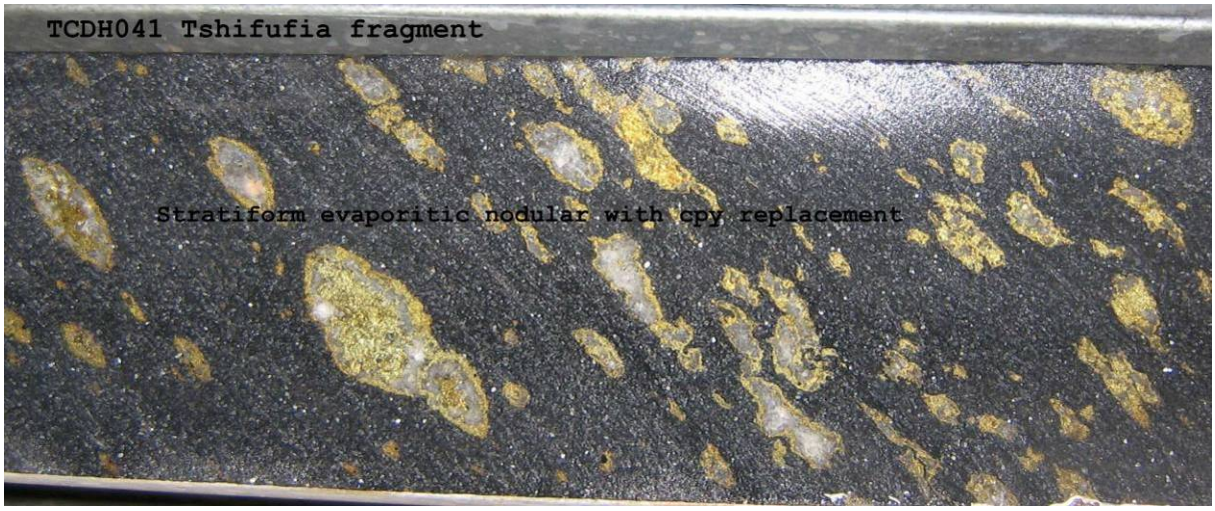

Figure 32: Dark grey laminated coarse-grained dolomite with replacement chalcopyrite-dolomite in stratiform evaporitic band-lower CMN - Tshifufia Fragment.

The CMN hosts the Mine Subgroup third orebody which is well developed in the Kinsevere copper deposit.

2.2.3 Breccia

Two types of breccia are encountered in the Kinsevere area: the monolithic breccia and the heterogeneous breccia (also known as the RAT breccia).

2.2.3.1 Monolithic breccia

The monolithic breccia is found within the units of the Mines Subgroup, such as the CMN. Locally, the monolithic breccia is found between two stratigraphic units of the Mines Subgroup. The monolithic breccia consists mostly of angular clasts of CMN (Fig. 33) which are cemented by clayey, malachite and manganese and iron oxide matrix when weathered. This breccia was interpreted as a crackle breccia resulting from an internal thrusting of Mines Subgroup layers (Cailteux and Kampunzu, 1995; Kampunzu and Cailteux, 1999; Kazadi, 2004) and hosts high-grade copper oxide mineralisation.

Figure 33: Brecciated well-bedded dolomite constituting the CMN monolithic breccias - KPDH002 Kinsevere Hill

2.2.3.2 Heterogeneous Breccia

The heterogeneous breccia is a significant lithology within the Roan Group, though it is still poorly understood and the subject of ongoing discussion (Cailteux, 1995; Kampunzu and Cailteux, 1999; Wendorff, 2000; 2003; 2005b; Jackson *et al.,* 2003). The heterogeneous breccia surrounds and separates different fragments of Roan Group and Mines Subgroup outcrops as is the case of the Kinsevere copper deposit (Fig. 9).

In the Kinsevere area, the heterogeneous breccia contains all the Mines Subgroup fragments and occurs along a fault zone separating the Tshifufia and Tshifufiamashi fragments.

The heterogeneous breccia is sometimes referred to as “RAT breccia”, and consists of a massive, mostly reddish to pinkish rock with clasts comprising rounded to sub-angular clasts of Mines Subgroup units such as RSF, SD, Grey and Red RAT, which are contained in a sandy dolomitic matrix (Fig. 34).

Figure 34: Heterogeneous breccia with RAT and Mines Subgroup clasts

At Kinsevere, the drill core shows that the average thickness of the RAT breccia varies from 10 to 160 metres. The RAT breccia is highly fractured in places and shows banded fabrics, giving a laminated appearance. These fractures are filled by hematite, calcite and dolomite, and rarely quartz (Fig. 35).

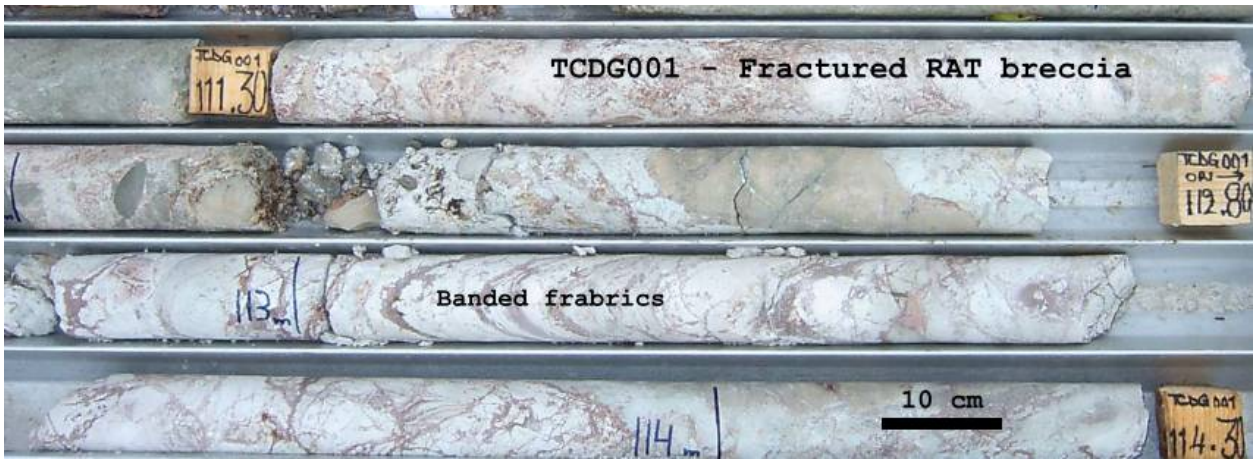

Figure 35: Highly fractured RAT breccia showing banded fabrics.

The heterogeneous breccia contains clasts ranging in size from millimetres to more than a hundred metres as is the case of the 100m-diameter CMN clasts in the western part of the Tshifufia fragment. It is also affected by calcite-dolomite veining which Cailteux and Kampunzu (1995) named “hydro-fractures” (Fig. 36). Hitzman (2008) regarded the highly fractured part of the breccia as an evaporitic dolomite unit. Cailteux and Kampunzu (1995) interpreted these hydro-fractures as a result of de-watering due to tectonic compression, and suggested a faulting origin for the mega-breccia. However, Jackson *et al.,* (2003) pointed out that faulting alone cannot explain the vast extent of the heterogeneous breccia because of the difficulty of forming large discordant diapirs without a mobile substrate, and the strata-bound geometry of clast contacts.

Figure 36: RAT breccia showing dolomite veins (hydro-fractures), TCDH010 - Tshifufia fragment.

2.2.3.3 Relationship between RATs, Mines Series and Breccia

Several interpretations exist regarding the relationship between the RAT Group (including Grey RAT and Red RAT) and the heterogeneous breccia. As mentioned above (Chapter 1), François (1973, 1974), Cailteux and Kampunzu (1995), Kazadi (2004) consider that the heterogeneous breccia consists of a post-sedimentary unit which formed during the thrusting event of the D_1 (Kolwezian phase), itself formed by the friction created during the thrusting of the RAT, Mines Subgroup and Dipeta strata. Thus, the heterogeneous breccia is considered as younger than the neighbouring strata.

In the Kinsevere area, drill core and open pits outcrops show that Red RAT consists of a laminated to bedded siltstone with a strong concentration of calcite-dolomite veins towards the basal contact with the crackle breccia beneath. These crackle breccias in turn overlie heterogeneous breccia (Fig. 37). There is no evidence of a tectonic contact between them.

Figure 37: The contact between the crackle breccia and the heterogeneous breccia (RAT breccia).

In the open pit outcrops, most of the RAT units, commencing with the undifferentiated to the Grey RAT going through the Red RAT, show a normal sequence of sediments without

any evidence of tectonic contact between them and which have been deposited respectively into two different environments, except that at the Red RAT and undifferentiated RAT it shows a highly tectonised zone beneath.

Evaporitic textures have been noted within both Grey and Red RAT. The greyish-green colouration of the Grey RAT and the features of the two facies (proximal and distal) with the evaporitic textures observed within it testify to the reduced environment during the deposition of this unit as stipulated by Oosterbosch (1950), François (1973), Katekesha (1975) and Cailteux *et al.,* (2005) and indicate that it was deposited in a supratidal-evaporitic environment (Cailteux *et al.,* 2005). The reddish-pink colouration of the RRAT and the undifferentiated RAT indicates the oxidation environment during the deposition of these units. All petrographical studies undertaken to date on the RAT and Mines Subgroup rocks (Audeoud, 1982, Okitaudji, 1989 and Cailteux *et al.,* 2005) testify that both Grey and Red RAT have a similar petrographical composition.

More recently, Hitzman (2008) suggested that the Grey RAT should be renamed R.1.4. (Table 5), based on the observation that Grey RAT and Red RAT interfinger with each other, instead of having a stratigraphic contact.

Grey RAT R2.1.1	R2.1.1 **(R1.4)**	Grey, generally massive or poorly bedded dolomitic siltstone or fine-grained sandstone commonly with sulphides; may include breccia. Up to 10m thick.
Red RAT R1	R1.3	Pink/red/salmon, massive/poorly bedded Mg-chlorite-dolomitic siltstones or fine-grained matrix-rich sandstones; with hematitic and specular hematite, local breccia. Up to 160m thick.
	R1.2	Pink/purple–grey chloritic and hematitic siltstone and/or fine-grained sandstone, silicified stromatolitic dolomite (5m) at the top in Kambove, absent in Kolwezi. 45m thick.
	R1.1	Purple-red hematitic and slightly dolomitic siltstone with white-beige sandstone bands (Kambove); brick-red sandstone (Kolwezi) > 40m thickness (base in tectonic breccia)

Table 5: Proposed lithostratigraphic table of the RAT group in Kolwezi (Hitzman, 2008)

Based on the colouration of the Grey RAT and the fact that the known lower ore body is hosted within the lower part of the Mines Subgroup (R2.1) including the Grey RAT, the present study considers the base of the Mines Subgroup just at the base of the Grey RAT to be the lowermost unit constituting the boundary between the grey bed and the red bed of the mineralisation within the Mines Subgroup (R2). However, it will be best to consider the Grey RAT and the Red RAT as part of the same stratigraphic unit, as suggested by most Katangan geologists. In addition, this study regards the breccia as a product of both the dissolution of the evaporitic minerals present within it and the shortening of the Katangan basin resulting from convergence between the Kalahari and the Congo cratons.

Otherwise, the contact between the RAT and the Mines Subgroup is considered as tectonised. In drill core, the top part of the overturned section (CMN) is sitting over the RAT dolomitic siltstone throughout the heterogeneous breccia with mostly angular clasts, 10-20cm of highly brecciated zone with quartz-limonite (Feox) noted on the top contact of the heterogeneous breccia. The presence of the thin brecciated zone shows an abnormal contact between the CMN and the RAT and might indicate a tectonic contact between these units (Fig. 38).

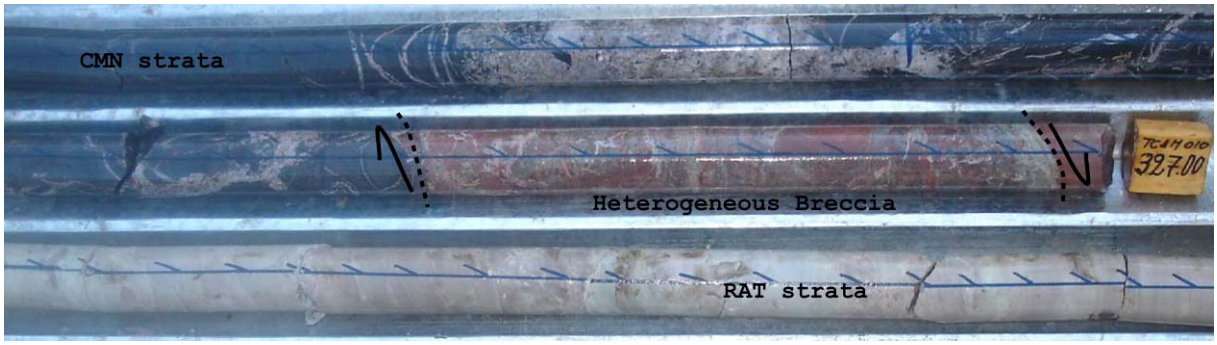

Figure 38: The contact between the Mines Series rocks (CMN) and the RAT Subgroup rocks (R1.3) - TCDH010 Tshifufia fragment.

Furthermore, the basal contact as observed on the open pit outcrop shows a normal succession between the D.Strat-Grey RAT and Red RAT without any tectonised contact between them (Fig. 39).

Figure 39: W-E section showing normal sequence from the Red RAT overlain by Grey RAT that shows a transitional contact with the overlain formation D.Strat-RSF (a). Proximal facies indicated by evaporitic texture within the Grey RAT. Tshifufia fragment. Looking North.

2.2.4 The Footwall and Hanging wall

The concept of footwall and hanging wall is used in thrust fault terminology. According to François (1973, 1974; 1987) and Kampunzu and Cailteux (1999), thrusting of the Roan fragment on the Kundelungu strata occurred during the Kolwezian event. In certain regions, the Kundelungu strata underlie the Roan fragments through the heterogeneous breccia. The Kundelungu in this case constitute the footwall, as is also the case of Kinsevere.

At Kinsevere, the footwall and hanging wall are represented by the lower part of the Kundelungu Group (Kalule Formations) which has outcropped in both SW and NE part of the Kinsevere area. In the Kinsevere drill core carried out in the Kinsevere area, none has shown the Kundelungu rock formations, so the contact between the Roan and the Kundelungu is

not well defined. Nevertheless, in the eastern and western flanks of both Tshifufiamashi and Tshifufia Pits, an abnormal (tectonic) contact is noted between these Supergroups.

Chapter 3

STRUCTURAL GEOLOGY DATA

The Kinsevere Mine is one of the stratiform Cu-Co deposits situated within the Lufilian Arc (Katangan basin). An understanding of the tectonic stress acting inside and outside of the Lufilian basin in general and in the SE part in particular, during and after the deposition of the Mines Subgroup sediments, is essential for the establishment of the relationship between the in-situ and the regional tectonic stress. Nevertheless, the stress and strength in the Earth's crust are not spatially homogenous. The heterogeneity of the stress and strength is marked by the complex geometry of faults, seismicity and diversity of the earthquake mechanisms (Rivera and Kanamori, 2002). However, the regional stress orientations might derive from large-scale stress data collections like the world stress map (Zoback, 1992; Sperner *et al.,* 2003). The determination of the orientation of a stress field is often based on the analysis of structures such as fold axes, faults with a known sense of movement, veins, joints and any other brittle deformation, which should be collected in the studied area. Through the diversity of the orientation of the stress that has been determined elsewhere in the Lufilian Arc, the orientation and magnitude of the stress field within the Katangan basin has been demonstrated to be highly variable throughout the basin, especially near faults (Unrug, 1988; Kampunzu and Cailteux, 1999; Kampunzu *et al.,* 2003).

To correlate the local stress field with the regional stress, a palaeostress analysis was conducted in the study area using a methodology to determine the reduced stress tensor and the magnitudes of the three principal stresses.

Several methods are used to calculate palaeostress from fault orientations and slip vectors, e.g. the Direct Stress Inversion (DSI, Angelier, 1991), the right dihedral method (RMD, Angelier and Mechler, 1977; Delvaux and Sperner, 2003) and the Numeric Dynamic Analysis (NDA, Turner, 1953; Spang, 1972; Sperner *et al.,*1993). Analysis of the palaeostress field can help to explain fault reactivation, the timing and patterns of fault linkage and help to analyse the migration of geofluids (Du Rouchet, 1981; Gartrell and Lisk, 2005).

To conduct the palaeostress analysis, in addition to the general structural architecture of the Kinsevere copper deposit, the improved right dihedral method (RDM, Angelier, 1977) was used. An additional procedure to the method, known as the rotational optimisation procedure (ROP), was completed by Delvaux and Sperner (2003).

To process all field data collected on fault planes, tension fractures, bedding planes, hinge lines, and fold axial planes, two types of software were used:

- The WinTensor program was used to conduct the palaeostress analysis of the brittle data collected in the Kinsevere area;
- Stereo 32 and SpheriStat were used to conduct the analysis of the folding features of the Kinsevere area, which was obtained from bedding planes, hinge lines and fold axial planes.

The following sections will be devoted to an overview of the methods used in the present study and the presentation of all structural data collected on site from all three Mines Subgroups fragments comprising the Kinsevere area.

3.1 General concepts of crustal stress analysis

In order to understand the right dihedral method, an introduction to the concepts of stress and strain will first be presented, followed by an introduction to the RDM.

In structural geology, two types of analysis may be undertaken, namely kinematic and dynamic analysis. The term “stress” can be applied to dynamic analysis, whereas the observable “strain” in rock (which results from stress) is considered in kinematic analysis.

Stress can be defined as a force concentrated or applied on a unit area. Otherwise, stress may be defined as the total sum of forces acting on all possible planes that pass through a point in the Earth’s crust, which has a tensor quantity. The stress is also defined as the force per unit area on a single plane, which is a vector quantity.

In a kinematic approach, the stress is considered as the vector acting on a unit surface area. In this case, the stress will comprise two components: the normal and the shear stress. The normal component represents the part of the stress acting perpendicular to the surface and is named normal stress (σ_N), while the shear component, named shear stress (σ_S) represents the part of the stress which is acting parallel to the surface (Fig. 40). When normal and shear stress rise sufficiently across a plane, they approach the Mohr-Coulomb criterion, which stipulates that rock failure occurs when Coulomb stress τf on a plane exceeds a critical value.

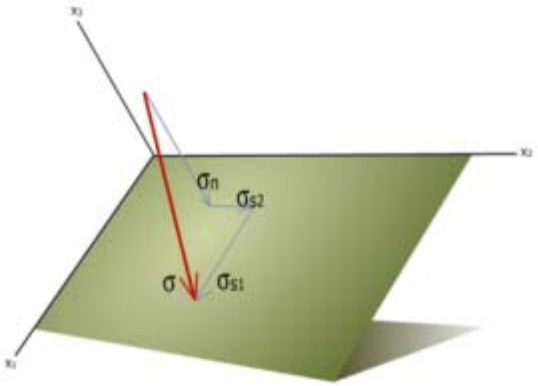

Figure 40: The normal σ_n and shear stress σ_s acting on a fault plane

If the stress as regarded as a vector, it requires magnitude and direction (strike/plunge). For any given orientation (strike and dip) of a surface passing through a given point in the crust, there is a different value of normal and shear stress. The arrows of all stresses acting on a given surface as vectors might be represented in a stress ellipsoid. In the light of Anderson’s theory (Anderson, 1942) stipulating that shear stress cannot exist on the contact between rock and atmosphere (the surface of the Earth can consequently be considered a “free surface”), it is possible to demonstrate that there are three mutually perpendicular

planes without shear stress, termed the principal planes of stress (Fig. 41). If the surface of the Earth is a free surface, it is occupied by one of the three principal planes of stress, with the other two planes being orientated vertically.

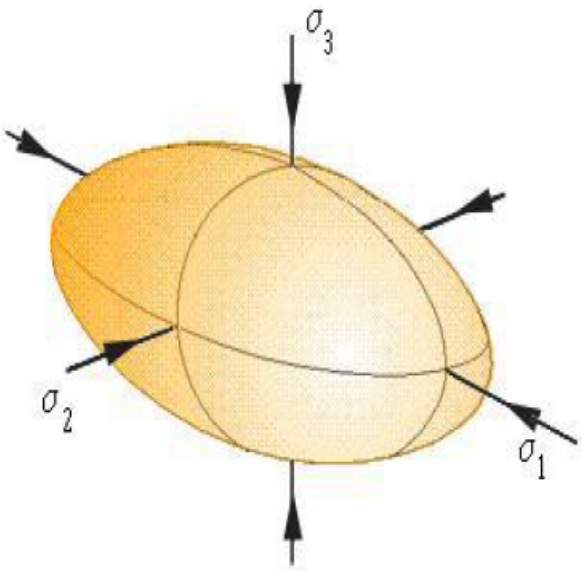

Figure 41: The stress ellipsoid showing the three principal stress axes σ_1, σ_2, and σ_3.

In the event that all principal stresses are equal in magnitude, the shear stress acting on the mass of rock will not exist. In this state, only the hydrostatic stress component is present ($\sigma_1=\sigma_2=\sigma_3$). However, in any other state of stress, a mean stress can be defined from these three principal stresses ($\sigma_m= (\sigma_1+\sigma_2+\sigma_3)/3$). The mean stress is the part of the stress that acts to change shape. Subtracting the mean stress from each of the principal stresses, we get the deviatoric stress defined by principal values (σ_1-σm, σ_2-σm, σ_3-σm). The deviatoric stress is the part of the stress that tends to cause changes of shape and is the part of greatest interest to structural geologist because it produces deformation.

The graphical depiction of Mohr's circle is dictated by ø, i.e. the angle between σ_1 and the fault plane along which the shear component of the stress tensor plays. Thus, the normal and shear resolved stresses acting on a fault plane are functions of σ_1 and σ_2. The Mohr's circle gives a graphical representation of the relationship between the principal stresses axes (σ_1, σ_2, σ_3) and the normal and the shear component (σ_n, σ_s) for any fault plane. The differential stress (σ_1-σ_3) is the diameter of the Mohr diagram.

Faults are defined as fractures that have appreciable movement parallel to their plane. Movement on a fault might be defined by striations contained in a plane or by the displacement of a block of rock mass with any type of displacement marker. In the first case, the fault is named slickensided fault, whereas in the second case it is called shear fracture. Anderson (1942) defined three types of faults (Fig. 42) which are identified as normal fault, thrust fault and wrench fault (strike slip):

1) A normal fault is when the hanging wall has moved down relative to the foot wall. Thus a graben will consist of a block that has dropped down between two subparallel

normal faults that dip towards each other; a horst will consists of two subparallel normal faults that dip away from each other so that the hanging wall block between the faults remains high. Listric faults are any normal faults that exhibit curved (concave) geometry so that they exhibit steep dips near the surface and become increasingly horizontally inclined with depth.

2) A thrust fault is when the hanging wall has moved up relative to the foot wall with a dip angle which may not exceed 45°. Reverse faults are defined as being any fault similar to the thrust fault regarding the sense of movement but with a dip angle of the fault plane equal to 45° or more than 45°.
3) A strike-slip fault is when the fault has movement parallel to the strike of the fault plane. Two types of strike-slip faults might be defined: the right lateral strike-slip fault (dextral) which occurs when the observer's right side moves towards him; and the left lateral strike-slip fault (sinistral) in the opposite (left side moves towards the observer).

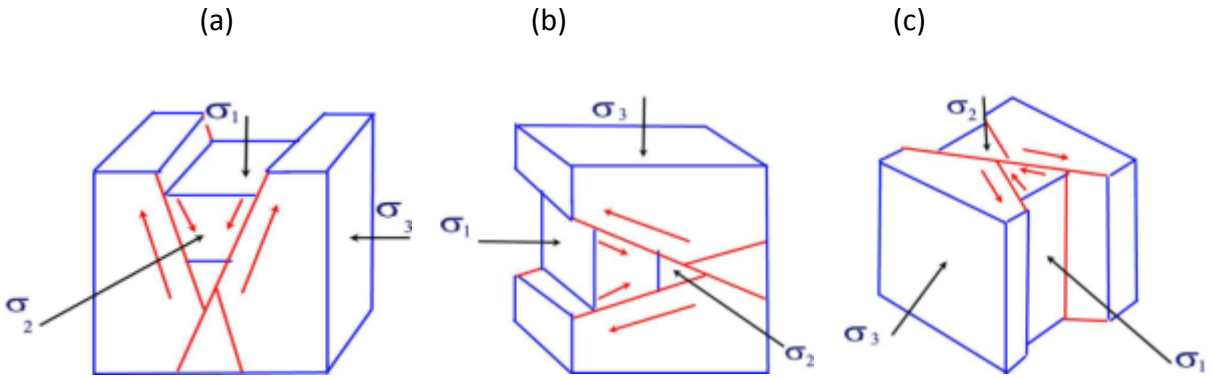

Figure 42: The three types of faults as defined by Anderson (1942): (a) Normal fault, (b) Thrust fault or reverse fault and (c) Strike-slip fault

In stress inversion methods, the objective is to calculate from the fault plane and slicken line orientation, including slip sense, the four parameters of stress tensors σ_1, σ_2, σ_3 and R which are respectively: the principal stress axis (maximum compression), the intermediate stress axis (intermediate compression), the minimum stress axis (minimum compression) and the ratio of the principal stress difference $R=(\sigma_2-\sigma_3)/(\sigma_1-\sigma_3)$. These four parameters are determined using the WinTensor computer program developed by Delvaux and Sperner (2003).

All stress inversion methods are based on the work of Wallace (1951) and Bott (1959), who assumed that slip on a plane occurs in the direction of the maximum resolved shear stress. The slip direction on the fault plane is interpreted from slickenside lineation and/or calcite-dolomite stepped textures. The data used for the inversion are the fault plane, slip line orientation. Stress tensors can be reconstructed using tension and compression structures (Delvaux *et al.,* 1997), in addition to fault planes with slip lines. Quartz veins, plume joints and dykes are considered as tension joints, developing perpendicular to the least

compressive stress axis (σ_3). Fractures resulting from cleavage are considered as compression joints, developing perpendicular to the maximum compressive stress axis (σ_1). For them, the resolved normal stress magnitude is either minimised or maximised.

3.2. Right dihedral method (RDM)

To analyse faults with slicken line orientations, including slip senses, Angelier and Mechler (1977) developed the right dihedral method (RDM) which is based on the principle stipulating that for any fault set occurring in a non-homogeneous material, four right dihedrals might be defined by the fault plane that accommodates the motion and the auxiliary orthogonal plane to the fault plane. The movement of rock masses in these dihedra will be indicated by the direction and the sense of the striations that contain the fault plane. These striations might show a dip-slip sense or a strike-slip movement. Thus, rock masses contained in two diagonally opposed dihedrals will define a compressive motion, while the others will define the extensional movement. Given that σ_1 is contained by the dihedral comprising the P axis and that the compressive dihedral contains the P axis, σ_1 will be contained by the compressive dihedral and σ_3 will be contained by the extensional dihedral which comprises T axis (Fig. 43).

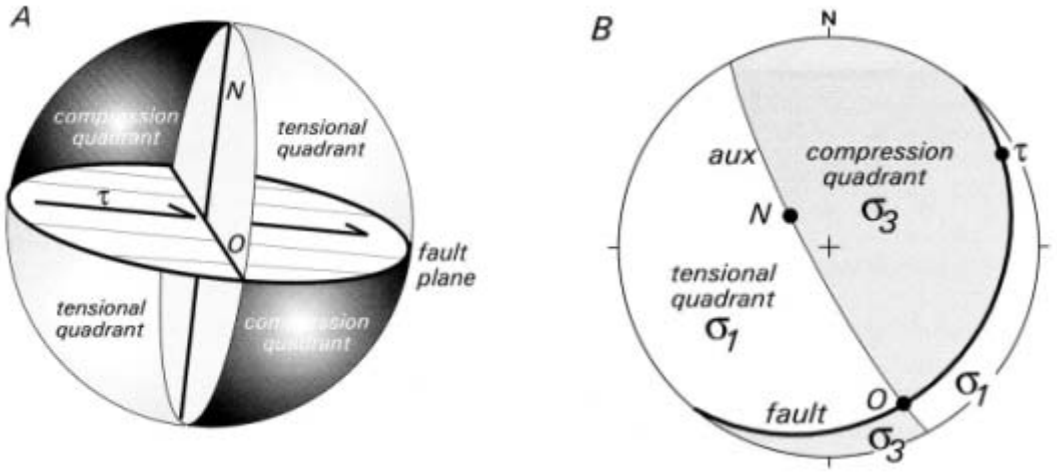

Figure 43: The principle of the improved right dihedral method

In Fig. 43, A shows that a fault, together with its auxiliary plane, forms a right dihedron. This dihedron consists of tensional quadrants that contain the σ1-axis and compressional quadrants that contain the σ3-axis. These are distinguished by using the fault's movement sense; B shows the right dihedron on the stereogram, showing the σ_1- and σ_3-orientation fields (quadrant).

The σ_1-and σ_3-orientation fields defined by individual faults are superimposed on the stereogram to constrain more closely the orientation of the principal axes.

In practice, the right dihedral of each individual fault is represented by a counting net with a number of pre-determined reference orientations. If these reference orientations fall

spatially in the compression dihedral, their corresponding counting values are set to 0 while if they fall in the extension dihedral, their counting values are set to 100. When evaluating a data set, all counting values or all the individual nets are summed up and divided by the number of faults. The resulting nets have counting values between 0 and 100. The orientation of σ_1 is fixed by the orientations in the counting net which have the minimum counting values and σ_3 is fixed by the orientations which have the maximum counting values. σ_2 is set orthogonal to both σ_1 and σ_3 by vectorial multiplication and the stress ratio R is estimated as a function of the counting value of the nearest point in the counting net. More details are given in Delvaux and Sperner (2003).

This method also allows the use of fractures planes (without slip lines), provided that the mechanism of their formation is correctly understood. As mentioned by Delvaux and Sperner (2003), the four parameters of the stress tensor for tension and compression fractures are respectively estimated as follow: σ_3 which, in producing tension fractures, is oriented within a cone angle of β degree around the normal to the plane and σ_1 is located at an acute angle of the tension plane. σ_1, in producing compression fractures, must be located within the cone angle of β degrees and parallel to the bisector of the acute angle of the cone angle of β degree, although σ_3 is located at an obtuse angle to the compression plane. Then, the orientation of the intermediate principal stress σ_2 is parallel to the orientation between the cone angle of β degree and the surface generated by the revolution of the inclined line with β degree from the fracture plane. The angle β of the cone angle is defined by the common friction angle as given by Byerlee (1978) which is equal to 16.7 degrees. The initial friction law developed by Jaeger (1969) justified this value used by Byerlee (1978). This value is based on the shear stress/normal stress relations. Thus, the discrimination of compression and tension joints when using the right dihedral method is based on the angle between the normal to the compression fracture and σ_1 or the angle between the tension fracture and σ_1. If this angle is more than the Byerlee value (16.7degrees), the resolved shear stress can produced slip on the plane.

3.2.1 Rotational optimisation procedure (ROP)

During the rotational optimisation procedure, different functions can be optimised according to the nature of tectonic structure used. For faults, the angular deviation between observed slickensides and computed shears is minimised together with the maximisation of friction coefficients for each fault plane. Fault planes with slip lines can be used not only for the reconstruction of stress tensors, but also for tension and compression structures (Delvaux and Sperner, 2003).

The rotational optimisation procedure implemented in WinTensor optimises the appropriate function by progressive rotation of the tested tensor around each of its axes, and by testing different values of R. The amplitude of rotation angles and values of R ratio testedare progressively reduced, until the tensor becomes stable.

3.2.2 Data filtering

Separation of fault populations resulting from successive tectonic regimes is based on iterative kinematic separation and progressive stress tensor optimisation to obtain homogeneous subsets, representing different stress regimes. Their chronological succession is established as a function of microstructural and geological criteria and relationships with known regional tectonic events. Critical considerations concerning the accuracy of stress inversion methods are given in Dupin *et al.,* (1993) and Pollard *et al.,* (1993). They conclude that uncertainties in stress tensor determination due to geological and mechanical factors generally fall within the range of measurement errors.

3.2.3 Stress field characterisation

The stress regime is defined by the nature of the vertical stress axes:

1) Normal faulting when σ_2 is the maximum horizontal stress axes (σ_2 SHmax) and σ_1 is vertical,
2) Strike-slip faulting when σ_1 is the minimum horizontal stress axes (σ_1 SHmax) and when σ_2 is vertical, and
3) Thrust/reserve faulting when σ_1 is the maximum horizontal stress axes (σ_1 SHmax) and σ_3 is vertical.

Ritz (1994) and Delvaux *et al.,* (1997) stipulate that the stress regimes also vary as a function of the stress ratio R and in the following states:

1) Radial extension (σ_1 vertical, $0<R<0.25$),
2) Pure extension (σ_1 vertical, $0.25<R<0.75$),
3) Trans-tension (σ_1 vertical, $0.75<R<1$ or σ_2 vertical, $1>R>0.75$),
4) Pure strike-slip (σ_2 vertical, $0.75>R>0.25$),
5) Transpression (σ_2 vertical, $0.25>R>0$) or σ_3 vertical, $0>R>0.25$),
6) Pure compression (σ_3 vertical, $0.25<R<0.75$),
7) Radial compression (σ_3 vertical, $0.75<R<1$)

The orientation of the principal stresses and the stress difference ratio (R) were determined by selecting measurements of small faults with obvious sense of movement.

The Improved right dihedral method can also be used to estimate the four parameters of the stress tensor for other types of brittle structures such as compression and tension joints.

3.3 Field results

The results, as presented below, were collected within the three Mines subgroup fragments that constitute the Kinsevere area. A number of data, such as plunge and trend of linear structures (hinge line of micro-folds and slicken lines on fault planes); strike and dip of planar structures (bedding planes, fractures, mineralised joints, fold axial planes, slickensided faults and shear fractures) were collected during the field work.

3.3.1 Tshifufiamashi fragment

Tshifufiamashi is the most northerly fragment in the Kinsevere area (Fig. 44). This fragment is affected by several brittle structures as well as mineralised joints, tension fractures, joints, quartz-calcite-dolomite veins, slickenside lineations and shear fractures indicating normal and reverse faults. In addition to these brittle structures, there are bedding planes and micro-folds, which are well exposed in the CMN strata. Hinge lines and fold axial planes of these micro-folds were also collected in the field with the objective of studying the relationship between different folding events.

This section will be devoted to the presentation of all measurements collected on each of the structural features, starting with the brittle structures.

3.3.1.1 Fractures

Joints and veins are the types of fractures which affect the Tshifufiamashi fragment. Some joints are filled with copper-cobalt mineralisation (malachite, heterogenite, sometimes sulphides of copper minerals such as chalcocite-bornite-chalcopyrite) while others do not contain any copper mineralisation except traces of black manganese oxides and haematite staining in lower Mines Subgroup strata (RAT especially). All the formations of the Tshifufiamashi fragment (Kamoto dolomite, SD and CMN) are affected by these fractures (Fig. 28).

This study regards all joints and veins as single fractures and they will be analysed as one set of data. As most of these single fractures are filled with manganese wad oxides and are not filled with any copper mineralisation, they will be considered as non-mineralised fractures.

The following data will be presented in accordance with the above-mentioned types: i.e. mineralised joints and unmineralised joints.

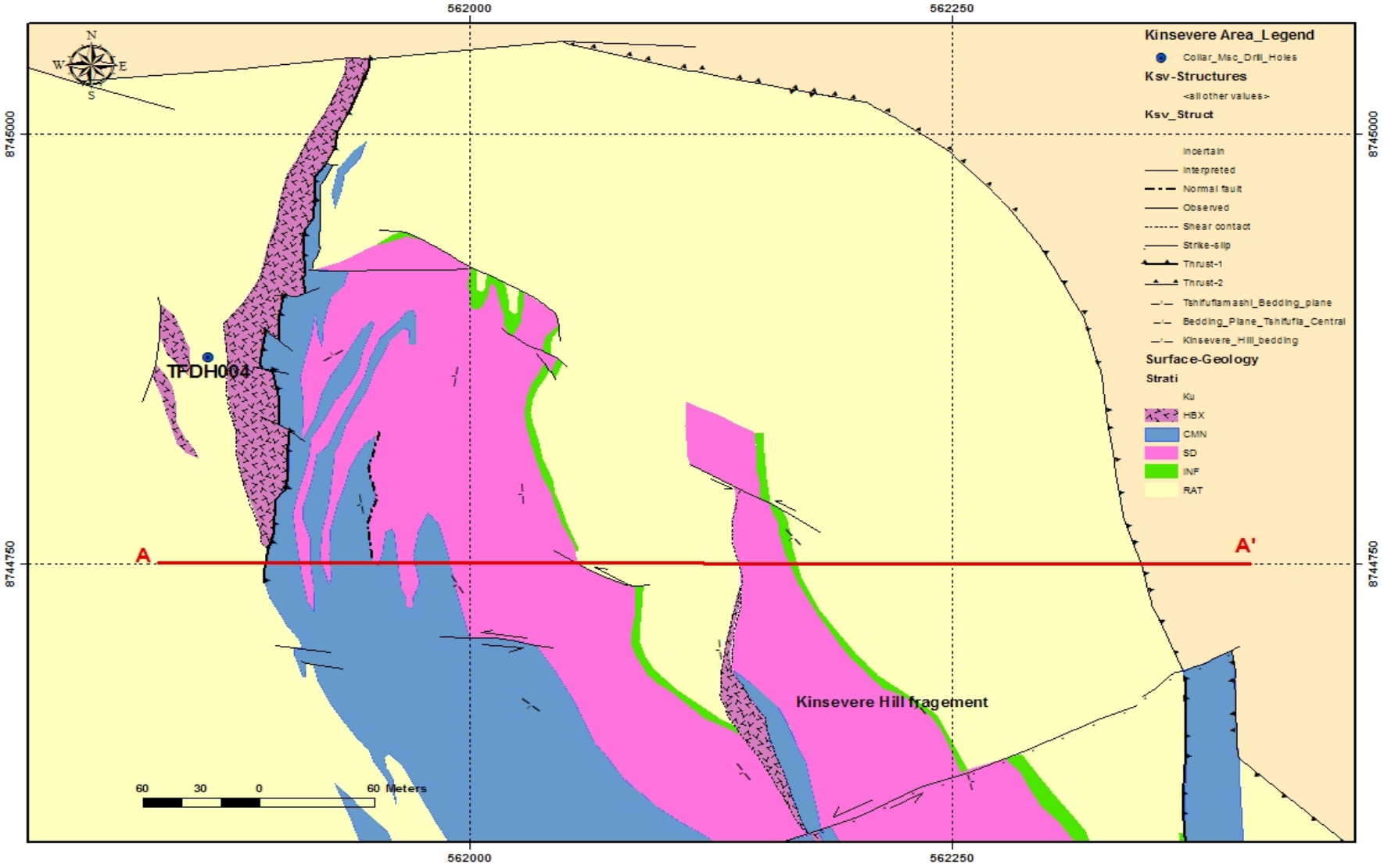

Figure 44: Geological map of the Tshifufiamashi fragment. Cross section A-A' refers to Fig. 10.

3.3.1.1.1 Mineralised joints (MJ)

Over 90 measurements of dip and dip direction of mineralised joints were collected from the Tshifufiamashi open pit outcrop (Table A.1). Three stress tensors were obtained from the mineralised joints population as a whole.

The first stress tensor is characterised by two groups of strike planes of the mineralised joints at Tshifufiamashi. The first group presents a general strike oriented SW-NE with a dip angle varying between 30° and 35°; while the second group show a general orientation strike SE-NW with dip angle varying between 55° and 60° (Fig. 45 (a) and (b)).

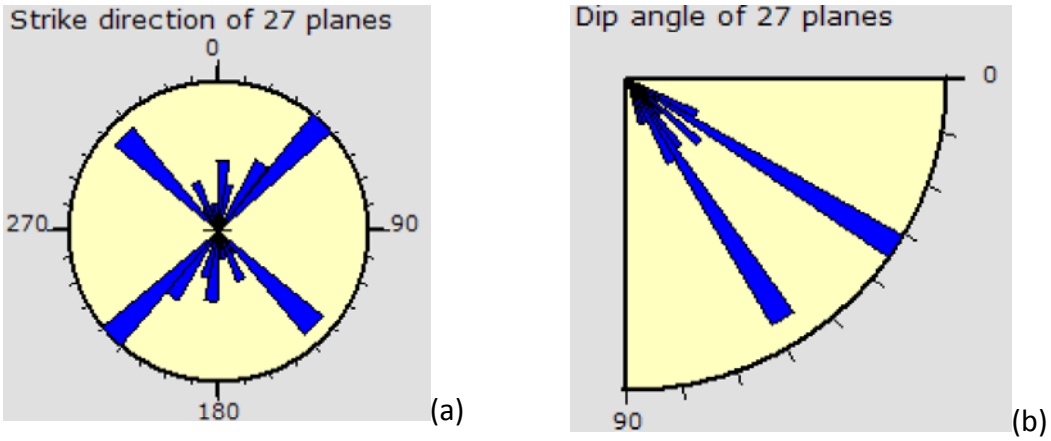

Figure 45: Rose diagram of strike plane (a) and dip (b) of the major phase of the mineralised joints in the Tshifufiamashi fragment.

The stress tensor deduced from these measurements gives the maximum principal stress axis (σ_1) 38/299, the intermediate principal stress axis (σ_2) 06/204 and the minimum principal stress (σ_3) 50/106, where the stress ratio (R) equals 0.75. The tensor belongs to the pure compression stress regime. It indicates SSW-NNE compression (Fig. 46).

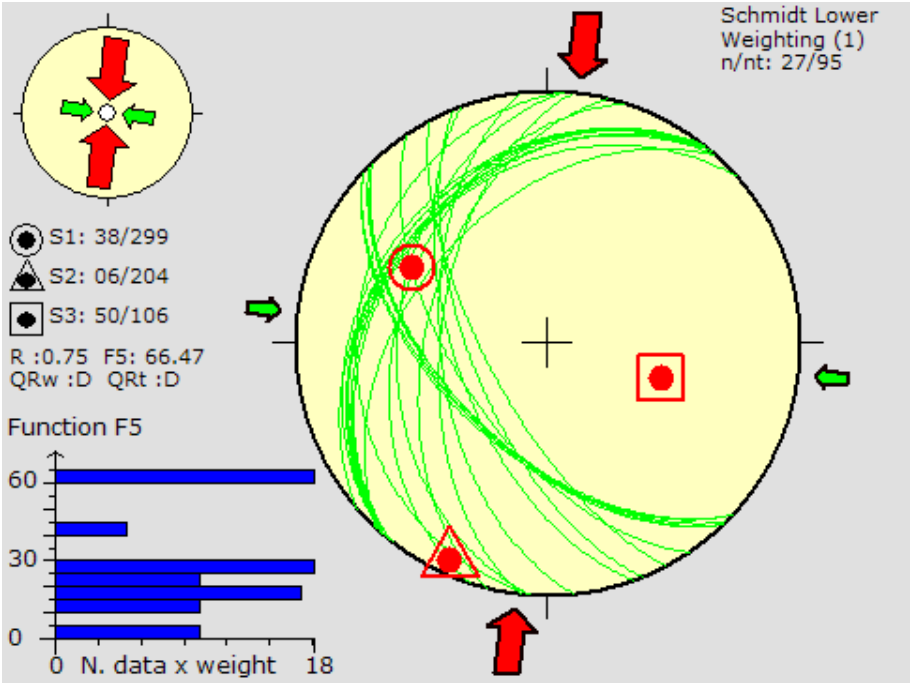

Figure 46: Stereonet of the rotational optimisation results of mineralised joints related to the first stress tensor obtained at Tshifufiamashi.

The second stress tensor is characterised by one major group of strike planes of the mineralised joints at Tshifufiamashi, oriented SE-NW with a dip angle varying between 45° and 50°, although two minor groups of strike planes can be noted. The first minor group presents a SSE-NNW orientation strike with 62° and 65°. The second minor group shows a general orientation trend WSW-ENE with a dip angle varying between 42° and 45° (Fig. 47 (a) and (b)).

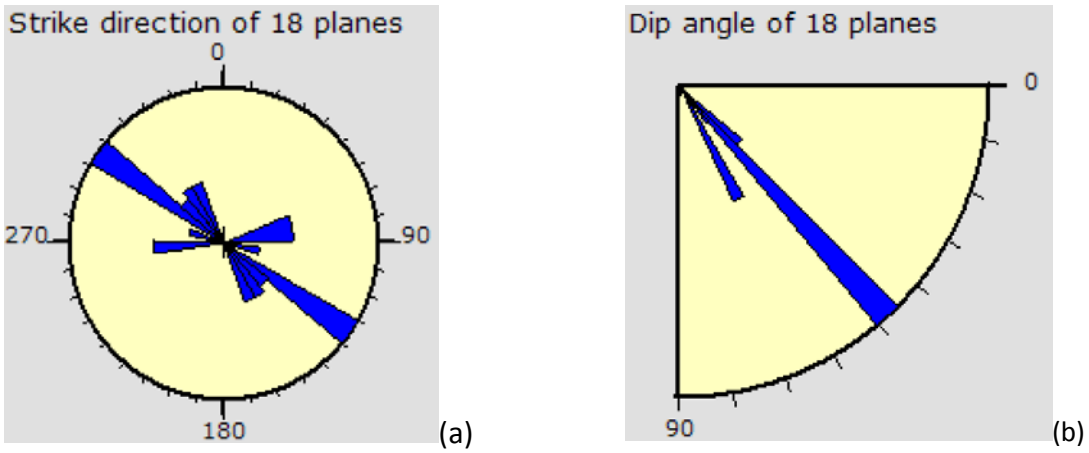

Figure 47: Rose diagram of strike plane (a) and dip plane (b) of the intermediated phase of the mineralised joints in the Tshifufiamashi fragment.

This stress tensor is characterised by the maximal principal stress axis (σ_1) 46/047, the intermediate principal stress axis (σ_2) 06/309 and the minimum principal stress axis (σ_3): 42/213 with a stress ratio (R) equal to 0.92.This tensor belongs to an oblique radial compression stress regime and indicates SE-NW compression and SW-NE extension (Fig. 48).

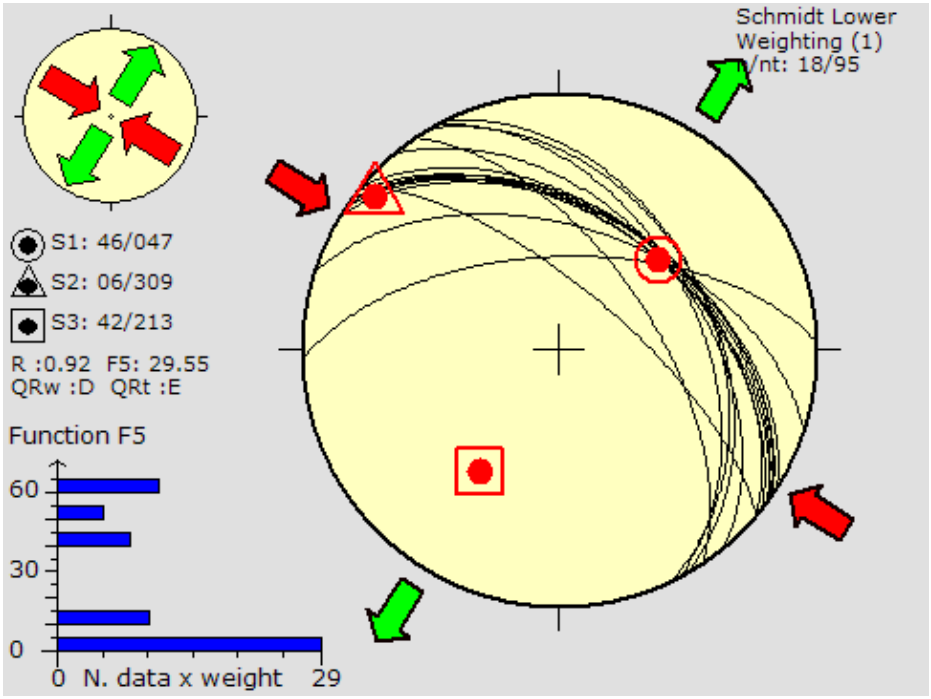

Figure 48: Stereonet of the rotational optimisation results of mineralised tension joints related to the second stress tensor obtained at Tshifufiamashi.

The third stress tensor obtained from the mineralised joint data collected at the Tshifufiamashi fragment is characterised by two groups of strike planes of the mineralised joints. The first group presents a general trend oriented WSW-ENE with a dip angle varying between 70° and 75°; the second group shows a general orientation trend ESE-WNW with dip angle varying between 75° and 80° (Fig. 49 (a) and (b)).

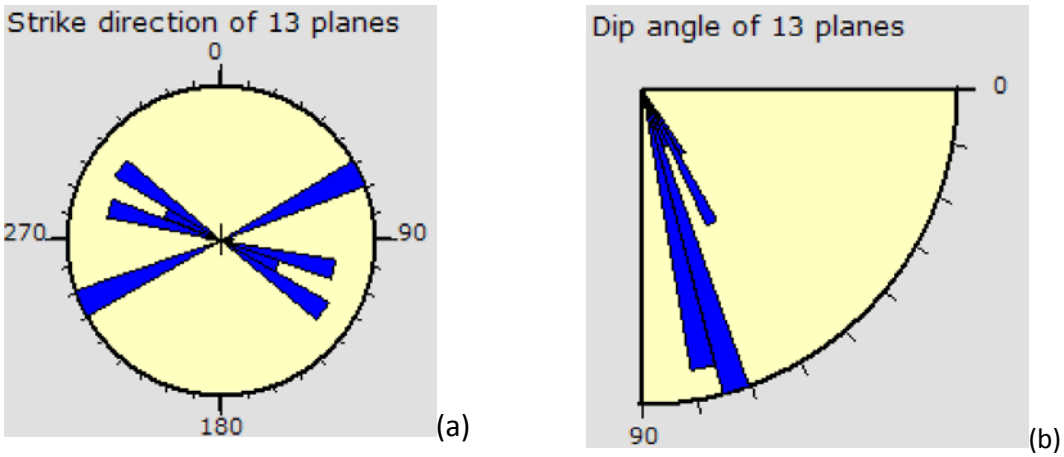

Figure 49: Rose diagram of strike plane (a) and dip plane (b) of the minor phase of the mineralised joints in the Tshifufiamashi fragment.

The third stress tensor obtained from the mineralised joints presents the maximum principal stress axis (σ_1) 50/263, the intermediate principal stress axis (σ_2) 36/111 and the minimum principal stress axis (σ_3) 13/011 with a stress ratio (R) equalling 0.8. This stress tensor belongs to the oblique extensive stress regime and indicates mainly SSW-NNE extension (Fig. 50).

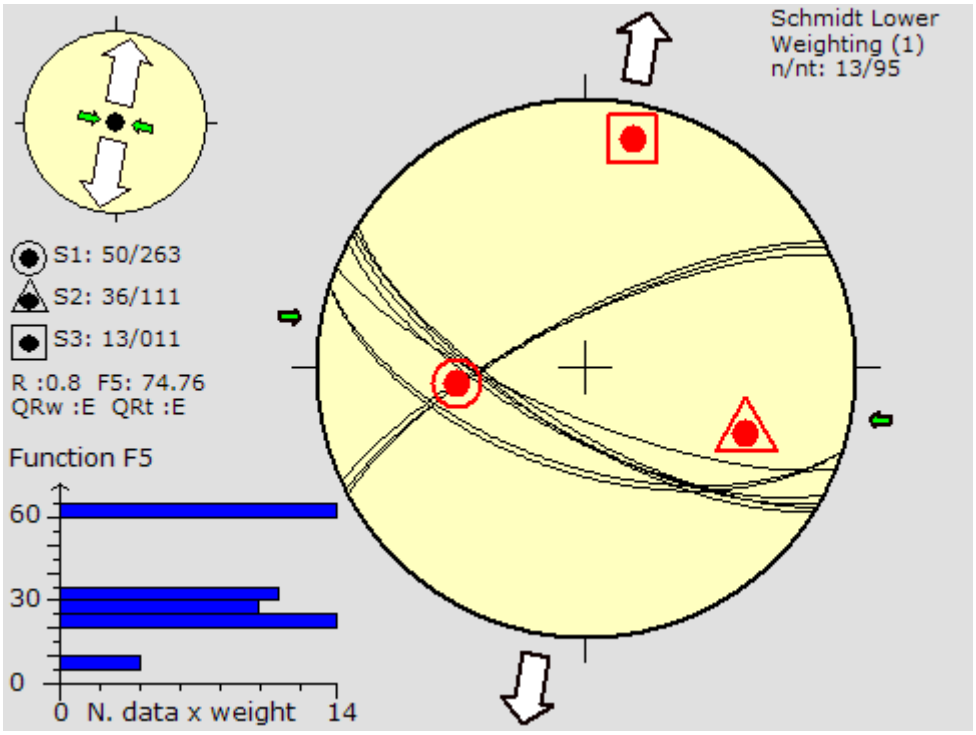

Figure 50: Stereonet of the rotational optimisation results of mineralised joints related to the third stress tensor obtained at Tshifufiamashi.

The following Table 6 summarises the principal stress axes (σ_1, σ_2 and σ_3) and the stress ratio (R) of the three stress tensors obtained from the mineralised joints observed in Tshifufiamashi open pit.

n	nt	Principal stress axis			R	SHmax	Shmin	R'	Stress Regime
		σ_1	σ_2	σ_3					
27	95	38/299	6/204	50/106	0.75	7	97	2.75	Pure COMPRESSIVE
18	95	46/047	06/309	42/213	0.92	121	31	0.92	Oblique radial COMPRESSIVE
13	95	50/263	36/111	13/011	0.8	103	13	0.8	Oblique EXTENSIVE

Table 6: Summary of all stress tensors (σ_1, σ_2 and σ_3), stress ratio (R) and the tectonic stress regime of the mineralised joint in the Tshifufiamashi open pit.

3.3.1.1.2 Unmineralised joints (UMJ)

Forty-five measurements of dip and dip direction were collected from the unmineralised joints in the Tshifufiamashi open pit (Table A.2). One stress tensor was obtained from all unmineralised joint populations.

This stress tensor is mainly characterised by two groups of strike planes. The first group strikes SSW-NNE with sub-vertical dip angle. The second group shows a WSW-ENE strike of planes with dip angles varying between 70° and 75°. There is a minor group that shows SW-NE orientated trend of the strike of the planes of the unmineralised conjugate fracture with dip angles varying between 30 and 40° (Fig. 51(a) and (b)).

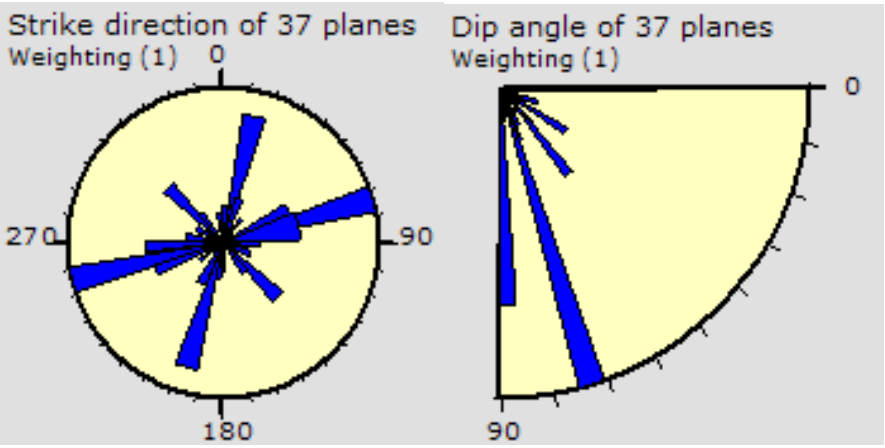

Figure 51: Rose diagram of strike plane (a) and dip plane (b) of the first phase of the unmineralised joints observed at Tshifufiamashi.

The stress tensor obtained from these measurements shows the maximum principal stress axis (σ_1) 39/029, the intermediate principal stress axis (σ_2) 38/160, and the minimum principal stress axis (σ_3) 26/274; with the stress ratio equalling 0.5. The tensor is characteristic of the oblique extensive stress regime and it indicates SE-NW extension (Fig. 52).

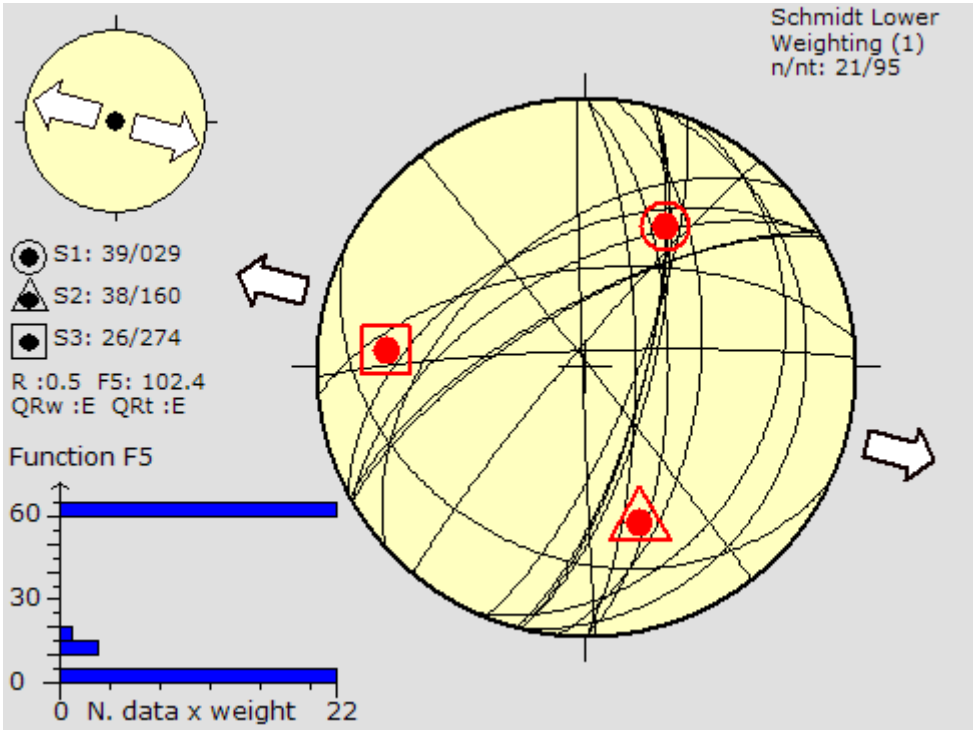

Figure 52: Stereonet showing the principal stress axis (σ_1, σ_2, σ_3) obtained with the improved right dihedral method combined with the rotational optimisation procedure of the unmineralised joints related to the stress tensor obtained at Tshifufiamashi.

Table 7 below gives a summary of the principal stress axis (σ_1, σ_2, and σ_3), the stress ratio and the stress regime of the stress tensor obtained from the unmineralised joints observed at Tshifufiamashi.

n	nt	Principal stress axis			R	SHmax	Shmin	R'	Stress Regime
		σ_1	σ_2	σ_3					
21	95	39/029	38/160	26/274	0.5	15	105	0.5	Oblique EXTENSIVE

Table 7: Summary of all stress tensors (σ_1, σ_2 and σ_3), stress ratio (R) and the tectonic stress regime of the unmineralised joint in the Tshifufiamashi open pit.

3.3.1.2 Faults

At Tshifufiamashi, both types of faults (slickensides and shear fractures) were observed, as at the two other fragments, Tshifufia and Kinsevere Hill. In this section, all stereonets related to the direction of the reduced shear stress of the stress tensor on the fault planes will be presented, in order to establish the kinematics of the brittle deformation occurring during the Lufilian orogeny.

3.3.1.2.1 Slickensided faults

One hundred and seventeen (117) measurements of strike and dip of the fault plane, and in addition, over one hundred (100) measurements of trend and plunge angle of striations were collected on the Tshifufiamashi open pit outcrop (Table A.9). Three stress tensors were obtained from the whole fault-slip populations.

The first stress tensor (54 measurements) is characterised mainly by a group of slickensided fault planes oriented in the SSW-NNE direction with dip angles varying between 55° and 60°.

This group shows two sets of striations. The principal group of striations show an azimuth oriented to the North (0°-5°) with a plunge angle varying between 25° and 30°, plunging to the North. The second set exhibits an azimuth oriented to the SW (220-230) with an angle varying between 15° and 20° plunging to the SW (Fig. 53 (a), (b), (c) and (d)).

A second (minor) group is characterised by the strike planes of slicken surfaces oriented SE-NW with dip angles varying between 35° and 40°. This minor group also shows two sets of striations; the first group displays an azimuth oriented SW (240°-250°) with an angle varying between 50° and 55° plunging to the SW. The second shows an azimuth oriented NW (300°) with a plunge angle varying between 55° and 60° towards the NW (Fig. 53 (a), (b), (c) and (d)).

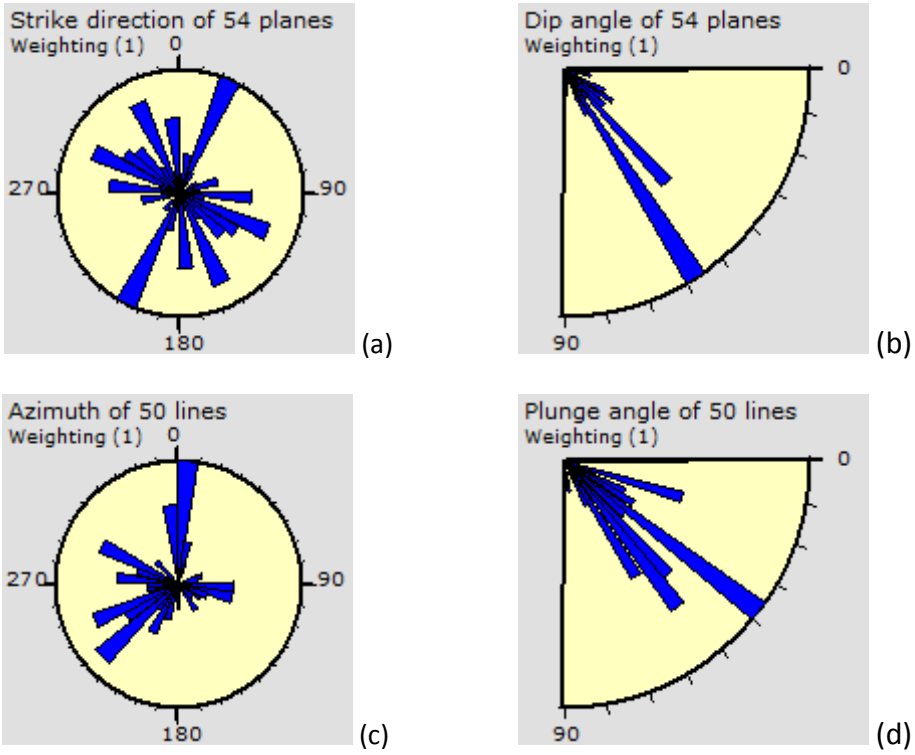

Figure 53: Rose diagrams of the strike plane (a) and dip plane (b), trend of fault slip (c) and plunge angle and (d) of slickensided faults observed at Tshifufiamashi of the first stress tensor.

The stress tensor deduced from these measurements is characterised by the maximum principal stress axis (σ_1) 01/218, the intermediate principal stress axis (σ_2) 00/128 and the minor stress axis (σ_3) 88/008, with the stress ratio (R) and the friction angle (ø) equalling 0.87 and 42.59, respectively. It belongs to the pure compression regime and indicates SW-NE compression (Fig. 54).

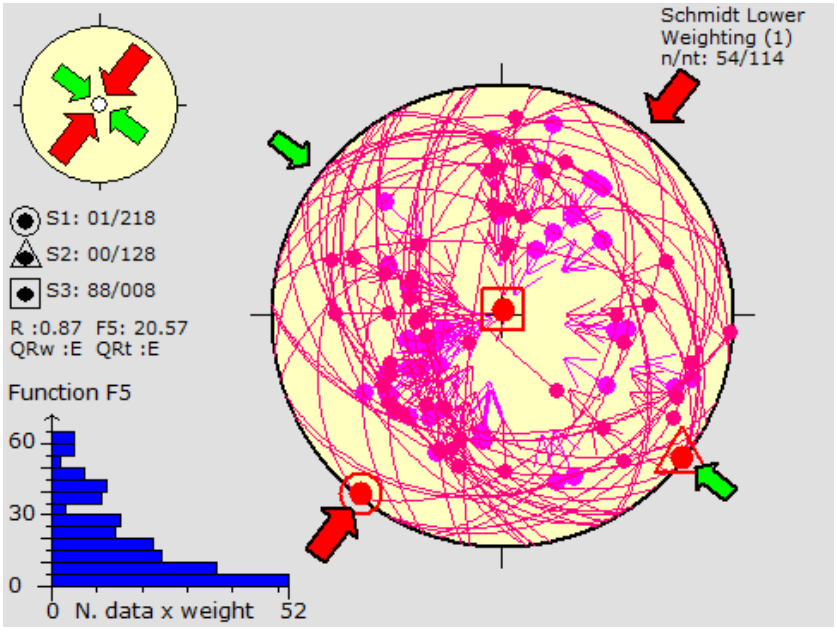

Figure 54: Stereonet showing the principal stress axis (σ_1, σ_2 and σ_3) obtained with the improved right dihedral method combined with the rotational optimisation procedure of the slickensided faults observed at Tshifufiamashi. Faults are displayed as the large circle and the slip striae are represented with an arrow indicating the slip sense.

The results obtained with fault-slip data, presented by stereonets of rotational optimisation, may also be presented using tangent-lineation with pole to plane displays and the corresponding slip direction as described by Hoeppner (1955) and Twiss and Unruh (1998). The following stereonet shows the fault slip acting on the fault plane related to this stress tensor (Fig. 55).

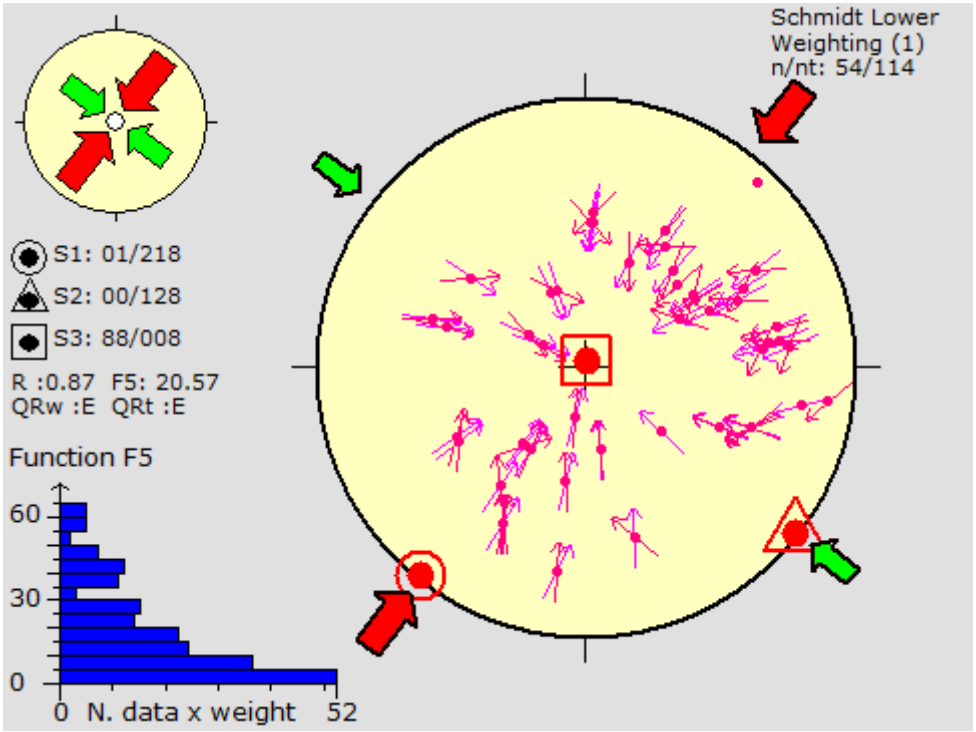

Figure 55: Stereonet using tangent-lineation with pole to plane displays with the corresponding slip direction of slickensided faults observed in Tshifufiamashi.

From the above stereonets, two groups of slip lines may be highlighted. The first group comprises fault slip indicating movement toward the North and the SW related to a stress tensor characterised by σ_1: 02/035, σ_2: 12/126 and σ_3: 77/294 with a stress ratio (R) equalling 0.75. This stress tensor belongs to the pure compression regime and indicates SW-NE compression (Fig. 56a). The second group represents fault planes with fault slip indicating mainly a southerly movement related to a stress tensor characterised by σ_1: 09/235, σ_2: 57/340 and σ_3: 31/140 with a stress tensor (R) equalling 0.47. This second stress tensor belongs to the pure strike-slip regime and indicates respectively SW-NE compression and SE-NW extension (Fig. 56b).

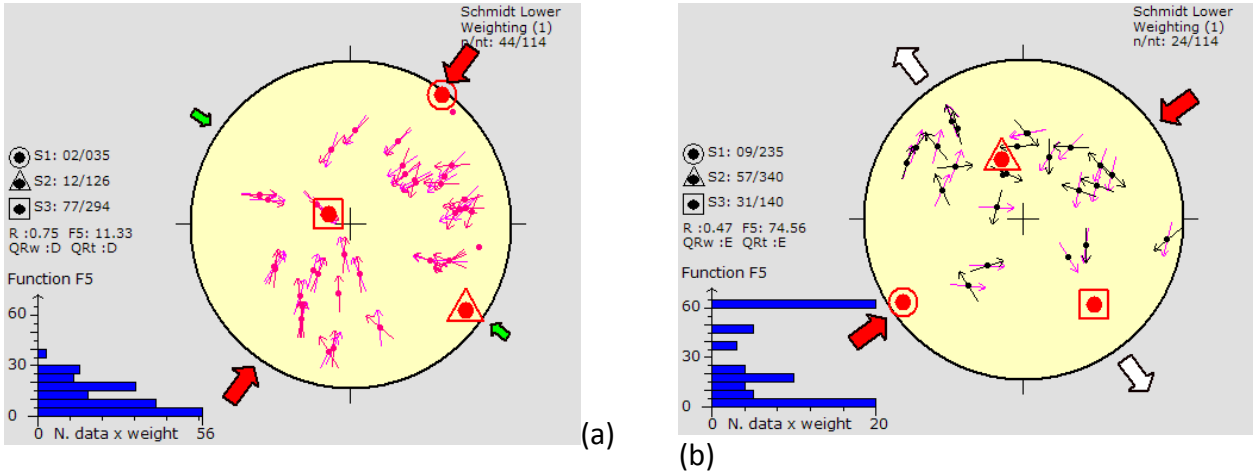

Figure 56: Stereonet showing tangent-lineation data with fault slip acting on fault planes. Stereonet (a) shows the first group related to a SE-NE radial compressional regime and (b) shows the second is related to a pure compression regime oriented SE-NW.

The second stress tensor shows two groups of slickensided surfaces. The first group shows a SE-NW oriented strike with dip angles varying between 80° and 85°. This group carries striations showing an azimuth oriented to the West (260°-270°) with a plunge angle varying between 15° and 20° plunging to the South (Fig. 57 (a), (b), (c) and (d)).

The second group has a N-S oriented strike and contains two minor sets having dip angles varying between 65° and 75°, and 35° and 40° respectively. The striations show an azimuth oriented to the SSW (190°-200°) with a plunge angle varying between 0° and 5° (Fig. 57 (a), (b), (c) and (d)).

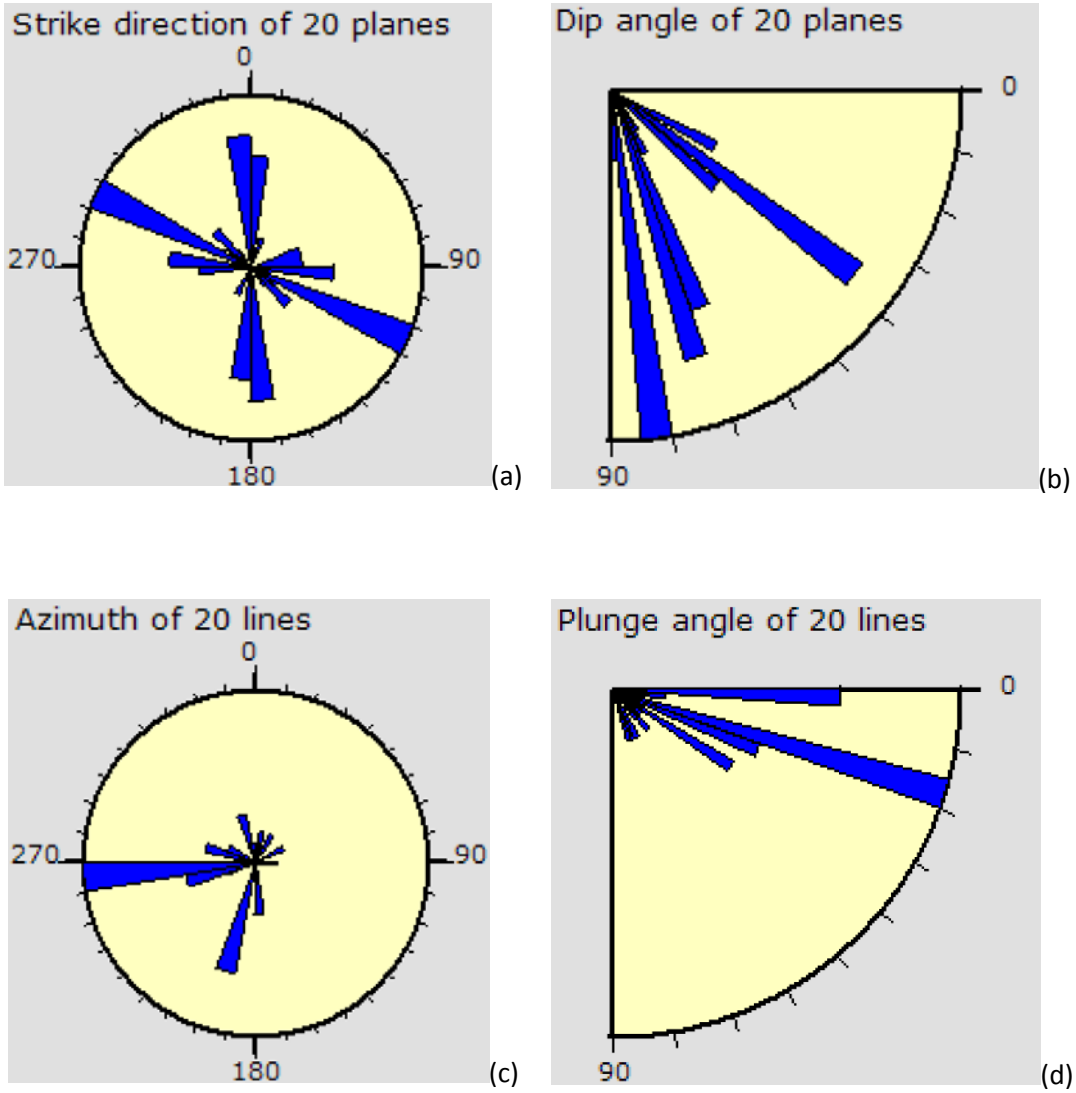

Figure 57: Rose diagrams of the strike plane (a) and dip plane (b), azimuth of fault slip (c) and plunge angle (d) of slickensided faults observed in Tshifufiamashi induced by the second stress tensor.

The stress tensor of this intermediate phase is characterised by the maximum principal stress axis (σ_1): 06/227, the intermediate principal stress axis (σ_2) 67/122, and the minimum principal stress axis (σ_3) 21/320, where the stress ratio equals (R) 0.24 and the friction angle (ø) is 40.12. The tensor belongs to the compressive strike-slip regime and it indicates SW-NE compression and SE-NW extension (Fig. 58).

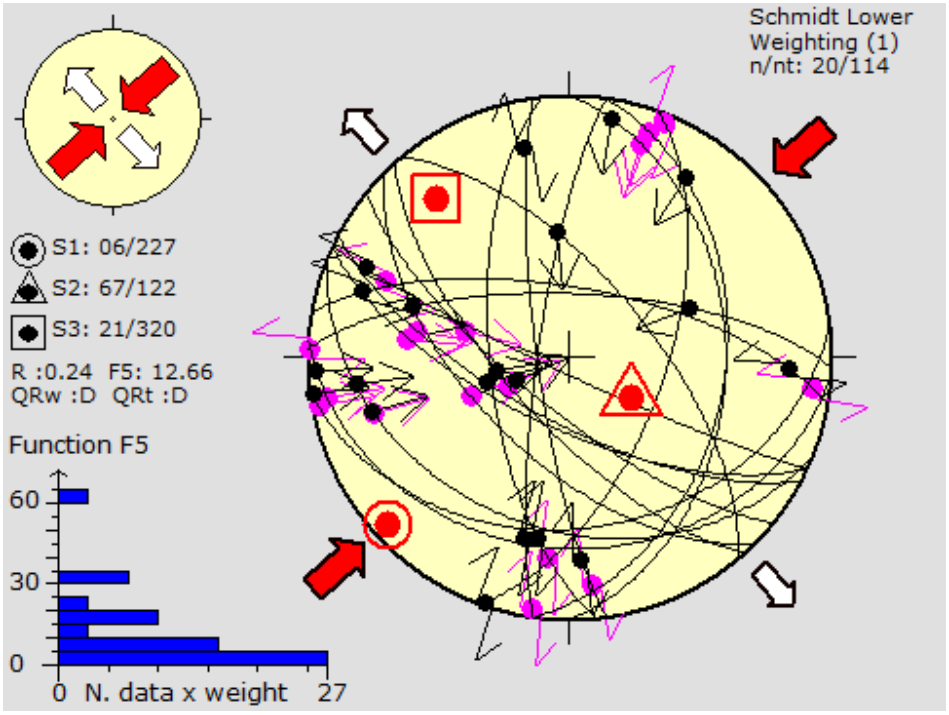

Figure 58: Stereonet obtained from dip and dip direction, azimuth and plunge angle of the fault observed on the open pit outcrop of the Tshifufiamashi fragment.

Presenting the results shown in the above stereonet, using tangent-lineation data from these fault-slips of the intermediate phase, two groups of slip lines acting on the fault planes can be noted: the first group comprises slip indicating a N-S dextral strike-slip movement (circled in red) and the second group represents slip indicating a sinistral E-W strike-slip movement (circled in black); both are related to the general strike-slip stress regime (Fig. 59).

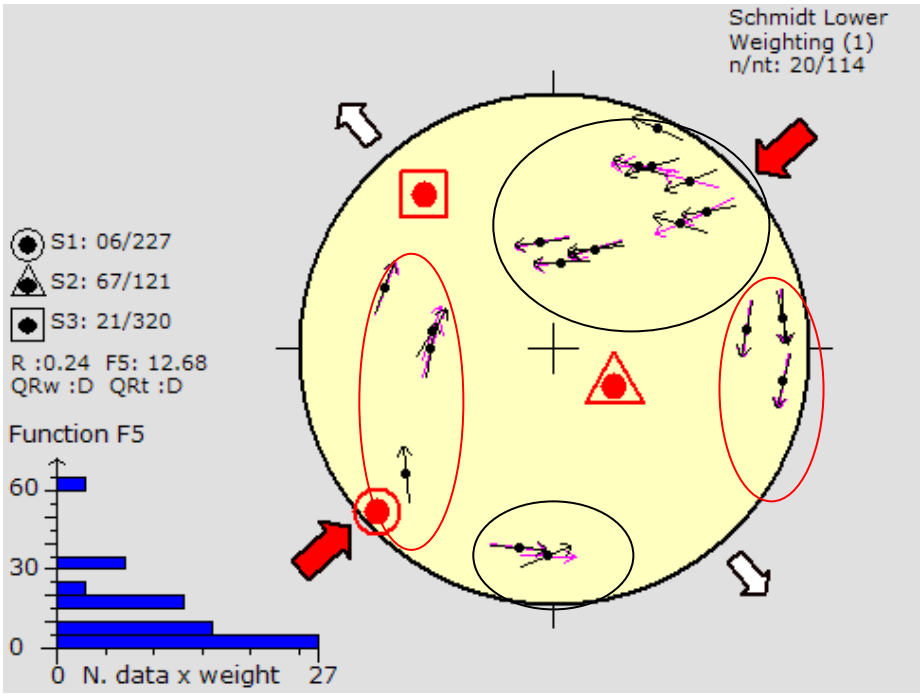

Figure 59: Stereonet showing tangent-lineation data obtained from fault-slip acting on the fault planes of the intermediate phase observed in Tshifufiamashi.

The third stress tensor obtained from the dip and dip direction of slickenside surfaces observed at Tshifufiamashi is characterised by a SE-NW orientation of strike planes with dip angles ranging between 55° and 60°. Slickensides on the fault plane can be grouped into two sub-groups, one of which is characterised by striations with an azimuth oriented to the East plunging to the East at an angle varying between 55° and 65°; the second group displays striations with azimuths oriented to the NE plunging to the NE with a plunge angle varying between 10° and 25° (Fig. 60 (a), (b), (c) and (d)).

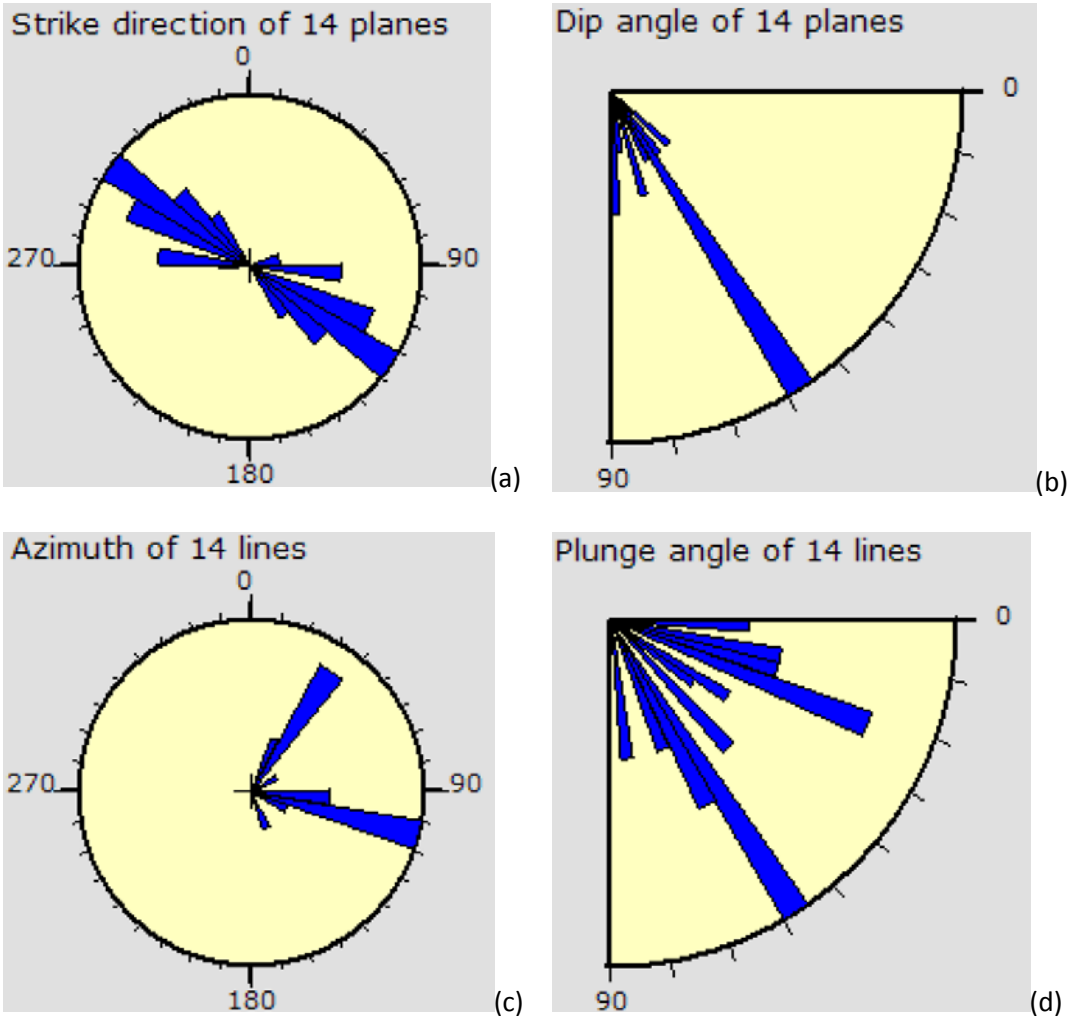

Figure 60: Rose diagrams of the strike plane (a) and dip plane (b), azimuth of fault slip (c) and plunge angle (d) of slickensided faults observed in Tshifufiamashi belonging to the third stress tensor.

The third stress tensor deduced from the fault-slip is characterised by σ_1:38/125, σ_2: 51/303 and σ_3: 00/034; with R and ø equal to 0.43 and 58.99 respectively. This tensor belongs to the pure strike-slip regime and indicates respectively a SE-NW compression and SW-NE extension (Fig. 61)

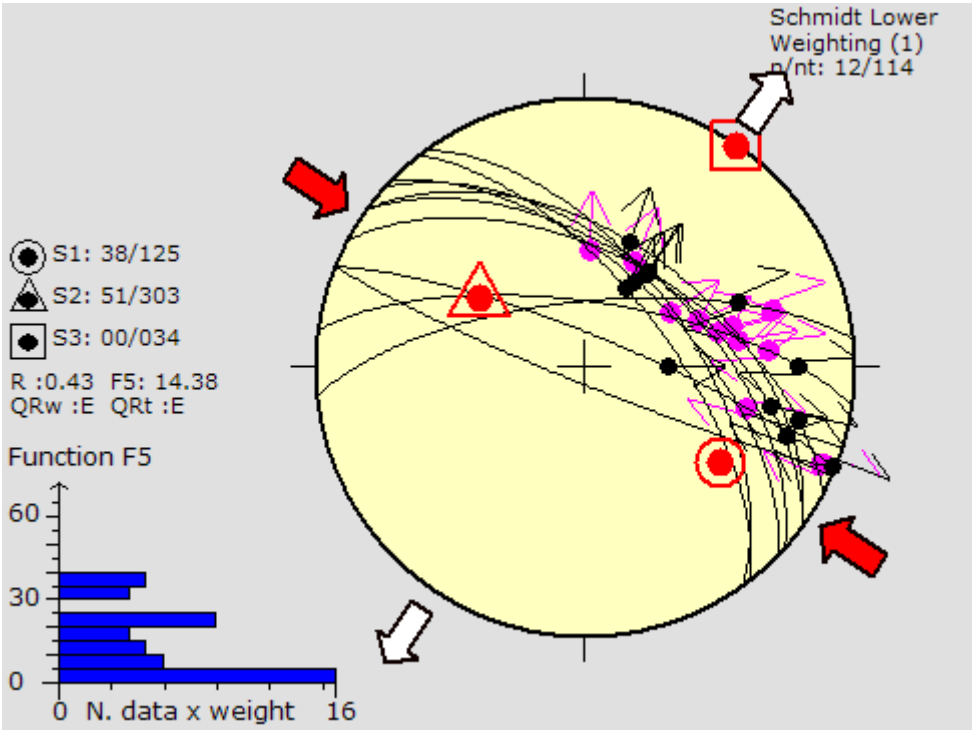

Figure 61: Stereonet showing the principal stress axis obtained with the improved dihedral method combined with the rotational optimisation procedure of the fault-slip data collected from the open pit outcrop at the Tshifufiamashi fragment.

Presenting the results shown in the above stereonet as conducted with respect to the intermediate phase, with tangent-lineation data from these fault-slips, it is noted that slip lines acting on the fault planes belonging to the third stress tensor indicate that the footwall is moving upward towards the SW and, conversely, the hanging wall is moving downward towards the NE (Fig. 62).

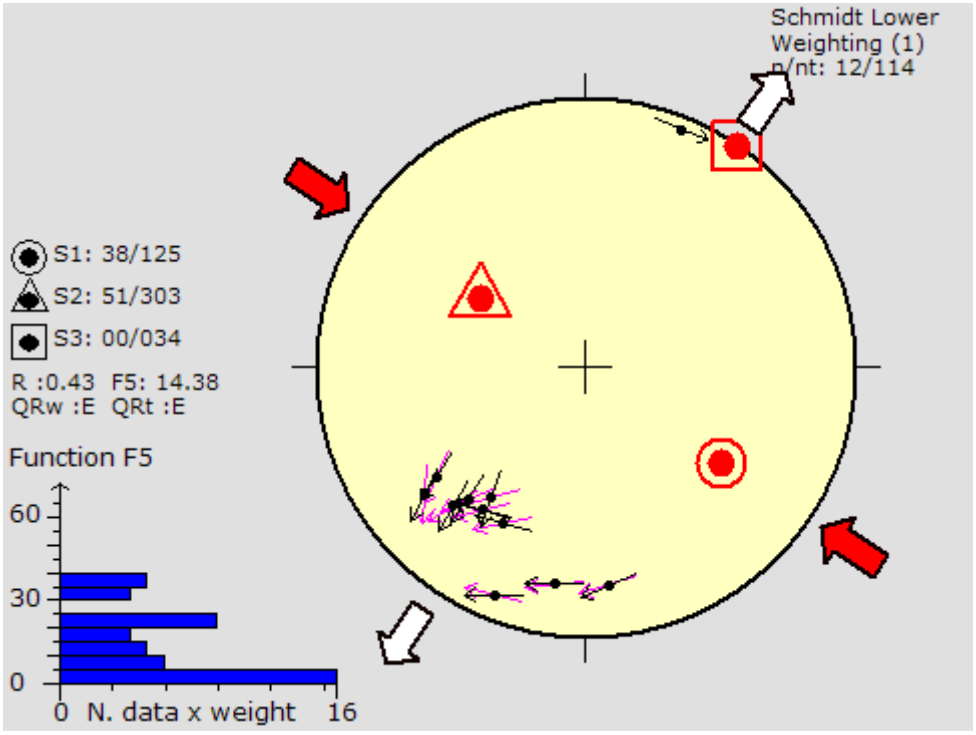

Figure 62: Stereonet with tangent-lineation data of fault slip acting on the fault planes belonging to the third stress tensor observed at Tshifufiamashi.

The following Table 8 summarises all stress tensors (σ_1, σ_2 and σ_3) and stress ratio (R) obtained from the slickenside data collected from the Tshifufiamashi open pit outcrops.

n	nt	Principal stress axis			R	SHmax	Shmin	R'	phi	Stress Regime
		σ_1	σ_2	σ_3						
68	95	01/218	00/128	88/008	0.87	38	128	2.87	42.59	Radial COMPRESSIONAL
20	114	06/227	67/121	21/320	0.24	49	139	1.76	40.12	Compressional STRIKE-SLIP
12	114	38/125	51/303	00/034	0.43	124	34	1.57	58.99	Pure STRIKE-SLIP

Table 8: Summary of all stress tensors (σ_1, σ_2 and σ_3), stress ratio and the stress regime of the slickensides at the Tshifufiamashi fragment.

3.3.1.2.2 Shear Fractures

Shear fracture is defined as a fracture plane for which there are reasonable indications that it has been activated by slip, but where no indications for the slip direction can be seen (Delvaux, 2010). These fractures might indicate the apparent dip-slip or strike-slip movement. Thirty-five measurements of both normal and reserve fault planes were collected at the Tshifufiamashi (Table A.4). Two stress tensors were obtained from the whole fault population.

The first stress tensor is characterised by a group of fault planes presenting SSW-NNE and SSE-NNW trends with dip angles varying between 50° and 70° (Fig. 63).

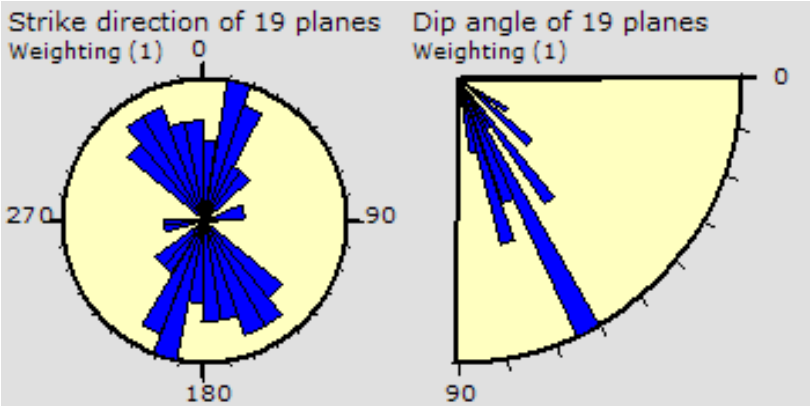

Figure 63: Rose diagram of strike planes (a) and dip planes (b) obtained from the fault plane of the observed reverse fault in the Tshifufiamashi open pit.

This stress tensor is characterised by the maximum principal stress axis (σ_1): 10/260, the intermediate principal stress axis (σ_2): 09/352 and the minimum principal stress axis (σ_3): 76/123, with the stress ratio (R) and the friction angle (ø) equalling respectively 0.5 and 42. This tensor belongs to the pure compression stress regime and indicates a WSW-ENE compression (Fig. 64).

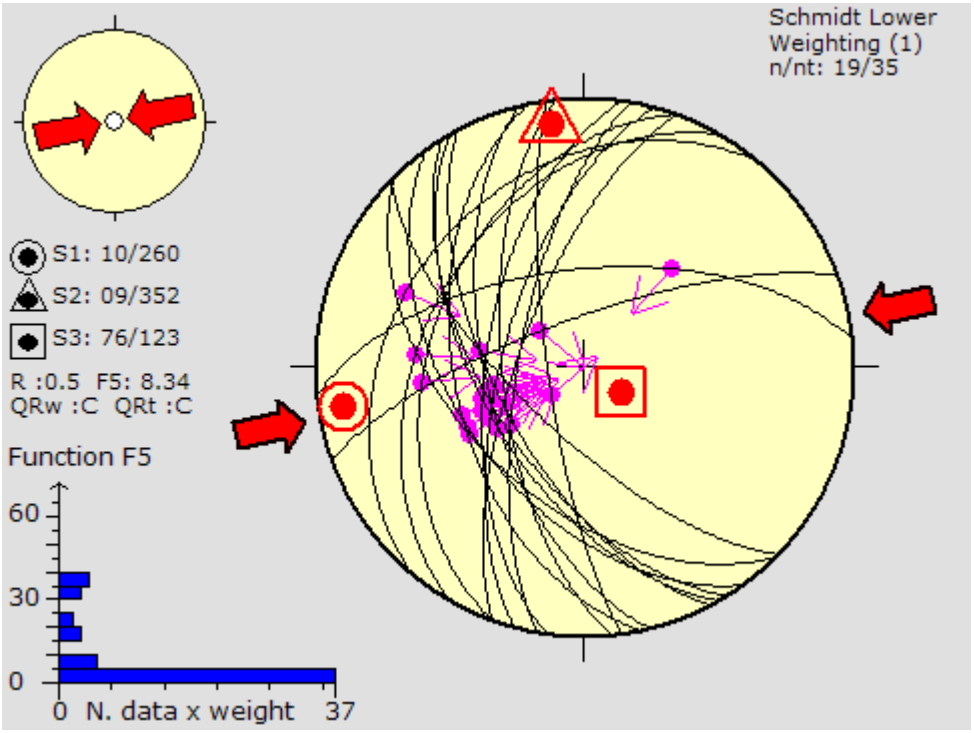

Figure 64: Stereonet showing the principal stress axis obtained with the improved dihedral method combined with the rotational optimisation procedure of the reserve shear fracture observed at the Tshifufiamashi fragment.

The second stress tensor is characterised by a group of fault planes showing SE-NW strike with dip angles varying between 40° and 50°, and 70° and 80°. There is a minor group of strike planes oriented SW-NE with dip angles varying between 20° and 30° (Fig. 65)

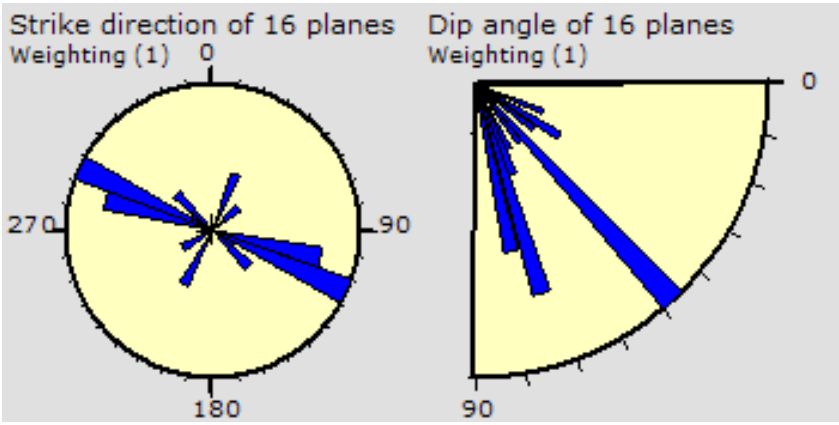

Figure 65: Rose diagram of strike planes (a) and dip planes (b) obtained from the fault plane of the observed normal fault in the Tshifufiamashi open pit.

The stress tensor deduced from these measurements shows the maximum principal stress axis (σ_1): 44/256, the intermediate principal stress axis (σ_2): 45/074 and the minimum principal stress axis (σ_3): 01/165, with the stress ratio (R) and the friction angle equal respectively 0.5 and 38.2. This tensor belongs to the oblique extensive stress regime and it indicates a SSE-NNW extension (Fig. 66).

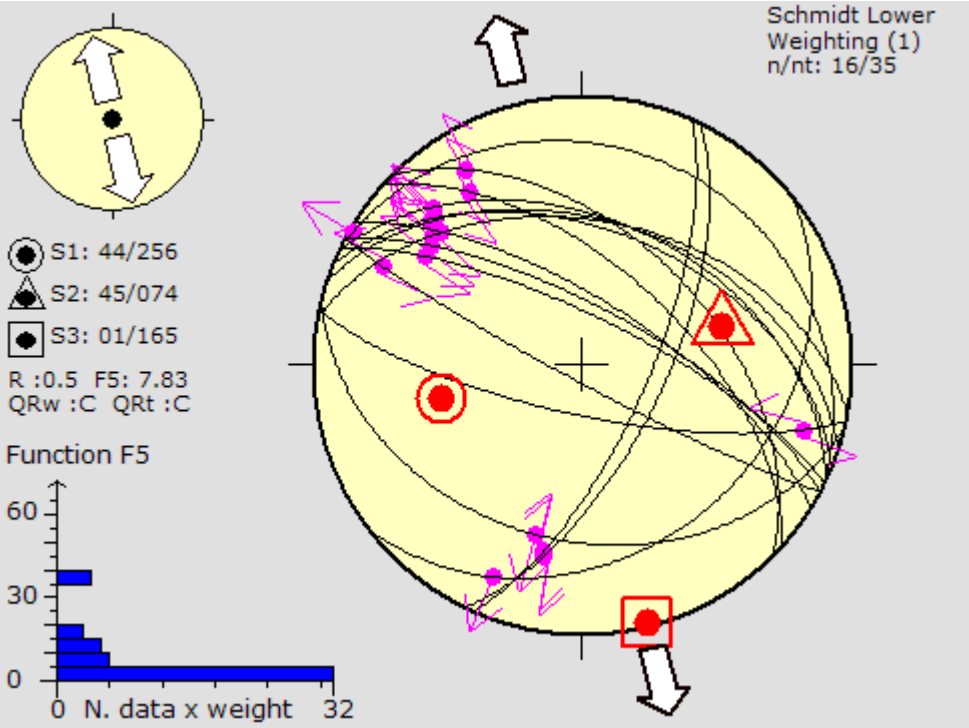

Figure 66: Stereonet showing the principal stress axis obtained with the improved dihedral method combined with the rotational optimisation procedure of the normal shear fracture observed at the Tshifufiamashi fragment.

The following Table 9 summarises all palaeostress tensors (σ_1, σ_2 and σ_3) and stress ratio (R) obtained from the shear fractures data collected at the Tshifufiamashi open pit.

n	nt	Principal stress axis			R	SHmax	Shmin	R'	phi	Stress Regime
		σ_1	σ_2	σ_3						
19	35	10/260	09/352	76/123	0.5	79	169	2.5	41.97	Pure COMPRESSIONAL
16	35	44/256	45/074	01/165	0.5	76	166	1.5	38.15	Oblique EXTENSIVE

Table 9: Summary of all stress tensors (σ_1, σ_2 and σ_3), stress ratio (R) and the stress regime of the shear fracture observed at the Tshifufiamashi fragment.

3.3.1.3 Folding

Folds are the most common structural features that develop within rocks. They occur at all scales (microns to mountain belts) and under all conditions (uppermost brittle crust, mantle, magma chambers). In the Tshifufiamashi fragment, concentric folds can be observed in the western limb of the open pit of the Mines Subgroup; the CMN strata are mainly affected by micro-folds, occasionally showing micro-fracturing. We processed all the structural features related to the folding using Stereo 32 software.

The orientation of bedding planes, hinge line (HL) and fold axial planes (FAP) were measured in the Tshifufiamashi open pit (Table A.5). Bedding generally dips steeply westwards, showing an upright succession with the youngest strata (CMN) outcropping in the western area of the pit while the oldest strata (RAT) were outcropping to the East of the pit.

The Phi diagram of poles to bedding of the Tshifufiamashi fragment (Fig. 67) reveals that bedding generally dips steeply westwards, showing a normal succession with the oldest

strata (RAT) in the East of the pit overlain by the youngest strata (CMN) in the West. The Phi diagram plotting from the bedding planes observed at Tshifufiamashi shows a fold axis oriented 305° (NW) and plunging 35° to the NW.

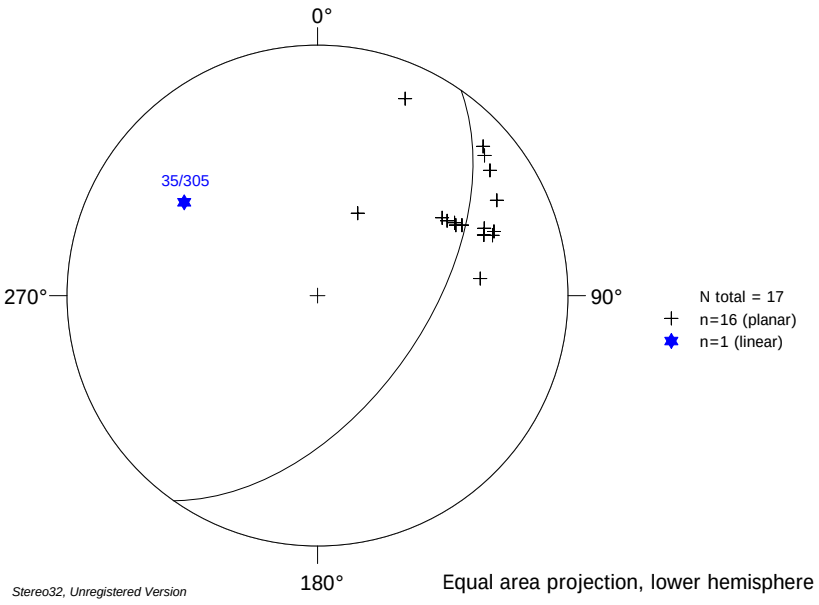

Figure 67: π diagram indicating the fold axis of the Tshifufiamashi fragment.

However, the bedding planes dip and dip direction collected from the small-scale deformed CMN strata observed in the western part of the Tshifufiamashi open pit (shown in a Phi diagram below) indicate that they are folded around a fold axis oriented 03/139 (Fig. 68).

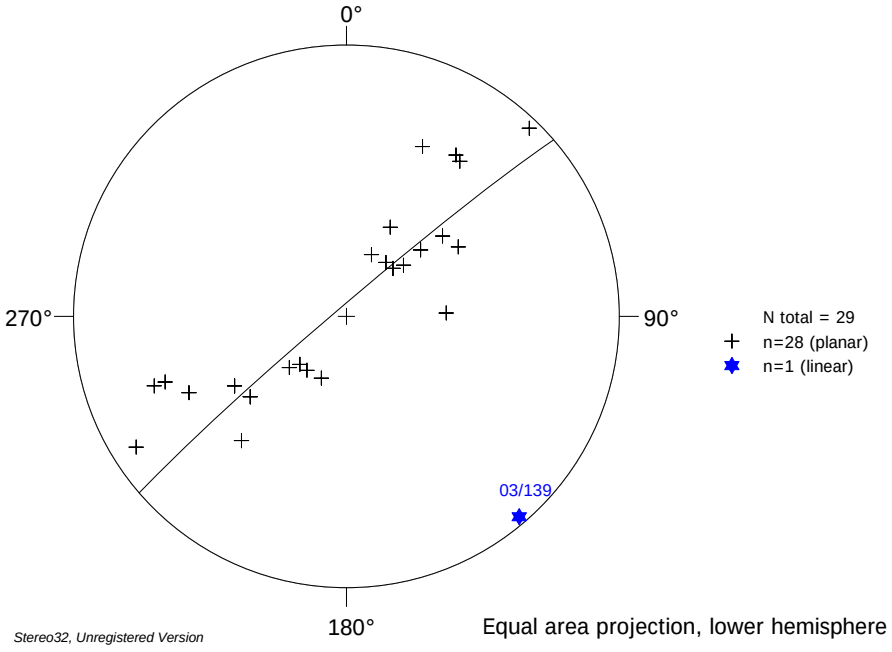

Figure 68: π diagram indicating the fold axis obtained from the bedding plane observed in Tshifufiamashi.

A plot of hinge lines indicates that they plunge gently to the SE (18°) with a trend of 126° (Fig. 69).

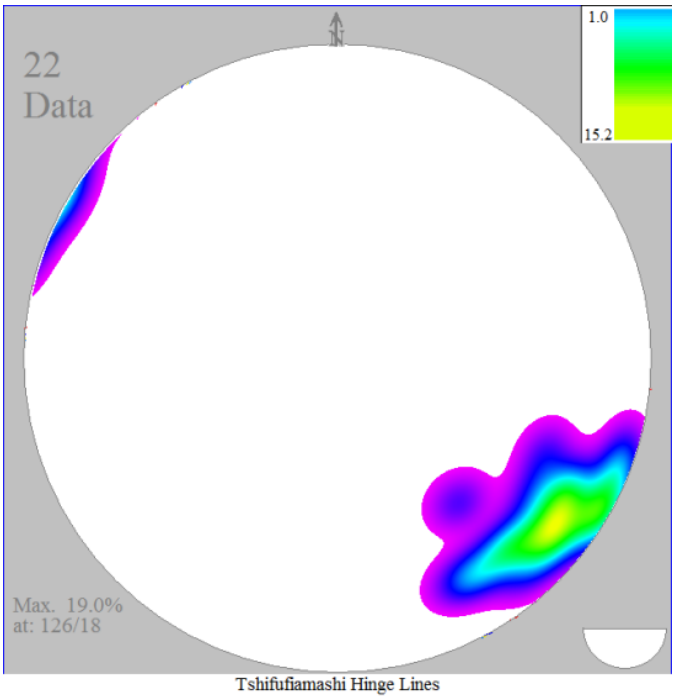

Figure 69: Stereonet showing the hinge lines data collected from the Tshifufiamashi fragment.

In the western limb of the open pit, at the base of the CMN strata towards the contact with the SD strata and to the top of the lower CMN strata, small-scale folds (Fig. 70a) with fold axial planes dipping generally gently SW were observed. Twenty-five measurements of the fold axial plane of these small-scale folds were collected and the stereonet obtained (Fig. 70b) indicating a NE vergence to these folds.

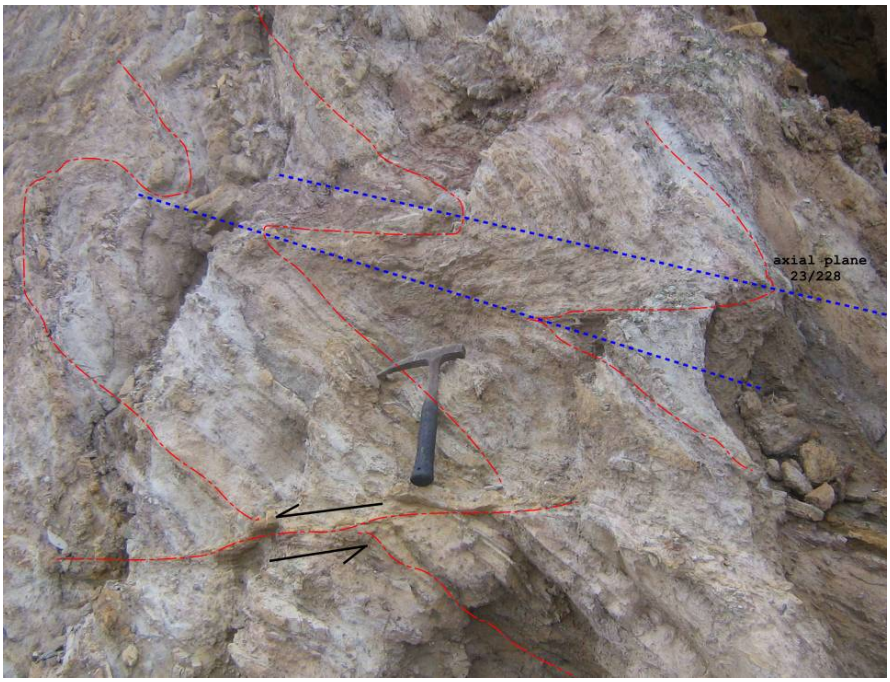

Figure 70 (a) Tight micro-folds in the CMN strata showing NE vergence in the Tshifufiamashi open pit. Looking South.

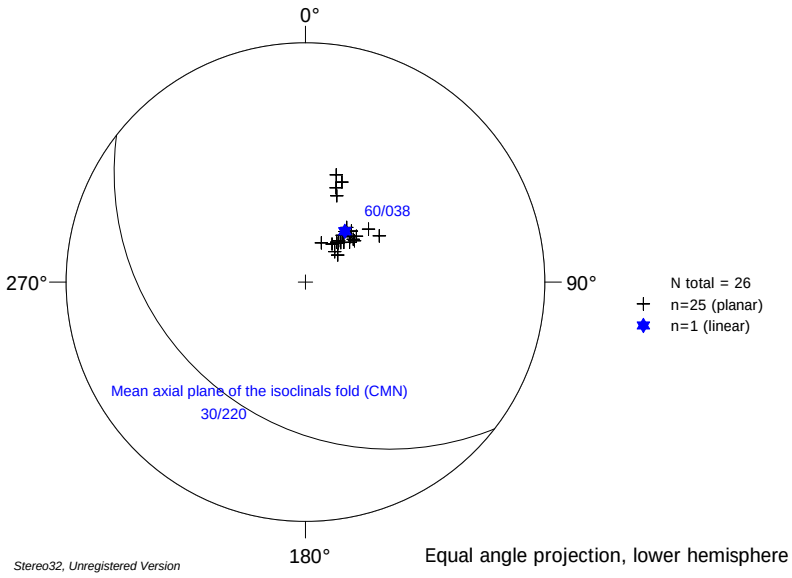

Figure 70 (b): π diagram of pole to small-scale fold axial planes collected in the Tshifufiamashi fragment.

The following Table 10 summarises the plunge angle/azimuth orientation of the fold axis and hinge lines and the dip and dip direction of the axial planes obtained from the field data collected from the Tshifufiamashi open pit.

Tshifufiamashi	Dip / plunging angle	Dip direction/Azimuth orientation
Fold axis of the fragment	35	305
Fold axis-Isoclinals (CMN)	03	139
Hinge line-isoclinals (CMN)	18	126
Fold axial plane-isoclinals (CMN)	30	220
Vergence of the fold	NE	

Table 10: Showing the dip/plunging angle, dip-dip direction/azimuth orientation and vergence of the folding event obtained at the Tshifufiamashi open pit.

3.3.1.4 Thrust faulting

Along a NE-SW section through the Tshifufiamashi open pit (Fig. 65), the upper part of the lower CMN displays small-scale folds with axial planes (kink planes) dipping to the South-West (45/228). The SW limbs of these folds are affected by reverse fault planes also dipping to the SW (59/219). The lower part of the upper CMN, which is overlain directly by these faulted folds, is characterised by micro-folds having axial planes parallel to those of the overturned folding in the CMN (30/207). The CMN is overlain by the Red RAT through a heterogeneous breccia.

The folded and faulted CMN shows thrust faulting taking place along a reverse fault plane indicating a movement toward the NE (Fig. 71).

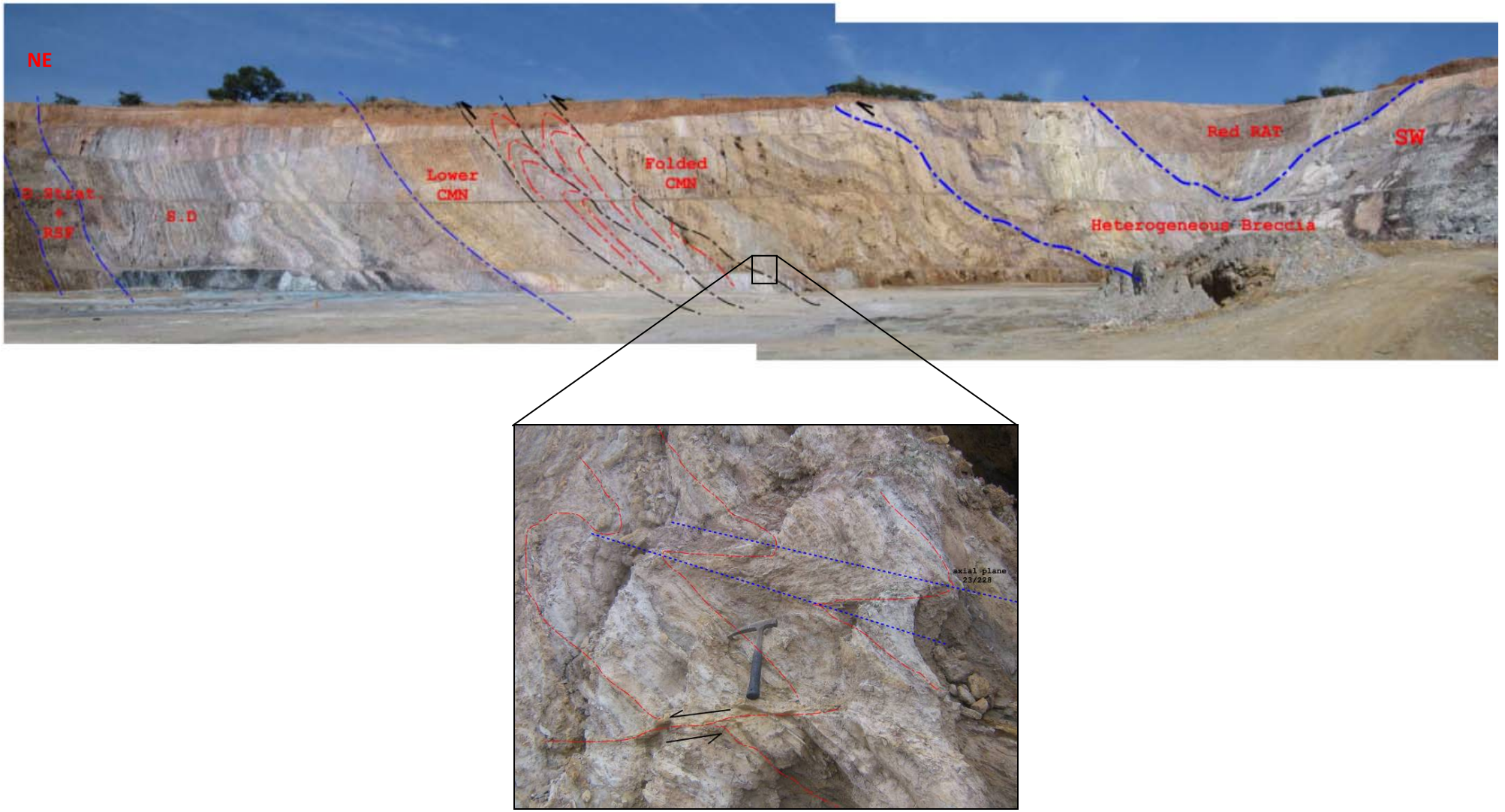

Figure 71: NE-SW section along the Tshifufiamashi open pit showing faulted-fold thrusting toward the NE. Looking South.

3.3.2 Tshifufia fragment

The Tshifufia fragment is situated into the middle of the Kinsevere area (Fig. 72) and hosts the biggest mining excavation known as the Central Pit. Tshifufia consists of an overturned limb of a regional fold with the younger formation (CMN) exposed in the western limb of the open pit, overlain by the oldest formations (RAT) that outcrop in the eastern limb. As in the case of Tshifufiamashi, this fragment is also affected by brittle structures, such as joints, slickensides and fault planes. The CMN strata which are the youngest formations are folded and fractured.

3.3.2.1 Fractures

The R2 Mines Subgroup strata of the Tshifufia fragment are affected by fractures in the same manner as the Tshifufiamashi fragment and can be divided also into two groups. The first group comprises mineralised fractures which consist mainly of joints occupied by copper-cobalt mineralisation composed of malachite and heterogenite, and copper-cobalt sulphides in unweathered lithologies. The second group comprises unmineralised fractures. The angle between these sets of mineralised joints is acute to moderate, varying between 30° and 60° (Fig. 73 (a), (b) and (c)).

The data has been processed in exactly the same way as that from Tshifufiamashi and is presented according to fracture type.

3.3.2.1.1 Mineralised Joints (MJ)

Two hundred and ten measurements were carried out from the mineralised joints in the Central pit (Table A.6). Four stress tensors were obtained from these measurements.

The first stress tensor is characterised by a group of mineralised joints showing a strike plane trending S-N with dip angle varying between 30° and 40° dipping East (Fig. 74 (a) and (b)).

The stress tensor deduced from these measurements (39) gives the maximum principal stress axis (σ_1): 05/172, the intermediate principal stress axis (σ_2): 47/076 and the minimum principal stress axis (σ_3): 42/266, with the stress ratio equalling 0.35. This tensor belongs to oblique compression and it indicates a SSW-NNE compression (Fig. 75).

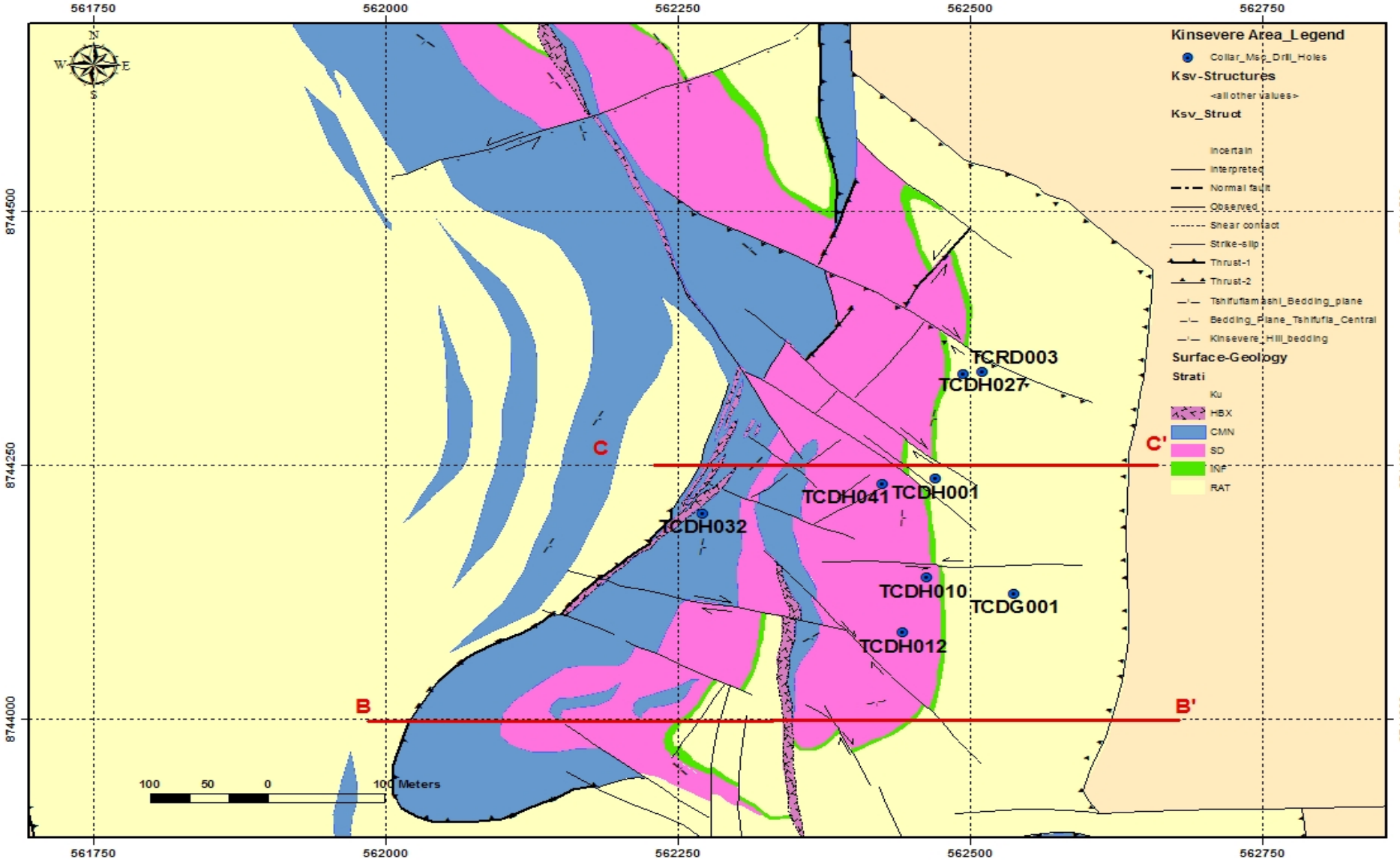

Figure 72: Geological map of the Tshifufia fragment. B-B' and C-C' cross-sections refer to Figs. 11 and 12. (Anvil Mining-Exploration, Houda, B., 2008).

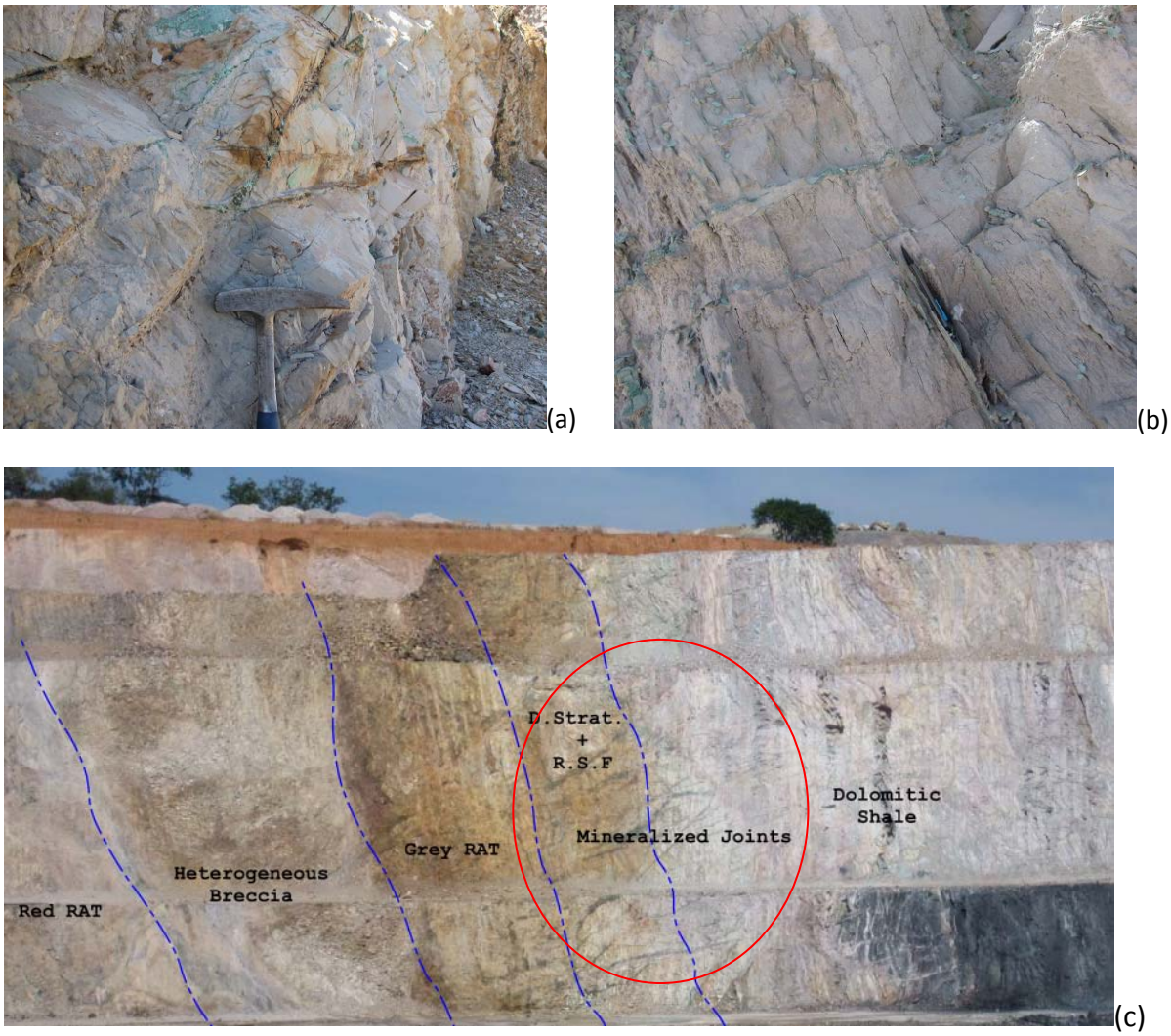

Figure 73: Mineralised joints in outcrop of the Central pit. (a) Acute angle between set of mineralised joint, looking East; (b) Mineralised joint cutting bedding planes, looking NW; (c) E-W section showing D.Strat + RSF strata affected by mineralised joints, looking South.

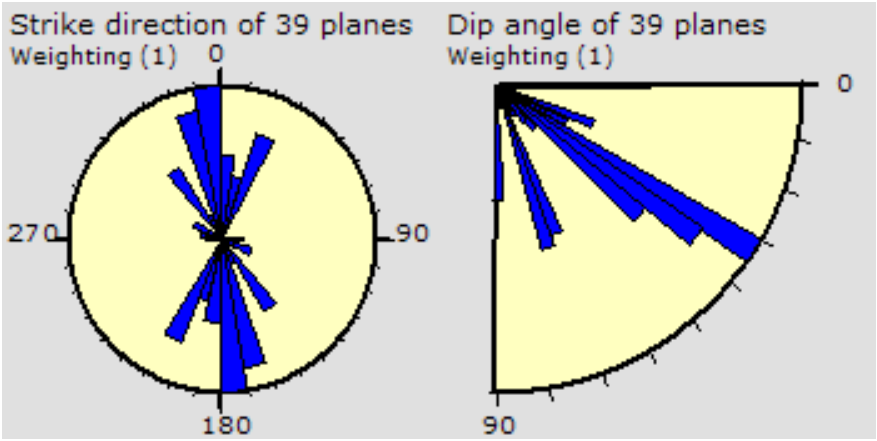

Figure 74: Rose diagram of strike plane (a) and Dip plane (b) obtained from the mineralised joints observed in the Tshifufia open pit and related to the first stress tensor.

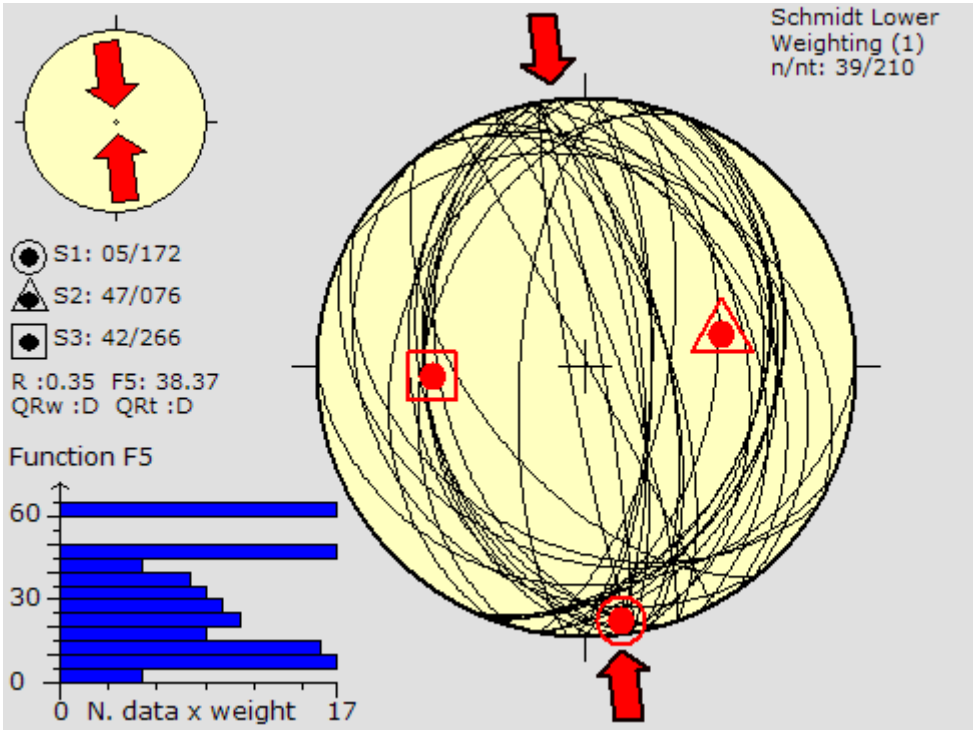

Figure 75: Stereonet showing the principal stress axis obtained with the improved dihedral method combined with the rotational optimisation procedure of the mineralised joints observed in the Tshifufia open pit.

The second stress tensor is characterised by a group of mineralised joints with SW-NE strike with dip angles varying between 70° and 85° (Fig. 76 (a) and (b)).

This stress tensor is characterised by the maximum principal stress axis (σ_1): 27/220, the intermediate principal stress axis (σ_2): 62/043 and the minimum principal stress axis (σ_3) 01/311, with the stress ratio (R) equalling 0.35. This tensor belongs to the pure strike-slip stress regime and it indicates respectively SW-NE compression and SE-NW extension (Fig. 77).

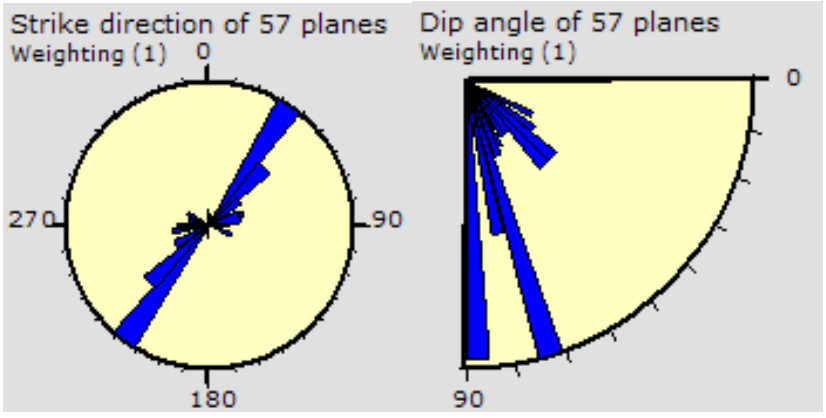

Figure 76: Rose diagram of strike plane (a) and dip plane (b) obtained from the mineralised joints observed in the Tshifufia open pit and related to the second stress tensor

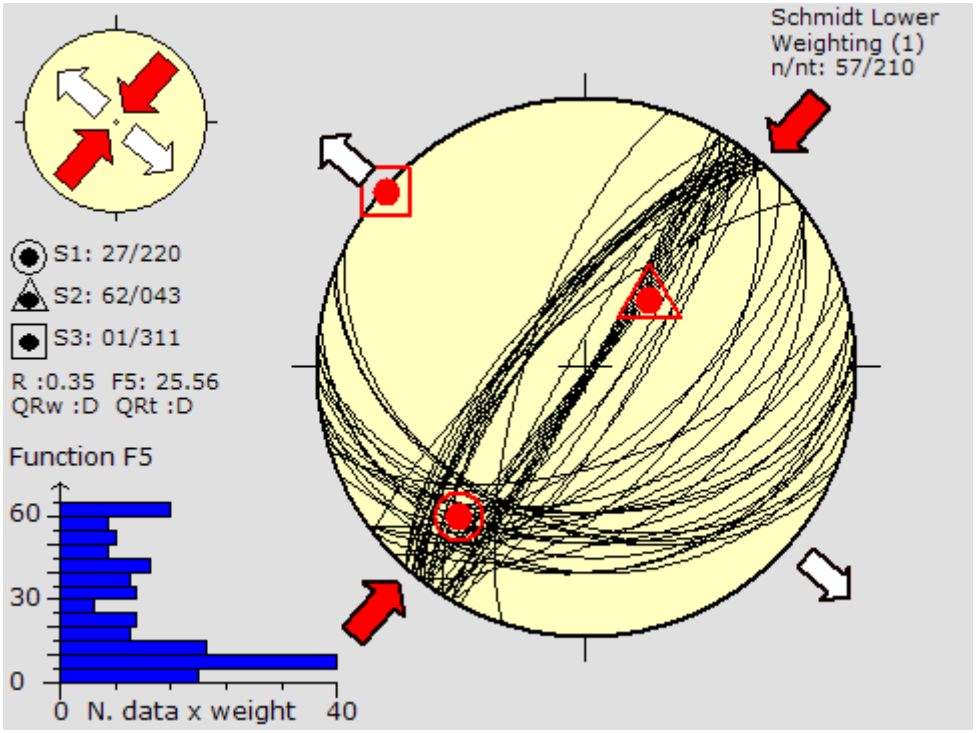

Figure 77: Stereonet showing the principal stress axis obtained with the improved dihedral method combined with the rotational optimisation procedure of the mineralised joints related to the second stress tensor at the Tshifufia open pit

The third stress tensor is characterised by a group of mineralised joints showing SE-NW trend with dip angles varying between 70° and 80° (Fig. 78 (a) and (b)).

The stress tensor obtained from the measurements (53) presents the maximal principal stress axis (σ_1): 03/123, the intermediate principal stress axis (σ_2): 62/025 and the minimum principal stress axis (σ_3): 26/214, with the stress ratio (R) equalling 0.95. This tensor belongs to the extensional strike-slip stress regime and it indicates respectively SW-NE extension and SE-NW compression (Fig. 79).

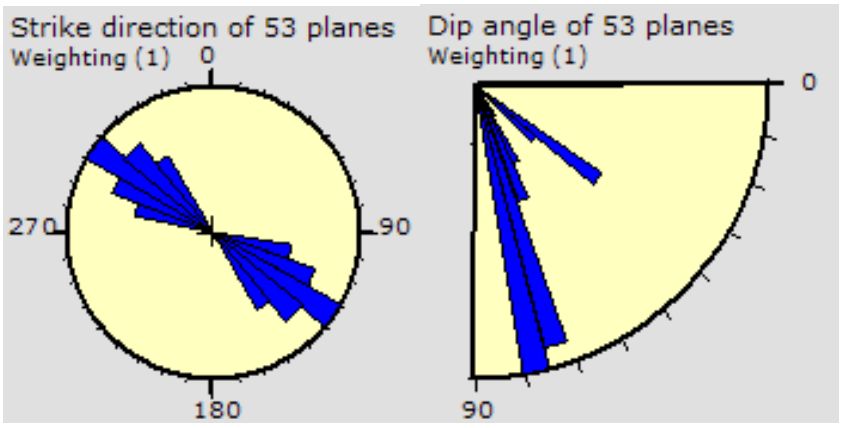

Figure 78: Diagram of strike plane (a) and dip plane (b) obtained from the mineralised joints observed in the Tshifufia open pit and related to the third stress tensor.

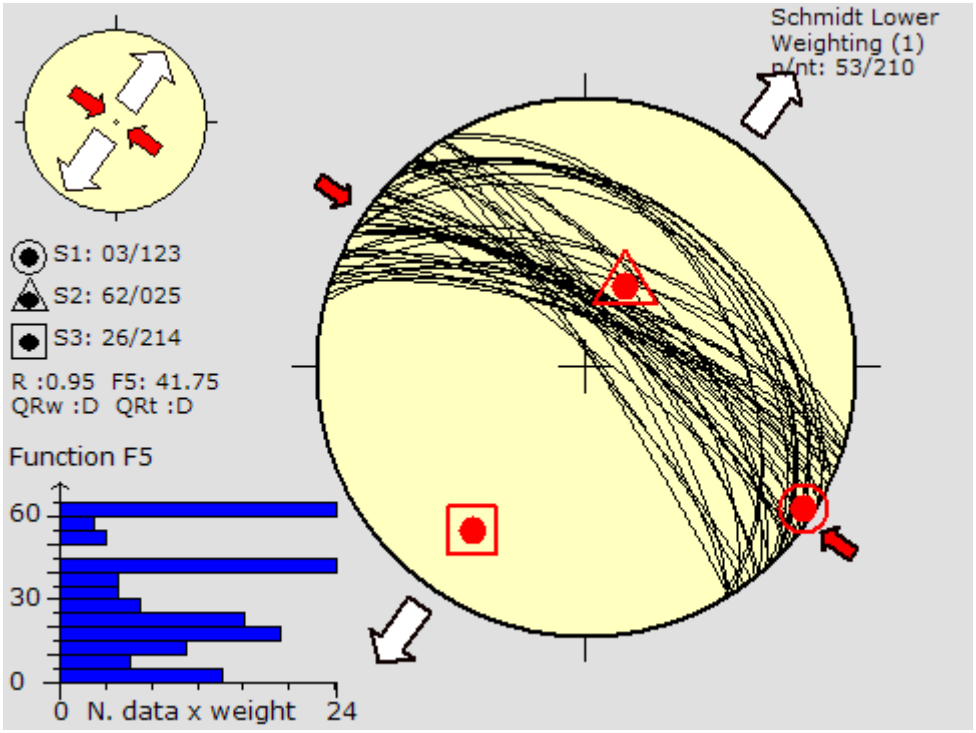

Figure 79: Stereonet showing the principal stress axis obtained with the improved dihedral method combined with the rotational optimisation procedure of the mineralised joints related to the third stress tensor at the Tshifufia open pit.

The fourth stress tensor is characterised by a group of mineralised joints and is characterised by a WNW-ESE trend with dip angle varying between 45° and 50° and 80° and 85° (Fig. 80 (a) and (b)).

The stress tensor related to these measurements (21) gives the maximal principal stress axis (σ_1): 32/291, the intermediate principal stress axis (σ_2): 49/152 and the minimum principal stress axis (σ_3): 21/035, with the stress ratio (R) equalling 0.2. The tensor belongs to the oblique extension stress regime and indicates SW-NE extension (Fig. 81).

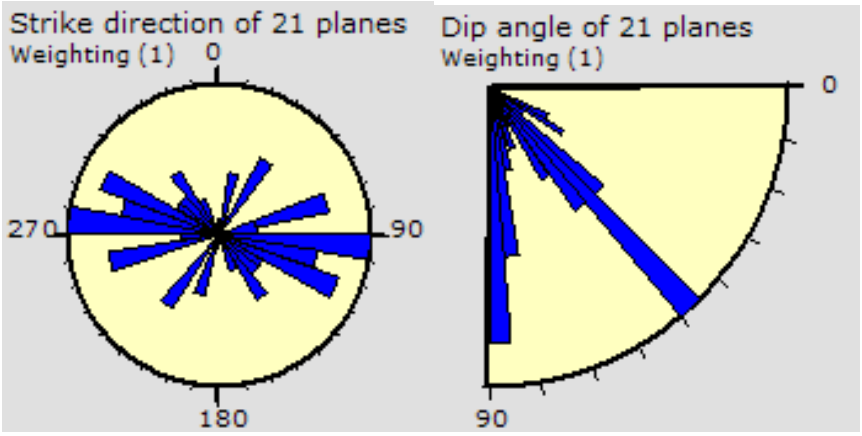

Figure 80: Rose diagram of strike plane (a) and dip plane (b) obtained from the mineralised joints observed in the Tshifufia open pit and related to the fourth stress tensor.

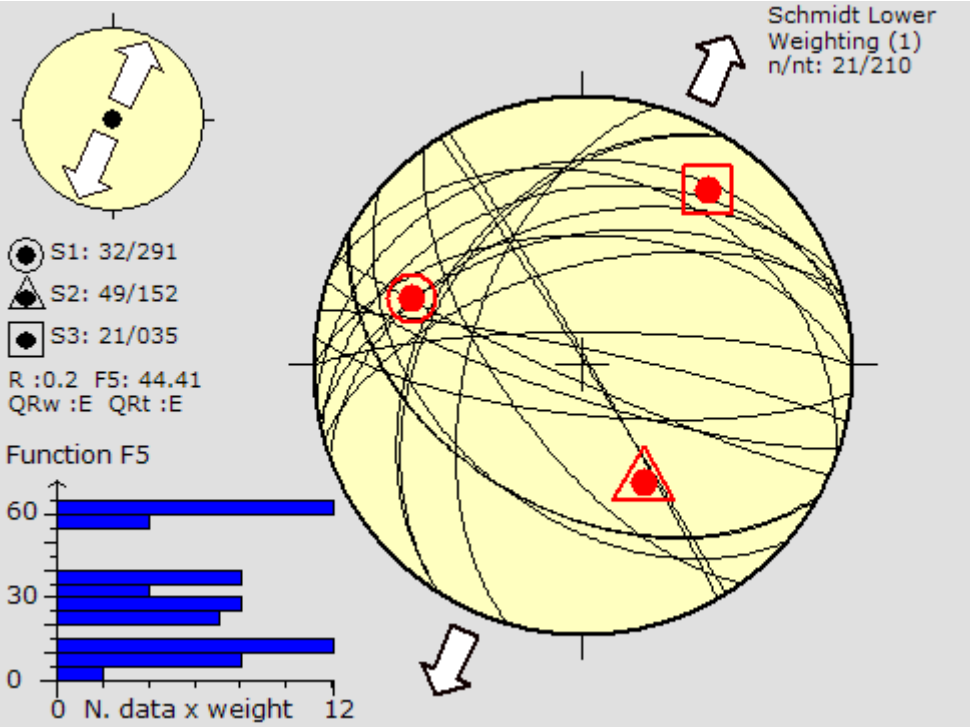

Figure 81: Stereonet showing the principal stress axis obtained with the improved dihedral method combined with the rotational optimisation procedure of the mineralised joints related to the fourth stress tensor at Tshifufia open pit.

The following Table 11 summarises all the principal stress axes (σ_1, σ_2 and σ_3) and stress ratio (R) of the tensor obtained from the mineralised joints observed in the Tshifufia pit.

n	Nt	Principal stress axis			R	SHmax	Shmin	R'	Stress Regime
		σ_1	σ_2	Σ_3					
39	210	05/172	47/042	42/266	0.35	173	83	1.65	Oblique COMPRESSIVE
57	210	27/220	62/043	01/311	0.35	41	131	1.65	Pure STRIKE-SLIP
53	210	03/123	62/025	26/214	0.95	125	35	1.05	Extensional STRIKE-SLIP
21	210	32/291	49/152	21/035	0.2	114	24	1.8	Oblique EXTENSIVE

Table 11: Summary of the principal stress axis (σ_1, σ_2 and σ_3), and stress ratio (R) of the palaeostress tensor of the mineralised joints in the Tshifufia fragment.

3.3.2.1.2 Unmineralised Joints (UMJ)

Fifty-three measurements of dip direction and dip angle of the unmineralised joints were collected on the outcrop of the Tshifufia open pit (Table A.7). Two stress tensors were obtained from the whole population of fractures.

The rose diagram of the strike plane (Fig. 82a) and the dip angle obtained from the first stress tensor reveals two groups of unmineralised joints based on the orientation of the strike of planes. The first group is characterised by planes showing a SSE-NNW strike, with dip angles varying between 35° and 45° (Fig. 82 (b)). The second group is characterised by planes with an E-W strike, with dip angles varying between 25° and 45°. There is a third group showing SSW-NNE striking planes with dip angle varying between 10° and 15°.

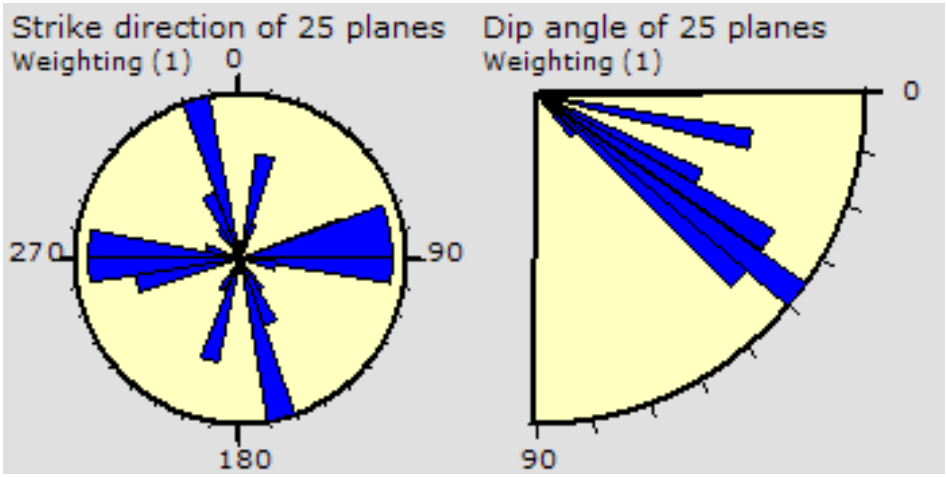

Figure 82: Rose diagram of strike of planes (a) and dip planes (b) obtained from the unmineralised joints observed in the Tshifufia open pit.

This stress tensor gives the maximum principal stress axis (σ_1): 23/010, the intermediate principal stress axis (σ_2): 03/101 and the minimum principal stress axis (σ_3): 66/199, with the stress ratio (R) equalling 0.5. This tensor belongs to pure compression and it indicates SSW-NNE compression (Fig. 83).

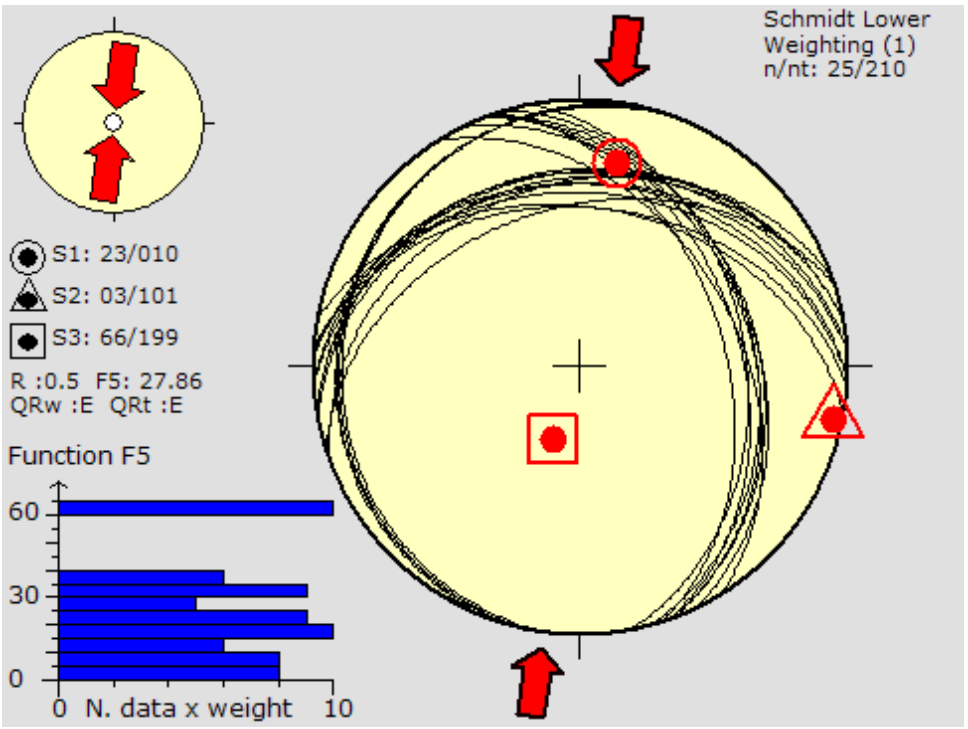

Figure 83: Stereonet showing the principal stress axis obtained with the improved right dihedral method combined with the rotational optimisation of the unmineralised tension joint related to the second stress tensor encountered in the Central open pit.

The second stress tensor is characterised by two groups of fracture planes based on the orientation of the strike planes. The first group is characterised by a general strike oriented SW-NE with dip angles varying between 70° and 75°. This group comprises two subgroups with the strike plane forming an angle of 30° between them. Although the second group present a

general trending of strike plane oriented ESE-WNW, with dip angles varying between 35° and 40°(Fig. 84).

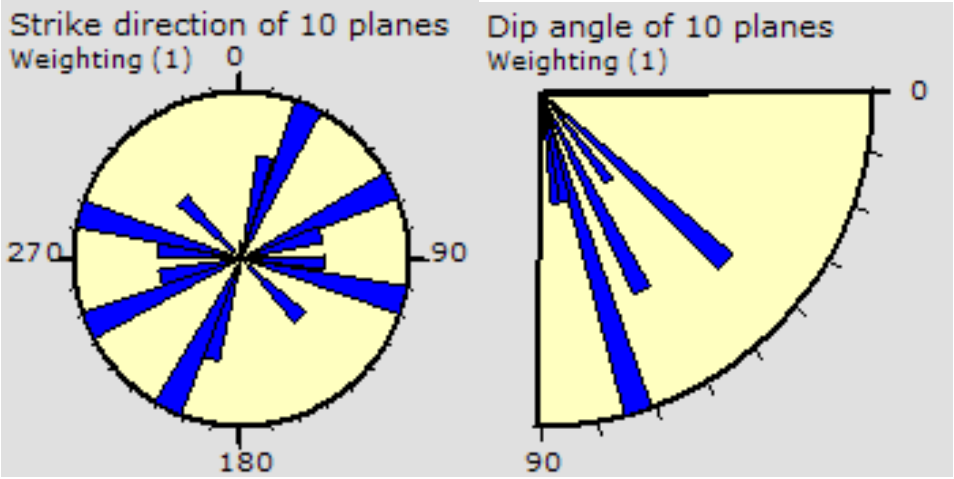

Figure 84: Rose diagram of strike plane (a) and dip plane (b) obtained from the unmineralised tension joint of the second stress tensor observed at the Tshifufia open pit.

This stress tensor gives the maximal principal stress axis (σ_1): 51/128, the intermediate principal stress axis (σ_2): 24/252 and the minimum principal stress axis (σ_3): 27/356, with the stress ratio (R) equalling 0.68. This stress tensor belongs to the pure extension stress regime and it indicates S-N extension (Fig. 85).

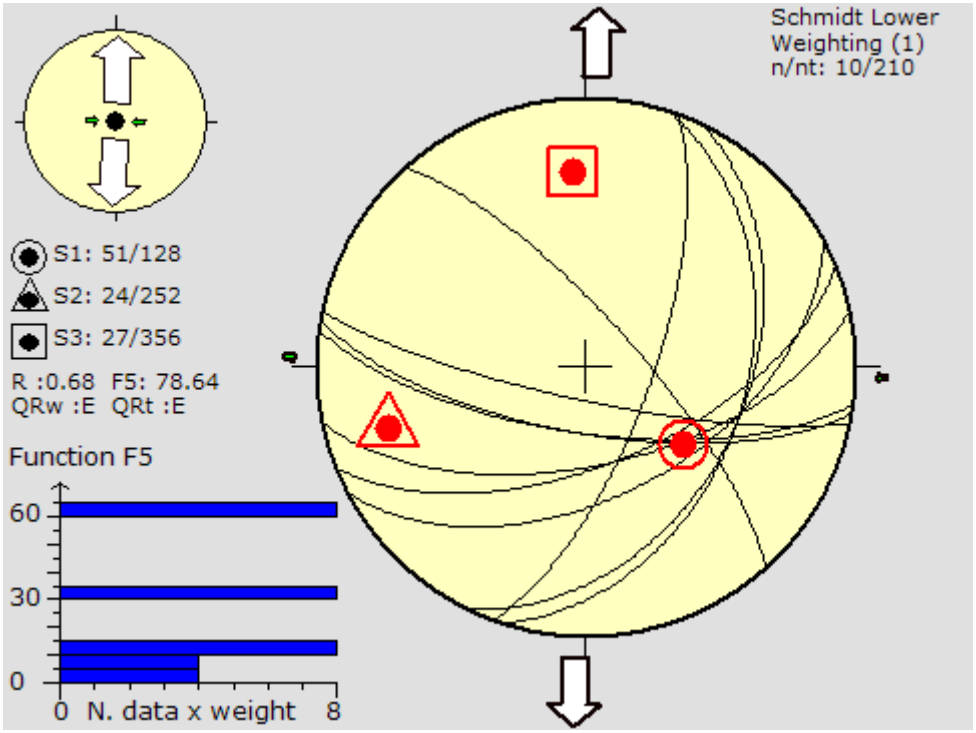

Figure 85: Stereonet showing the principal stress axis obtained with the improved right dihedral method combined with the rotational optimisation of the unmineralised tension joint related to the second stress tensor encountered in the Central open pit.

The following Table 12 summarises all the principal stress axes (σ_1, σ_2 and σ_3) and stress ratio (R) of the tensor obtained from the unmineralised tension joints observed in the Tshifufia Pit.

n	nt	Principal stress axis			R	SHmax	Shmin	R'	Stress Regime
		σ_1	σ_2	σ_3					
25	210	23/010	03/101	66/199	0.5	8	98	2.5	Pure COMPRESSIONAL
10	210	51/128	24/252	27/356	0.68	92	2	0.7	Pure Extensional

Table 12: Summary of the principal stress axes (σ_1, σ_2 and σ_3), and stress ratio (R) of the palaeostress tensor of the unmineralised tension joints in the Tshifufia fragment.

3.3.2.2 Faults

Several fault planes were observed in the Central open pit including slickensided faults (Fig. 86a and b) and shear fractures. The fault slip data were treated according to the type of faults. One hundred and fifteen items of data were collected from the fault planes observed at the Tshifufia open pit.

3.3.2.2.1 Slickensided faults

Approximately sixty measurements (Table A.8) of fault slips were collected at the Tshifufia open pit. Three stress tensors were obtained from these measurements.

The first stress tensor presents a group of slickensided fault planes striking in the WSW-ENE direction and dip 40° to 65° to both SE and NW. A secondary group of slickensided fault planes that strike in the SW-NE direction and dip 65° to 70° to both ESE and WNW was observed. The fault-slips acting on these fault planes trend to the WSW (Fig. 87).

Figure 86: Fault plane containing strike-slip slicken lines well marked by clayey mineral (a) and calcite (b); (a) looking South-East and (b) looking South.

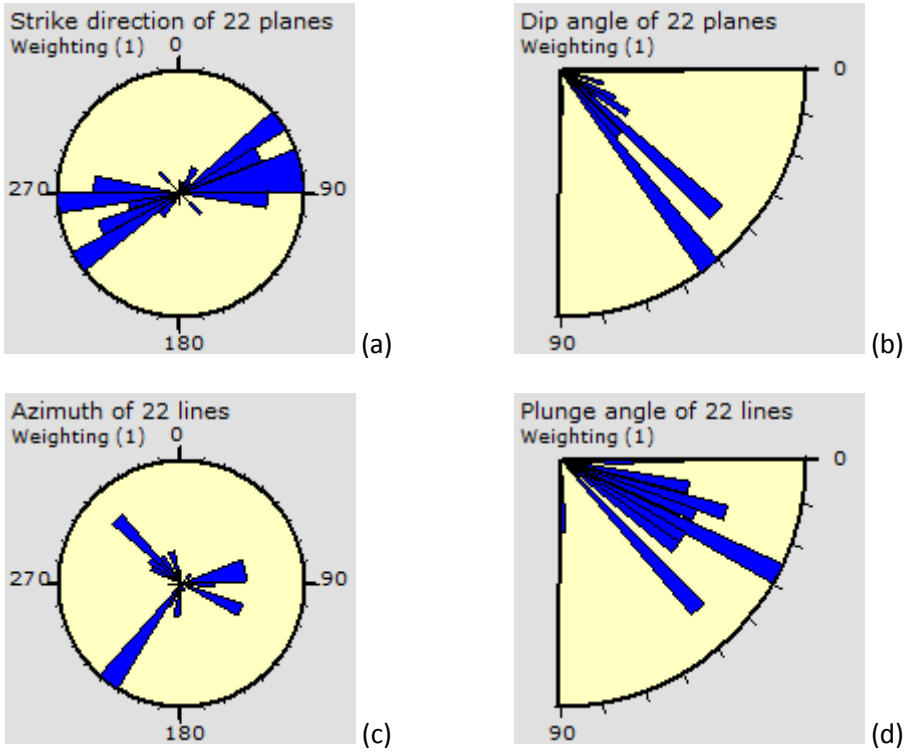

Figure 87: Rose diagrams of the strike plane (a) and dip plane (b), azimuth of fault slip (c) and plunge angle (d) of the first stress tensor deduced from the observed slickensided faults at Tshifufia.

This stress tensor is characterised by the maximum principal stress axis (σ_1): 13/333, the intermediate principal stress axis (σ_2): 48/078 and the minimum principal stress axis (σ_3): 38/232, with the stress ratio (R) and friction angle (ø) equal to 0.29 and 36.65 respectively. This stress tensor belongs to the oblique compressional stress regime and it indicates SE-NW compression (Fig. 88).

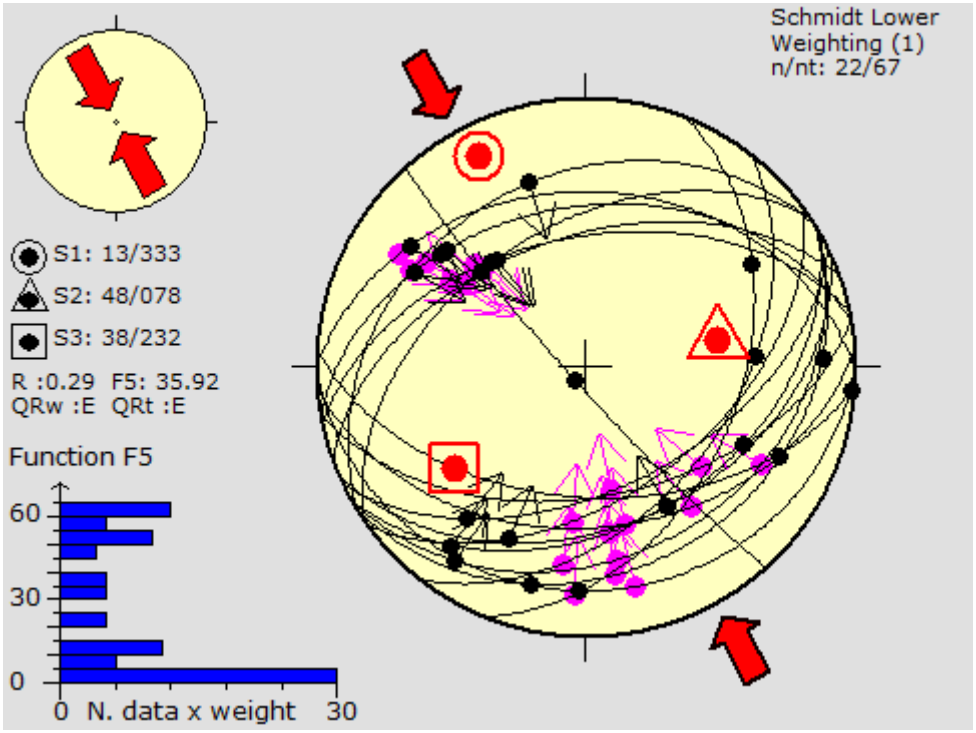

Figure 88: Stereonet showing the principal stress axis obtained with the improved right dihedral method combined with the rotational optimisation of the slickensided faults related to the first stress tensor encountered at the Tshifufia open pit.

Presenting the results shown in the stereonet above, using tangent-lineation data from these fault-slips, in a similar treatment of data as for the Tshifufiamashi fragment, two groups of fault-slips acting on these fault planes may be noted. The first group comprises all fault-slips, indicating a movement towards the SE. The second group comprises all striations revealing a movement towards the NW. These two groups of striations are acting on the fault planes that indicate conjugate reverse faults (Fig. 89).

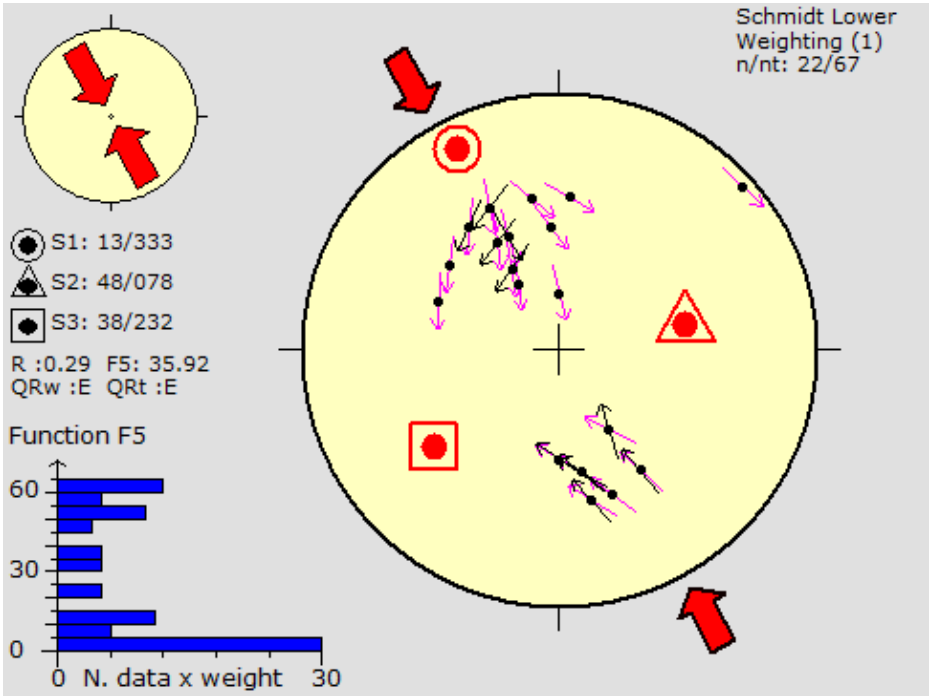

Figure 89: Stereonet showing tangent-lineation data obtained from fault-slip acting on the fault planes of the first stress tensor deduced from the fault-slip observed at the Tshifufia fragment

The second stress tensor is characterised by slickensided fault planes striking in the WSW-ENE direction dip to angle varying between 80° and 85°. This group carries dip-slip striations plunging to the SE. The second group is characterised by the slickensided fault planes striking in the WSW-ENE direction and dipping to the SSE. These slickensided faults carry both strike-slip and dip slip striations plunging to the SE and NE respectively (Fig. 90 (a), (b), (c) and (d)).

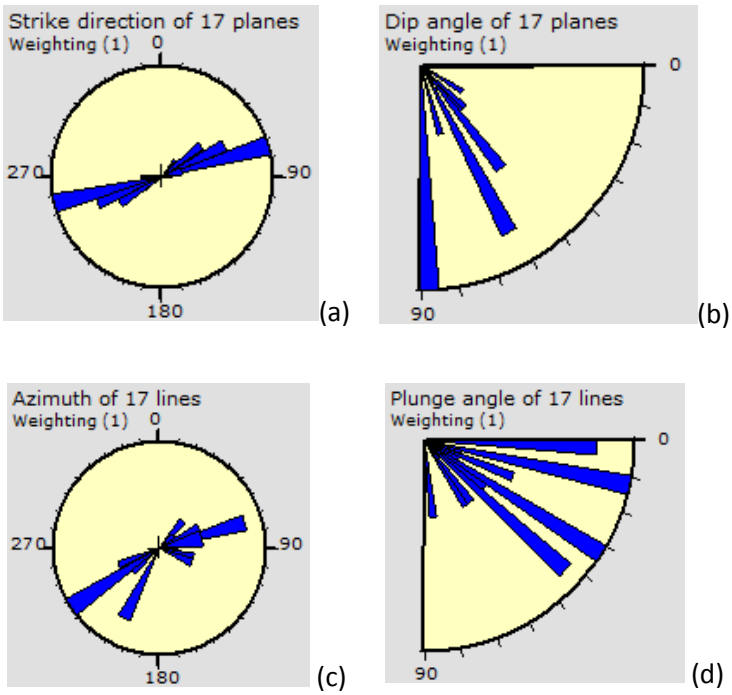

Figure 90: Rose diagrams of the strike plane (a) and dip plane (b), azimuth of fault slip (c) and plunge angle (d) of slickensided faults observed in Tshifufia induced during the second phase.

The stress tensor deduced from these measurements gives the maximum principal stress axis (σ_1): 21/033, the intermediate principal stress axis (σ_2): 52/154 and the minimum principal stress axis (σ_3): 28/290, with the stress ratio (R) and the friction angle (ø) at 0.23 and 36.57 respectively. This stress tensor belongs to the compressional strike-slip regime and it indicates SW-NE compression and SE-NW extension (Fig. 91).

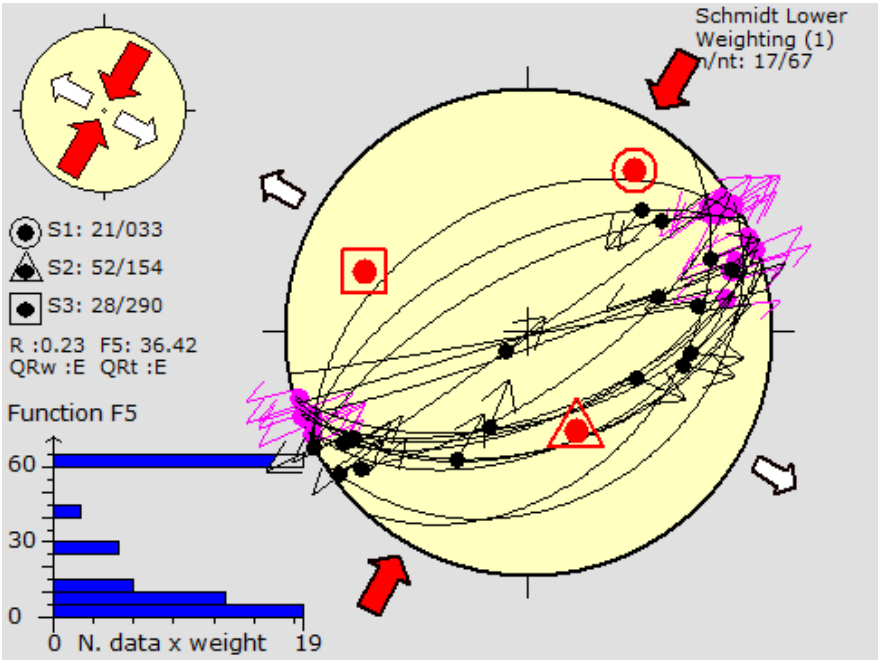

Figure 91: Stereonet showing the principal stress axis obtained with the Improved right dihedral method combined with the rotational optimisation of the slickensided faults related to the second stress tensor obtained at the Tshifufia open pit.

The results shown in the stereonet above, using tangent-lineation data from these fault-slips, reveal one group of fault-slips acting on these fault planes. This group comprises fault-slip indicating a sinistral strike-slip movement in the SW-NE direction (Fig. 92).

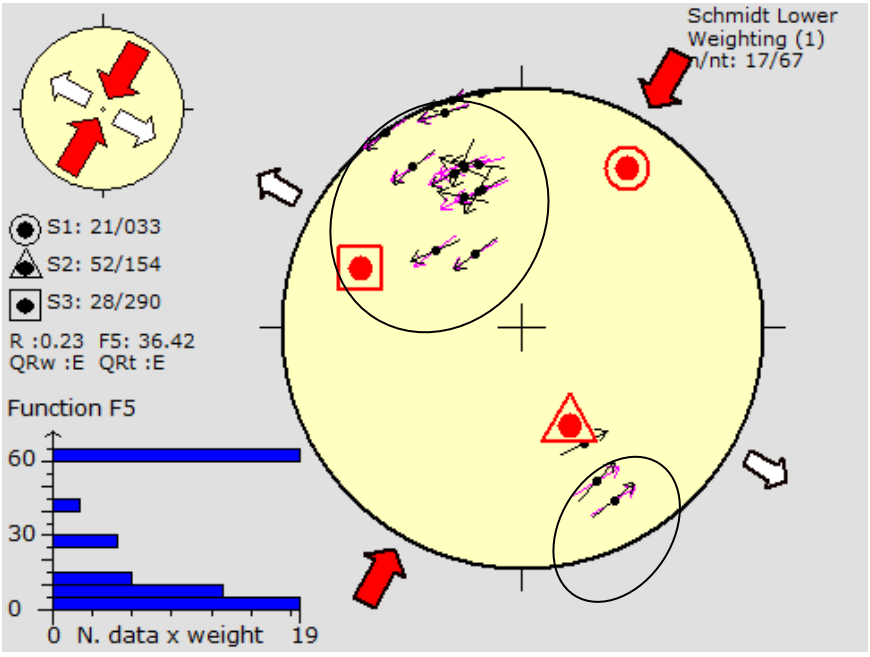

Figure 92: Stereonet showing tangent-lineation data obtained from fault-slip acting on the fault planes of the second stress tensor deduced from the fault-slip observed at the Tshifufia.

The third stress tensor obtained from the orientation of the slickensided fault planes observed at the Tshifufia presents one group of fault planes. These fault planes are oriented in the WSW-ENE direction and are dipping to both the SE and the NW, and rarely are they sub-vertical. Two groups of fault-slips acting on these fault planes can be highlighted. The first group comprises

the dip-slip striations trending to the NNW. The second group is characterised by the strike-slip striations trending to the ESE (Fig. 93).

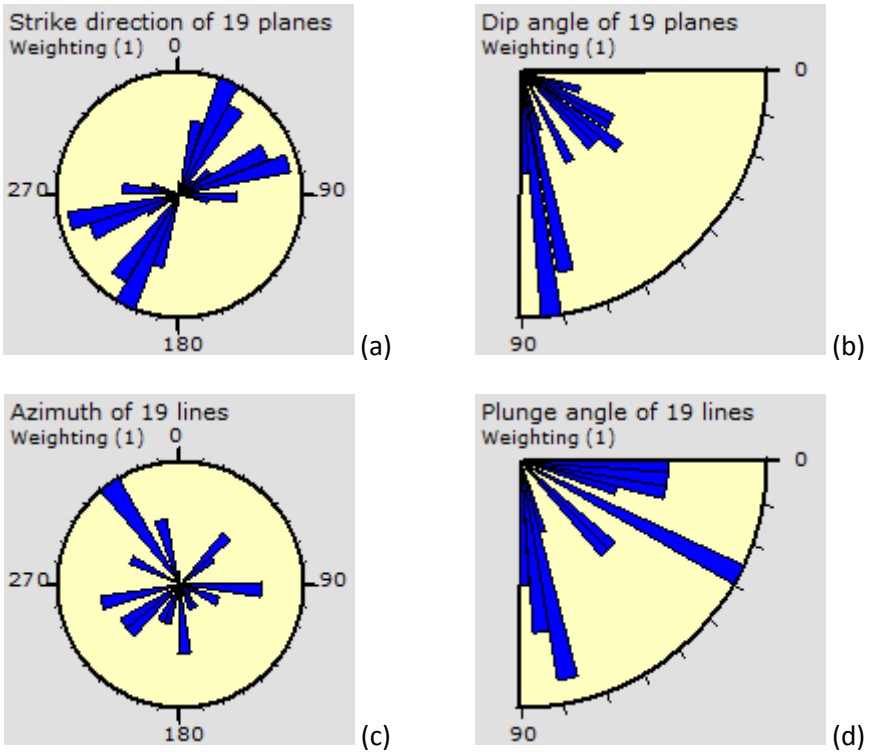

Figure 93: Rose diagrams of the strike plane (a) and dip plane (b), azimuth of fault-slip (c) and plunge angle (d) of slickenside observed in Tshifufia belonging to the third stress tensor.

The stress tensor obtained from these measurements shows the maximum principal stress axis (σ_1): 65/319, the intermediate principal stress axis (σ_2): 02/055 and the minimum principal stress axis (σ_3): 24/146, with the stress ratio (R) and the friction angle (ø) at 0.49 and 44.11 respectively. This stress tensor belongs to the pure extensional stress regime and it indicates SE-NW extension (Fig. 94).

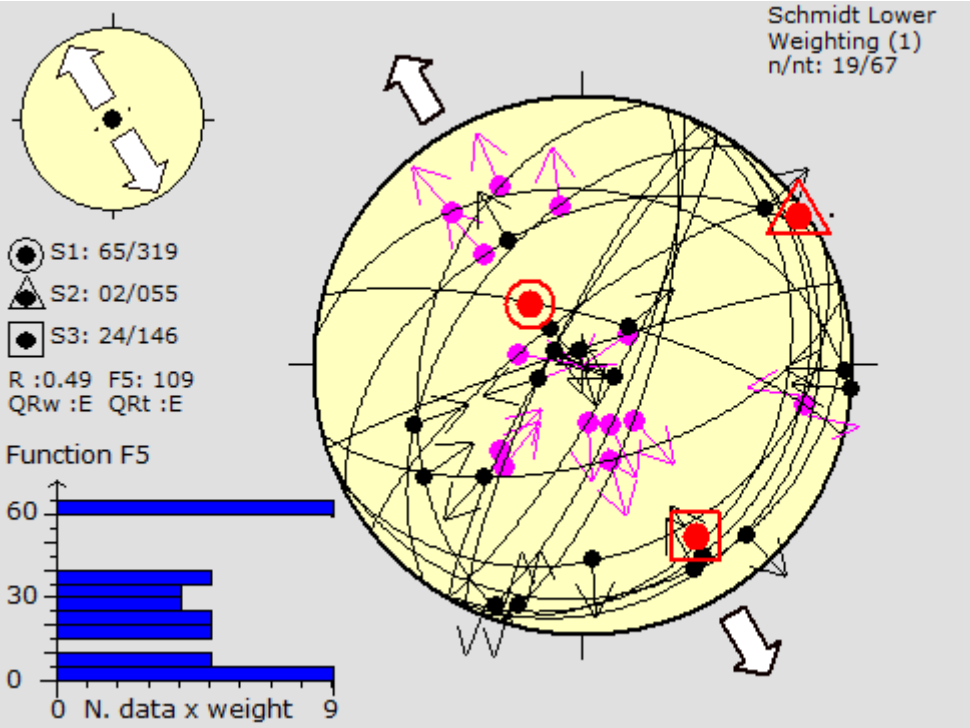

Figure 94: Stereonet showing the principal stress axis obtained with the improved right dihedral method combined with the rotational optimisation of the slickensided faults related to the third stress tensor obtained at the Tshifufia open pit.

Presenting the results shown in the stereonet above, using the tangent-lineation data from these fault-slips, two groups of striations acting on the fault planes of the third stress tensor are noted. The first group indicates a movement toward the NW and the second group presents a movement toward the SE. A third group shows striations indicating movement towards the SW (Fig. 95).

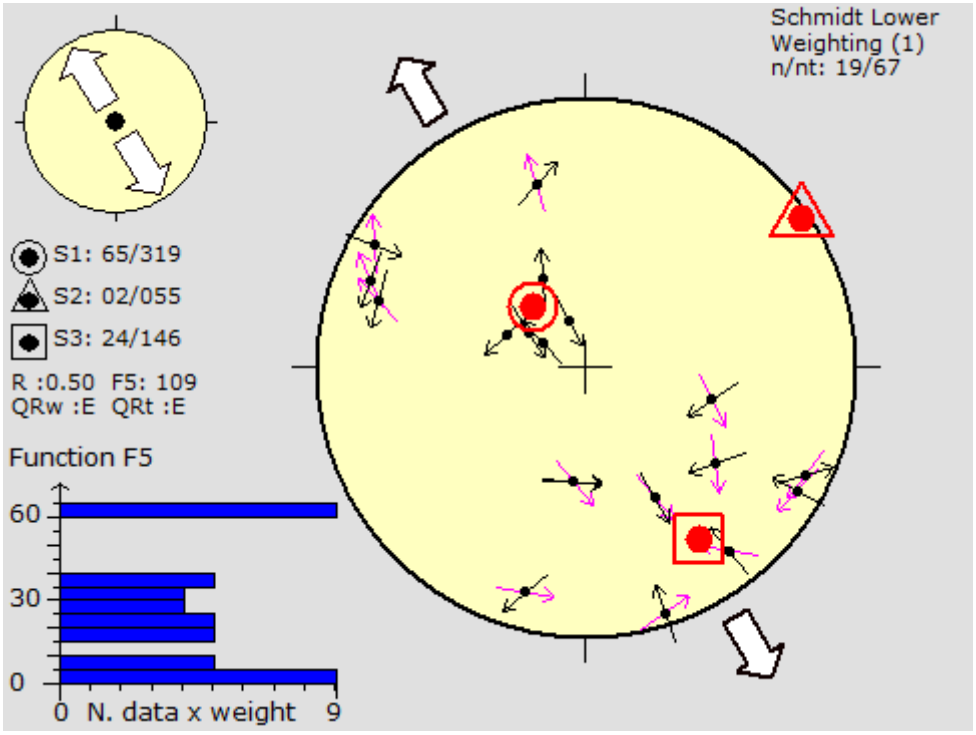

Figure 95: Stereonet showing tangent-lineation data obtained from fault-slip acting on the fault planes of the third stress tensor deduced from the fault-slip observed at the Tshifufia.

The following Table13 summarises all the principal stress axes (σ_1, σ_2 and σ_3) and stress ratio (R) of the tensor obtained from the slickensided faults observed in the Tshifufia pit.

n	Nt	Principal stress axis			R	SHmax	Shmin	R'	phi	Stress Regime
		σ_1	σ_2	σ_3						
30	67	13/333	48/078	38/232	0.29	151	61	2.59	36.65	Oblique COMPRESSIONAL
14	67	21/033	52/154	28/290	0.23	30	120	1.49	36.57	COMPRESSIONAL strike-slip
15	67	65/319	02/055	24/146	0.54	149	59	0.63	44.11	Pure EXTENSIONAL

Table 13: Summary of the principal stress axes (σ_1, σ_2 and σ_3) and stress ratio (R) of the palaeostress tensor of the slickensided faults encountered at the Tshifufia fragment.

3.3.2.2.2 Shear fractures

Sixty measurements of shear fractures were collected at the Tshifufia open pit (Table A.9). The results obtained from these measurements reveal two stress tensors.

The first stress tensor is characterised mainly by a group of planes striking N-S with dip angles varying between 40° and 45° (Fig. 96 (a) and (b)). However, there is a second group of planes striking E-W with dip angles varying between 20° and 30°, 55° and 70°.

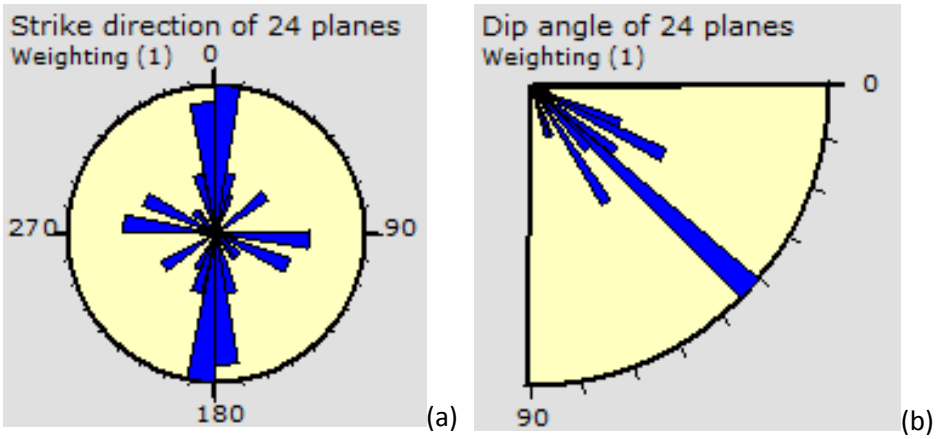

(a) (b)

Figure 96: Rose diagram of strike plane (a) and dip plane (b) obtained from the fault plane of faults observed in the Tshifufia open pit.

The stress tensor obtained from these measurements gives the maximum principal stress axis (σ_1): 06/239, the intermediate principal stress axis (σ_2): 00/329 and the minimum principal stress axis (σ_3): 82/069, with the stress ratio (R) and the friction angle at 0.5 and 48.87 respectively. This stress tensor belongs to the pure compression stress regime and it indicates a SW-NE compression (Fig. 97).

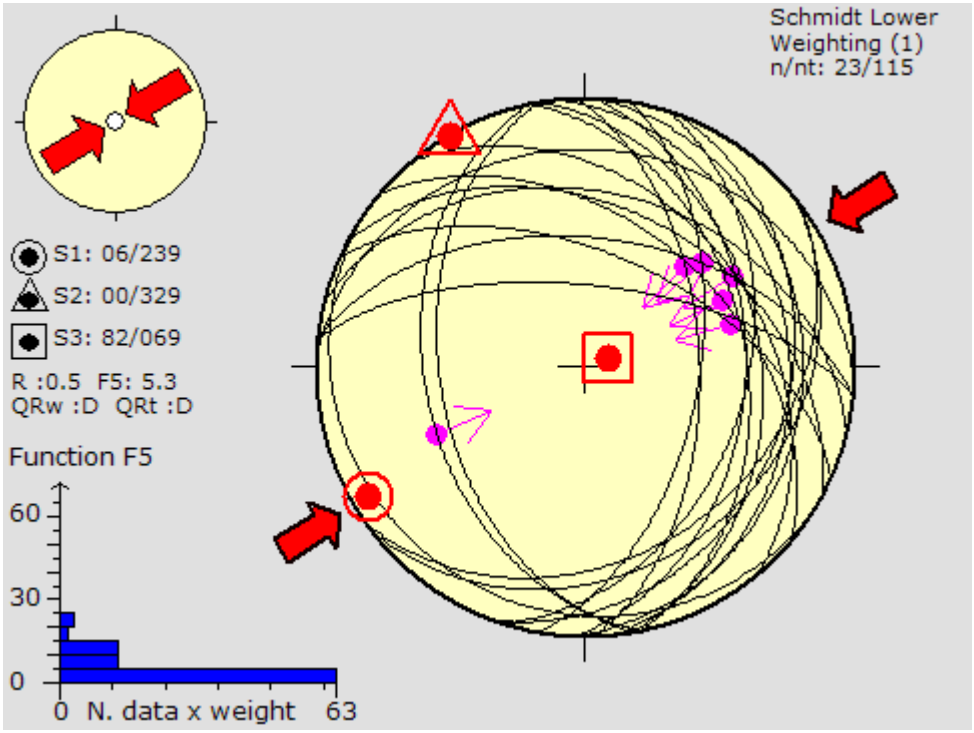

Figure 97: Stereonet showing the principal stress axis obtained with the improved right dihedral method combined with the rotational optimisation of the shear fracture related to the first stress tensor obtained at the Tshifufia open pit.

The second stress tensor obtained from the fault plane of the shear fractures encountered at the Tshifufia open pit presents two groups of strike or fault planes. The first group comprises all fault planes showing strike planes oriented SSW-NNE and SSE-NNW respectively, with sub-vertical dip angles. These fault planes form an approximate angle of 30° (Fig. 98 (a)). The second group is characterised by planes striking E-W with dip angles varying between 35° and 45°, 75° and 80° (Fig. 98 (a) and (b)).

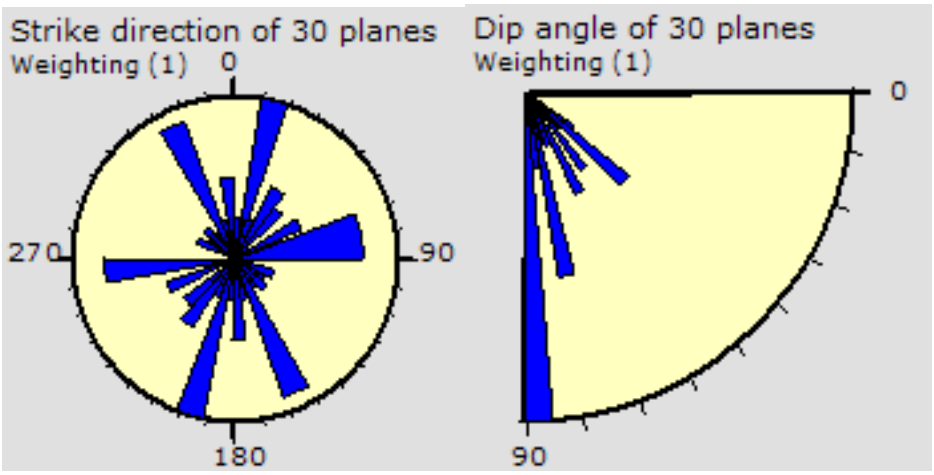

Figure 98: Rose diagram of strike plane (a) and dip plane (b) obtained from the shear fractures observed in the Tshifufia open pit.

The stress tensor obtained from these measurements shows the maximal principal stress axis (σ_1): 58/237, the intermediate principal stress axis (σ_2): 27/025 and the minimum principal stress

axis (σ_3): 14/123, with the stress ratio (R) and the friction angle (ø) at 0.56 and 38.92 respectively. This stress belongs to the pure extensive stress regime and it indicates SE-NW extension (Fig. 99)

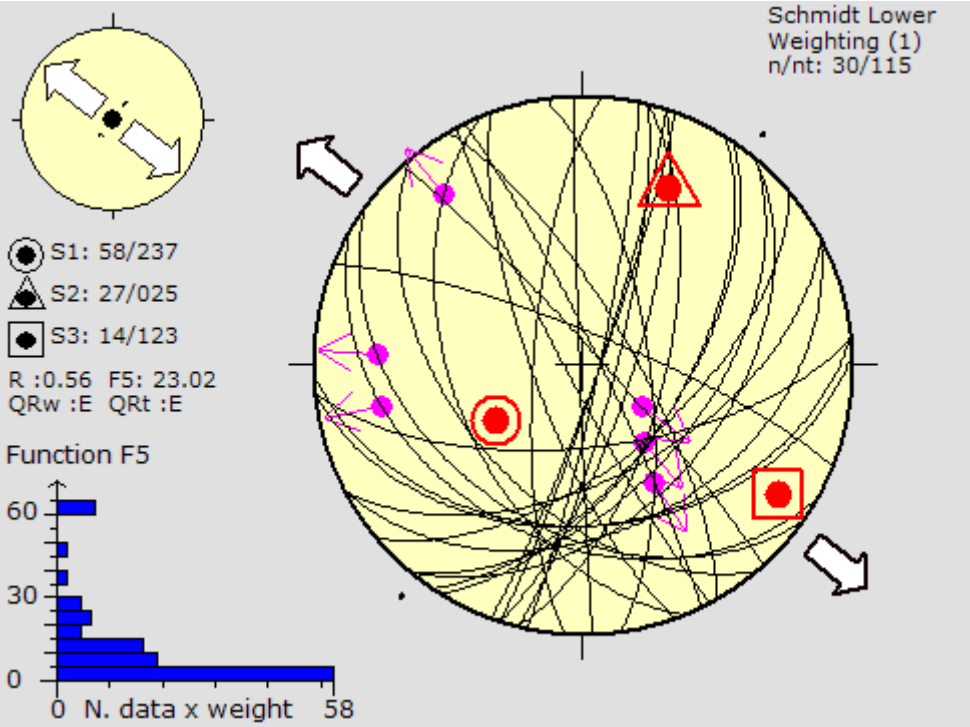

Figure 99: Stereonet showing the principal stress axis obtained with the improved right dihedral method combined with the rotational optimisation of the shear fracture related to the second stress tensor obtained at the Tshifufia open pit.

Table 14 below summarises the principal stress axis (σ_1, σ_2 and σ_3), the stress ratio and the friction angle Ø obtained from the shear fractures data collected at the Tshifufia pit.

n	Nt	Principal stress axis			R	SHmax	Shmin	R'	phi	Stress Regime
		σ_1	σ_2	σ_3						
24	115	06/239	00/329	82/069	0.5	59	149	2.5	48.87	Pure COMPRESSIONAL
30	115	58/237	27/025	14/123	0.56	38	128	0.56	38.92	Pure EXTENSIONAL

Table 14: Summary of the principal stress axis (σ_1, σ_2 and σ_3), stress ratio (R) and the friction angle obtained from the shear fractures data collected at the Tshifufia pit.

3.3.2.3 Folding

As was the case at the Tshifufiamashi fragment, folds were observed in the western limb of the Central pit and the CMN strata are strongly affected by small-scale folds. These micro-folds are often fractured (Fig. 31 (a) and (b)).

Orientations of the bedding planes of both the Tshifufia fragment (Table A.10) and the small-scale folds observed in the CMN strata were collected separately. In addition to bedding

orientations, the orientation of the hinge lines (HL) and fold axial planes (FAP) of these small-scale folds observed in the CMN open pits outcrops were measured (Table A.10).

The π diagram of poles to bedding of the Tshifufia fragment (Fig. 100) reveals that bedding generally dips steeply eastwards, showing an overturned succession with the youngest strata (CMN) in the West of the pit overlain by the oldest strata (RAT) in the East. The π diagram plotting from the bedding planes observed at Tshifufia shows a fold axis trending 218° (SW) and plunging 19°.

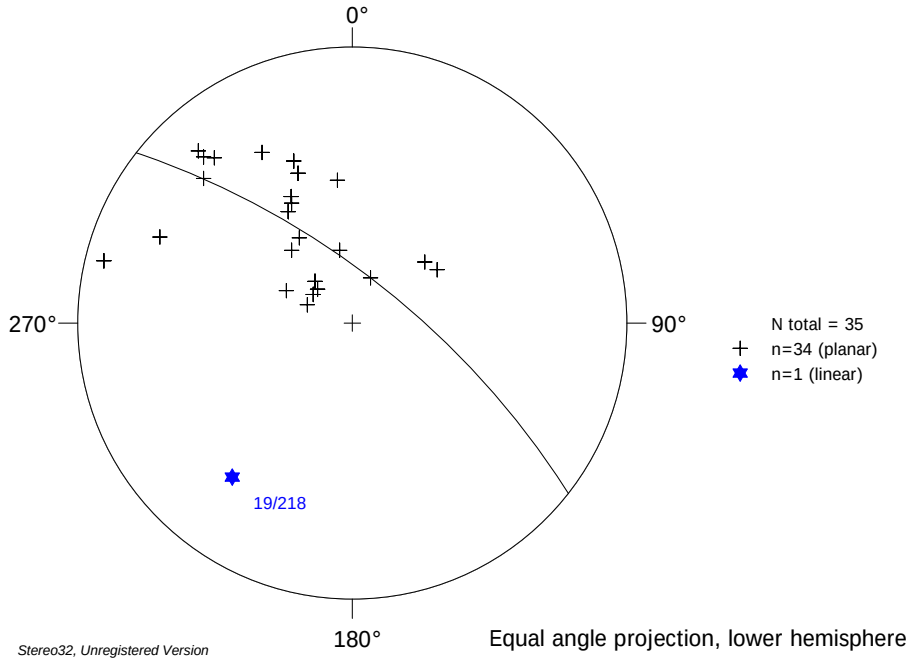

Figure 100: π diagram of poles to bedding indicating the fold axis obtained from bedding observed at Tshifufia.

The bedding plane measurements collected from the well-folded CMN strata observed in the western part of the Central pit are shown as the π diagram in Figure 101, indicating that a fold axis trends 227° (SW) and plunges south-westwards at an angle of 05° (Fig. 101).

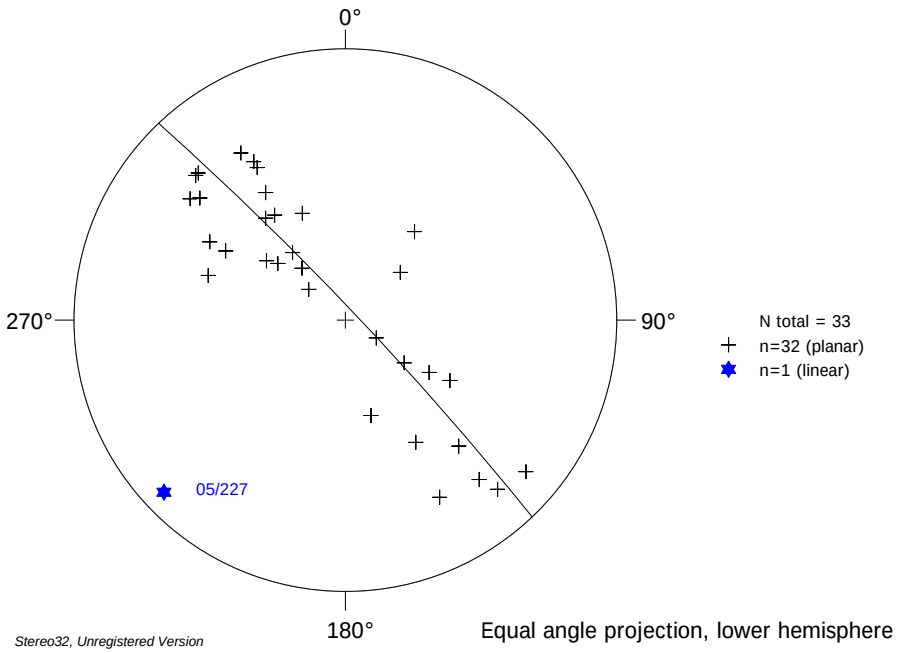

Figure 101: πi diagram plotting pole to bedding planes and indicating the fold axis obtained from the bedding planes of the tight micro-folds observed in the CMN strata at Tshifufia.

Figure 102 is a stereographic projection of fold axial planes collected from the isoclinal micro-folds observed in the West limb of the Central pit; it indicates a NW (317°) dip direction with a dip angle of 33° (Fig. 102), and the axial plane indicates a south-easterly vergence of folding.

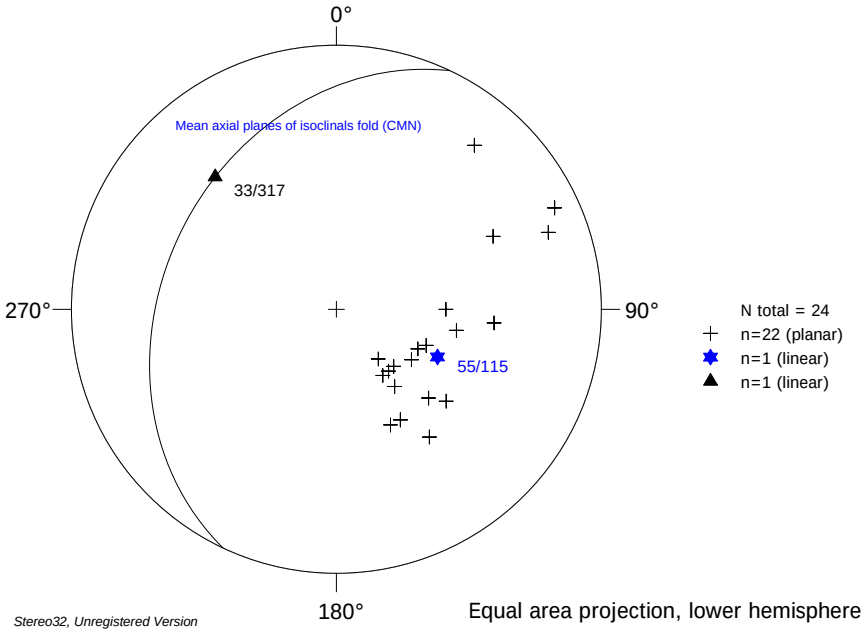

Figure 102: Stereographic projection showing fold axial planes of the tight micro-folds observed in the CMN strata of the Tshifufia fragment where the black crosses represent the poles and the blue star represents the great circle.

The hinge lines caused by the folding event evident in the Tshifufia fragment indicate a general SW orientation (azimuth 231°), plunging gently to the SW (18°) (Fig. 103).

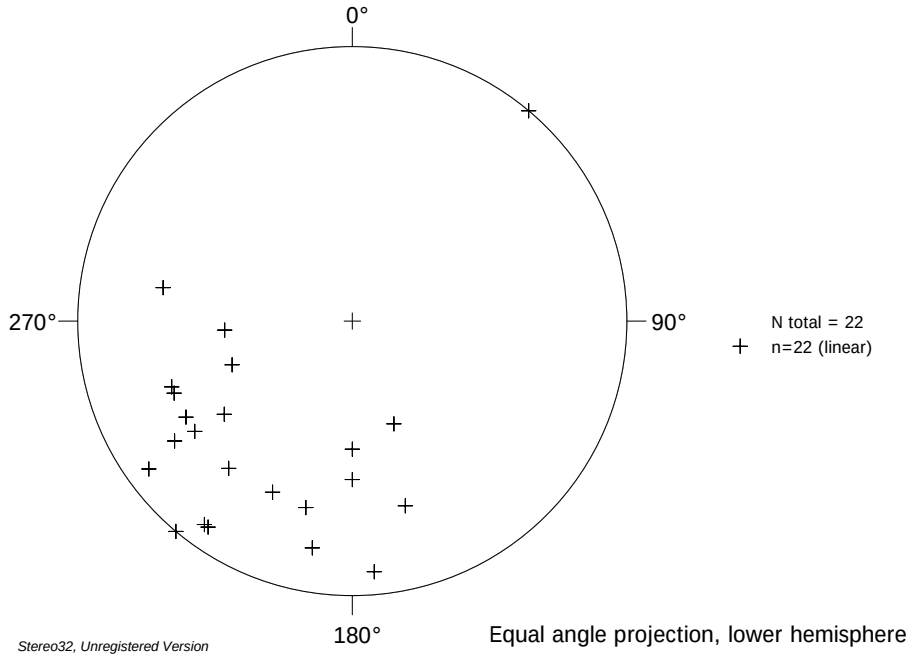

Figure 103 (a): Stereographic projection of raw data collected from the hinge line observed in the Tshifufia fragment.

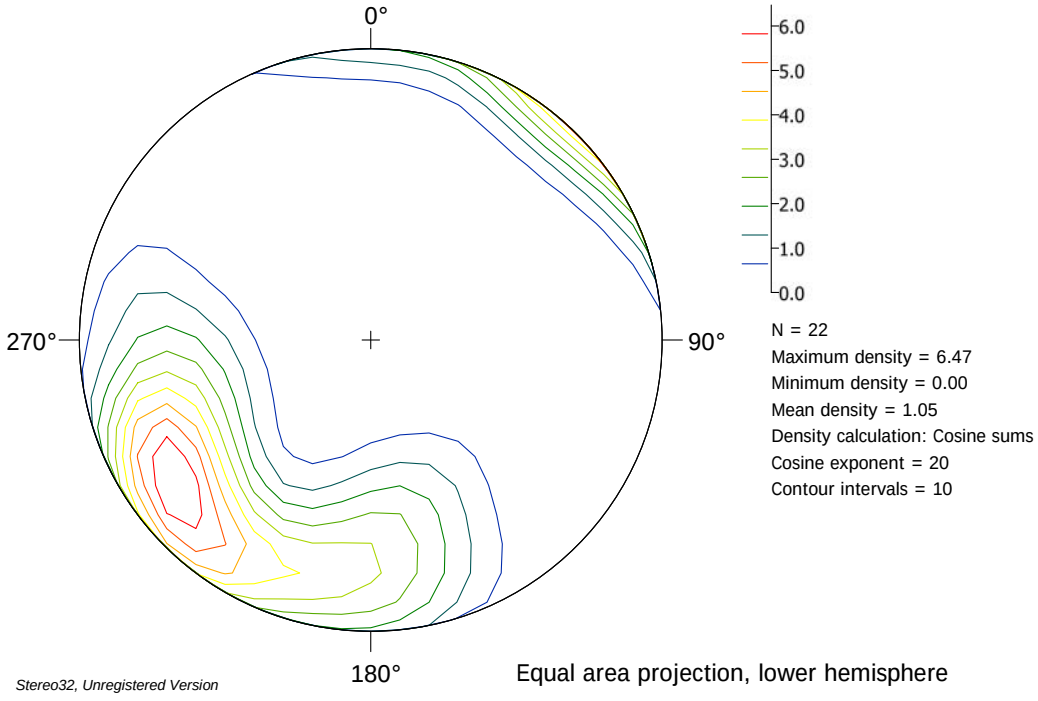

Figure 103 (b): Stereographic projection showing contour of the hinge lines data collected from the Tshifufia fragment.

Table 15 below summarises the plunge angle/azimuth of the fold axes and hinge lines and the dip and dip direction of the axial planes obtained from the field data collected from the Tshifufia open pit.

Tshifufia fragment	Dip / plunging angle	Dip direction/Azimuth orientation
Fold axis of the fragment	19	218
Fold axis-isoclinals (CMN)	05	227
Hinge line-iscoclinals (CMN)	18	231
Fold axial plane (CMN)	33	317
Vergence of the fold	SE	

Table 15: Showing the dip/plunging angle, dip-dip direction/azimuth orientation and vergence of the folding event obtained in Tshifufia open pit.

3.3.2.4 Thrust faulting

Several fault planes indicating distinctive movement caused by thrusting were observed in the Tshifufia Central open pit. These features indicating the possible thrust fault system can be subdivided into two types: the first subgroup comprises contraction thrust faults that are characterised by fault planes parallel to bedding planes and the second subgroup comprises fault planes cutting across the bedding plane.

In the North side of the Tshifufia open pit, a kink band folding was observed in the SD strata (Fig. 104). It is characterised by a slightly undulating fault plane striking N-S, on which a northward movement is indicated. The hanging wall and the footwall lithologies are the same, but show micro-folds characterised by parallel fold axial planes striking N-S (178°) and dipping 45° to the West. These parallel fold axial planes form an angle of dip of 45° with the thrust fault plane, while the hinge lines have a trend of 175°, plunging 15° to the South.

These kink band folds were also observed in the CMN strata, where they are oriented 56/278 or striking SSW-NNE and dip to WNW (Fig. 104).

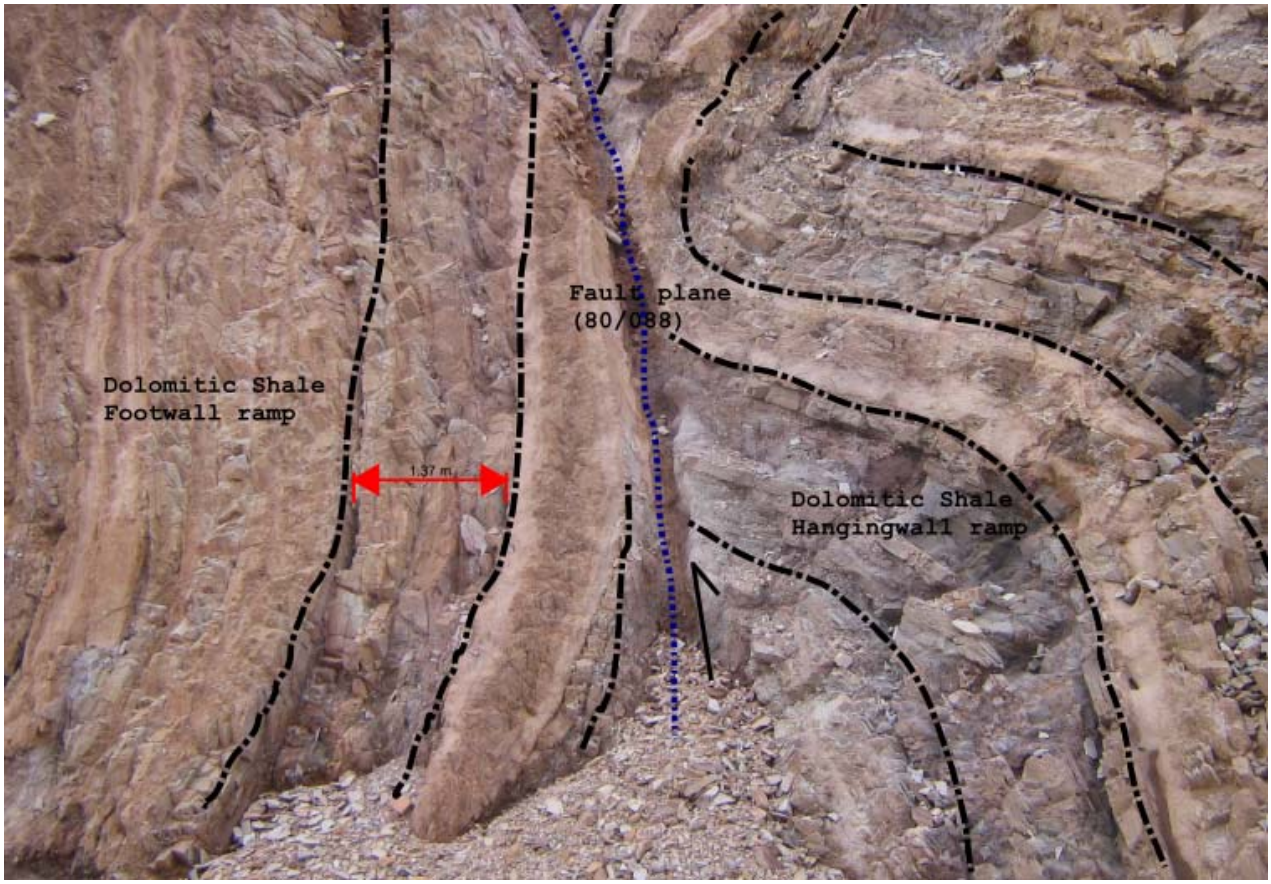

Figure 104: Kink band fold affecting the SD strata and indicating a thrust movement towards the North-Tshifufia Central open pit Kinsevere Copper Deposit. Looking North.

The second group of thrust faults cross-cuts bedding of the R2 Mines Subgroup strata. This type of thrust faulting was observed in the South of the Tshifufia open pit (Fig. 105). The thrust faulting is accommodated by a 0.2-2m wide fault zone, dipping to the SE (30/115) and indicating a sinistral movement to the SE (Fig. 112). This fault zone contains a heterogeneous breccia comprised mainly of RAT strata rounded clasts set in an argillaceous, slightly dolomitic matrix.

Figure 105: E-W section along the Central open pit showing an overturned limb of R2 Mines Subgroup strata and two types of thrust faults. The first type (in red) affects the CMN strata along a thrust oriented SSW-NNE (56/278) and the second type of fault (in blue) shows a fault plane oriented SW-NE (30/115) with heterogeneous breccias between these R2 Mines Subgroups strata. Looking South.

3.3.3 Kinsevere Hill fragment

Kinsevere Hill is an unexploited fragment located to the South-East in the Kinsevere concession (Fig. 106). The Kinsevere Hill fragment consists of the upright limb of a regional-scale fold in which the younger CMN strata outcrop to the West of the hill and overlie the oldest strata (RAT) which crop out to the East of the Kinsevere Hill (Fig. 9). All data presented in this study were collected from the surface rocks outcropping on the top of the hill and from the artisanal shafts present in the area.

The Kinsevere Hill fragment is separated from the other fragments (Tshifufiamashi and Tshifufia) by an inferred strike-slip fault with sinistral displacement (Fig. 9). Similar to the other fragments, the Kinsevere Hill fragment is affected by brittle structures such as fractures (mineralised and unmineralised joints) and fault planes with striations. The CMN strata show several micro-folds, which are well exposed in the Tshifufiamashi and Tshifufia open pits situated to the NW of Kinsevere Hill.

3.3.3.1 Fractures

The R2 Mines Subgroup strata of the Kinsevere Hill fragment are affected by brittle fractures among which two groups may be distinguished; the first group comprises all fractures (joints) filled by copper-cobalt oxides (malachite and heterogenite) and sulphides; and the second group comprises unmineralised fractures (joints). Over sixty measurements were taken over the Kinsevere region of the mineralised and the unmineralised fractures (Table A.11). The results will be presented in accordance with the following groups.

3.3.3.1.1 Mineralised Joints (MJ)

Two stress tensors are obtained from the measurement of dips and dip directions collected from the mineralised joints observed in the Kinsevere Hill region.

The rose diagram (Fig. 107 (a) and (b)) of the first stress tensor obtained from the dip direction and dip angle of the mineralised joints are generally oriented SW-NE with dip angles varying between 30° and 50°, then 60° and 70°.

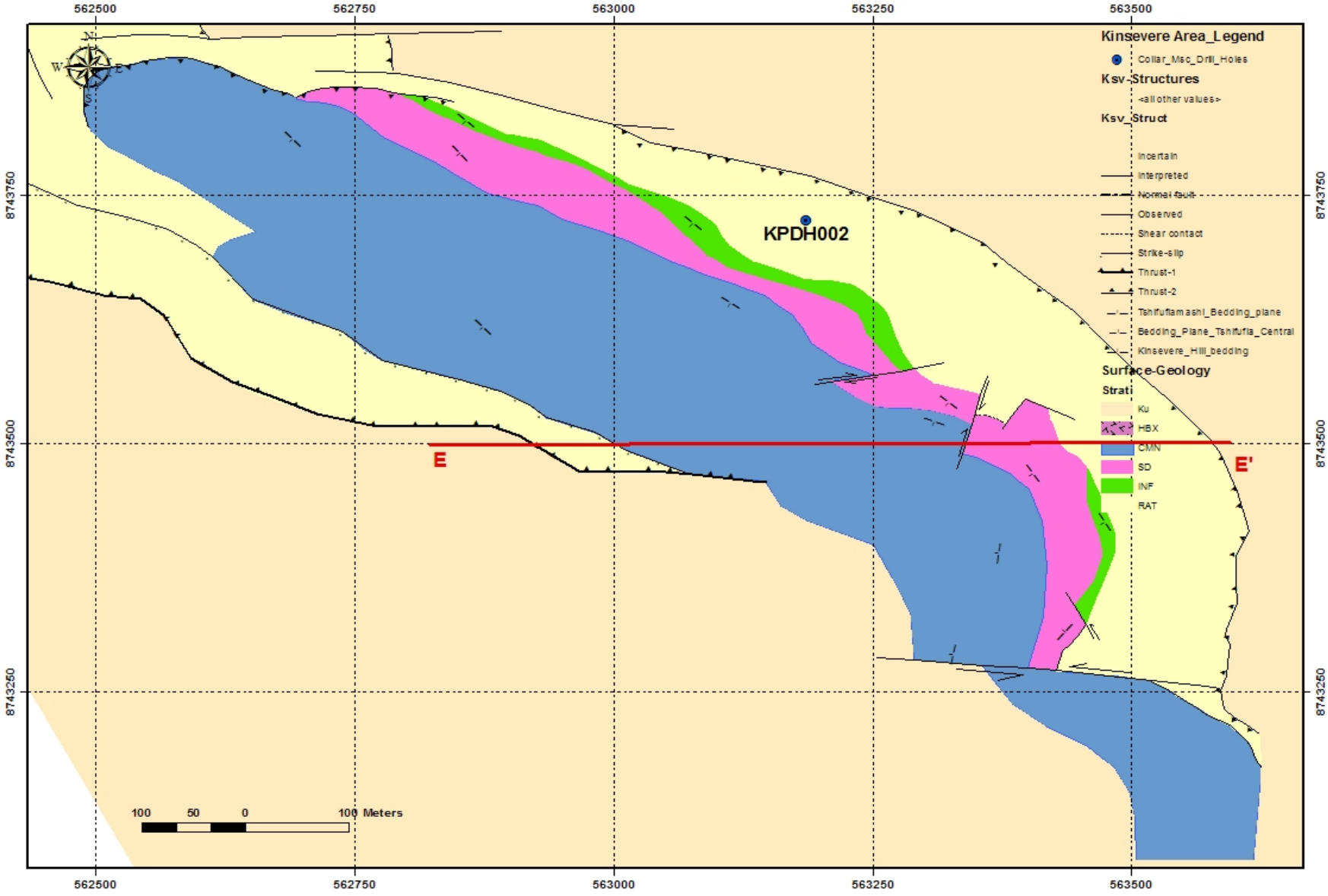

Figure 106: Geological map of the Kinsevere Hill fragment. Cross-section E-E' refers to Fig.13.

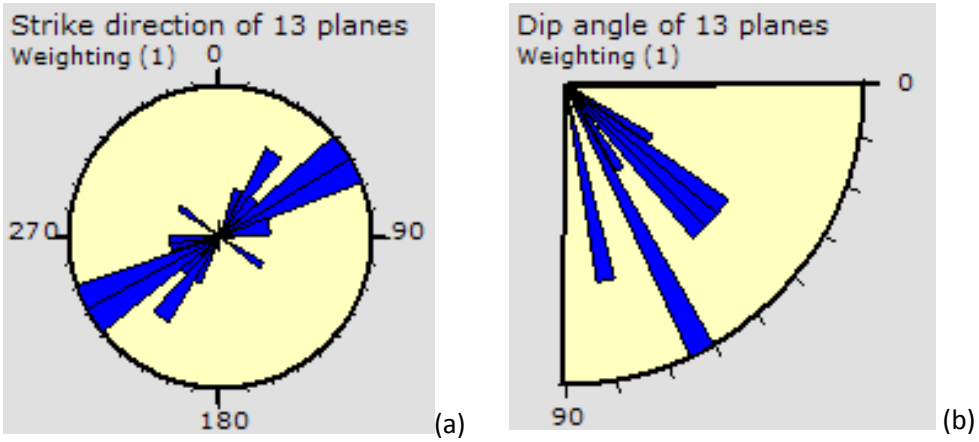

(a) (b)

Figure 107: Rose diagram of strike plane (a) and dip plane (b) obtained from the mineralised joints induced during the first stress tensor observed at Kinsevere Hill.

The stress tensor deduced from these measurements gives the maximal principal stress axis (σ_1): 18/255, the intermediate principal stress axis (σ_2): 43/003 and the minimum principal stress axis (σ_3): 40/148, with the stress ratio (R) and the friction angle (ø) at 0.95 and 70.15 respectively. This stress tensor belongs to the oblique compressive regime and it indicates SW-NE compression (Fig. 108)

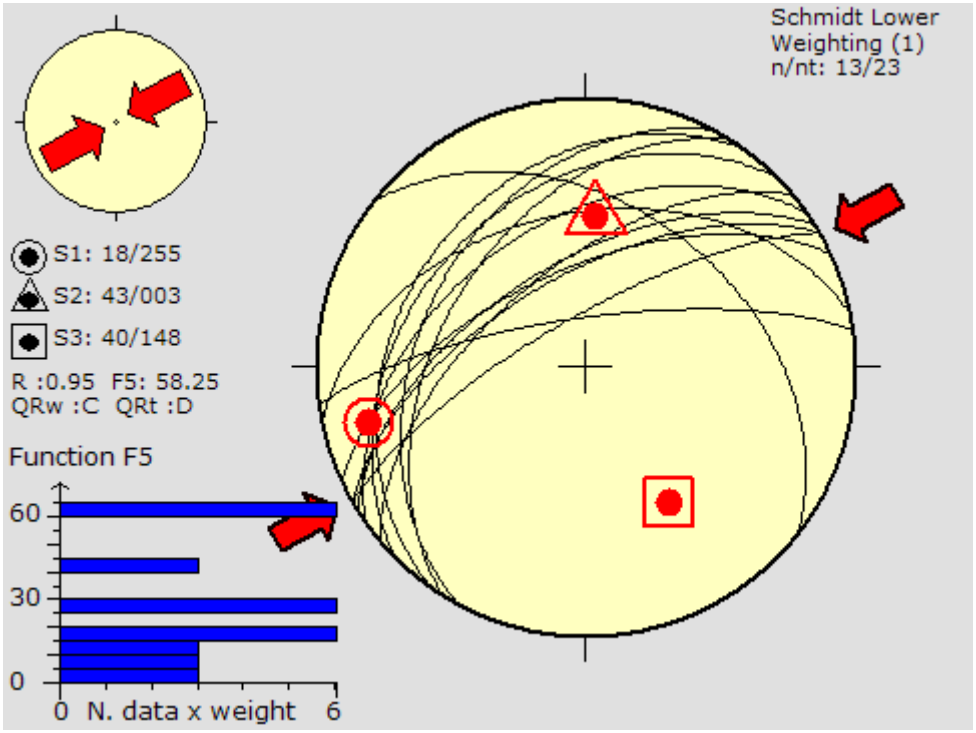

Figure 108: Stereonet showing the principal stress axis obtained with the improved right dihedral method combined with the rotational optimisation of the mineralised joints related to the first stress tensor obtained at Kinsevere Hill.

The second stress tensor obtained from the mineralised joints shows a rose diagram with strike of planes that are characterised by two main directions (Fig. 109 (a) and (b)). The first group shows a general strike of planes oriented WNW-ESE with angles dipping between 35°-50° (75°-80°); while the second group of mineralised joint planes strike SE-NW with dip angles varying

between 55° and 65°. The strike orientation of these two groups intersects at an acute angle of 60°.

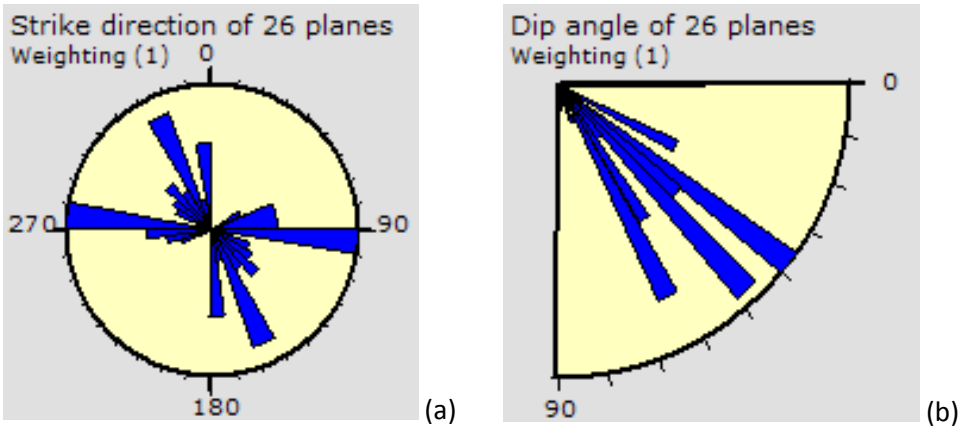

Figure 109: Rose diagram of strike plane (a) and dip plane (b) obtained from the mineralised joints formed related to the second stress tensor observed at Kinsevere Hill.

The stress tensor obtained from these measurements is characterised by the maximum principal stress axis (σ_1): 39/287, the intermediate principal stress axis (σ_2): 15/290 and the minimum principal stress axis (σ_3): 47/037, with the stress ratio (R) and the friction angle (ø) at 0.88 and 59.79 respectively. This stress tensor belongs to the pure strike-slip regime and it indicates SE-NW compression and SW-NE extension (Fig. 110).

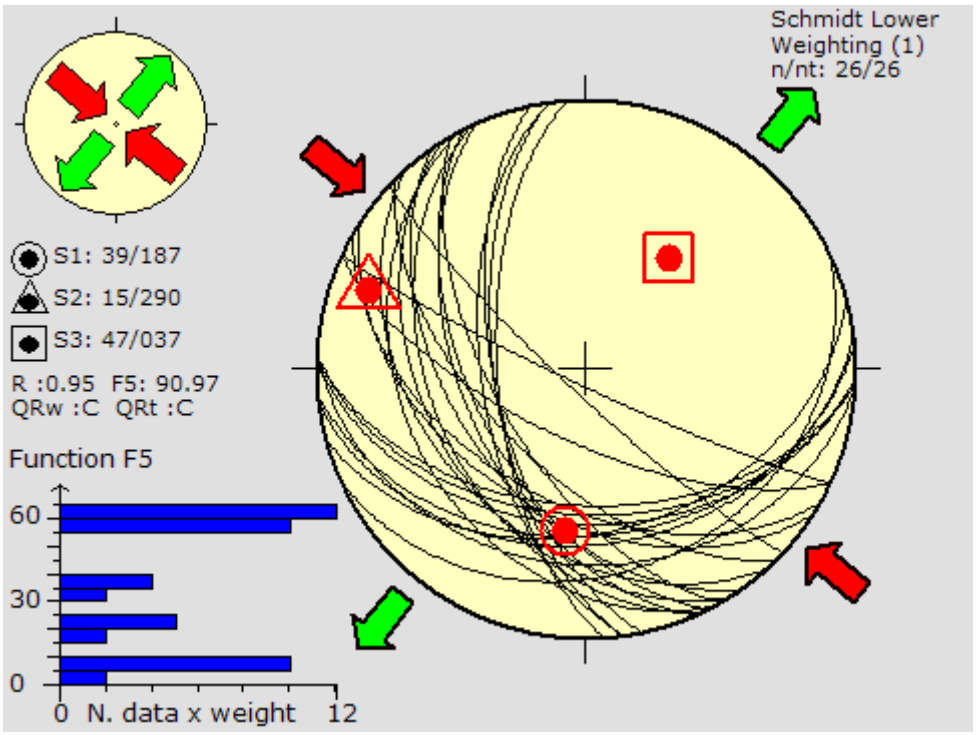

Figure 110: Stereonet showing the principal stress axis obtained with the improved right dihedral method combined with the rotational optimisation of the mineralised joints related to the second stress tensor obtained at Kinsevere Hill.

Table 16 below summarises the principal stress axis (σ_1, σ_2 and σ_3), the stress ratio and the friction angle Ø obtained from the mineralised joints data collected at Kinsevere Hill.

n	nt	Principal stress axis			R	SHmax	Shmin	R'	phi	Stress Regime
		σ_1	σ_2	σ_3						
13	57	18/255	43/003	40/148	0.95	61	151	1.05	70.15	Oblique Compressive
26	57	39/187	15/290	47/037	0.95	135	166	2.82	63.85	Pure Strike-slip

Table 16: Summary of the principal stress axis (σ_1, σ_2 and σ_3), stress ratio (R) and the friction angle obtained from the mineralised joints data collected at Kinsevere Hill.

3.3.3.1.2 Unmineralised joints (UMJ)

Twenty-five measurements of dip and dip direction of the unmineralised joints were collected from Kinsevere Hill and one stress tensor was obtained. This stress tensor shows two main directions of the strike planes. The first group is characterised by the general strikes oriented WSW-ENE and the second group shows a general strike oriented SE-NW. Both show the dip angle varying between 45° and 85° (Fig. 111 (a) and (b)).

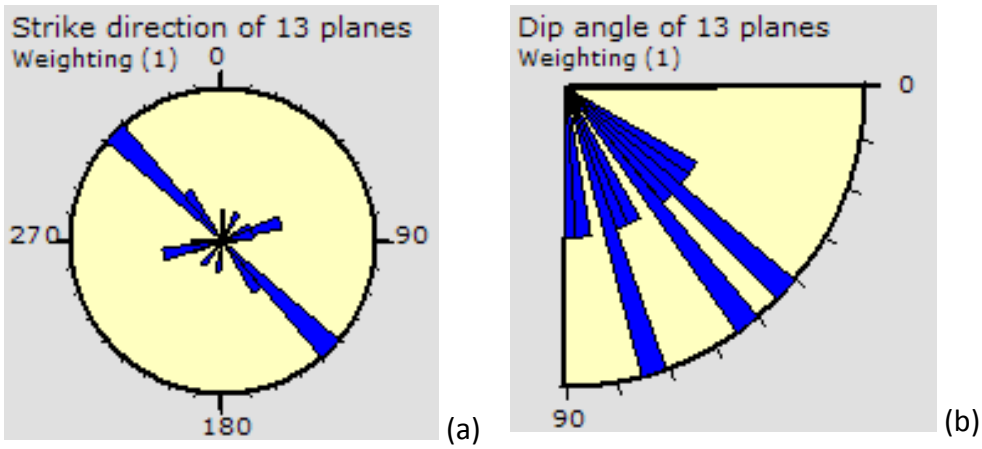

(a) (b)

Figure 111: Rose diagram of strike planes (a) and dip planes (b) obtained from the unmineralised joints at Kinsevere Hill

The stress tensor obtained from these measurements is characterised by the maximum principal stress axis (σ_1): 35/290, the intermediate principal stress axis (σ_2): 39/163 and the minimum principal stress axis (σ_3): 30/045, with the stress ratio (R) equal to 0.8. The stress tensor belongs to the pure extensive stress regime and it indicates a SW-NE extension (Fig. 112).

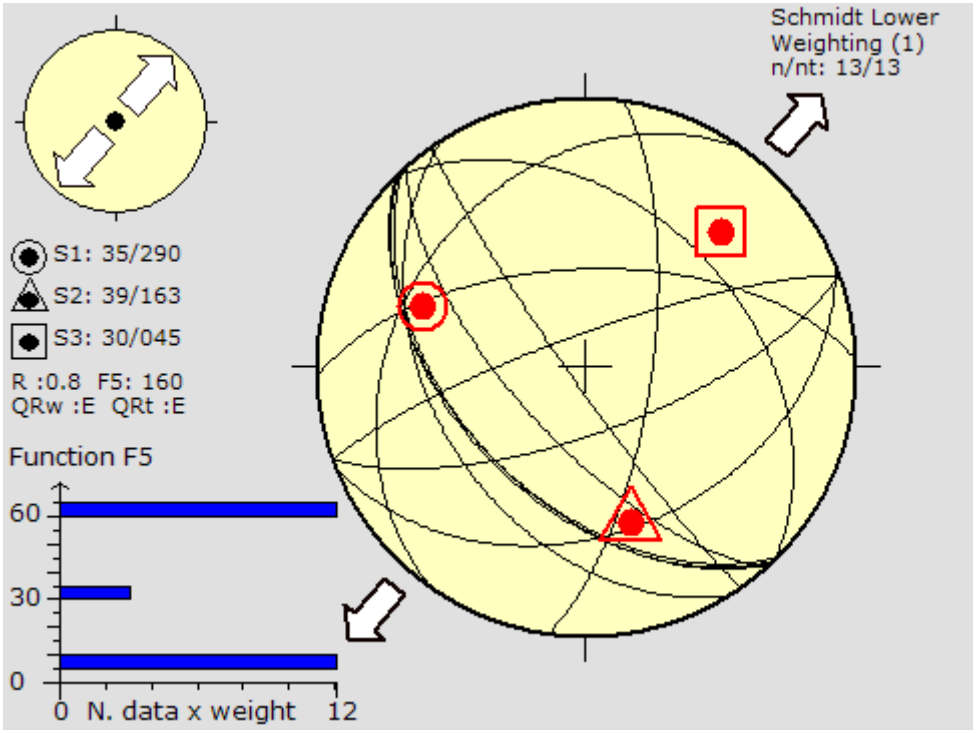

Figure 112: Stereonet showing the principal stress axis obtained with the improved right dihedral method combined with the rotational optimisation of the unmineralised joints observed at Kinsevere Hill.

3.3.3.2 Faulting

Seventeen slickensided fault planes were observed at Kinsevere Hill and within artisanal shafts (Table A.12). Two stress tensors were obtained from these slickensided faults.

The first stress tensor is characterised by the fault planes striking in the SSE-NNW direction and dipping steeply to both SW and NE (Fig. 113 (a) and (b)). These fault planes contain dip-slip striations plunging to the NNE (Fig. 113 (c) and (d)).

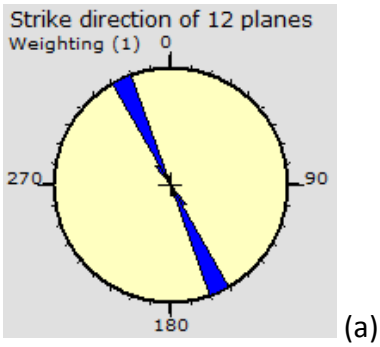

(a)

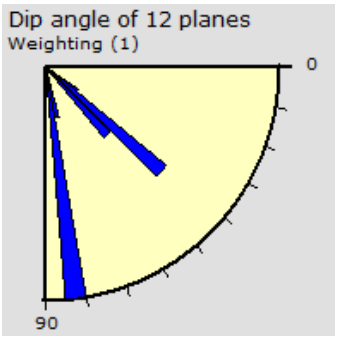

(b)

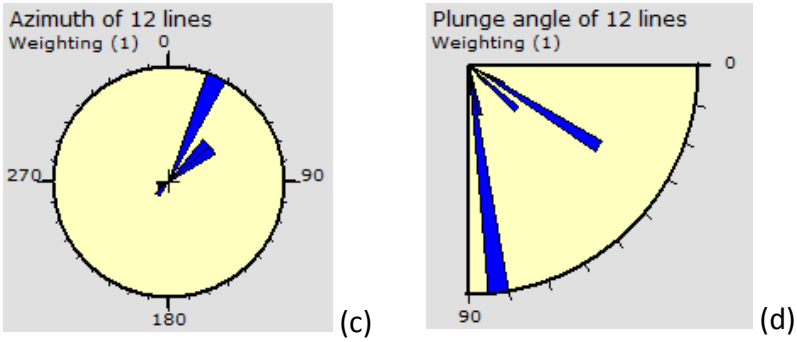

(c) (d)

Figure 113: Rose diagrams of the strike plane (a) and dip plane (b), azimuth of fault-slip (c) and plunge angle (d) of slickensided faults observed at Kinsevere hill.

The stress tensor obtained from these fault planes gives the maximal principal stress axis (σ_1): 32/050, the intermediate principal stress axis (σ_2): 11/148 and the minimum principal stress axis (σ_3): 54/255, with the stress ratio (R) and the friction angle (ø) at 0.67 and 51.84 respectively. This stress tensor belongs to the pure compression stress regime and it indicates SW-NE compression (Fig. 114).

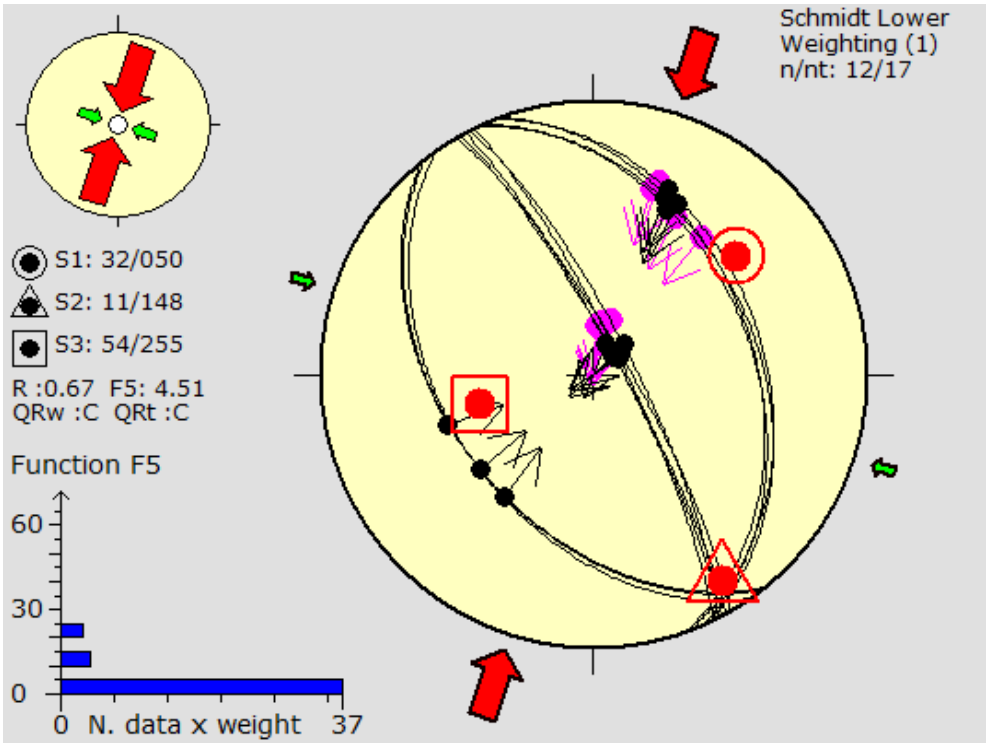

Figure 114: Stereonet showing the principal stress axis of the first tensor obtained with the improved right dihedral method combined with the rotational optimisation of the slickensided faults observed at Kinsevere Hill.

Two groups of slip lines acting on these fault planes have been highlighted in the presentation of the results shown in the above stereonet, using tangent-lineation data from these fault-slips. The first group comprises fault-slips indicating a movement towards the NNE and the second group represents fault-slips indicating a movement toward the SSW (Fig. 115).

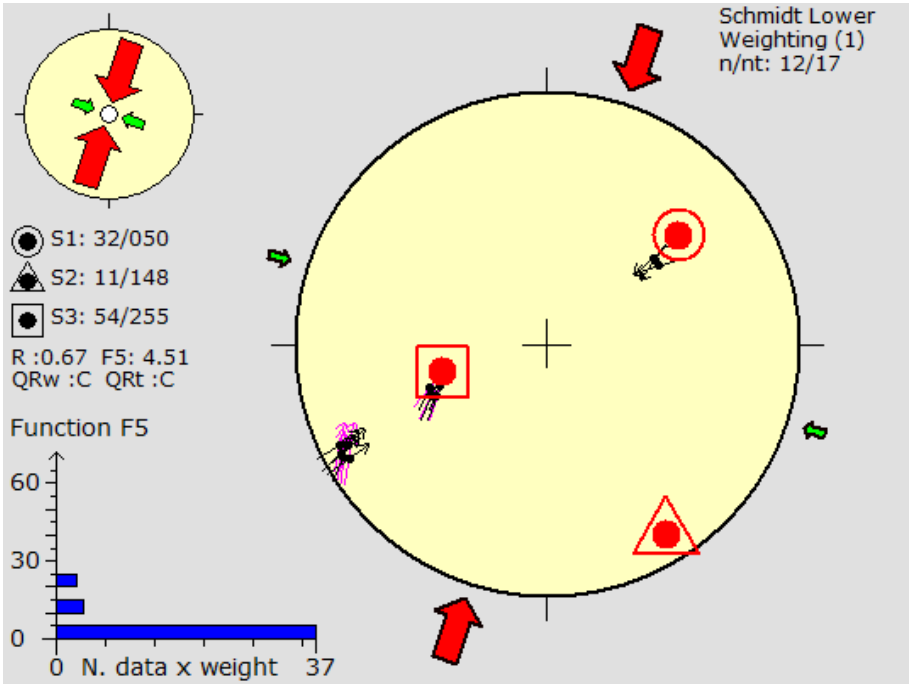

Figure 115: Stereonet showing tangent-lineation data obtained from lineation acting on the fault planes and belonging to the stress tensor deduced from the faults observed at Kinsevere Hill.

The second stress tensor is characterised by the fault planes striking in the N-S direction and dipping mostly to the West (Fig. 116a and b). These fault planes carry striations plunging to the North (Fig. 116 (c) and (d)).

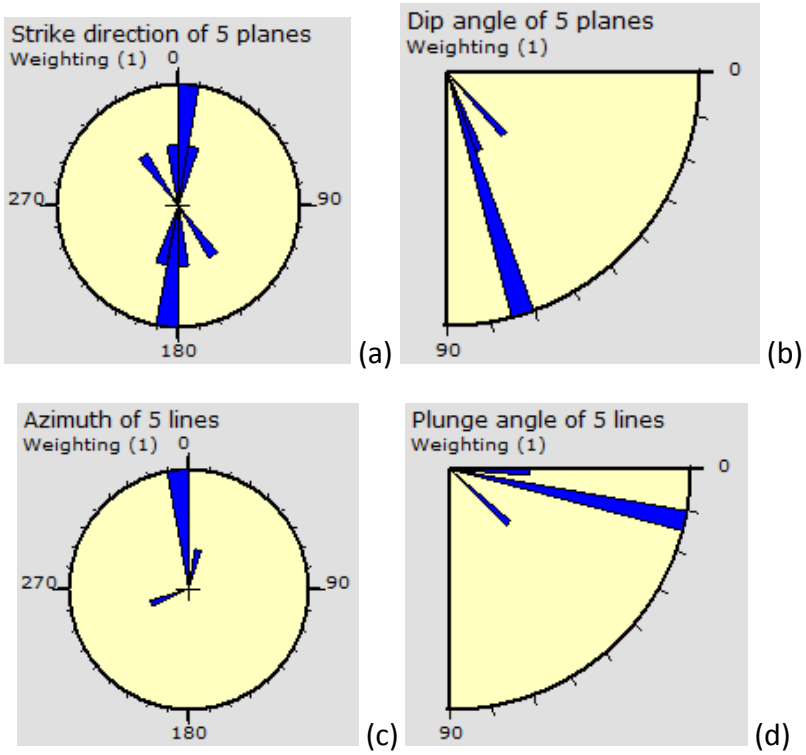

Figure 116: Stereonet showing the principal stress axis of the second tensor obtained with the improved right dihedral method combined with the rotational optimisation of the slickensided faults observed at Kinsevere Hill

This stress tensor shows the maximal principal stress axis (σ_1): 16/151, the intermediate principal stress axis (σ_2): 62/274 and the minimum principal stress axis (σ_3): 22/054, with the stress ratio (R) and the friction angle (ø) at 0.97 and 56.88 respectively. This stress tensor belongs to the extensional strike-slip stress regime and it indicates SW-NE extension and SE-NW compression (Fig. 117).

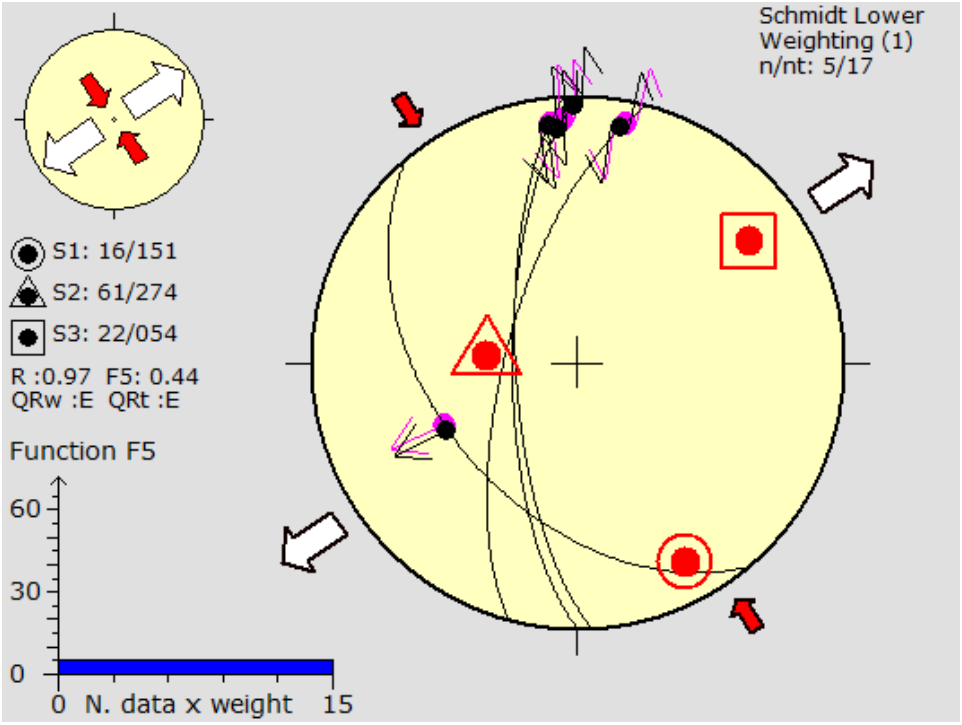

Figure 117: Stereonet showing the principal stress axis of the second tensor obtained with the improved right dihedral method combined with the rotational optimisation of the slickensided faults observed at Kinsevere Hill.

Presenting the results shown in the above stereonet, using tangent-lineation data from these fault-slips, the slip lines acting on these fault planes indicate a movement towards both the N and the NE (Fig. 118).

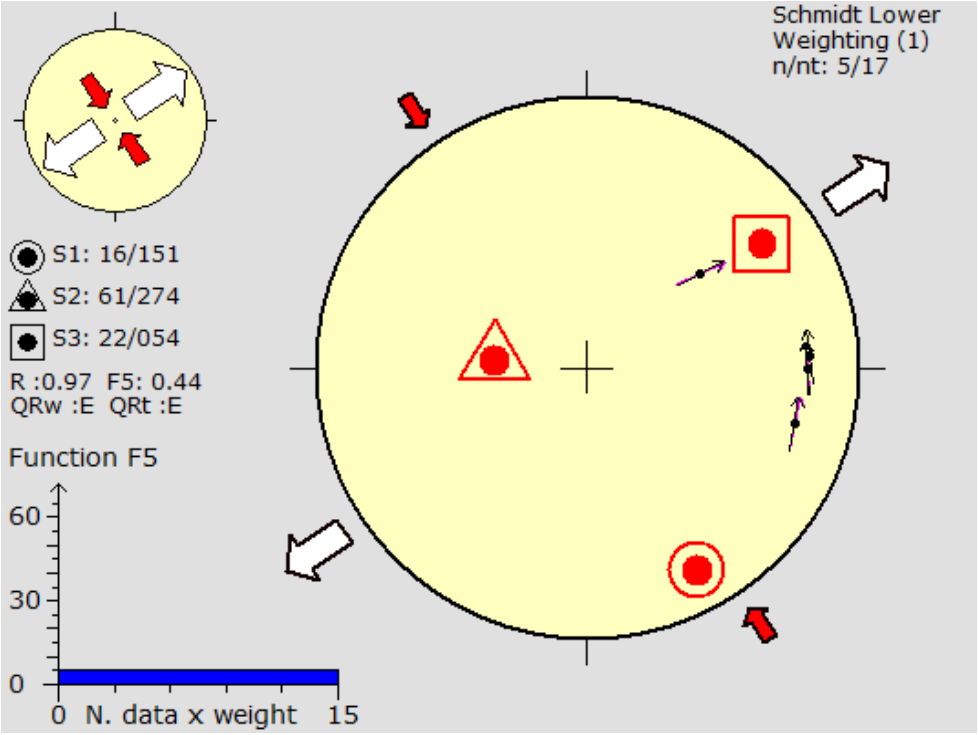

Figure 118: Stereonet showing tangent-lineation data obtained from fault slip acting on the fault planes of the stress tensor deduced from the fault-slip observed at Kinsevere Hill.

Table 17 below summarises the principal stress axis (σ_1, σ_2 and σ_3), the stress ratio and the friction angle Ø obtained from the mineralised joints data collected at Kinsevere Hill.

n	Nt	Principal stress axis			R	SHmax	Shmin	R'	phi	Stress Regime
		σ_1	σ_2	σ_3						
12	17	32/050	11/148	54/255	0.67	18	108	2.73	51.84	Pure compressional
5	17	16/151	61/274	22/054	0.97	146	56	1.03	56.88	Extensional strike-slip

Table 17: Summary of the principal stress axis (σ_1, σ_2 and σ_3), stress ratio (R) and the friction angle obtained from the mineralised joints data collected at the Kinsevere Hill.

3.3.3.3 Folding

The CMN strata outcropping in artisanal shafts of the western side of Kinsevere were folded and fractured.

Bedding orientations of the entire Kinsevere Hill R2 fragment, the orientation of the hinge lines (HL) and the fold axial planes (FAP) of the folds in the CMN strata were measured (Table 131-132-133).

The Phi diagram of poles to bedding of the Kinsevere Hill (Fig. 119) reveals that bedding planes are generally steeply dipping to the South-West, showing an upright succession with the youngest strata (CMN) outcropping at the western side of the Kinsevere Hill. CMN are underlain by the oldest strata (RAT) which are outcropping to the eastern side of the Hill. The fold axis inferred from the bedding planes measurements of the entire upright limb as outcrops in the Kinsevere Hill area is oriented 332° (NW) and plunges 06° to the NW.

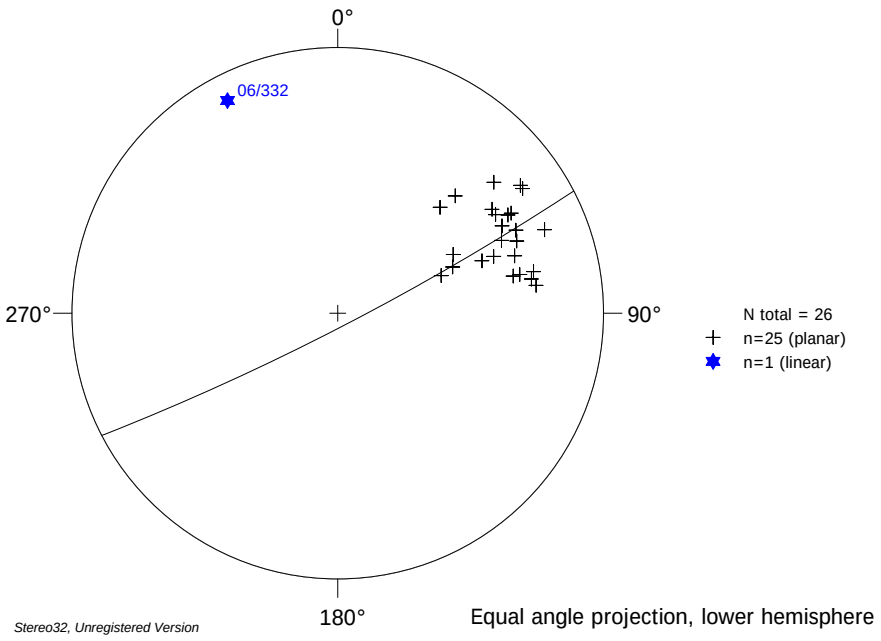

Figure 119: π diagram indicating the fold axis obtained from the bedding planes observed at Kinsevere Hill.

However, the bedding plane orientations collected from the small-scale folds observed within the CMN strata on the western side of the Kinsevere Hill shows a Phi diagram (Fig. 120) indicating a fold axis orientated 321° (NW) and plunging NW with a plunge angle of 03°.

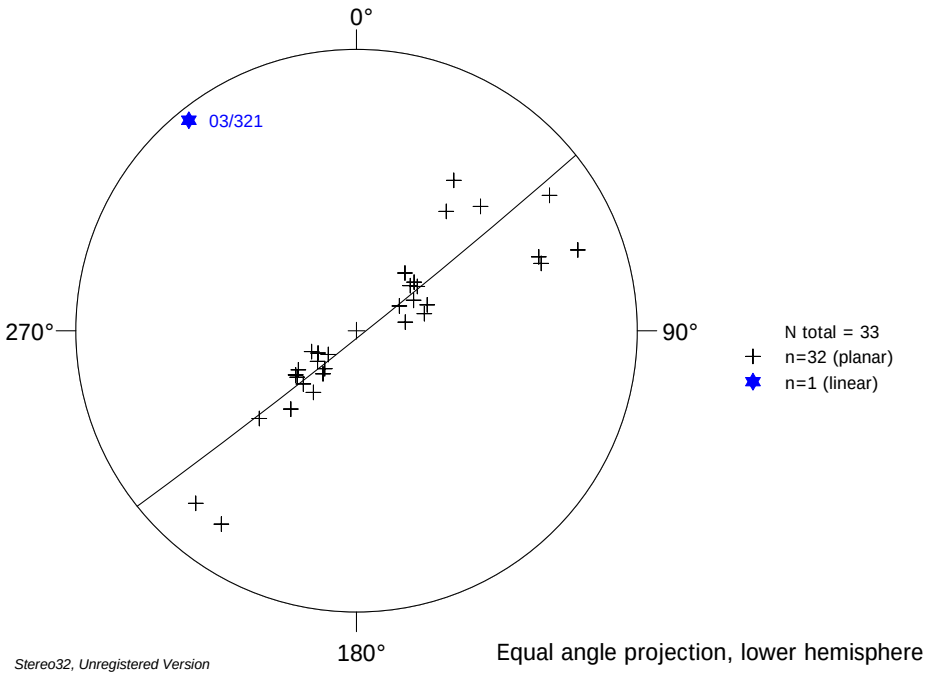

Figure 120: π diagram indicating the fold axis obtained from the bedding planes collected from the isoclinal fold observed in the CMN strata at Kinsevere Hill.

The stereographic projection of fold axial planes observed in micro-folds of the west limb of the Kinsevere Hill indicates a SW (223°) dipping direction with a dip angle of 24° (Fig. 121). This axial plane indicates a NE vergence of the folding in the Kinsevere Hill area.

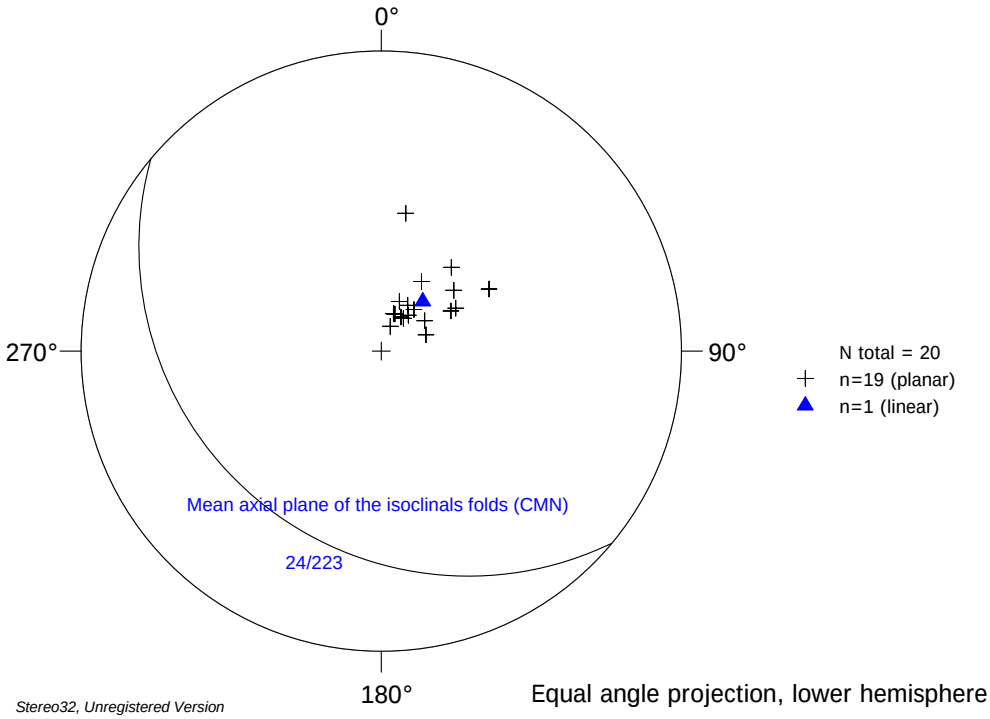

Figure 121: Stereographic projection showing the fold axial plane contour of the Kinsevere Hill fragment where the black crosses represent the fold axial plane poles. The blue triangle represents the average pole and the large black circle represents the average plane.

The hinge lines of the isoclinals folds observed in the CMN strata indicates an azimuth oriented SE (117°) and gently plunging to the SE (09°) (Fig. 122).

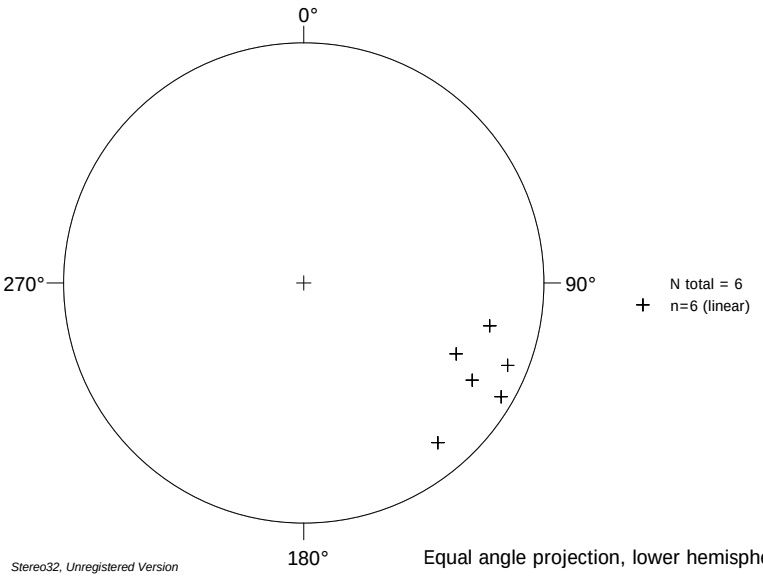

Figure 122: Stereographic projection of raw data collected from the hinge line observed in the Kinsevere Hill fragment.

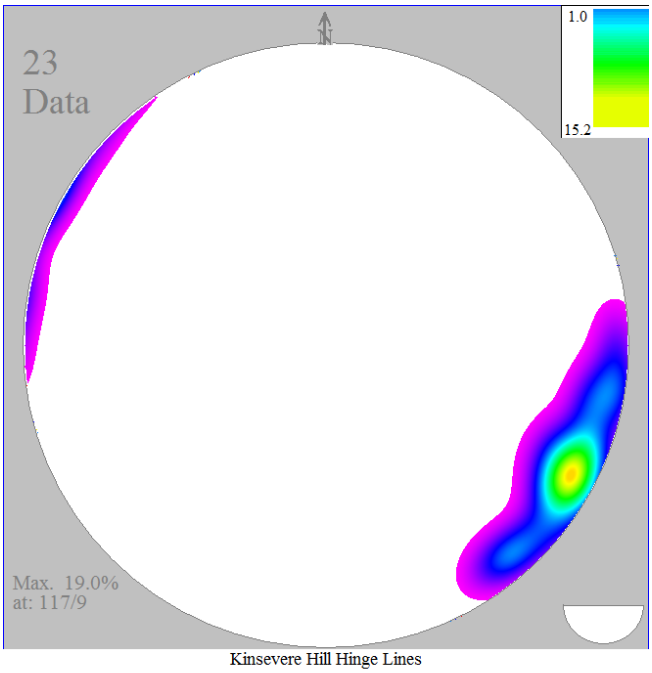

Figure 122 (b): Stereographic projection of the hinge lines data collected from the Kinsevere Hill fragment.

Table 18 below summarises the plunge angle/azimuth orientations of fold axis and hinge lines and the dip and dips directions of the axial planes obtained from the field data collected from Kinsevere Hill.

Kinsevere fragment	Dip / plunging angle	Dip direction/Azimuth orientation
Fold axis of the fragment	06	332
Fold axis-Isoclinals folds (CMN)	03	321
Hinge line-Isoclinals folds (CMN)	09	117
Fold axial plane-Isoclinals folds (CMN)	24	223
Vergence of the fold	NE	

Table 18: Showing the dip/plunging angle, dip-dip direction/azimuth orientation and vergence of the folding event obtained in the Kinsevere Hill fragment.

3.4. Synthesis of results

Table 19 and the map (Appendix 2 – Figs. 131-139) below provide a summary of all the reduced stress tensors obtained from the brittle deformations collected from the three fragments that comprise the Kinsevere copper deposit and the location of the orientation of these reduced stress tensors.

It is noted that from the inventory of the palaeostress carried out at the Kinsevere region, ten types of reduced stress tensors may be distinguished, as shown in the Table 19. The significance and timing of these ten reduced stress tensors are discussed in the following chapter.

Fragment	Brittle type	Tensor ID	n	nt	Principal stress axis			R	SHmax	Tensor Type	Orientation
					σ1	σ2	σ3				
Tshifufiamashi	MJ	T1	27	95	38/299	06/204	50/106	0.75	7	Pure Compressive	SSW-NNE Compression
		T2	18	95	46/047	06/309	42/213	0.92	121	Oblique radial Compressive	SE-NW Compression ; SW-NE Extension
		T3	13	95	50/263	36/111	13/011	0.8	103	Oblique Extensive	SSW-NNE Extension
	UMJ	T1	21	95	39/029	38/160	26/274	0.5	15	Oblique Extensive	SE-NW Extension
	Fault-slip	T1	54	114	01/218	00/128	88/008	0.87	38	Radial Compressional	SW-NE Compression
		T2	20	114	06/227	67/121	21/320	0.24	49	Compressional strike-slip	SW-NE Compression; SE-NW Extension
		T3	12	114	38/125	51/303	00/034	0.43	124	Pure Strike-slip	SE-NW Compression ; SW-NE Extension
	Shear fractures	T1	19	35	10/260	09/352	76/123	0.5	79	Pure Compressional	WSW-ENE Compression
		T2	16	35	44/256	45/074	01/165	0.5	76	Oblique Extensive	SSE-NNW Extension
Tshifufia	MJ	T1	39	210	05/172	47/072	42/266	0.35	173	Oblique Compressive	SSE-NNW Compression
		T2	57	210	27/220	62/043	01/311	0.35	41	Pure Strike-slip	SW-NE Compression; SE-NW Extension
		T3	53	210	03/123	62/025	26/214	0.95	125	Extensional Strike-slip	SE-NW Compression; SW-NE Extension
		T4	21	210	32/291	49/152	21/035	0.2	114	Oblique Extensive	SSW-NNE Extension
	UMJ	T1	25	210	23/010	03/101	66/199	0.5	8	Pure Compressional	SSW-NNE Compression
		T2	51	210	51/128	24/252	27/356	0.68	92	Pure Extensional	S-N Extension
	Fault-slip	T1	29	67	11/038	17/132	68/278	0.53	36	Pure Compressional	SW-NE Compression
		T2	17	67	05/151	27/244	61/052	0.83	147	Radial Compressional	SE-NW Compression
		T3	21	67	83/347	04/212	04/122	0.54	32	Pure Extensional	SE-NW Extension
	Shear fractures	T1	24	54	06/239	00/329	82/069	0.5	59	Pure Compressional	SW-NE Compression
		T2	30	54	58/237	27/025	14/123	0.56	38	Pure Extensional	SE-NW Extension
Kinsevere Hill	MJ	T1	13	57	18/255	43/003	40/148	0.95	61	Oblique Compressive	SW-NE Compression
		T2	26	57	39/187	15/290	47/037	0.95	135	Pure Strike-slip	SE-NW Compression; SW-NE Extension
	UMJ	T1	13	57	35/290	39/163	30/042	0.66	131	Oblique Extensive	SW-NE Extension
	Fault-slip	T1	12	17	32/050	11/148	54/255	0.67	18	Pure Compressional	SSE-NNW compression.
		T2	5	17	16/151	61/274	22/054	0.97	146	Extensional strike-slip	SE-NW compression; SW-NE Extension

Table 19: Results of the reduced palaeostress tensors obtained from the mineralised and unmineralised joints (MJ and UMJ), slickensided faults (fault-slip) and shear fractures data.

Chapter 4

INTERPRETATIONS AND DISCUSSIONS

This chapter will be devoted to both analysis of the results presented in the chapter 3 and discussion of existing tectonic models that were presented in Chapter 1. This interpretation will be undertaken through the analysis of the folding events, as recorded in the three fragments studied in the Kinsevere region, the analysis of the fracturing events represented by the mineralised and unmineralised conjugate fractures, the analysis of the faulting events represented by the shear fractures and slickensided faults and the analysis of the evidence for a thrusting event observed at the Tshifufiamashi Pit (situated to the North) and in Tshifufia Pit, located in the centre of the region. The aim of this chapter is to explain the geological history and the structural architecture of the South-Eastern part of the Lufilian Arc.

4.1 Folding analysis

The Kinsevere Hill and Tshifufiamashi fragments consist of a fold limb with upwards-younging formations. The bedding planes are striking SE-NW and SSE-NNW and steeply dipping to the SW and WSW in these two areas, respectively (Figs. 67 and 106). CMN strata outcrops to the West and the oldest formation (Red RAT) are exposed to the East. In contrast, the Tshifufia area is underlain by an overturned limb with the oldest formation (Red RAT) exposed to the East, overlain by the youngest formation (CMN) outcropping to the West. Bedding planes are striking S-N to SSW-NNE and steeply dipping to the East and to the ESE in the Tshifufia fragment, suggesting that they are part of an overturned limb (Fig.72). The CMN strata are affected by tights/isoclinal folds in the entire Kinsevere area. As mentioned in earlier chapters, these fragments are separated by two sinistral strike-slip faults between Kinsevere Hill and the Tshifufia fragment, and the Tshifufia and Tshifufiamashi fragments.

4.1.1 F_1 folding events.

The F_1 folding event is marked by the development of the small-scale tight to isoclinal overturned folds in the CMN strata only and is interpreted on the basis of the dip-direction of the bedding planes observed in the Kinsevere area (Fig. 70a). These small-scale folds might have been developed during an early stage of the compressional phase and can be inferred to be parasitic folding on more regionally-developed folds which developed subsequently during the same compressional phase. The π diagrams (Figs. 68 and 120) obtained from the orientation of the bedding planes of the well-folded CMN strata in both R2 Mines Subgroup fragments (Tshifufiamashi [Fig. 68] and Kinsevere Hill [Fig.119]) which exhibit small-scale folding, indicate a SE oriented fold axis that gently plunges to the SE in Tshifufiamashi (Fold axis=03/139) and plunges to the NW in Kinsevere Hill (03/321). In Tshifufia, the π diagram (Fig. 101) obtained from the bedding planes of the same well-folded CMN strata indicates a SW oriented fold axis (05/227).

Parallel to these fold axes, the fold hinge lines observed in the well-folded CMN strata are generally parallel to the fold axes obtained from the π diagrams (Figs 68, 101 and 120). The hinge lines show a SW trend in Tshifufia (18/231) (Fig. 103) and a SE trend in both Tshifufiamashi (18/126) (Fig. 69) and Kinsevere Hill (09/117) (Fig. 113). The tight/isoclinal folds also show a SW dipping fold axial plane in both Tshifufiamashi (30/220) (Fig.68) and Kinsevere Hill (24/223) (Fig. 112) and a NW dipping fold axial plane in Tshifufia (33/317) (Fig. 102), implying NE vergence in Tshifufiamashi and Kinsevere Hill, with SE vergence in Tshifufia. It is important to note the perpendicular relationships between the folding geometry recorded from the Tshifufia area, compared to both the Tshifufiamashi and Kinsevere Hill areas. Despite these differences in orientation, the folding style is similar in all three areas, and the Tshifufia fragment is interpreted to have rotated clockwise by ~90° between the two parallel sinistral strike-slip faults (cf. section 4.3) after the folding was imposed. Thus, all early-formed small-scale folding in the area is interpreted as F_{1a}, irrespective of its orientation. Assuming that the vergence of folding (prior to rotation) was NE, this implies that F_1 folding was a response to general SW-NE shortening. This SW-NE compressional orientation might be interpreted as the major compressive regime in the South-Eastern part of the Lufilian Arc.

Evidence for the F_{1b} folding event is recorded from the orientation of bedding in RAT, DSTRAT+RSF and SD. These strata are generally sandstone and silicified dolomite and show less evidence for small-scale folding. Instead, folding is larger-scale, or strata can be interpreted to be only one limb of a more regionally-developed fold. The fold axes obtained from the π diagrams of bedding in these strata in both the Tshifufiamashi and Kinsevere Hill fragments plunge gently NW, which is sub-parallel to the trends of fold axes of F_{1a} folds that were recorded in the CMN strata. This is also the case for the Tshifufia fragment, where both F_{1a} and F_{1b} fold axes plunge gently SW. (Compare, for example, Fig. 67, 119). The F_{1b} folds are likely to have re-folded smaller-scale F_{1a} folds, so that a Luiswishi-type syncline showing NE-vergence with overturned limb thrusted towards the NE is produced locally. The F_{1c} fold elements have produced a refolded syncline producing a synform/antiform couplet with a refolded F_{1b} axial plane (Fig. 125 below).

A simple F_{1a} and F_{1b} model for the development of folding in the study area cannot account for the outcrops in the Tshifufia pit (Fig. 124), where the strata dips generally in an easterly direction (whereas in Tshifufiamashi and Kinsevere Hill it dips steeply West; refer to cross-section). This different younging direction in the Tshifufia area is unlikely to be explained simply by clockwise rotation related to sinistral strike-slip faulting outlined above. Differences in F_{1a} and F_{1b} fold geometry differ by about 90° between Tshifufiamashi and Tshifufia, whereas up to 180° of rotation would be required to account for eastward (rather than westward) dipping strata in the Tshifufia area. Instead, the eastward-dipping Tshifufia limb can be interpreted to represent a third F_1 refolding event (F_{1c}) with a similar fold axial

plane to the F_{1b} folds. The Tshifufia area may thus represent the eastward-dipping eastern limb of a synform/antiform couplet (Fig. 125) formed by refolding of F_{1b} folds by an F_{1c} event, coupled with c. 90° clockwise rotation between two neighbouring sinistral strike-slip faults (Fig. 125, parts 3 and 4).

	F_{1a}	F_{1b}	F_{1c}
	CMN Strata	**Lower R2 + SD**	
Tshifufiamashi	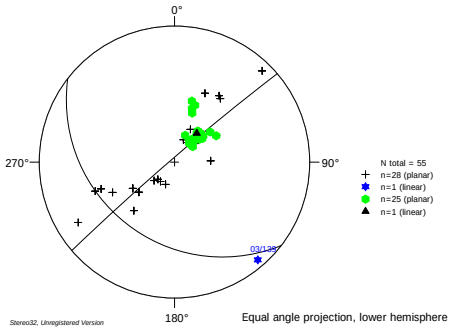	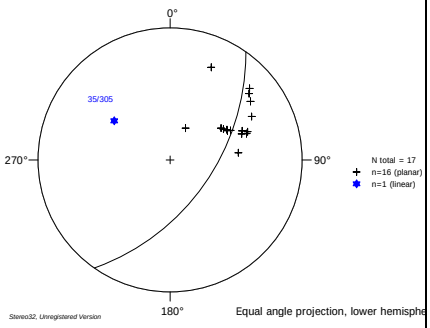	NE-Vergent Regional-scale re-folding (see Fig.124)
Tshifufia	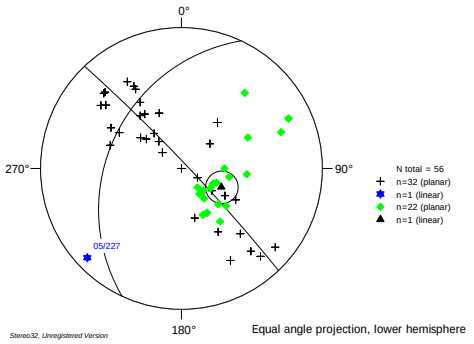	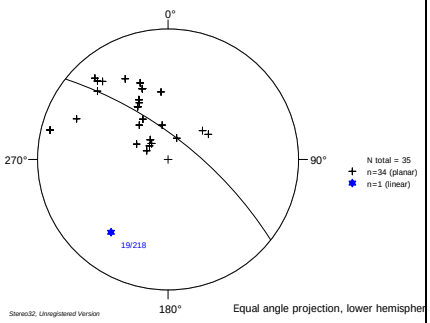	
Kinsevere Hill	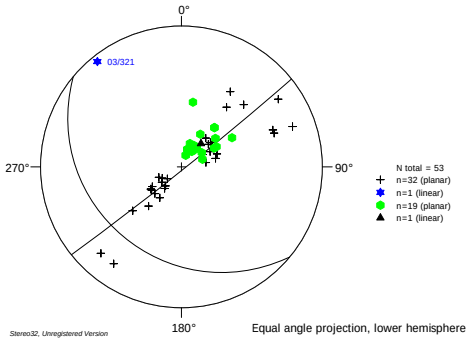	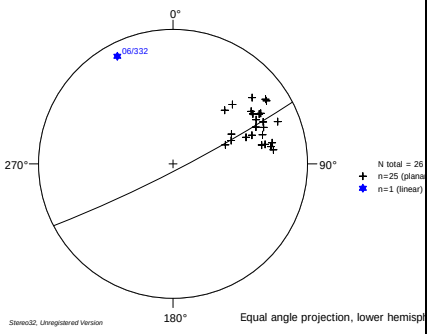	

Figure 123: Summary of Phi diagrams and fold axial planes for F1a and F1b folding in the study area. Lower R2 = RAT+D.STRAT+RSF. Green bullet = Fold axial planes and Black cross = Pole to bedding of tight/isoclinal folds.

Given that the R2 Mines Subgroups fragments in the Kinsevere area (Tshifufiamashi, Tshifufia and Kinsevere Hill) are separated by two sinistral strike-slip faults respectively, the Tshifufia fragment situated between these two strike-slip faults rotated in a clockwise direction. Therefore, all structures that are contained within the Tshifufia fragment have similarly rotated in the same clockwise direction. Thus the fold axis and the hinge line obtained from the tight/isoclinal folds encountered in the CMN strata show a SW-NE trend, parallel to the fold axis inferred from the bedding planes and plunges to the SW with NW dipping fold axial plane indicating a SE fold vergence. This clockwise rotation might be related to the known strike-slip faulting event occurring during the Monwezian phase (D_2) of the Lufilian orogeny (Fig. 125, part 4).

Thus, the Kolwezian event (D_1) did not take place in a single continuous phase but instead took place over three stages characterised mainly by folding associated with faulting and thrusting.

4.2 Fracturing analysis

Mineralised and unmineralised joints were found in all R2 Mines subgroups in the Kinsevere area. Palaeostress tensors obtained after the analysis of mineralised joints have produced results that were shown in Table 19 of Chapter 3 and illustrated in Appendix 2 – (Figs. 131-139).

4.2.1 Analysis of the mineralised joints.

Mineralised joints present in Tshifufiamashi and Kinsevere Hill fragments form mainly two groups striking SE-NW and SW-NE respectively. In rare instances, these joints strike in an E-W direction. The direction of the mineralised joint groups intersects the general strike of the bedding planes in both these areas. Five stress tensors have been obtained from the measurements of these joints. Three of these tensors belong to a compressive stress regime (pure and oblique radial compressive), one of them to a strike-slip stress regime (pure strike-slip) and the last one to an extensive system (oblique extension).

However, the mineralised joints observed in the Tshifufia pit lie within two main groups striking generally SW-NE (or SSW-NNE) and SE-NW (or SSE-NNW), with rare strike directions towards N-S and E-W (ESE-WNW). Four stress tensors were obtained from joints in this fragment, one of which belongs to the compressive regime, two to the strike-slip system (pure strike-slip and extensive strike-slip) and one to the extensive regime (oblique extensive).

Based on the results presented above, nine stress tensors were obtained from the mineralised joints in the entire Kinsevere area. Four of them belong to the compressive stress regime (pure, radial oblique and oblique compression), three belong to the strike-slip

regime (pure and extensional strike-slip) and two belong to the extensive stress regime (oblique extension).

4.2.1.1 Compressive stress regime

The stress tensors belonging to a compressive regime obtained from the mineralised joints observed in Tshifufiamashi and Kinsevere Hill are orientated SSW-NNE and SW-NE, respectively. However, the compression stress tensor obtained in Tshifufia is oriented SSE-NNW. A second stress tensor belonging to the compressive regime (oblique radial compression) was obtained from the Tshifufiamashi fragment and shows a compression oriented SE-NW and extension oriented SW-NE. The compression direction corresponds with that obtained in the Tshifufia fragment.

The direction of the compressive tensors responsible of the establishment of the mineralised joints in Tshifufiamashi and Kinsevere Hill is perpendicular to both the orientation of the fold axis of the F_{1b} regional folds and the measured average of the hinges lines of the F_{1a} tight/ isoclinal folds observed in the CMN. The direction of the principal stress axes σ_1 derived from the stress tensors in both Tshifufiamashi and Kinsevere Hill are oriented SW-NE (38/299 in Tshifufiamashi and 18/255 in Kinsevere Hill). These σ_1 directions are appropriate to induce a regional fold characterised by a SW dipping fold axial plane in both Tshifufiamashi and Kinsevere Hill (see section 3.1.1). In Tshifufia, it is also noted that the direction of the compressive tensor is perpendicular to both the average orientation of hinge lines of the well-folded CMN strata and the fold axis, both of which plunge gently SW. The general direction of the maximum principal stress axis σ_1 is oriented SE-NW (05/172), and could account for the observed fold geometry in the Tshifufia area, shown in section 3.1.1.

The calculated results indicate that σ_1 (SHmax) and σ_3 (Shmin) are generally sub-horizontal and σ_2 is sub-vertical in all the stress tensors that belong to the compressive system with σ_1 varying between SSW and SW in Tshifufiamashi and Kinsevere Hill. In addition, σ_1 (SHmax) is sub-horizontal and σ_3 (Shmin) sub-vertical in all stress tensors which belong to the compressive system with σ_1 varying between SW and SE in Tshifufia. These stress tensors are derived from the mineralised joints in the study area and the fact that the σ_1 axes are orientated perpendicular to fold hinges suggests that mineralised joints and folding may have occurred together. Such NE-SW directed compression is likely to relate to the major compressive phase of the Lufilian orogeny. The palaeostress tensors obtained from the mineralised joints show a clockwise rotation in the Tshifufia fragment. This clockwise rotation is also linked to the spatial location of the Tshifufia fragmentwhich is situated between the two sinistral strike-slip faults.

4.2.1.2 Strike-slip stress regime

In the Tshifufiamashi and Kinsevere Hill fragments, the stress tensors belonging to the strike-slip regime (pure and extensional strike-slip) obtained from the mineralised joints indicate respectively SE-NW compression and SW-NE extension. In the Tshifufiamashi fragment, this

stress tensor corresponds to the second compressive stress regime (oblique radial compressive). These stress tensors are derived from the reactivated mineralised joints which relate to a regional SE-NW dextral strike-slip faulting which is observed in both Tshifufiamashi and Kinsevere Hill.

Two types of stress regimes belonging to the strike-slip regime were obtained in Tshifufia. The first indicates SW-NE compression and SE-NW extension and the second indicates SE-NW compression and SW-NE extension. It appears that these stress tensors are not synchronous with each other. The SW-NE trending mineralised joints belonging to a dextral strike-slip system and does resulted from the stress tensor characterised by SW-NE compression and SE-NW extension. Meanwhile, the SE-NW trending mineralised joints, which belong to the sinistral strike-slip system, result from the stress tensor indicating SE-NW compression and SW-NE extension. The compression direction obtained from the strike-slip tensors within the Kinsevere area is parallel to the stress tensor responsible for the establishment of the mineralised joints and therefore, to the folding. This relationship is demonstrably true in both Tshifufiamashi and Tshifufia. The direction of the extensive stress tensor, on the other hand, is perpendicular to the folding axial plane within all fragments. It is clear that the mineralised joints belonging to the strike-slip regime post-date those belonging to the compression system.

The calculated results indicates that σ_1 (SHmax) and σ_3 (Shmin) are sub-horizontal, while σ_2 is sub-vertical in all stress tensors belongs to strike-slip systems in Tshifufia with σ_1 swinging from NW to SW, producing a change of the strike-slip system from pure strike-slip (Fig. 77), with the stress ratio (R)=0.35 tending towards R=0, indicating a transpressive strike-slip system, to an extensional system, indicating a transtensile system with the stress ratio (R)=0.95 tending towards (R)=1 (Fig. 79) (Ritz, 1994). The differently oriented stress tensor from the Tshifufia fragment can similarly be interpreted to reflect clockwise rotation from the palaeostress tensors obtained from the mineralised joints induced during the sinistral strike-slip regime. These mineralised joints postdate the major compressive system that led to the superimposed folding events.

4.2.1.3 Extensive stress regime

The stress tensor belonging to the extensive regime obtained from the mineralised joints are mainly oblique extensional. They show WSW-ENE and ESE-WNW strike in both Tshifufiamashi and Tshifufia fragments (Figs. 49 and 80). The σ_3 trends in a SSW-NNE direction in both Tshifufiamashi and Tshifufia (Figs. 50 and 81). The ESE-WNW and WSW-ENE striking mineralised joints as observed in both Tshifufiamashi and Tshifufia strike perpendicular to the orientation of the minimum principal stress axis σ_3 (13/011 in Tshifufiamashi; 21/035 in Tshifufia) of the stress tensor obtained from them.

The extensional direction obtained in both Tshifufia and Tshifufiamashi correlates well with the compressional direction of the strike-slip system which shows SE-NW compression. Based on the above observations, it seems that the mineralised joints belonging to the

extensive system have been opened up first during the compressive phase and then filled out later by the Cu-Co enrichment mineralisation mixed with manganese oxides. This extensional system is here inferred to be induced as a tectonic response to the compressional system arising from the strike-slip regime noted in the Kinsevere area.

4.2.2 Analysis of the unmineralised joints.

Unmineralised joints have been also observed within the Tshifufiamashi, Kinsevere Hill and Tshifufia fragments. They show two main strikes: WSW-ENE and SSW-NNE in Tshifufiamashi (Fig.51), ESE-WNW and SE –NW in Tshifufia (Fig.84) and SE-NW and ESE-WNW at Kinsevere Hill (Fig.110). Four stress tensors have been obtained from the unmineralised joints in all these fragments. Three of them belong to the extensive regime (pure and oblique extensive) and one belongs to the compressive regime (pure compressional).

4.2.2.1 Compressive stress regime

The stress tensor belonging to the compressive regime was obtained only in Tshifufia and indicates SSW-NNE compression. This direction corresponds with the compression of the strike-slip system that was obtained in the same area.

The calculated result indicates that σ_1 (SHmax) is sub-parallel to the strike planes of the unmineralised joints and σ_3 (Shmin) is sub-perpendicular to the strike planes of the unmineralised joints with σ_1 (23/010) trending to the NNE. From the direction of the maximum principal stress axis σ_1 (23/010) and the strike of these unmineralised joints, two sets of conjugate fractures could be highlighted. The first group corresponds to all unmineralised joints striking SSE-NNW and is related to a dextral strike-slip system, and the second group corresponds with all unmineralised joints showing E-W striking and are related to the sinistral strike-slip system.

4.2.2.2 Extensive stress regime

Three of the stress tensors obtained from the unmineralised joints belong to the extensive stress regime (pure and oblique). In Tshifufiamashi, the stress tensor obtained from the unmineralised joints indicates SE-NW extension, striking ESE-WNW and SSE-NNW. On the other hand, in both Tshifufia and Kinsevere Hill, they strike SW-NE and SE-NW, and SE-NW, respectively.

The calculated results indicate that σ_1 (SHmax) and σ_3 are sub-perpendicular to the strike planes of the joints in Tshifufiamashi and Kinsevere Hill with σ_1 swinging from NW in the Kinsevere area to NE in the Tshifufiamashi area. In addition, σ_1 (SHmax) is sub-perpendicular to the strike of the planes joints in Tshifufia, with σ_1 sub-parallel to the strike planes of the joints planes and trending to the SE.

4.3 Faulting analysis

The data in Table 19 and Appendix 2 show that four out of the seven stress tensors belong to a compressive regime (pure and radial compressional), two belong to a strike-slip regime (pure and compressional) and one to an extensive regime (oblique extensive).

4.3.1 Compressive stress regime

The tensors that illustrate compression-dominated regimes are indicated throughout the entire Kinsevere area. Two major compressional directions are obtained: SW-NE in both the Tshifufiamashi and Kinsevere Hill fragments and SE-NW in the Tshifufia fragment (Figs.54, 88 and 114).

The calculated results for the major compressive direction in Tshifufiamashi and Kinsevere Hill indicate that σ_1 (SHmax) is generally sub-perpendicular to the strike of fault planes and σ_3 (Shmin) is mostly sub-parallel to the fault planes in all the stress tensors. These stresses belong to a major compressional regime (pure compressional) with σ_1 plunging gently to the NE or the SW in Tshifufiamashi and Kinsevere Hill. These stress tensors are responsible for the conjugate reverse faults that strike in the SE-NW direction and dip SW-NE at both Tshifufiamashi and Kinsevere Hill. These fault planes suggest two generations of faulting in Tshifufiamashi and Kinsevere Hill. These stress tensors show the friction angle (ϕ) equalling 49.65° in Tshifufiamashi and 50.62° in Kinsevere Hill (Tables 8-17). According to Byerlee (1978) criteria, the discrimination of fault domains is based on the value of the friction angle ($\phi < 16.7°$= no faulting domain; $16.7° \leq \phi \geq 40.4°$ = reactivation domain; $\phi \geq 40.4°$= newly formed fault domain). On account of their high values of ϕ, the SE-NW striking conjugate reverse faults observed in both Tshifufiamashi and Kinsevere Hill area are likely to have been newly formed (i.e. not reactivated earlier faults), and the NE-SW directed stress suggests that they are most likely to have formed during the Kolwezian event (D_1).

In the Tshifufia area, a major direction of compressional stress tensors showing SE-NW compression was obtained. The calculated results of these stress tensors also indicated that σ_1 (SHmax) is sub-perpendicular to the strike of the fault plane and σ_3 (Shmin) is sub-parallel to the fault planes with σ_1 plunging to the NW. These stress tensors are responsible for the WSW-ENE oriented conjugate reverse faults dipping to the SSE and NNW that are observed in the area. Slickenside surfaces have two generations of striations. One generation indicates a South-Eastwards dip-slip movement and the other indicates sinistral strike-slip movement along the WSW-ENE fault plane. These slickensided faults are characterised by a friction angle (ϕ) of less than 40.4° (36.65°). The SE-NW compressional direction of this tensor coincides with the SE-NW oriented compressive stress tensor induced under the strike-slip regime that produced mineralised joints (Fig. 110) which formed during the Monwezian event (D_2) and is perpendicular to the SW-NE compressive stress tensor derived from the other fragments. SW-NE compression is likely to be responsible for the formation of the mineralised joints that formed during the folding phase of the Kolwezian event (D_1). Combining these observations with the Byerlee (1978) criteria on discrimination of the

faulting domains, these SE-NW conjugate reverse faults observed in the Tshifufia area were possibly formed during the Kolwezian (D_1) Pan-African tectonic inversion and then reactivated and rotated in a clockwise direction during the major strike-slip event characterizing the Monwezian event (D_2). The latter event induced the second generation of fault-slip on these fault planes. The clockwise rotation is related to the two parallel sinistral strike-slip faults that separate the fragments in the Kinsevere area.

4.3.2 Strike-slip stress regime

The tensors that show strike-slip-dominated regimes (pure and compressional strike-slip) are shown in the entire Kinsevere area (Figs.57-91-117). The pure strike-slip regime indicates SW-NE oriented compression with SE-NW oriented extension and the compressional strike-slip shows SW-NE oriented compression with SE-NW oriented extension.

The calculated results of the compressional stress tensor indicates that σ_1 (SHmax) is sub-parallel to the strike of the fault planes and σ_3 (Shmin) is sub-perpendicular to the strike of the fault planes. In addition, σ_2 is perpendicular to the σ_1-σ_3 plane and sub-perpendicular to the strike of the fault planes with σ_1 plunging to SW in the Tshifufiamashi and to NE in Tshifufia. This stress tensor is responsible for the conjugated S-N dextral and E-W sinistral faults in the Tshifufiamashi and WSW-ENE reverse faults in the Tshifufia fragments. This stress tensor gives a friction angle (ϕ) equal to 40.12, which indicates that these faults were also reactivated during the Monwezian event (D_2). The calculated results of the pure strike-slip regime show σ_1 (SHmax) and σ_3 (Shmin) as sub-horizontal and horizontal; σ_2 sub-vertical with σ_1 plunging to SE and σ_3 trending to the NE with no plunge. This stress tensor is responsible for the SE-NW oriented dextral strike-slip faults that show a friction angle (ϕ) equal to 58.99°. The friction angle value indicates that these dextral strike-slip faults were formed during the late Monwezian event (D_2), which was characterised by the major strike-slip displacement.

The SW-NE compressional direction obtained from the stress tensor's calculated results in Tshifufiamashi and Tshifufia coincides with the compressional direction of the strike-slip tensor of the stress tensor obtained from the mineralised joint in the Tshifufia fragment. It is noted that reverse faults were formed in association with the mineralised joints that are, in turn, related to the NE-vergent folds observed in the area. These reverse faults were subsequently reactivated as the tensor evolved from compressional strike-slip to a pure strike-slip stress regime. This also induced new SE-NW sinistral strike-slip faults and may explain the difference in orientation of σ_1 and σ_2 stress axes that were present during the Monwezian (D_2) event.

4.3.3 Extensional stress regime

One stress tensor shows an extension-dominated regime (oblique extensive) which, was obtained in the Tshifufia area. The calculated results of this stress tensor indicate that σ_1 (SHmax) is sub-vertical and plunging steeply NW, while σ_3 (Shmin) is sub-horizontal and

plunging gently to the SSE. This stress tensor is responsible for the conjugate normal faults which strike SW-NE and dip SE or NW in the Tshifufia fragment. It has been noted that normal faults cross-cut the mineralised joints and are often associated with breccias (Fig.73). These normal faults show a friction angle (ϕ) of 41.71°. The SSE-NNW orientation of the extensional stress tensor obtained from these normal faults is sub-parallel to the orientation of the extensional stress tensor obtained from the unmineralised joints in the same area (Figs. 85 and 95). The value of the friction angle (ϕ=41.71°: non-reactivated) indicates that both the unmineralised joints and the normal faults observed in the entire Kinsevere area were induced during a late event which could be related to the early stage of the opening of the East African Rift System (EARS) that occurred during the Permian-Triassic period.

4.4 Thrusting analysis

In the Kinsevere area, thrust-and-fault systems were observed in the walls of the Tshifufiamashi and Tshifufia open pits.

In the Tshifufiamashi area a NE-SW cross-section (Fig. 71) shows an upright limb of the Mines Subgroup (R2) which is affected by tight/isoclinal folding and thrust fault deformation, which verge towards the NE. In the western part of Tshifufiamashi, a 10-14m wide zone of heterogeneous breccia separates the upright limb of the Mines Subgroup (R2) from the RAT footwall. The contact between the overlying heterogeneous breccia and the CMN is sheared. Two groups of these thrust faults may be highlighted: the first group comprises bedding-parallel heterogeneous breccias while the second group comprises cross-cutting heterogeneous breccia. The stereographic projection of the fold axial planes collected from these tight/isoclinals (small-scale) folds in Tshifufiamashi indicates a NE vergence of the early folding event and is confirmed here by the NE trending fault-slips which act on the SE-NW reverse faults that were observed in the Tshifufiamashi region.

In the Tshifufia fragment, the E-W cross section (Figure 105) reveals an overturned limb of Mines Subgroup (R2) that sits on top of the RAT group by 50cm (Fig. 38) wide heterogeneous breccias, which may indicate a shear contact between these two Roan Subgroups. The thrust system comprises two groups of faults. The first group has a vergence that is parallel to the trend of the vergence of the isoclinal folds (SE), which was observed in the Tshifufia southern wall. The SE vergence derived from NW dipping fold axial planes seen in the tight/isoclinal folds affecting the CMN strata indicates that these brittle-ductile structural features were induced during the same tectonic event as the thrust faulting (D_1).

4.5 Partial conclusions.

As mentioned above, the interpreted results indicate that the structural relationships between different brittle-ductile features, as observed in the study area, reveal two major stages of folding that are associated with faulting. These two fold stages have been superimposed and have similarly oriented fold axial planes (with subsequently imposed ~90° variation in azimuth), which are probably attributable to a progressive folding and thrusting

event that is associated with the NE-directed emplacement of the Kinsevere copper deposit during the Lufilian orogeny.

The presence of SW dipping axial planes (for Tshifufiamashi and Kinsevere Hill) or locally NW dipping axial planes (Tshifufia) leads to an interesting geometrical problem, in view of the fact that these beds are overturned in the Tshifufia fragment. A simple model involving NE-vergent (or SE-vergent after clockwise rotation) fold-thrust sequence would not account for overturned rocks with the younging direction towards the West in the Tshifufia area (Fig. 124).

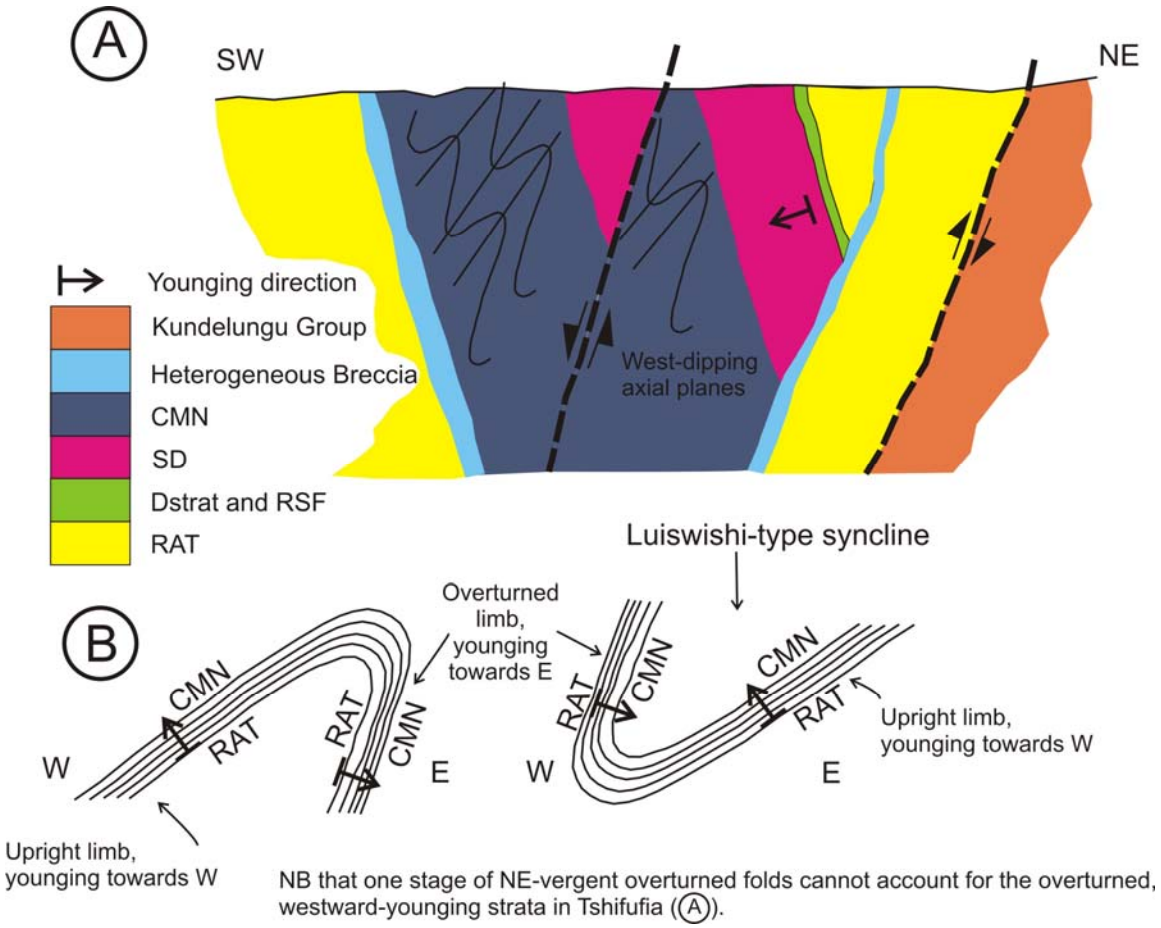

Figure 124: Simplistic overturned folding (B) (generation of NE-vergent fold) cannot account for the overturned, westward-younging strata observed in Tshifufia (A)

The outcrop and fold geometry therefore implies that the strata were overturned before being incorporated into the present fold system (Fig. 125). It is therefore possible that an early folding event (F_{1ab}), with SW-dipping tight to isoclinal folding was refolded (F_{1c} folding) by similarly NE-vergent folds later in the Lufilian orogenic event, to form the presently measured overturned limb in Tshifufia. Areas such as Luiswishi Mine to the SW of Kinsevere show only evidence for F_{1b} folding, where a NE-vergent syncline has an upright NE limb and an overturned SW limb. The general NE-vergence of the Lufilian Arc in this area seems at odds with the SE-vergence recorded at Tshifufia, and can best be explained by

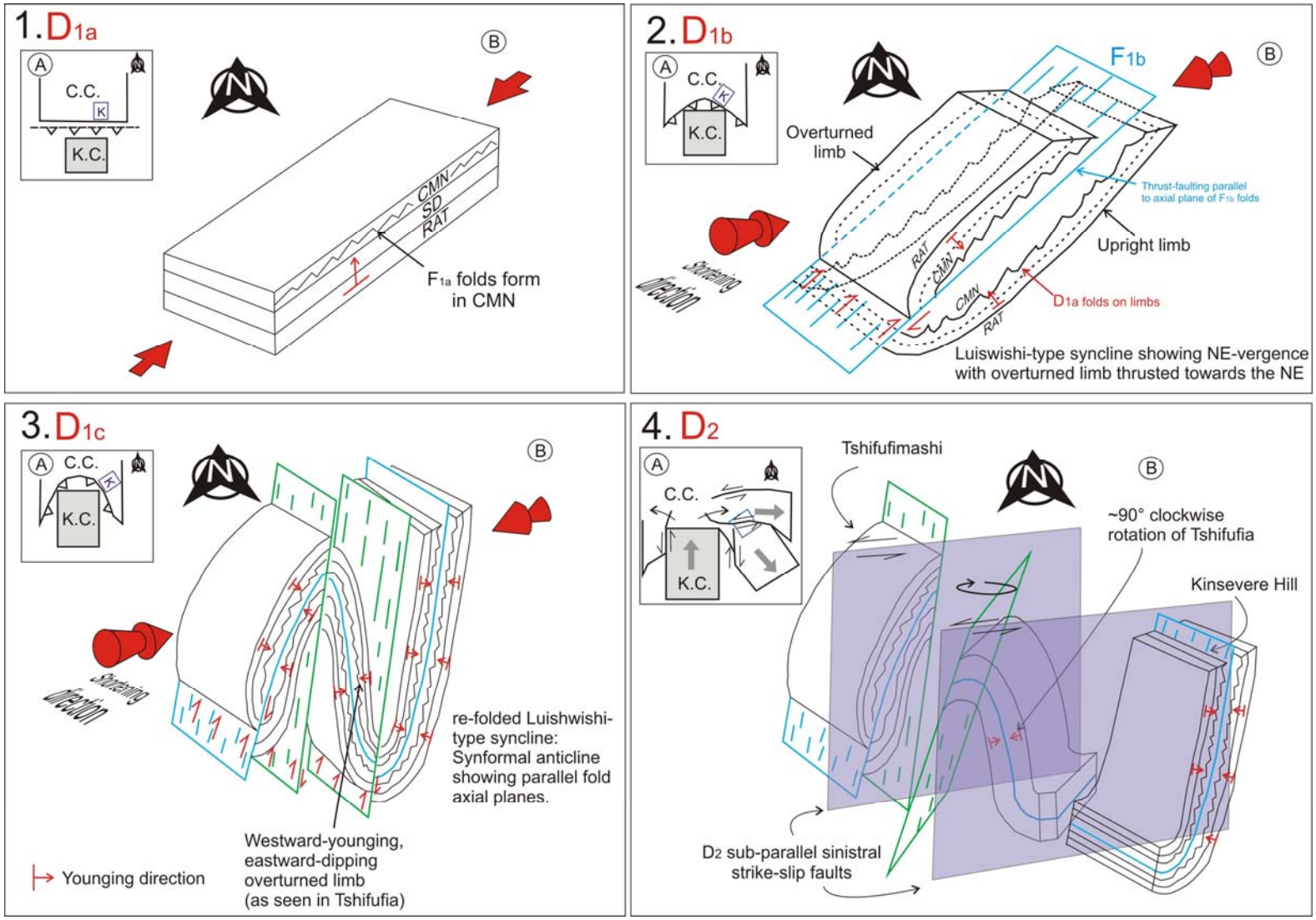

Figure 125: 3D model illustrating the history of the structural deformation in the Kinsevere area (B). (A) Indentor model of the tectonic deformation developed (modified after Kampunzu and Cailteux, 1999). K.C: Kalahari craton, C.C: Congo craton, K: Kinsevere. Blue plane: fold axial plane 1b, Green plane: fold axial plane 1c; Grey plane: strike-slip fault plane.

clockwise rotation during sinistral strike-slip faulting (see section 3.3.2). $F_{1a,}$ F_{1b} and F_{1c} are all considered to be parts of the same NE-vergent F_1 event, even though refolding of earlier folds has taken place. The systematic vergence suggests that they have all formed at different times as a result of ongoing SW to NE shortening (D_1). This F_1/D_1 event most likely formed during the Kolwezian event which is generally regarded as the regional D_1 event across the entire Lufilian Arc (François, 1973; Unrug, 1983; Kampunzu and Cailteux, 1999). The early F_{1ab} folding and late stage F_{1c} folding events may tie in with the two separate generations of arc development that can be discerned from the map (Fig. 126).

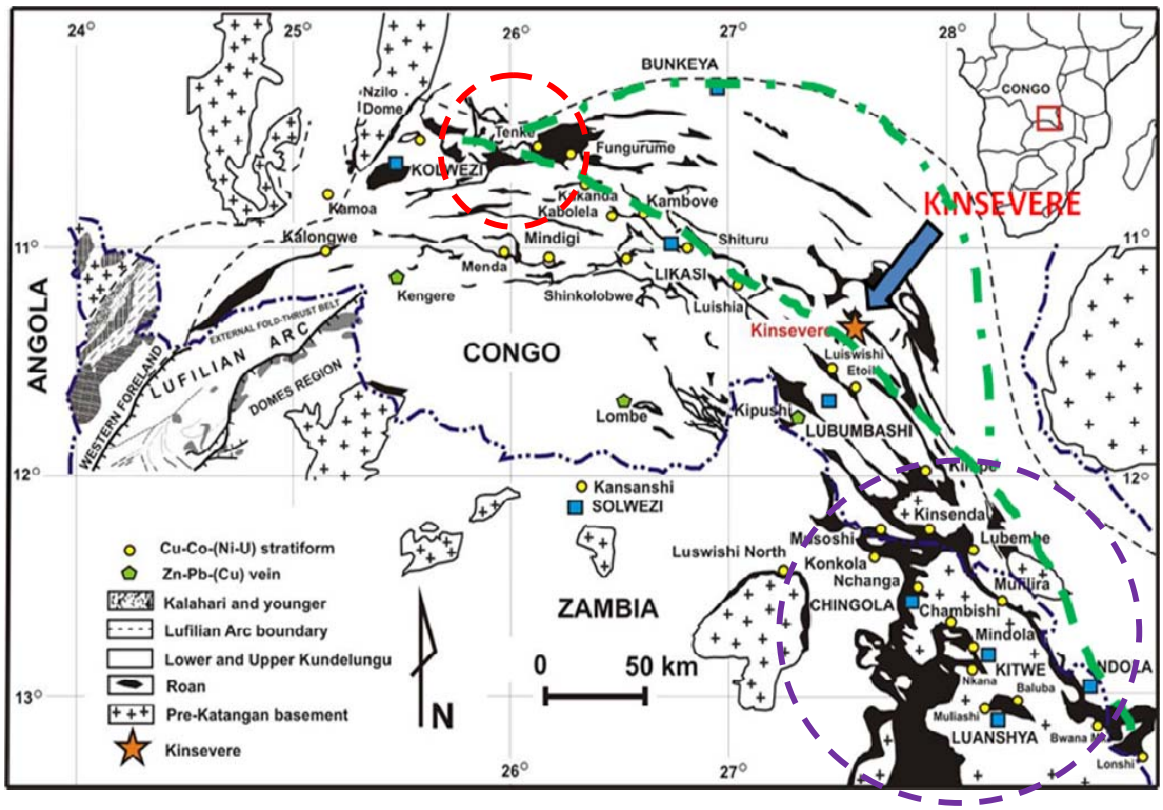

Figure 126: Sharp-related subdivision of the Lufilian Arc generated two arcs, a large arc situated in the southwest and a small arc developed to the NE. These arcs are separated by the tectonic lineament along which the Kinsevere Copper deposit is situated. Tenke F. Fungurume area (circled in red) and Domes region (circled in purple) (modified after Cailteux *et al.*, 1994; Broughton and Rogers, 2010).

Looking more closely at the shape of the Lufilian Arc, it appears that two arcs have been generated. A main arc is situated across the entire Katangan Supergroup, whereas a smaller, earlier-formed arc is situated only to the N-E (Fig. 126). Both arcs may be separated by a tectonic lineament from the dome region to the Tenke-Fungurume area. If the early-formed (NE) arc was later affected by development of the main arc, the earlier-formed arc would undergo some clockwise rotation and areas close to the lineation separating the two stages of arc development might reasonably be expected to show evidence of both stages of arc

development, so that early-formed folds would become refolded during main arc development. The Kinsevere area is located exactly along this lineament and has been interpreted to show two stages of similarly NE-vergent folding. It should also be noted that Unrug (1983), and Kampunzu and Cailteux (1999), show clockwise rotation of eastern parts of the Lufilian Arc (and clockwise rotation of western parts of the Lufilian Arc) and SE-wards tectonic escape by sinistral strike-slip faulting in the eastern arc, during progressive phases of indentation of the Kalahari craton into the Congo craton. On the basis of this model, it would be reasonable to assume that some regional clockwise rotation of early-formed structures has occurred, together with some local clockwise rotation between adjacent, parallel, sinistral strike-slip faults.

When analysing the fracturing in the study area, the interpretation above (section 4.2) shows that mineralised joints can be interpreted as having been induced during the early phase of the Lufilian orogeny, mainly characterised by the compressional stress tensors, and subsequently rotated in a clockwise direction during a strike-slip event.

The earliest mineralised joints observed in the Kinsevere area correspond to an early compressive regime and are interpreted as synorogenic fracturing belonging to the Kolwezian event (D_1). It is noted that there is a coincidence between the stress tensors obtained from the mineralised joints and the stresses derived from the Kinsevere regional folds. It is seems that the joints were opened during the compressive system of the Lufilian orogeny that led to the folding occurring during the Kolwezian phase (D_1) as mentioned by François (1973, 1974), Unrug (1983, 1988) and Kampunzu and Cailteux (1999). These compressive open fractures acted as pathways for the mineralising fluid and deposited copper-cobalt mineralisation within.

In the Tshifufiamashi and the Kinsevere Hill fragments, the stress tensors belonging to the Kolwezian event (D_1) are characterised mainly by SW-NE compression with σ_1 (SHmax) varying from SSW to SW. Although in the Tshifufia fragment, the Kolwezian phase (D_1) shows SSE-NNW compression with σ_1 varying between S and SSE. Based on the analysis of the stress ratio (R) calculated from the reduced stress tensors of the mineralised joints in the Kinsevere area, it is noted that the calculated magnitude is relatively high in the Tshifufia fragment with the stress ratio (R) relatively low (R=0.35) in the Tshifufiamashi and Kinsevere Hill areas. This high magnitude calculated from the stress tensor in Tshifufia might explain the high fracturing zone obviously accompanied by breccias in this fragment. The comparison between the trends of the compression regimes as obtained in the Kinsevere area indicated a clockwise rotation from South-West to South-East with a reduced stress tensor induced under a high magnitude SHmax in Tshifufia and lower magnitude in both Tshifufiamashi and Kinsevere Hill.

The stress tensor belonging to the strike-slip regime, as observed in the Tshifufia fragment, has been rotated in a clockwise direction under a strike-slip to extensive environment which post-

dated the major folding event (major structure) of the Lufilian Arc and which could be related to the major strike-slip movement during the Monwezian event (D_2).

Dewaele *et al.,* (2006), El Desouky *et al.,* (2009), Haest and Muchez (2011) interpreted two types of Cu and Co sulphides in the Lufilian Arc, of which the second type related to the vein types that were induced during the Lufilian orogeny. In the Kinsevere area, mineralised joints related to the strike-slip stress regime consist mainly of copper-cobalt enrichment and are interpreted as post-dating both the folding event and the early and synorogenic fracturing accompanying the folding. These mineralised joints are interpreted here as having been induced first during the compressional regime and then mineralised later during the Monwezian event (D_2). Unrug (1997) and Delvaux *et al.,* (2010) mention that a tectonic inversion period characterised by compressive system corresponds to the intraplate deformation related to the Pan-African orogeny located to the South of the African continent during the Triassic period. This inversion is not entirely governed by the intraplate deformation but also in part by the movement of the Kalahari craton (Bumby and Guiraud, 2005). Based on the findings of Cailteux *et al.,* (2005) and El Desouky *et al.,* (2009), Kampunzu *et al.,* (2009) concluded that all the secondary enrichment mineralisation took place during the D_2 (Monwezian) strike-slip regime. Although the mineralised joints observed in the Kinsevere area are here interpreted as having opened-up during a compressional regime, the subsequent mineralisation is thought to relate to the strike-slip system.

The mineralised joints observed in the Kinsevere area constitute a tectonic response to the Kolwezian compression (D_1). These joints would have opened up following the trends of the minimum principal stress axis σ_3 (Shmin) and were mineralised by the enrichment resulting from the advent of the mineralising fluids during the Monwezian strike-slip event (D_2). These conclusions are based on the fact that mineralised joints show the similar clockwise rotation of the calculated stress tensors as that obtained from the mineralised joints formed under both the compression and strike-slip regimes.

However, the unmineralised joints observed in the Kinsevere area show two strike directions; N-S extension in the Tshifufia area and SW-NE (SSW-NNE) at both Tshifufiamashi and Kinsevere Hill. These joints were most likely opened up after mineralisation as a tectonic response to the East African Rifting extension during the Permian to Triassic period. Delvaux *et al.,* (1992) mention two main directions of extension in the East African Rifting System, ENE-WSW and NW-SE. The ENE-WSW extension obtained in the East African Rifting System would be responsible for the ESE-WSW compressive stress tensor and consequently responsible for the development of the late and unmineralised joints induced under S-N (SSE-NNE) extensive stress tensor, as obtained in the Tshifufia and Kinsevere Hill area. The SW-NE extensive stress tensor

obtained from the unmineralised joints observed in the Tshifufiamashi area can be accounted for by the NW-SE extension in the East African Rift.

Therefore, unmineralised joints observed in the Kinsevere area were formed during a late extensive event that could be related to the early stage of the opening of the East African Rifting System, as is the case of several fragments in the Katangan basin (Delvaux *et al.,* 2010).

Thus, the tectonic model presented in this study suggests that the brittle–ductile features, as observed and analysed above, were induced during the following three phases:

(1) The initial phase, which is mainly characterised by compressional stress tensors that correspond to the Kolwezian phase (D_1). The three stages of the folding observed and interpreted in the study area belong to this initial phase. These two stages as interpreted might come from two superimposed compression regimes producing a faulted synformal anticline affected later by two sinistral strike-slip faults producing a clockwise rotation locally in the Tshifufia fragment. So the faulted synformal anticline shows a parallel fold axis oriented SE-NW in the Tshifufiamashi and Kinsevere Hill fragments.

(2) The intermediate phase, which is characterised by strike-slip stress tensors that correspond to the Monwezian phase (D_2). The D_2 reactivated a certain number of D_1 faults and rotated in a clockwise direction all brittle-ductile features in the Tshifufia fragment, lying between the two parallel D_2 sinistral strike-slip faults, producing a clockwise rotation in the entire South-Eastern part of the Lufilian Arc.

(3) Finally the D_3 is characterised mainly by extensional stress tensors which could be related to the early stage of the opening of the EARS phase (D_3). The unmineralised joints and most of the normal faults which cross-cut all the fragments in the Kinsevere area are related to this late event.

4.6 Discussions

The tectonic evolution of the Lufilian Arc is, to date, still the subject of controversy. In particular, the precise origin of the breccias within the Roan that are somehow related to deformation is still debated, with theories ranging from a sedimentary olistostrome origin (Binda and Porada, 1995; Wendorff, 2000, 2003, 2005b) to a tectonic friction breccia origin (François, 1973; Cailteux *et al.,* 1994; Cailteux and Kampunzu, 1995; Kampunzu and Cailteux, 1999). More recently, it has also been suggested that the breccias represent former evaporitic horizons (Jackson *et al.,* 2003; Selley *et al.,* 2005).

The sedimentary model which interpreted the breccia as foreland sedimentary deposits, and the intervening coherent strata as olistoliths (Wendorff, 2000, 2003, 2005) has been questioned

by several authors working within the Katangan basin (Cailteux *et al.,* 2005; Selley *et al.,* 2005; Batumike *et al.,* 2007).

The model proposing the fault-and-thrust friction related origin involves the shortening of the Katangan basin, locally producing SW-NE oriented regional compression which is related to the convergence of the Kalahari and Congo cratons, with displacement vectors radiating perpendicularly to the arcuate trend of the fold belt (Demesmaeker, 1963; François, 1973; 1987; Unrug, 1983; Daly, 1986; Cailteux and Kampunzu, 1995; Kampunzu and Cailteux, 1999). In this model, the breccia is inferred to have formed in fault zones situated below the extensive thrust sheets and the brecciation has been formed through a process including friction-related fragmentation and fluid over-pressuring below relatively impermeable evaporitic horizons.

The more recent salt tectonic model developed by Jackson *et al.,* (2003) and Selley *et al.,* (2005) re-interprets the fault-and-thrust friction breccias model. This model combines two concepts: the first one is the salt extrusion which occurred during the early stage of the extension related to the deposition of the Katangan sediments; the second is the fold-and-thrust friction-related origin that involves the shortening of the Katangan basin. Evaporitic strata were recorded within the Katangan basin which shows a transition to restricted marine or lacustrine environments of deposition. Within this model, the salt diapirs are related to an early stage of the shortening of the Katangan basin that occurred along evaporitic strata situated in the lower part of the Roan Group (RAT) where the sole of the thrust is located (Cailteux *et al.,* 1994; Kampunzu and Cailteux, 1999; Jackson *et al.,* 2003; Selley *et al.,* 2005). The evaporitic horizon facilitated the overpressuring of the fluid beneath the thrust sheets, diapirism, and extrusion of salt glaciers. In the Zambian Copperbelt, the evaporitic horizons are located in the equivalent lithostratigraphical unit of the RAT Subgroup, which is situated between the Mutonda and the Musoshi Subgroups. Jackson *et al.,* (2003) state that the thrust and the brecciated horizons within the RAT Subgroup and Mines Subgroups contain an enormously thick unit comprising weak minerals such as evoparites, which have been overpressured and created a breccia after the dissolution of these evaporitic layers.

In the model presented by Kampunzu and Cailteux (1999), the evaporitic horizons have similarly played an important role in the movement of the thrust sheets during the Kolwezian phase (D_1). They attributed the hydrofractures to the friction generated by the thrusting of sheets combined with the overpressuring of the fluid due to the compression. However, the hydrofractures are mainly infilled by calcite and, often, dolomite veins. As hydrofractures are thought to have facilitated the thrusting movement, are present in levels where evaporitic minerals (textures) have been observed and are often associated with brecciated zones, these hydrofractures would be related to the dissolution of the salt diapir during an early stage of the shortening as suggested by Jackson *et al.,* (2003) and Selley *et al.,* (2005).

In the Kinsevere area, the confusing spatial relationships between the fragments might be related to salt diapirism that occurred during an early extension stage. Other researchers (François, 1973; François, 1987; Cailteux and Kampunzu, 1995; Kampunzu and Cailteux, 1999) envisage these confusing spatial relationships between fragments as being linked to the formation of a fold and thrust belt. For example, at the base of the Tshifufia fragment, in the western wall of the open pit, the downwards-facing R2 Mines Subgroup strata positioned in the overturned limb of an F_1 fold are juxtaposed with upwards-facing RAT strata along a heterogeneous breccia (Figs.71 and 105), while the normal upwards-facing Mines Subgroup is missing. In the Tshifufiamashi in the western part of the open pit, a similar situation is noted; the upwards R2 Mines Subgroup strata positioned in the upright limb of the F_1 fold are juxtaposed with downwards-facing RAT strata, also along a contact marked by heterogeneous breccia, and the downwards overturned limb R2 Mines Subgroup of the F_1 fold is missing. The geometry and overprinting relationships of early fold generations (F_{1ab} and F_{1c}) are entirely consistent with stacking and imbrications associated with progressive NNE to NE-vergent thrust emplacement. These shear zones which act as boundaries to the fragments in the Kinsevere area could have been originally listric normal faults, with locally low-angle geometries developed within and at the base of Mines and RAT Subgroups along the weaker strata that were dissolved and are inferred to be the vanished evaporites (Jackson *et al.,* 2003). In one section of the Tshifufia pit, ramp-flat geometry related to thrusting can be interpreted from SD strata, as a hanging-wall cut off against the fault plane. Such geometry would generally be expected to occur on sub-horizontal fault surfaces, though in Tshifufia, subsequent thrusting and asymmetric folding have rotated the fault to a sub-vertical orientation (Fig. 104). Thrust faults such as these could have been reactivated as normal faults that initially developed during the early extension and which were inverted during the thrusting related to the main compression of the Kolwezian phase (D_1). The actual structural architecture as observed within the Kinsevere area cannot be easily explained by the process of footwall-collapse and foreland propagation of thrusts that produces a simple thrust belt.

For a better understanding, it is necessary to turn to the basic concept of the regional tectonic setting in comparison with the depositional environment of the lower Roan, and to those of salt tectonics.

The tectonic setting of the Lufilian fold and thrust belt has been divided into four distinct North-convex tectonic zones (Selley *et al.,* 2005) which are, from North to South: the External Fold and Thrust belt, the Domes Regions, the Synclinorial Belt and the Katangan High. The northern External Fold and Thrust Belt reveals extensional features which are similar to those in the study area (Fig. 127). The field, petrographic and fluid inclusion studies undertaken within the Roan Group show that both RAT and Mines Subgroup sediments have been deposited in a confined evaporitic environment (Pirmolin, 1970; Bartholomé *et al.,* 1973; Katekesha, 1975;

Cailteux, 1978 a and b, 1983, 1994; Audeoud, 1982; Cluzel, 1985, 1986, Okitaudji, 1989, Guilloux, 1992; Cailteux *et al.,* 1994; Tshiauka *et al.,* 1995).

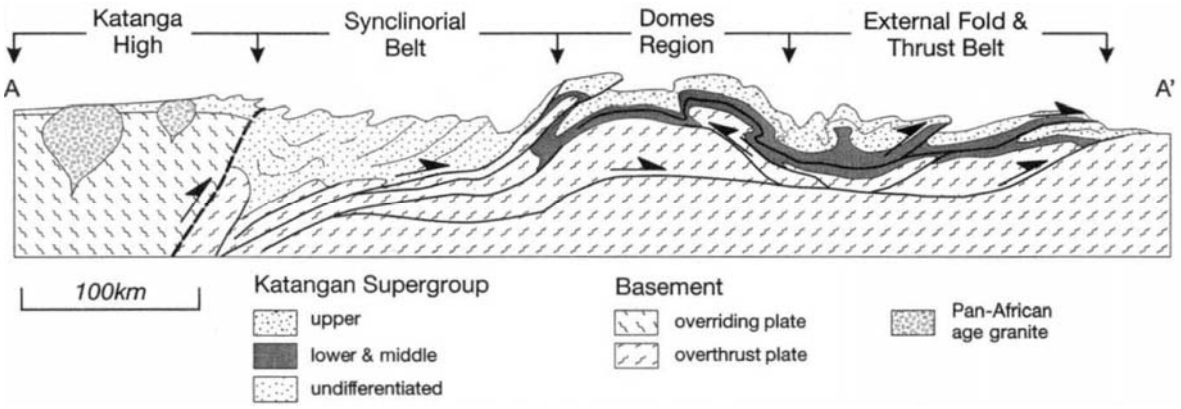

Figure 127: Tectonic setting and structural architecture of the Lufilian fold belt, S (A)-N (A') schematic cross-section of the central part of the Lufilian fold belt, highlighting the variation in structural style between tectonic zones (modified from Porada, 1989; Selley *et al.,* 2005)

Jackson *et al.,* (2003) and Selley *et al.,* (2005) interpret a pre-existing salt diapir phase as being related to the evaporitic strata deposited in marine to lacustrine environments. Several studies conducted in both types of the Roan strata indicate that the evaporitic sequence was characterised by the halite salt phase and an associated anhydrite phase (Cailteux *et al.,* 1994; Tshiauka *et al.,* 1995; McGowan *et al.,* 2006; El Desouky *et al.,* 2010). In the Kinsevere area, evaporitic horizons were observed within the RAT Subgroup and the CMN (Kambove dolomites-Mines Subgroup) rocks and brecciated zones are thought to be related to these evaporitic horizons.

However, several structure types are related to salt tectonic development, which are active, passive and reactive salt structures, and the salt detached fault system (Vendeville and Jackson, 1992; McGeary and Plummer, 1994; Giles and Lawton, 1999; Bahroudi and Koyi, 2003; Stewart, 2007). Among these salt-related structures, the active-passive, and related salt structures are formed when there are evaporitic salt layers beneath clastic sedimentary units. These structures will develop when a tectonic environment becomes increasingly active. Active tectonics could be extensional or compressional (thrust). In the case of extensional tectonics, faulting will both reduce the strength of the overburden and thin it, while in an area affected by thrust (compressional) tectonics, buckling of the overburden layer will allow the salt to rise into the cores of anticlines (Vendeville and Jackson, 1992). The reactive salt structures will be related to the extensional tectonics and the active salt structures to the compressional tectonics (Fig. 128).

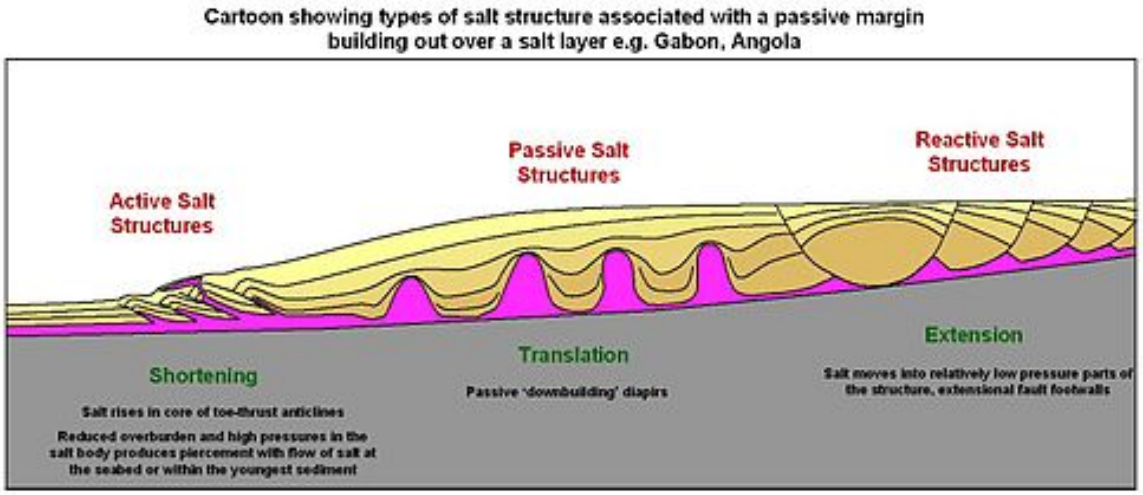

Figure 128: Cartoon showing type of salt structure associated with passive margin building out over a salt layer (Vendeville and Jackson, 1992)

The early extension event within the Neoproterozoic as presented by Selley *et al.,* (2005) is related to the existence of a thick salt stratum beneath the Roan sediments deposited within a rifting extensional type basin. With the thickening of the layers of sediments above the salt strata, the pressure in salt-bearing layers would increase and to push up the overlying layers as a salt diapir. Because the deposition of the Katangan sediments is occurring in an extensional context, the reactive salt structures will be formed before the dissolution of the salt bearing layers. Jackson *et al.,* (2003) mentioned that the evaporitic mineral contained within these salt bearing layers is mostly halite (NaCl). As mentioned by Jackson *et al.,* (2003), since the Katangan basin was submitted to a high magnitude of pressure due to the convergence of the Kalahari and Congo cratons, associated with the dissolution of the salt-bearing layers, the Lufilian belt became sequentially shortened to half of its initial width, which accounts for such well-developed folding and thrusting, even though the salt has now largely dissolved (Fig. 129). Thus, areas where salt has been dissolved are subject to collapse and are now represented by brecciated zones within the strata and act as weak planes which are likely to be exploited as thrust faults during any subsequent shortening.

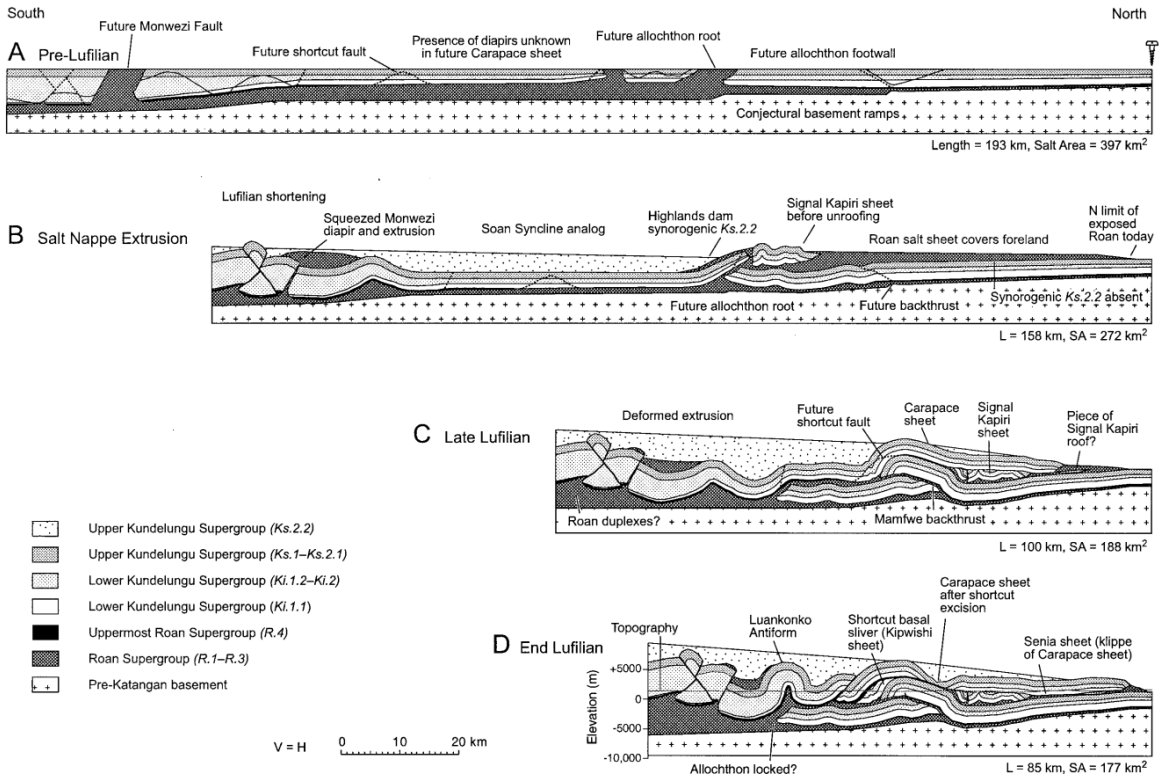

Figure 129: Restoration of the regional section of the western part of the Lufilian fold belt using GeoSec2D restoration software. Bedding lengths were maintained by flexural slip during unfolding. The cross-sectional area of Roan evaporite-gigabreccia, which is highly speculative, was decreased forward through time to allow dissolution of evaporites. The restoration omits progressive erosion during deformation. No vertical exaggeration (Jackson *et al.*, 2003)

However, Kampunzu and Cailteux (1999) suggested that the breccias are related to the interaction between the evaporitic layers and the deformation without indicating what kind of deformation. Also, they have noted that the low-strength evaporitic layers contributed to the zones of decollement during the Kolwezian phase (D_1). François (1987; 1993) concluded that the existence of the breccias related to the evaporitic horizons within the Katangan basin might indicate that the Monwezi strike-slip fault represents a diapir-induced structure.

The analysis of faulting within the Kinsevere area concludes the observation of a reactivation of the D_1 faults during the Monwezian strike-slip faulting (D_2). These faults are characterised by two generations of fault-slips, which are correlated to the conjugated S-N dextral and E-W sinistral strike-slip faults. Kampunzu and Cailteux (1999) note that striations and slickensides occurring in several open pits and underground mines are obscured by the discordant breccias along faults. If slickensides and striations (slickensided faults) are obscured by breccias, this means that these breccias were induced during an early stage preceding the reactivation phase, which belongs to the Monwezian event.

Consequently, the early extensional stage with which salt diapirism is associated is closely linked to the existence of the evaporitic horizons within the Katangan basin. This might be an option that can explain the mechanism of development of the brecciated zones that are considered to be the precursor of any future movement (faulting and/or thrusting) during the compressional phase of the Lufilian orogeny (Jackson *et al.,* 2003).

Concerning the analysis of the palaeostress tensors obtained from different brittle deformational zones, such as mineralised joints, unmineralised joints and faults, in the Kinsevere area, the results within the present study corroborate different conclusions of previous studies undertaken in the Lufilian Arc. The results obtained make a contribution towards a better understanding of the previous models.

The palaeostress obtained from the mineralised joints in the Kinsevere area shows that the mineralised joints are related to the compressional, strike-slip and extensional stress regimes. The mineralised joints belonging to the compressional stress regime are interpreted here as synorogenic fractures related to the major F_1 folding phase, while the mineralised joints, belonging to the strike-slip and extensional stress regimes, are interpreted as a product of enrichment from the leaching of the diagenetic mineralisation that was deposited in the fractures opening up during the strike-slip and extensional period. These mineralisations are considered here to be post-orogenic.

Several hypotheses have been proposed on the origin of the copper and cobalt mineralisation in the Lufilian Arc since the discovery of the Cu-Co deposits in the Democratic Republic of Congo and in Zambia. The various theories on the origin of mineralisation range from the diagenetic to the epigenetic model passing through the magmatic, hydrothermal and syngenetic models. In the present analysis, the mineralisation to which the palaeostress study refers is related to the fracturing.

The stress tensor calculated from the mineralised joints belonging to the early Kolwezian phase (D_1) indicated SW (SSW)-NE (NNE) oriented compression in the Tshifufiamashi and Kinsevere Hill regions and rotated in a clockwise direction to SSE-NNW oriented compression in the Tshifufia region. Based on this stress tensor, the synorogenic model of the copper mineralisation that is related to the fracturing induced during the major F_1 and F_2 folding events supports the recent epigenetic model of the copper mineralisation proposed by McGowan (2003). The epigenetic model involves migrating copper-rich basinal brines or metamorphic fluids being introduced into the Roan during the Lufilian orogeny. The mineralised joints belonging to the intermediate Monwezian (D_2) phase were induced under mostly strike-slip related stress tensors that indicate respectively a SE-NW oriented compression and SW-NE oriented extension in the Tshifufiamashi and Kinsevere Hill regions and show an anti-clock wise rotation in the Tshifufia region which indicates a SW-NE oriented compression and SE-NE

extension. The conjugate mineralised joints belonging to this stress tensor regime were opened up during the strike-slip event and provided the pathway for the mineralizing fluids coming from the dissolution of the metal brines in the pre-existing diagenetic copper mineralisation. The migration direction of the mineralizing fluid is indicated by the trend of σ_2 which is trending SE-NW in the Tshifufiamashi and Kinsevere Hill region and is trending SW-NE in the Tshifufia region. Thus, the palaeostress obtained from the mineralised joints observed in the entire Kinsevere area support the multiphase model of copper and cobalt mineralisation as mentioned by Dewaele *et al.,* (2006). This multiphase model comprises mineralisation that ranges from the diagenetic to the epigenetic style. It is also noted that the epigenetic style of mineralisation is considered to be additional to the syngenetic and early diagenetic process which controlled most of the Neoproterozoic Copperbelt in Central Africa, as mentioned by Cailteux *et al.,* (2005).

In addition to the palaeostress tensor obtained from the mineralised joints, the majority of the palaeostress tensors taken from the other brittle deformational zones observed in the Kinsevere area indicate a clockwise rotation with the maximum principal stress axis from the SE to the SW. The trends of the clockwise rotation obtained from the calculated stress tensors from the Kinsevere area coincide with the trends inferred by Unrug (1983) on the deflection of the shearing obtained by Moore (1967) on the Muva quartzites which gave a rotation from SE to SW. Unrug (1983) noted a differential crustal shortening that is indicated by the evidence of a difference in the thrusting magnitude which occurs within the Katangan basin. In the western part of the Lufilian arc (Kolwezi area), the crustal shortening consists of the sum of the folding and the overthrusting of nappes which amounted to less than its initial length (François, 1974; Jackson *et al.,* 2003). In the eastern part of the Lufilian arc (SE of ZCB), Unrug (1983) did not see any evidence of the overthrusting of nappes similar to that observed in the Kolwezi area. He concluded that a clockwise rotation in the Katangan basin, which is related to this differential crustal shortening, occurred during the Lufilian orogeny.

Kampunzu and Cailteux (1999) re-interpreted the combined aeromagnetic and geological maps of the Lufilian Arc compiled by Gecamines. They noted a clockwise rotation that was indicated by the dismembered deep-seated magnetic throw (DSMT) observed within the entire Lufilian Arc. This deep-seated magnetic throw shows a SSE-NNW trend in the western region (Luankoko and Kitongwe), a SSW-NNE trend in the central region (Kela) and SE-NW trend in the eastern region (Lupoto). These DSMT markers are respectively affected by the Monwezi, Kansuki and Lupoto strike-slip faults. They are linked to the sinistral strike-slip movement occurring in the Lufilian basin during the Monwezi strike-slip time (D_2). In the Kinsevere area, this clockwise rotation is supported by the trend of the fold axes and other palaeostress tensors that were obtained from both fracturing and faulting features observed in the Tshifufia fragment. The latter is situated between two sinistral strike-slip faults which separated all the R2 Mines

Subgroup's fragments in the study area. However, all palaeostresses rotate in a clockwise direction locally in accordance with the Tshifufia fragment. Kampunzu and Cailteux (1999) reached the conclusion that the strike-slip faulting which is related to the clockwise rotation could explain the present-day NW-SE trend of the D_1 structures in the eastern part of the Lufilian Arc, approximately from Kakanda in Congo to Mufulira and Ndola in Zambia. They also explained the existence of the Congolese Roan type observed in Mufulira by this clockwise rotation (Fig. 130). The present study provides a kinematic argument for the clockwise rotation, which was previously observed in the Lufilian Arc. This rotation is mainly supported by the palaeostress tensors belonging to the strike-slip system that is also related to the superimposed folding events (F_1 and F_2) observed within the Kinsevere area.

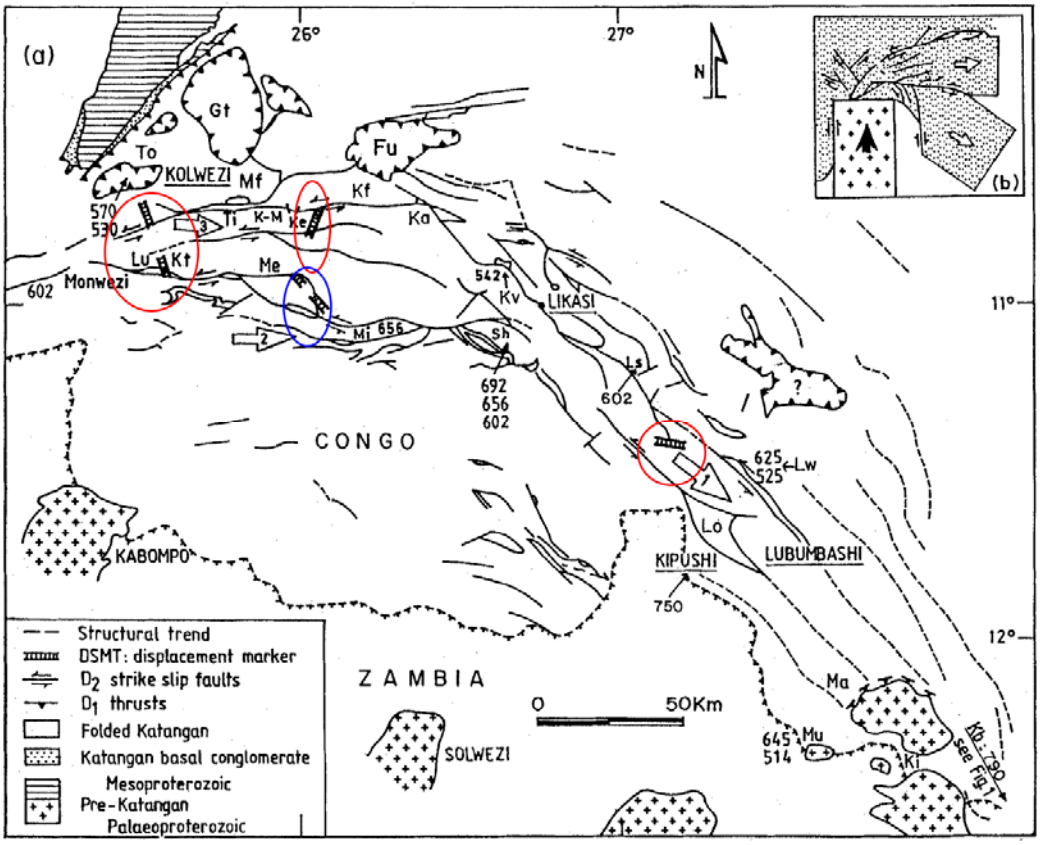

Figure 130: (a) Map showing the importance of strike-slip faults in the evolution of the Lufilian fold belt. DSMT: "Deep-seated magnetic throw" marker; Mu: Musoshi, Ki: Kinsenda, Ma: Mabaya, Mf: Mwanfwe, Lo: Lupoto, Ls: Luishia, Lw: Luiswishi, Sh: Shinkolobwe, Me: Menda, Mi: Mindingi; Ka: Kakanda, Kv: Kambove, Ke: Kela, Kf: Kinsanfu fault zone, Kt: Kitongwe, Ti: Tilwezembe, K-M: Kalumbe-Myunga, Lu: Luankoko, To: Tombolo Kilppe, Gt: Gule-Tondo Klippe, Fu: Fungurume Kilppe and Kb: Kabwe in Zambia. The numbers given are ages dating D2 diachronous movements in Ma, while arrows with numbers represent qualitatively major block motions and numbers refer to succession of extrusion phases. Probable age sequence: arrow 1: ca. 690Ma; arrow 2: ca. 660 Ma and arrow 3: ca.600 Ma; (b); Fault observed in unilaterally confined indentation experiments and related successive extrusions of blocks 1 and 2 (after Peltzer *et al.*, 1982; Kampunzu and Cailteux, 1999).

The palaeostress study conducted in the Kinsevere area contributes to a better understanding of the tectonic model presented above and provides kinematic arguments to certain concepts raised by these models. The observations made on the exploration drill cores and on the open pit outcrops presented in this work provide evidence of evaporitic horizons in the different units of RAT (Grey and Red) and CMN. These evaporitic units are often associated with brecciated zones that are related to the slickensided faults belonging to the Kolwezian phase (D_1). Both hypotheses struggle with the origin of the implementation of the heterogeneous breccias observed in the Roan and on the mechanism of its implementation.

On the question raised regarding the existence of an early extension during the Lufilian orogeny, different structures that might be related to the extensional system were observed and inferred in the Kinsevere area. Are these structures related to the salt diapirism as suggested by Jackson *et al.,* (2003) and Selley *et al.,* (2005)? The present study considers that the salt diapirism that led to the salt extrusion during the early stage of the compressional regime following the tectonic inversion is one of the possibilities. However, different palaeostresses obtained from brittle deformations observed in the Kinsevere area are closely related to the different tectonic phases of the Lufilian orogeny as described by Demesmaeker *et al.,* (1963), François (1973, 1974, 1987), Cailteux *et al.,* (1994) and Kampunzu and Cailteux (1999).

Thus, the actual structural architecture of the Lufilian fold belt may be the product of combining both salt diapirism and thrusting related to the shortening of the Katangan basin resulting from the convergence of the Kalahari and Congo cratons during the Neoproterozoic period.

Chapter 5

CONCLUSIONS

This study was undertaken with the objective of achieving a better understanding of the structural geology of the Kinsevere area by formulating a kinematic model for the formation of the brittle structures observed in the different Mines Subgroup fragments present in the study area. It was also conducted in an effort to understand the stratigraphy of the Mines Subgroup, with emphasis on the contact between the Grey and Red RAT. These elements help to provide a better understanding of the relationship between tectonism and the presence of copper mineralisation observed within fractures in the study area.

The analysis of fold geometry in the Kinsevere area suggests that the geological architecture consists of a thrusted and re-folded syncline with steeply dipping, dismembered limbs. Our study suggests that the Tshifufia fragment represents an east-dipping limb of the synformal anticline, while the Tshifufiamashi and Kinsevere Hill fragments comprise the western limb. Two distinct folding events have been identified. The first folding event (F_1) is related to the early stage of the compressive system (D_1) characterised by small-scale folds with South-West dipping axial planes in the Tshifufiamashi and Kinsevere Hill fragments and by North-West dipping axial planes in the Tshifufia fragment (after the clockwise rotation). These small-scale fold axial planes are parallel to the inferred fold axial plane of the large-scale synformal anticline defined by the three fragments. The second folding event (F_{1b}) is related to the late stage of the compressive system (D_1) and is indicated by the fold axis defined by bedding planes present in the fragments. Based on the orientation of the folding geometry as observed in the Tshifufia fragment, which is situated between the two sinistral strike-slip faults that separated all R2 Mines Subgroups fragments in the Kinsevere area, a clockwise rotation is noted locally during the Monwezian phase (D_2).

The palaeostress tensors obtained from the analysis of brittle structures and slickenside lineations associated with faults in the Kinsevere area suggest that three deformation events occurred. The first event involved SW-NE compression resulting from the convergence of the Kalahari and the Congo cratons during the early Neoproterozoic (D_1). This was followed by the development of a strike-slip fault system between the late Neoproterozoic and early Palaeozoic (D_2). The third deformation event resulted from the development of an extensional system between the Permian and Triassic (D_3).

The kinematic analysis of brittle structures presented in this study indicates that the compressive system of the Kolwezian phase (D_1) involved two sequential deformation events that are characterised by two types of compressive stress tensors. Early pure compressive stress tensors indicate South-West to North-East compression, while subsequent radial oblique

compressive stress tensors indicate South-East to North-West compression associated with South-West to North-East extension:

1. The pure compressive stress tensor corresponds to the early stage of compressional stress responsible for the development of SW dipping folds (F_1) observed in the Kinsevere area. This folding event is associated with the copper-mineralised joints in the Tshifufiamashi region. It is also associated with SW-NE and S-N oriented copper-mineralised joints and reverse faults in the Tshifufia region. These faults are most often associated with the brecciated zones. The palaeostress tensors generated by these joints and faults suggests a dominantly SW-NE oriented compressional regime in the entire Kinsevere area, except in the Tshifufia fragment where the palaeostress tensors obtained from the mineralised joints are parallel to the SE-NW trending fold axes (F_1) due to the D_2 sinistral strike-slip faults between which the Tshifufia fragment is situated.

2. The radial and oblique compressive stress tensors correspond to the late compressive phase. These were only observed in the Tshifufiamashi region which is marked by the development of SE-NW oriented mineralised joints. This late compressive phase coincided with the beginning of the strike-slip system.

The compressional system (D_1) was followed by the development of a strike-slip system that corresponds to the intermediate Monwezian (D_2) phase. It is characterised in the study area by the development of conjugate mineralised joints oriented mainly SW-NE and SE-NW and occasionally E-W and S-N. This fracturing is associated with SE-NW and SW-NE-oriented conjugate strike-slip faults. Some of these strike-slip fault planes display two generations of movement, indicating that the Monwezian is also characterised by a reactivation phase. The palaeostress tensors obtained from brittle D_2 structures indicate that these were induced by a tectonic escape geodynamic system leading to indenter type Orogenic system. This was characterised by the transition from a transpressive system (characterised by a stress ratio (R) tending towards zero) to an extensional system (characterised by a stress ratio (R) tending towards 1). These movements suggest a regional clockwise rotation during this phase of deformation. This clockwise rotation is locally supported by the clockwise direction observed in the Tshifufia fragmentwhich rotated with all the structural features. The clockwise rotation is related to the sinistral strike-slip faults between which the Tshifufia fragment is situated. The kinematic analysis of palaeostress tensors associated with the strike-slip stress regime indicates that the SSE-NNW compression resulted from the deflection of pre-existing structures. This event generated a radial oblique stress tensor during SW-NE oriented compression and was accompanied by SE-NW oriented extension.

The extensional palaeostress tensors observed in the Kinsevere area correspond to the late phase (D_3) of the Lufilian orogeny. This extensional system is characterised by the development

of unmineralised fractures observed throughout the Kinsevere area. These late fractures cross-cut the mineralised joints and are associated with SW-NE and SE-NE oriented normal faults. These faults preserve an internal friction angle (ϕ) greater than 40.4°, indicating that they were induced by a late geodynamic event associated with N-S and SE-NW oriented extension. This late deformation phase (D_3) could be related to the East African Rifting System which developed during the Permian to Triassic periods.

Several different structural models have been evoked to explain the geology of the Central African Copperbelt. This study was focused on two of these hypothesis: (1) a model involving pure compression that occurred in two distinct phases (Demesmaeker *et al.,* 1963; François, 1973; Kampunzu and Cailteux, 1999), and (2) an extension-related salt tectonic model based on salt extrusion during an early stage of deformation within the Katangan basin (prior to basin inversion) (Jackson *et al.,* 2003; Selley *et al.,* 2005). One line of evidence that supports the salt tectonic model is the presence of several evaporitic horizons that were observed in different stratigraphic units of the lower Roan, including the RAT and the Kambove dolomites (CMN). Within the RAT, no tectonic contact was observed between the Grey and Red RAT units. Evaporitic textures preserved in the Grey and Red RAT units are indicative of both distal and proximal depositional environments. These observations suggest that Grey and Red RAT should be regrouped into a single unit and that the Grey RAT probably forms the uppermost part of the RAT Subgroup. Within the Kambove dolomites (CMN) evaporitic textures are mostly pseudomorphic nodules and these were observed within several stratigraphic levels and were also found near brecciated zones. The distribution of these evaporitc nodules is similar within the RAT Subgroup. Thus, the RAT breccias are interpreted as the product of a combination of the dissolution of pre-existing evaporitc layers and thrusting that resulted from compression due to the shortening of the Katangan basin. Furthermore, within the Kinsevere area, there is no evidence for salt extrusion during an early extensional phase within the Katangan basin. Finally, the palaeostresses interpreted from brittle structures in the Kinsevere area correlate well with deformation related to compressive and strike-slip events that occurred after the tectonic inversion of the Katangan basin.

Concerning the relationship between mineralisation and tectonics in the Lufilian Arc, the calculated stress tensors obtained from the mineralised joints suggests that these were induced during a compressive stress regime. This deformation event involved SW-NE compression followed by the development of a sinistral strike-slip regime. These events led to the clockwise rotation showing a SW-NE compression and SE-NW extension in the Tshifufia fragment in comparison to the SE-NW compression and SW-NE extension obtained in both the Tshifufiamashi and Kinsevere Hill fragments. These results differ from previously published interpretations for the Lufilian Arc (Cailteux *et al.,* 2005; El Desouky *et al.,* 2009; Kampunzu *et al.,* 2009; Delvaux *et al.,* 2010). The interpreted trend of the compressive stress regime at

Kinsevere coincides with the general trend of compression observed in most deposits situated in the SE part of the Lufilian Arc. It is also perpendicular to both the axis of the Kinsevere regional fold and to the hinge line of the well-folded CMN strata observed in the western limb of each fragment in the Kinsevere area (Tshifufiamashi, Tshifufia, etc.). Thus, the copper mineralisation occurring within fractures, veins and joints in the Kinsevere area is related to the folding event.

In conclusion, the current structural architecture of the Lufilian Arc might have formed from a combination of two events. The first involved salt extrusion which occurred during an early extensional stage. This was related to the deposition of fine-grained carbonate and evaporitic strata that is evidence of a transition to restricted marine or lacustrine environments as proposed by Jackson *et al.,* (2003) and Selley *et al.,* (2005). The second event was characterised by development of a fold-and-thrust belt resulting from the compression-related shortening of the Katangan basin. This probably occurred subsequent to the tectonic inversion of the basin during the late Neoproterozoic, as proposed by numerous authors (Demesmaeker *et al.,* 1963; François, 1973, 1987; Unrug, 1983; Daly, 1986; Cailteux and Kampunzu, 1995; Kampunzu and Cailteux, 1999; Key *et al.,* 2001).

5.1 Suggestions for further study

In order to better understand the structural evolution of the Lufilian Arc in both the Congolese and the Zambian Copper Belts, additional kinematic analyses should be completed for several copper and cobalt deposits. These deposits should be selected based on their position along three sections oriented SE-NW in the western part of the Lufilian Arc, S-N in the central part of the Lufilian Arc, and SW-NE in the eastern part of the Lufilian Arc.

Additional fluid inclusion studies should be conducted to link the copper and cobalt mineralisation encountered in fractures, veins and joints in the Lufilian arc to the kinematic evolution of the Lufilian Arc.

Acknowledgements

I would like to thank Anvil Mining Limited for allowing me to pursue further post-graduate scholarship in their Kinsevere Copper Deposit; I would like to offer special thanks to Mr. Bill Turner, the former Anvil Mining CEO, for his availability and open-mindedness in regard to my research which have immensely improved my professional understanding and judgment.

To Dr. Adam J. Bumby, my supervisor, I would like to express my gratitude to you for your guidance, constructive criticism, invaluable suggestions and, last but not least, your ever-in-time critical reading of the manuscript. Your constructive criticism has greatly improved the quality of this dissertation. I would also like to express my sincere gratitude to Prof. Roland Merkle for his critical guidance. Thank you.

My sincere gratitude goes to Dr. Damien Delvaux (MURAC-Tervuren, Belgium) for his advice, and especially for allowing me to use the WinTensor program to process all field data; Dr. Jacques Cailteux, David Broughton, Dr Houda Bouamar, Roger Tyler and Steffen Kalbpskof for their critical review of my manuscript and guidance during my studying and working period.

My special thanks goes to Ivanplats SA, especially to David Broughton (Vice President/Exploration, Marna Cloete (Chief Financial Officer), Lex Geraghty (Senior Geologist); to Drs. David Selley and Bull Stuart (University of Tasmania, Australia), Thomas Rogers (African Mining Consulting-Managing Director), David Edwards, Serge Kayembe, Mike Kirschbaum, Kasongo Kimba's family and Sarah Linnevelt for being available and standing ready to help whenever I needed help. My special thanks also go to Lucien Shimuna, the African Minerals draughtsman, for helping me to draw all cross-sections needed in this dissertation.

To my lovely wife Mary-Thaous Banza and my children Maria Banza, Stuart Banza and Divine Banza, if this turns out to be an achievement, it is for you. I thank you for your support and appreciate your sacrifices.

To my Parents Alexandre Kazadi Kilongo and Suzanne Nyembo wa Ngoie. I thank you for having taught us the value related to education, self-control and work. Let the Almighty God bless you and remember you during your old age.

Finally, I would like to thank the Almighty God to whom I owe all.

Pretoria, February 2012

KAZADI BANZA Samuel-Barry

REFERENCES

ADERCA, M.B., (1950). Contribution à la connaissance géologique des gisements stannifères Kibariennes et leurs métallogénie. *CSK*, *50è ann, Congres Scientifique, . Elisabethville* 1950, Vol II, tome II, pp. 377-400.

ANDERSON, E.M., (1942). *The dynamic of faulting and dyke formation with applications to Britain.* Edingburgh: Olivier & Boyd. , p.206.

ANGELIER, J., MECHLER, P., (1977). Sur une méthode graphique de recherche des contraintes principales également utilisable en tectonique et en séismologie : la méthode des dièdres droits. *Bulletin de la société géologique de France* 7(19),n°6, p 1309-1318.

ANGELIER, J., (1977). La reconstruction dynamique et géométrique de la tectonique des failles a partir des mesures locales (plan de faille, stries, sens de jeu, rejets) ; quelques précisions. *Compte-Rendus de l'Académie des Sciences de Paris, Série D, tome 285*,p 637-640.

ANGELIER, J., (1989). From orientation to magnitudes in palaeostress determinations using fault slip data. *Journal of Structural Geology 11*, 37-50.

ANGELIER, J., (1991). Inversion directe de recherche 4-D: comparaison physique et mathématique de deux méthodes de détermination des tenseurs des paléo- contraintes en tectonique de failles. *Compte- Rendus de l'Académie des Sciences de Paris* 312, II, 1213-1218.

ANGELIER, J., (1994). Fault-slip analysis and palaeostress reconstruction. In: P.L. Hancock (ed.) *Continental Deformation*, Pergamon, Oxford, p.101-120.

ANVIL EXPLORATION, (2008). Internal report made by Houda Bouamar, Exploration department, October 2008. unpublished.

AUDEOUD, D., (1982). Les minéralisations uranifères et leur environnement à Kamoto, Kambove et Shinkolobwe (Shaba-Zaïre). Pétrographie, Géochimie et inclusions fluides. Thèse de 3eème cycle, Centre de Recherches sur la Géologie de l'Uranium (Nancy, France) and University Claude-Bernard (Lyon, France), p.211.

BAHROUDI, H. and H. A. KOYI, H.A., (2003). Effect of spatial distribution of Hormuz salt on deformation style in the Zagros fold and thrust belt: an analogue modelling approach. *Journal of the Geological Society,* 160, 719-733

BARRA, F., BROUGHTON, D., RUIZ, J., and HITZMAN, M., (2004). Multi-stage mineralisation in the Zambian Copperbelt based on Re-Os isotope constraints (abs): *Geological Society of America.* Abstracts with Program, vol. 36, p.6-7.

BARTHOLOME, P., EVRARD, P., KATEKESHA, F., LOPEZ-RUIZ, J., and NGONGO, M., (1973). Diagenetic ores-forming process at Kamoto, Katanga, Republic of Congo in Amstutz, G.C., and Bernard, A.J. (eds), *Ore in sediments*: New York, Springer-Verlag, p.21-41.

BARTHOLOME, P., (1974). On the diagenetic formation of ores in sedimentary beds, with special reference to Kamoto, Shaba, Zaire. *Centenaire de la Société Géologique de Belgique. Gisements stratiformes et provinces cuprifères*. Liège, 203–213.

BATEMAN, A.M., (1930). Ores of the northern Rhodesian Copperbelt: *Economic Geology*, v.25, p.365-418.

BATUMIKE, MJ. KAMPUNZU, A.B. and CAILTEUX, J.L.H., (2006). Petrology and Geochemistry of the Neoproterozoic Nguba and Kundelungu Groups, Katangan Supergroup, southeast Congo : Implication for provenance, paleoweathering and geotectonic setting : *Journal of African Earth Sciences* 44, 97-115.

BATUMIKE, MJ., CAILTEUX, J.L.H. and KAMPUNZU,A.B., (2007). Lithostratigraphy, basin development, base metal deposits and regional correlations of the Neoproterozoic Nguba and Kundelungu rock succession; Central African Copper Belt: *Gondwana Research* 11, 432-447.

BEACH, A., (1980). Numerical models of hydraulic fracturing and interpretation of syntectonic veins. *Journal of Structural Geology*., 2: 425-438

BELLIERE, J., (1966). Le métamorphisme blastomylinitique: source possible de jus pegmatitique migrant. *Annales de la societe geologique de Belgique,* tome 90 (1966-67); pp. B185-B199.

BELLIERE, J., (1969). Polymétamorphisme et superposition de tectoniques dans le massif calcareux de Kikosa (Katanga, Congo), *Annales de la Société Géologique de Belgique* 92, (1969). pp. 78-88

BINDA, P.L. and PORADA, H., (1995). Observations on the Katangan Breccias of Zambia; Royal Museum of Central Africa-Belgium, *Annales de la Société Géologique de Belgique*, vol. 101; p. 49-62

BOTT, M.H.P., (1959). The mechanisms of oblique slip faulting. *Geological. Magazine*. 96, 109-117.

BRACE, WF., PAILDING, BW., and SCHLOTZ C., (1966). Dilatancy in the fracture of cristalline rock. *Journal of Geophysical Research*, 71: p.3939-3953

BROCK, B.B., (1961). The structural setting of the Copperbelt. In Mendelsohn,F. (Ed.), *The Geology of the Northern Rhodesian Copperbelt*. Macdonald, London, 81-89.

BROUGHTON, D. and ROGERS, T., (2010) Discovery of the Kamoa Copper Deposit, Central African Copperbelt, Democratic Republic of Congo: *Society of Economic Geologists*, Special Publications, 15, p. 287-297.

BROUGHTON, D., HITZMAN, M., SELLEY, D., SCOTT, R., BULL, S., LARGE, R. McGOLDRICK, P., CROACKER, M. and POLLINGTON, N. (2007). Geology and ore deposits of the Zambian copperbelt; in Andrew, C.J. *et al.,* eds., Digging Deeper - *Proceedings of the 9th Biennial SGA Meeting* : Irish Association for Economic Geology, Dublin, pp. 203-207.

BUFFARD, R., (1988). Un rift intracontinental du précambrien supérieur: le Shaba méridional (Zaïre). Evolution sédimentaire et tectonique du super- groupe de Roan au groupe de Kundelungu inférieur (Supergroupe de Kundelungu). Thèse de doctorat, Faculté des Sciences, Université de Maire. France, 316 pp.(Unpublished)

BULL. S., and SELLEY, D., (2005). A sequence stratigraphic interpretation of the Congolese Copperbelt. In AMIRA, P872 progress report, *Sediment-hosted copper deposits of Congolese, Zambian and Central Australian basin systems*, (unpublished), December, 2005.

BUMBY, A.J and GUIRAUD, R., (2005). The Geodynamic setting of the Phanerozoic basin of Africa. *Journal of African Earth Sciences 43*, 1-12.

BYERLEE, J., (1978). Friction of rocks. *Pure and Applied Geophysics*, 116: 615-626.

CAHEN, L., (1954). Résultats géochronologiques obtenus sur des minéraux du Congo jusqu'en Mai 1954, *Bulletin de la société géologique de Belgique* Vol 77, p. B268-B281.

CAHEN, L., (1970). Etat État actuel de la géochronologie du Katanguien. *Annales des Sciences Géologiques, Musée Royal de l'Afrique Central, Tervuren, Belgium. Serie in 8°,* 45 pp. 7-14

CAHEN, L., PASTEELS, P., LEDENT D., BOURGUILLOT R., VAN WANBEKE L., EBERHARDT P., (1961). Recherche sur l'âge absolu des minéralisations uranifères du Katanga et de Rhodéesie du Nord. *Annales des Sciences Géologiques Musée, Royal de l'Afrique Central*, Tervuren, Belgium, Serie in 8°, 41 pp. 1-54

CAHEN, L, DELHAL, J.and DEUTSCH S., (1967). Rubidium-strontium geochronology of some granitic rocks from the Kibaran belt (Central Katanga, Rep. of the Congo). *Annales des Sciences Géologiques, Musée Royal de l'Afrique Centrale*, Tervuren, Belgium. Série in 8°, 59, 65 pp.

CAHEN, L. DELHAL, J, LEDENT D, PASTEELS, P.,(1970). Isotopic data relative to the age and petrogenesis of dome forming granites in the Copperbelt of Zambia and SE Katanga. *Annales des Sciences Géologiques, Musée Royal de l'Afrique Central*, Tervuren, Belgium.Série In 8°, 65 pp. 69-97

CAHEN, L., LEDENT D., FRANÇOIS, A., (1971). Sur l'âge des granites de Kambove Ouest et de Kamoto principal et révision des connaissances relatives aux minéralisations uranifères du Katanga et du Copperbelt de Zambie. In *Annales de la Société Géologique de Belgique*, 94 (3) ; pp. 185-198

CAHEN, L., SNELLING, N.J., DELHAL, J., VAIL, J.R., BONHOMME, M. & LEDENT, D., (1984). *The geochronology and evolution of Africa*, Clarendon Press Oxford, 512 pp.

CAILTEUX, J., (1973). Minerais Minérais cuprifères et roches encaissantes à Musoshi, Province du Shaba, République du Zaïre. *Annales de la Société Géologique de la Belgique*, 96 p. 495-521.

CAILTEUX, J., (1977a). Particularité stratigraphique et pétrographique du faisceau inférieur du groupe des Mines au centre de l'arc cuprifère Shabien. In *Annales de la Société Géologique de la Belgique*, 100, pp. 55-71

CAILTEUX, J., (1977b). La succession stratigraphique du CMN (ou R-2.3) au centre de la sous-province cuprifère Shabienne. In *Annales de la Société Géologique de la Belgique*, 100, 73-85

CAILTEUX, J., (1978). Description d'une nouvelle roche de type diorite dans la brèche de Kolwezi. Unpublished Company Report, oc. Rapport Gécamines, Rapport Annuel 832 pp.

CAILTEUX, J., (1983). Le Roan Shabien dans la région de Kambove (Shaba-Zaïre) : Étude sédimentologique et métallogenique. Thèse de Doctorat. Facultes des Sciences Appliquées. Université de Liège (Belgique) 232 pp. (Unpublished)

CAILTEUX, J., (1991). La tectonique intra-Katanguienne dans la partie Nord-Ouest de l'Arc Lufilien (Shaba, Rep. du Zaïre). In *Annales de la Société Géologique de Belgique* . T.113 (fascicule 2). 1990. pp 199-215.

CAILTEUX, J., (1994). Lithostratigraphy of the Neoproterozoic Shaba-type (Zaire) Roan Super group and metallogensis of associated stratiform mineralisation; *Journal of African Earth Sciences*, 19, 4, pp. 279-301

CAILTEUX, J., BINDA, P., KATEKESHA, WM., KAMPUNZU, A.B., INTIOMALE, M.M.,; KAPENDA, D., KAUNDA, C., NGONGO, K., TSHIAUKA, T. and Wendorff, M; (1994). Lithostratigraphical correlation of the Neoprotrozoic Roan Supergroup from Shaba (Zaire) and Zambia in the Central African Copper-Cobalt metallogenic province; in *Journal of African Earth Sciences*. 194 pp. 265-278

CAILTEUX, J. and KAMPUNZU AB, (1995). The Katangan tectonic breccias in the Shaba Province (Zaire) and their genetic significance;. In Wendorff, M and Tack, L (eds.) *Late Proterozoic Belt in central and Southern Africa*; Annales des Sciences Géologiques, Musée Royal de l'Afrique Central, Tervuren, Belgium, 101 : pp. 49-62.

CAILTEUX, J.L.H., KAPUTO, A.K., and KAMPUNZU, A.,B., (2003). Structure, lithostratigraphy and Cu-Co mineralisations of the Mines Subgroup at Luiswishi; Central Africa Copper Belt; in Cailteux, J., ed., *Proterozoic Sediment-hosted Base Metal Deposits of Western Gondwana*, Lubumbashi, D. R. Congo, July 14–24, 2003: Episodes 27, No. 3, p. 209-213.

CAILTEUX, J., KAMPUNZU, A.B., LEROUGE, C., KAPUTO, A.K., and MILESI, J.P., (2005). Genesis of sediment-hosted stratiform copper-cobalt deposits, Central African Copperbelt. *Journal of African Earth Sciences,* 42, pp. 134-158.

CLUZEL, D., (1985). Géologie et métallogénie de la "Série des mines" au Shaba (ex-Katanga) méridional (Zaïre), Méta évaporites et reprises hydrothermales : *Comptes Rendus de l'Académie des Sciences de Paris*, série II, vol.301, pp.1209-1212.

CLUZEL, D., (1986). Contribution à l'étude du métamorphisme des gisements cupro-cobaltifères stratiformes du Sud-Shaba, Zaïre. Le district minier de Luishia, *Journal of African Earth Sciences* 5, 6, pp. 557-574

CONDIE, K.C., (2002). The supercontinent cycle; are there two patterns of cyclicity? *Journal of African Earth Sciences* 35, 179-183.

COSI, M., De BONIS, A., GOSSO, G., HUNZIKER, J., MARTINOTTI, G., MORATTO, S., ROBERT, J.P., RUHLMAN, F., (1992). Late Proterozoic thrust tectonics, high-pressure metamorphism and uranium mineralisation in the Domes area, Lufilian Arc, Northwestern Zambia. *Precambrian Research* 58, 215-240.

COWARD, MP. and DALY, MC (1984). Crustal lineaments and shear zones in Africa: their relationship to plate movements. *Precambrian Research* 24, pp 27-45.

DALY, M.C., (1986). Crustal shear zones and thrust belts: their geometry and continuity in Central Africa. Philosophical Transaction. *Royal Society of London* A 317, 111-128.

DAVIDSON, D.M., (1931). The geology and ore deposits of Chambishi, Northern Rhodesia: *Economic Geology* 26, p. 131-152.

DEJONGHE, L., (1995). The copper deposit of Kinsenda (SE Shaba, Zaıre): astrata-bound mineralisation hosted in siliciclastic formations of the Roan (Upper Proterozoic). In: Wendorff, M., Tack, L. (Eds.), *Late Proterozoic Belts in Central Africa*. Musée Royal de l'Afrique Centrale, Tervuren, Belgique, *Annales des Sciences Géologiques* 101, 87–94.

DEJONGHE, L., and NGOYI, K., (1995). Le gisement de Kinsenda (Sud-est du Zaire): une concentration cuprifère stratoide dans les formations détritiques du Roan (Protérozoïque Supérieur). *Chronique de la recherche minière*, 521 : 19-37.

DELVAUX, D., LEVI, K., KAJARA, R. and SAROTA, J., (1992). Cenozoic palaeostress and kinematic evolution of the Rukwa-North Malawi rift valley (East African rift system)-*Bulletin du Centre de Recherches et Exploration des produits Elf Aquitaine*, 16, 2, 383-406.

DELVAUX, D., MOEYS, R., STAPEL, G., PETIT, C., LEVI, K., MIROSHNICHENKO, A., RUZHICH, V., SANKOV, V., (1997). Palaeostress reconstructions and geodynamics of the Baikal region, Central Asia. . Part II: Cenozoic rifting. In: Cloetingh, S., Fernandez, M., Munoz, J.A., Sassi, W., and Horvath, F. (Editors), *Structural controls on sedimentary basin formation. Tectonophysics* 282: 1-38.

DELVAUX, D., SPERNER, B., (2003). Stress tensor inversion from fault kinematic indicators and focal mechanism data: the TENSOR program. In: *New Insights into Structural Interpretation and Modelling* (D. Nieuwland Ed.). Géologique Society, London, Spécial Publications 212, 75-100.

DELVAUX, D., (2010). WinTensor user guide: Optimisation functions, July 2010 (unpublished).

DELVAUX, D., KIPATA, L., SEBAGENZI, S., CAILTEUX, J.L.H. and SINTUBIN, M., (2010). Mineralisation et contexte structural au Katanga (RDC). Dans le secteur minier de la RDC à la croisée des chemins ; colloque international « *la quête des ressources en Afrique central-2* ». Tervuren (Belgique), Déc. 2010.

DEMESMAEKER G, FRANÇOIS A., et OOSTERBOSCH, R (1963). La tectonique des gisements cuprifères stratiformes du Katanga. In : J. lombard and P. Nicolini (eds), *Gisements stratiformes de cuivre en Afrique* ; 2ème partie ; Tectonique ; Lusaka 1962. *Assemblée des services géologiques d'Afrique*, Paris, 47-115

DE MAGNEE, I., and FRANÇOIS, A., (1988). The origin of the Kipushi (Cu, Zn, Pb) deposit in direct relation with a Proterozoic salt diapir, Copperbelt of Central Africa, Shaba, Republic of Zaire, in FRIEDRICH, G.H., *et al.,* eds., *Base metal sulfide deposits*: Berlin, Springer-Verlag, p.74-93.

DERRICKS, .J.J., and VAES, J.F., (1956). Le gîte d'uranium de Shinkolobwe : Etat actuel des connaissances du point de vue géologique et metallogenique. Actes de la conférence internationale sur l'utilisation de l'énergie atomique à des fins pacifiques. Genève VI, *Géologie de l'uranium et du thorium,* 108-144

DERRICKS, J.J., and OOSTERBOSCH, R. (1958). Les gîtes de Swambo et de Kalongwe comparé à Shikonlobwe: contribution à l'étude de l'uranium du Katanga-Deuxième conférence Internationale sur l'utilisation de l'énergie atomique à des fins pacifiques. II. Nations Unies, Genève,p 623-695

DEWAELE, S., MUCHEZ, Ph., VETS., J., FERNANDEZ-ALONZO, M., TACK, L. (2006). Multiphase origin of the Cu-Co ore deposits in the western part of the Lufilian fold-and-thrust belt, Katanga (Democratic Republic of Congo): *Journal of African Earth Sciences* 46, 455-469.

DRYSDALL, A.R., JOHNSON, R.L., MOORE, T.A. and THIEME, J.C. (1972). Outline of the geology of Zambia. Géologie en Mijinbouw, v.51, p.265-276.

Du ROUCHET, J., (1981). Stress fields, a key to oil migration. AAPG Bulletin 65 (1), p. 74 -85.

DUPIN, J.M., SASSI, W. and ANGELIER, J. (1993). Homogeneous stress hypothesis and actual fault-slip: a distinct element analysis. *Journal of structural Geology*, 15, 1033-1043.

DURNEY, D.W. and RAMSAY, J.G (1973). Incremental strains measured by syntectonic crystal growths. In: *Gravity and tectonic*, édité par K.A Dejong et R. Scholtz, J Willy, New York, pp. 67-96

EL DESOUKY, H., HAEST, M., MUCHEZ, PH. DEWAELE, S. CAILTEUX, JLH and HEIJLEN, W., (2007). Fluid evolution in the Katangan Copperbelt, DRC. In Andrew, C.J., *et al.,* eds., Digging Deeper: *Proceeding of the 9th Biennial SGA Meeting:* Irish Association for Economic Geology, Dublin, p 213-216.

EL DESOUKY, H., MUCHEZ, PH., and CAILTEUX, J.L.H., (2009) Two Cu-Co sulfide phases and contrasting fluid systems in the Katangan Copperbelt, Democratic Republic of Congo. *Ore geology reviews* 36: 315-332.

EL DESOUKY, H., MUCHEZ, PH. BOYLE, AJ, SCHENEIDER, J., CAILTEUX, J.L.H., DEWAELE, S., VON QUADT, A. (2010). Genesis of sediment-hosted stratiform copper-cobalt mineralisation at Luiswishi and Kamoto, Katanga Copperbelt (DRC). *Mineralium Deposita*, DOI: 10.1007/s00126-010-0298-3.

ELLIOT, D., (1976). The energy balance and deformation mechanisms of thrust sheets. Philosophical Transanctions Royal. *Society of London* n° A 283, pp 289-312

ENGELDER, J.T., (1974). Microscopic wear grouvers on slickensides: Indicators of paleosismicity. *Journal of Geophysical Research,* USA, 79, pp. 4387-4392

FLEISCHER, V.D., GARLICK, W.G., and HALDANE, R., (1976), Geology of the Zambian Copperbelt, in Wolf, K.H., ed., *Handbook of strata-bound and stratiform ore deposits*: v.6, p.223-352.

FLETCHER, A., HOFFMANN A.W., (1974). Simple models of diffusion and combined diffusion-infiltration metasomatism. In: Hofmann AW, Gilleti VJ, Yoder HS Tr eds *Géochemical transport and Kinematics* carnegie Institution of Washington Publication, n° 634 pp. 246-262

FORDE A., and BELL TH., (1994). Late Structural Control of mesothermal Vein-hosted gold deposits in central Victoria, Australia: Mineralisation mechanisms and exploration potential. *Ore Geology Reviews*, 9: 33-59

FRANÇOIS, A., (1973). *L'extrémité occidentale de l'arc cuprifère shabien*. Etude géologique, Gécamines, Likasi (Shaba-Zaïre), 65 p.

FRANÇOIS, A., (1974). Stratigraphie, tectonique et minéralisation dans l'arc cuprifère du Shaba (Rep. Du Zaïre) In ; P. Bartholomé (éd) *Gisements stratiformes et provinces cuprifères*. Centenaire de la société géologique de Belgique. Liège, 79-101.

FRANÇOIS A., (1987). Synthèse géologique sur l'Arc cuprifère du Shaba (Rép. Du Zaire). Centenaire de la société géologique de Belgique, pp.15-65.

FRANÇOIS A., (1994). La structure tectonique du Katanguien dans la région de Kolwezi (Shaba, République du Zaïre) : *Annales de la Société Géologique de Belgique*, v.116, p.87-104.

FRANÇOIS, A., (1995). Problèmes relatifs au Katanguien du Shaba. Musée Royal de l'Afrique Centrale, Tervuren (Belgique): *Annales des Sciences Géologiques* 101, 1-20.

FRANÇOIS, A. et CAILTEUX, J., (1981). La couverture Katanguienne entre les socles de Nzilo et de Katonto, Rép. Du Zaïre, Région de Kolwezi. *Annales des Sciences Géologiques,* Musée Royal de l'Afrique Central, Tervuren, Belgique, 87, 50p.

FRANK, F.C., and LAWN. B.R., (1967). On the theory of herzian fractures. Proceedings of the Royal Society of London., A 299; 291-306

GARLICK, W.G., and BRUMMER, J.J., (1951). The age of the granites of the Northern Rhodesian Copperbelt: *Economic Geology*, v.46, p.478-498.

GARLICK, W.G., (1961). Structural evolution of the Copperbelt. In F. Mendelson editions, *The geology of the Northern Rhodesian Copper Belt*. Macdonald, London, 89-105

GARLICK, W.G., FLEISCHER, V.D., (1972). Sedimentary environment of Zambian Copper deposition. Geology en Mijinbouw 51, 277-298.

GARTRELL, A.P., LISK, M., (2005). Potential new method for palaeostress estimation by combining three-dimensional fault restoration and fault slip inversion techniques: first test on the Skua field, Timor Sea. In: Boult, P., Kaldi, J. (Eds.), *Evaluating Fault and Cap Rock Seals*. AAPG Hedberg Series, 2, pp. 23-26.

GETTINGS, M.E., (1988). Variation of depth to the brittle-ductile transition dues to cooling of a midcrustal intrusion. *Geophysical Research. Lett*., 153, pp 213-216

GLIES, K. A., and LAWTON, T. F., (1999). Attributes and evolution of an exhumed salt weld, La Popa basin, northeastern Mexico: Geology. v. 27 no. 4 p. 323-326

GOGUEL J., (1977). Le mécanisme des éruptions phréatiques dans l'activité volcanique. C.R *Sommaire de la Société Géologique de France*; 5 : 277-279

GRAY, A., (1932), The Mufulira copper deposit, Northern Rhodesian: *Economic Geology*, v.27, p.315-343.

GROSEMAN, P., (1948). Mine de Luishia, Rapport inédit

GROSEMAN, P., (1949). Etudes Géologiques dans les monts Kibara. Annales des Services des Mines, CSK.

GUILLOUX, L., (1992). Etude chimique des séries porteuses de quelques grands gisements de type Kuperfirschiefer. Conséquence metallogeniques. Thèse d'Etat, Université de Lyon, France. Sciences de la Terre, Nancy, Mémoire, vol. 43, 659p.

GYSIN, M., (1934). Les tillites métamorphiques de la Haute Lufira. (Congo belge). In:*Comptes rendus des séances de la société de physique et d'histoire naturelle de Genève*, 51/3: 210-213

HAEGEMANN, S.G., GROVES, D.I., RIDLEY, J.R., and VERNCOMBE, J.R., (1992). The archean lode gold deposits at Wiluna western Australia; High-level brittle-style mineralisation in a Strike-slip regime. *Economic Geology*, 87: 1022-1053.

HAEST, M., and MUCHEZ, P., (2011). Stratiform and vein-type deposits in the Pan-African orogen in central and southern Africa: Evidence for multiphase mineralisation. *Geologica Belgica* (2011) 14/1-2: 23-44.

HITZMAN M., (2008). The RAT observations and Implications from the Tenke-Fungurume region concerning stratigraphy, Breccias and Hematitic alteration. Power point presentation, International conference AMIRA P.872, Lubumbashi, DRC. October, 2008.

HOBBS, B.E., (1995). Principals involved in mobilization and remobilization ore deposit reviews, 2: 37-45

HOEPPNER, R., (1955). Tektonik im Schiefergebirge. Geol. Rdsch. 44, 26-58.

HOUDA, B., (2008). Internal geology report, Anvil Mining, Exploration department, October, 2008. Unpublished.

JACKSON, M.P.A., WARIN, O.N., WOAD, G.M., and HUDEC, M.R., (2003). Neoproterozoic allochthonous salt tectonics during the Lufilian orogeny in the Katangan Copperbelt, central Africa: *Geological Society of America Bulletin,* v.115, p 314-330.

JAEGER, J.C., (1969). *Elasticity, Fracture and Flow with Engineering and Geological Applications*. 3rd Edition, Meuthuen, London, 268p.

JOHN, T., SCHENK, V., MEZGER, K., and TEMBO, F., (2004). Timing and PT evolution of whiteschist metamorphism in the Lufilian Arc-Zambezi Belt Orogeny (Zambia); implications for the assembly of Gondwana. *Journal of Geology*, 112, 71-90.

KAMPUNZU, A.B., KANIKA, M., KAPENDA, D., TSHIMANGA, K., (1993). Geochemistry and Geotectonic setting of late Proterozoic Katangan basic rocks from Kibambale in Central Shaba (Zaire). *International Journal of Earth Sciences* 82, 619-630.

KAMPUNZU, A.B. and CAILTEUX, J., (1999). Tectonic evolution of the Lufilian Arc (central Africa copperbelt) during Neoproterozoic pan African orogenesis. *Gondwana Research*, 2 401-421

KAMPUNZU, A.B., TEMBO, F., MATHEIS, G., KAPENDA, D., and HUNTSMAN-MAPILA, P., (2000). Geochemistry and tectonic setting of mafic igneous units in the Neoproterozoic Katangan basin Central Africa: Implication of Rodinia break-up: *Gondwana Research*, v.3, p.125-153.

KAMPUNZU, A.B., CAILTEUX, J.L.H., BATUMIKE, J.M., LORIS, N.B.T., (2003). Syn-orogenic sedimentation in the Katangan belt: myth or reality? Multi-proxy constraints. In: Cailteux, J.L.H. (Ed.), *Proterozoic sediment-hosted base metals deposits of Western Gondwana* (IGCP 450), 3rd conference, Abstract. volume. Lubumbashi, Congo, pp. 98–102.

KAMPUNZU, A.B., CAILTEUX, J.L.H., KAMONA, A.F., INTIOMALE, MM. and MELCHER, F., (2009). Sediment-hosted Zn-Pb-Cu deposits in the central African Copperbelt. *Ore Geology Reviews*, 35: 263-297.

KATEKESHA, WM (1975). Conditions de formation du gisement cupro-cobaltifère de Kamoto principal (Shaba-Zaïre) ; Thèse de doctorat, Université de Liège (Belgique) ,237 p (unpublished)

KAZADI, B., S-B., (2004). Etude microtectonique de la brèche de Roan de Luiswishi. Implications cinématiques. Mémoire de fin d'étude. Département de Géologie, Faculté des Sciences, Université de Lubumbashi, 2004, (unpublished).

KENNEDY, WQ. (1964). The structural differentiation of Africa on the Pan-African (±500 m.y.) tectonic episode. University of Leeds, *8th annual report of the Research Institute of the African Geology* 1962/63, 8: 48-49.

KEY, R.M., LIYUNGU, A.K., MOSLEY, P.N., NJAMU, F., BANDA, J., SOMWE, V., (2001). The geology and stream sediment geochemistry of the Mwinilunga sheet. *Memory of the Geological Survey Department of Zambia* 5, 242.

KEY, R.M., LIYUNGU, A.K., NJAMU, F.M., SOMWE, V., BANDA, J., MOSLEY, P.M., ARMSTRONG, R.A., (2002). The western end of the Lufilian arc in NW Zambia and its potential for copper deposits. *Journal of African Earth Sciences* 33, 503-528.

KRONER, A., (1977). Precambrian mobile belts of southern and eastern Africa, ancient sutures or sites of ensialic mobility. A case for crustal evolution towards plate tectonics, *Tectonophysics* 40, 101-135.

LEFBVRE, J.J., (1978). Le groupe de Mwashya megacyclothème terminal du Roan (Shaba, Zaire Sud-Oriental) Approche lithostratigraphique et étude de l'environnent sédimentaire. *Annales de la société géologique de Belgique* 101, 209-225.

LEFEBVRE, J.J., and PATTERSON, L.E (1982). Hydrothermal assembly of aluminum serpentine, florentine and Kyanite in the Zairian Copperbelt. *Annales de la société géologique de Belgique* 105, 55-71.

LORIS, N.B.T.H., (1996). Etude des minéralisations uranifères du gisement cupro-cobaltifère de Luiswishi (Shaba-Zaïre) : Contextes géologiques et géochimiques. Discussion des modèles génétiques. Thèse de doctorat en Sciences, Ecole polytechnique de Mons (Belgique), 275p.

LORIS, N.B.T., CHARLET, J.M., PECHMANN, E., CLARE, C., CHABU, M. and QUINIF, Y., (1997). Caractéristiques minéralogiques, cristallographiques, physico-chimiques et âges des minéralisations uranifères de Luiswishi (Shaba, Zaïre) : *Proceeding International Cornet Symposium*, September 5th-9th, 1994, Mons, Royal Academy Overseas Sciences, p.285-306.

MASTER, S., RAINAUD, C., ARMOSTRONG, R.A., PHILPIS, D., and ROBB, L.J., (2002). Contributions to the geology and mineralisation of the Central African Copperbelt: II. Neoproterozoic deposition of the Katanga Supergroup with implication for regional and global correlations (abs): *11th IAGOD Symposium and Geocongress*. Windhoek, Namibia, Geology Survey Namibia.

McGEARY, D. and PLUMMER, C. C., (1994). Physical Geology: Earth revealed, Wm . C. Brown Publishers, Dubuque, p.475-476

McGOWAN, R., (2003). The Origin of the Nchanga Copper-Cobalt Deposits of the Zambian Copperbelt. Unpublished PhD thesis, University of Southampton, 247 p.

McGOWAN, R.R., ROBERTS, S., BOYCE, A.J., (2006). Origin of the Nchanga Copper-Cobalt Deposits of the Zambian Copperbelt. *Mineralium Deposita*, 40, 617-638.

MEERT, J.G. and VAN DER VOO, R. (1996). Paleomagmatic and 40Ar/39Ar study of the Sinyai Dolerite, Kenya: Implications for Gondwana assembly, *Journal of Geology* 104 (1996), 131-142.

MENDELSON, F., (1961). *The geology of the Northern Rhodesian Copperbelt*, Macdonald, London, 523 p.

MOORE, T.A., (1967). The Geology of the Ndola and Bwana Mkubwa area: explanation of degree 1228, part of SE Quarter and 1328 part of NE Quarter. Report of the Geological Survey of Zambia, 20: 99 pp.

MUCHEZ, PH., BREMS, D., EL DESOUKY, S., HASET, M., VANDERHAENGEN, P., HEIJLEN, W., and MUKUMBA, W., (2007). Base metal ore deposit evolution and geodynamics in the central African copperbelt; in Andrew, C.J., *et al.,* eds., Digging Deeper-Proceeding of the 9th Biennial SGA Meeting: Irish Association for Economic Geology, Dublin, p 209-212.

NGOY, L., (1992). Les minéralisations cuprifères du Katanguien associées aux dômes granitiques Ubendiens (Province métallogenique Zaïro-Zambienne). L'exemple du gisement de Kinsenda-Luina (Zaïre), Thèse de doctorat; Université Libre de Bruxelles, 253 p.

OKITAUDJI, R.L., (1989). Géologie sédimentaire et concentration syngénétique du Cu et du Co dans la série des Mines du Shaba, Zaïre, Thèse de doctorat. Facultes desSciences, Institut National Polytechniques de Lorraine,(France) 476 p.

OKITAUDJI, R.L., (2001). Modèle de formation des gisements de cuivre-cobalt du Shaba en République Démocratique du Congo. *Bulletin de l'Académie Lorraine des Sciences*, 40, 4.

OLSON, J., and POLLARD, DD., (1989). Inferring palaeostresses from natural fracture paternes: A new method. *Geology 17*: 345-348

OOSTERBOSCH, R., (1950). La série des Mines dans le polygone de Fungurume. *Commémoration du 50 eme anniversaire du comité spécial du Katanga (CSK),* Brussels, vol. 14, pp 1-18.

OOSTERBOSCH, R., (1962). Les mineralisations dans le système de Roan au Katanga. In Lombard J, Nicolini P (Eds.) *Gisements stratiformes de cuivre en Afrique*.Association des Services Géologiques Africains, 71-136.

PLACET, J., (1976). Géologie du Shaba. Une évolution des principaux gites de cuivre, plomb, zinc, uranium. Etude non publiée. Gecamines.

PELTZER, G. TAPPONNIER, P. and COBBOLD, P., (1982). Les grandes décrochements de l'Est Asiatique, évolution dans le temps et comparaison avec un modèle expérimental. *Comptes Rendus de l'Academie des Sciences de Paris, Vol.*294, pp. 1341-1348.

PHILIPS, W.J., (1972). Hydraulic fracturing and mineralisation. *Journal of the Geological society of London,* 128, pp. 337-359.

PIRMOLIN, J., (1970). Inclusion fluides dans la dolomie du gisement stratiformes de Kamoto (Katanga Occidental). *Annales de la société Géologique de Belgique* 93, 397-406.

POLLARD, DD., SALTZER, SD and RUBIN, A., (1993). Stress inversion methods: are they based on faulty assumption? *Journal of Structural Geology*, 15 (8), 1045-1054.

PORADA, H., (1989). Pan-African rifting and orogenesis in southern to equatorial Africa and eastern Brazil. *Precambrian Research*, 44, 103-136.

PORADA, H., and BERHORST,V., (2000). Towards a new understanding of the Neoproterozoic-Early Paleozoic Lufilian and Northern Zambezi belts in Zambia and Congo/Zaire: *Journal of African Earth Sciences,* v.30, p.727-771.

RITZ, J.F., (1994). Determining the slip vector by graphical construction. Use of a simplified representation of the stress tensor. *Journal of structural Geology* 16, 737-741.

RIVERA, L. and KANAMORI, H., (2002). Spatial heterogeneity of tectonic stress and friction in the crust, *Geophysics Research* Lett., 29 doi: 10.1029/2001 GL013803.

ROBERT, M., (1940). Contribution a la géologie du Katanga. Le système du Kundelungu et le système schisto-dolomitique (1ere partie). Memoire Institut Royal pour le Congo-Belge, in-4^{o} Sections des Sciences naturelles et medicales VI, 108p.

SCHOLTZ, CH., (1989). Mechanics of faulting. In: *Annual review of earth and planetary sciences*. Volume 17 (A89-51245 22-46). Palo Alto, CA, Annual Reviews, Inc., 1989, p. 309-334.

SCHOLTZ, CH., (1990). *The mechanics of earthquakes and faulting*. Cambridge University. Presse, 439 p.

SELLEY D., BROUGHTON D., SCOTT R., HITZMAN M., BULL S., LARGE R., McGOLDRICK P., CROAKER M., POLLINGTO, N. and BARRA F., (2005) A new look at the geology of the Zambian Copper Belt. In: Hedenquist JW, Thompson JFH, Goldfarb R, Richards J (eds) *Economic Geology 100th Anniversary Volume*. Society of Economic Geologists, Littleton, Colorado, USA, pp 965-1000

SPANG, J.H., (1972). Numerical method for dynamic analysis of calcite twin lamellae. *Bulletin of the Geological Society .of America*, 83, 467-472.

SPERNER, B., RATSCBACHER, L., and OTT, R., (1993). Fault striae analysis: a turbo Pascal program package for graphical presentation and reduced stress tensor calculation. *Computers and Geosciences, 19*, 1361-1388.

SPERNER, B., MULLER, B., HEIDBACH, O., DELVAUX, D., REINECKER, J. and FUCHS, K., (2003). Tectonic Stress in the Earth's Crust: Advances in the World Stress Map Project. In: New Insights into Structural Interpretation and Modelling (D. Nieuwland Ed.). *Geological Society of London*, Special Publications, 212: 101-116.

STEVEN, N. M., (2000). A Shaba-type Cu-Co-(Ni) deposit at Luamata, west of the Kabompo dome, Northwestern Zambia: *Exploration and Mining Geology*, v.9, p.277-287.

STEWART, S. A., (2007). Salt tectonics in the North Sea Basin: a structural style template for seismic interpreters, *Special Publication of the Geological Societyof London* 272, 361-396

TEMBO, F., KAMPUNZU, A.B., PORADA, H., (1999). Toleitic magmatism associated with continental rifting in the Lufilian fold belt of Zambia. *Journal of African Earth Sciences*, 403-425.

TSHIAUKA,T., KATEKESHA,W.M., CAILTEUX,J., INTIOMALE,M.M., KAMPUNZU,A.B., KAPENDA,D., CHABU,M., NGONGO,K., MUTOMBO,K., NKANIKA,W.R. (1995). Lithostratigraphy of Neoproterozoic Katangan sedimentary sequences in the Musoshi Copper District (SE Shaba, Zaire) and incidences o copper and cobalt economic geology in Central Africa. In Wendorff, M. and Tack, L.(Eds), Late Proterozoic Belts in central and southwestern Africa. *Annales des Sciences Géologiques* Musée Royal de l'Afrique Central, Tervuren, Belgique v.101, pp. 23-48.

TURNER, F.J., (1953). Nature and dynamic interpretation of deformation lamellae in calcite of three marbles. *American Journal of Sciences*, 251, 276-298.

TWISS, R.J., and UNRUH, U.R., (1998). Analysis of fault slip inversions: Do they constrain stress or strain rate? *Journal of Geophysical Research*, 103, 12205-12222.

UNRUG, R., (1983). The Lufilian Arc: a microplate in the Pan-African collision zone of the Congo and the Kalahari cratons. *Precambrian Research*, v.21, pp.181-196.

UNRUG, R., (1988). Mineralisation controls and source of metals in the Lufilian Fold Belt, Shaba (Zaire), Zambia and Angola. *Economic Geology 83*, 1247-1258.

UNRUG, R., (1997). Rodinia to Gondwana: the geodynamic map of Gondwana supercontinent assembly. *GSA today 7*, 1-6.

VAN DOORNINCK, N., (1928). De Lufilische plooing.G. Naeff, Den Haag (unpaginated).

VENDEVILLE, B.C., and JACKSON, M.P.A., (1992). The rise of diapirs during thin-skinned extension, *Marine and Petroleum Geology, 9*: 331-353

WALLACE, R.E., (1951). Geometry of shearing stress and relation to faulting. *Journal of Structural Geology 59*, 118-130.

WILSON, T.J., HANSON, R.E and WARDLAW, W.S., (1993). Late Proterozoic evolution of the Zambezi belt, Zambia: Implications for regional pan-African tectonics and shear displacement in Gondwna. In Findlay, R.H., Banks, M.R., Unrug, R., and Veervers, J. (eds), *Gondwana 8-Assembly, evolution and dispersal*. Balkima, Rotterdam, pp. 69-82.

WILSON, T.J., HANSON, R.E., (1997). Gondwana assembly: the view from southern Africa and East Gondwana. *Journal of Geodynamics*, v.23, pp.263-286.

WENDORFF, M., (2000). Revision of the stratigraphical position of the “Roches Argilo Talqueuse” (R.A.T). In the Neoproterozoic Katangan Copperbelt, South Congo. In *Journal or African Earth Sciences*; Vol 30. n° 3, pp. 717--726.

WENDORFF, M., (2003). Stratigraphy of the Fungurume Group-evolving foreland basin succession in the Lufilian fold-thrust belt, Neoproterozoic-Lower Paleozoic, Democratic Republic of Congo: South African., *Journal of Geology*, v.106, p.17-34.

WENDORFF, M., (2005a). Evolution of Neoproterozoic-Lower Palaeozoic Lufilian arc, Central Africa: a new model based on syntectonic conglomerates. *Journal of the Geological Society of London*, 162, 5-8.

WENDORFF, M., (2005b). Sedimentary genesis and lithostratigraphy of Neoproterozoic megabreccia from Mufulira, Copperbelt of Zambia. *Journal of African Earth Sciences*, 42, 61-81.

WESTERHOF, A.B. PHIL, LEHTONEN, M.I., MAKITIE, H., MANNINEN, T., PEKKALA, Y., GUSTAFSSON, B. and THON, A., (2008). The Tete-Chipata: a new multiple terrane element from the western Mozambique and southern Zambia. *Geological survey of Finland, special paper 48*, 145-166, 9 figures.

ZOBACK, M.L., (1992). First and second order patterns of stress in the lithosphere: the world stress Map project, *Journal of the Geophysical Research, 97*: 11703-11728.

APPENDIX 1

FIELD DATA (WINTENSOR FORMAT)

Table A.1: Dip and dip direction of the mineralised joints (MJ) field data collected at Tshifufiamashi

Stat.ID	Format	Type	Dip	Dip Dir	Slip sense	Conf. Level	Weigh factor	Activ. Type	Strae intensity	Subset input
TM_MTJ_001	11	4	65	248	T	C	5	1	0	2
TM_MTJ_002	11	4	70	242	T	C	5	1	0	2
TM_MTJ_003	11	4	60	198	T	C	5	0	0	1
TM_MTJ_004	11	4	75	335	T	C	5	0	0	1
TM_MTJ_005	11	4	60	236	T	C	5	2	0	2
TM_MTJ_006	11	4	50	182	T	C	5	2	0	2
TM_MTJ_007	11	4	89	52	T	C	5	1	0	2
TM_MTJ_008	11	4	85	228	T	C	5	1	0	2
TM_MTJ_009	11	4	50	332	T	C	5	1	0	2
TM_MTJ_010	11	4	45	312	T	C	5	1	0	2
TM_MTJ_011	11	4	30	114	T	C	5	1	0	2
TM_MTJ_012	11	4	20	104	T	C	5	1	0	2
TM_MTJ_013	11	4	60	250	T	C	5	1	0	2
TM_MTJ_014	11	4	89	268	T	C	5	1	0	2
TM_MTJ_015	11	4	30	206	T	C	5	1	0	2
TM_MTJ_016	11	4	55	276	T	C	5	1	0	2
TM_MTJ_017	11	4	45	40	T	C	5	1	0	2
TM_MTJ_018	11	4	45	50	T	C	5	1	0	2
TM_MTJ_019	11	4	55	264	T	C	5	1	0	2
TM_MTJ_020	11	4	40	274	T	C	5	1	0	2
TM_MTJ_021	11	4	50	284	T	C	5	1	0	2
TM_MTJ_022	11	4	55	96	T	C	4	1	0	2
TM_MTJ_023	11	4	85	358	T	C	4	1	0	2
TM_MTJ_024	11	4	50	318	T	C	4	1	0	2
TM_MTJ_025	11	4	60	56	T	C	4	1	0	2
TM_MTJ_026	11	4	75	202	T	C	4	1	0	2

Stat.ID	Format	Type	Dip	Dip Dir	Slip sense	Conf. Level	Weigh factor	Activ. Type	Strae intensity	Subset input
TM_MTJ_027	11	4	40	174	T	C	3	2	0	2
TM_MTJ_028	11	4	45	62	T	C	5	2	0	2
TM_MTJ_029	11	4	70	162	T	C	5	1	0	2
TM_MTJ_030	11	4	70	210	T	C	5	2	0	2
TM_MTJ_031	11	4	70	104	T	C	5	2	0	2
TM_MTJ_032	11	4	75	112	T	C	3	1	0	2
TM_MTJ_033	11	4	40	288	T	C	5	1	0	2
TM_MTJ_034	11	4	60	358	T	C	5	1	0	2
TM_MTJ_035	11	4	25	274	T	C	3	1	0	2
TM_MTJ_036	11	4	55	226	T	C	5	1	0	2
TM_MTJ_037	11	4	40	60	T	C	3	0	0	2
TM_MTJ_038	11	4	50	18	T	C	5	0	0	2
TM_MTJ_039	11	4	45	34	T	C	2	0	0	2
TM_MTJ_040	11	4	30	308	T	C	2	2	0	2
TM_MTJ_041	11	4	89	228	T	C	4	1	0	2
TM_MTJ_042	11	4	45	164	T	C	3	1	0	2
TM_MTJ_043	11	4	70	182	T	C	1	1	0	2
TM_MTJ_044	11	4	40	64	T	C	1	1	0	2
TM_MTJ_045	11	4	70	40	T	C	1	1	0	2
TM_MTJ_046	11	4	75	90	T	C	1	1	0	2
TM_MTJ_047	11	4	85	310	T	C	1	1	0	2
TM_MTJ_048	11	4	60	330	T	C	1	1	0	2
TM_MTJ_049	11	4	80	230	T	C	1	1	0	2
TM_MTJ_050	11	4	65	90	T	C	4	1	0	2

Table A.2: Dip and dip direction of the unmineralised joints (UMJ) field data collected at Tshifufiamashi

Stat.ID	Format	Type	Dip	Dip Dir	Slip sense	Conf. Level	Weigh factor	Activ. Type	Strae intensity	Subset input
TM_UMTJ_001	11	4	60	198	T	C	5	0	0	2.1
TM_UMTJ_002	11	4	58	198	T	C	5	0	0	2.1
TM_UMTJ_003	11	4	75	335	T	C	5	0	0	2.1
TM_UMTJ_004	11	4	70	162	T	C	5	1	0	2.1
TM_UMTJ_005	11	4	70	210	T	C	5	2	0	2.1
TM_UMTJ_006	11	4	70	104	T	C	5	2	0	2.1
TM_UMTJ_007	11	4	60	358	T	C	5	1	0	2.1
TM_UMTJ_008	11	4	55	226	T	C	5	1	0	2.1
TM_UMTJ_009	11	4	45	34	T	C	2	0	0	2.1
TM_UMTJ_010	11	4	30	308	T	C	2	2	0	2.1
TM_UMTJ_011	11	4	89	228	T	C	4	1	0	2.1
TM_UMTJ_012	11	4	45	164	T	C	3	1	0	2.1
TM_UMTJ_013	11	4	70	212	T	C	3	2	0	2.1
TM_UMTJ_014	11	4	68	162	T	C	2	1	0	2.1
TM_UMTJ_015	11	4	70	158	T	C	2	1	0	2.1
TM_UMTJ_016	11	4	71	170	T	C	2	1	0	2.1
TM_UMTJ_017	11	4	72	104	T	C	5	2	0	2.1
TM_UMTJ_018	11	4	75	333	T	C	5	0	0	2.1
TM_UMTJ_019	11	4	74	332	T	C	5	0	0	2.1
TM_UMTJ_020	11	4	72	330	T	C	2	0	0	2.1
TM_UMTJ_021	11	4	72	211	T	C	3	2	0	2.1
TM_UMTJ_022	11	4	72	105	T	C	2	2	0	2.1
TM_UMTJ_023	11	4	71	160	T	C	4	1	0	2.1
TM_UMTJ_024	11	4	69	208	T	C	4	2	0	2.1
TM_UMTJ_025	11	4	68	160	T	C	4	1	0	2.1

Stat.ID	Format	Type	Dip	Dip Dir	Slip sense	Conf. Level	Weigh factor	Activ. Type	Strae intensity	Subset input
TM_UMTJ_026	11	4	60	354	T	C	4	1	0	2.1
TM_UMTJ_027	11	4	45	36	T	C	2	0	0	2.1
TM_UMTJ_028	11	4	45	40	T	C	2	0	0	2.1
TM_UMTJ_029	11	4	45	32	T	C	3	0	0	2.1
TM_UMTJ_030	11	4	55	223	T	C	3	1	0	2.1
TM_UMTJ_031	11	4	56	226	T	C	4	1	0	2.1
TM_UMTJ_032	11	4	47	38	T	C	3	0	0	2.1
TM_UMTJ_033	11	4	47	36	T	C	5	0	0	2.1
TM_UMTJ_034	11	4	44	35	T	C	5	0	0	2.1
TM_UMTJ_035	11	4	30	310	T	C	5	2	0	2.1
TM_UMTJ_036	11	4	28	311	T	C	5	2	0	2.1
TM_UMTJ_037	11	4	32	312	T	C	5	2	0	2.1
TM_UMTJ_038	11	4	30	309	T	C	5	2	0	2.1
TM_UMTJ_039	11	4	33	319	T	C	5	2	0	2.1
TM_UMTJ_040	11	4	54	223	T	C	5	1	0	2.1
TM_UMTJ_041	11	4	56	225	T	C	3	1	0	2.1
TM_UMTJ_042	11	4	34	309	T	C	3	2	0	2.1
TM_UMTJ_043	11	4	33	310	T	C	3	2	0	2.1
TM_UMTJ_044	11	4	32	308	T	C	32	2	0	2.1
TM_UMTJ_045	11	4	71	331	T	C	2	0	0	2.1

Table A.3: Dip/dip direction and plunge/azimuth of the slickensided faults field data collected at Tshifufiamashi

Stat.ID	Format	Type	Dip	Dip Dir	Plunge	Azimuth	Slip sense	Conf. Level	Weigh factor	Activ. Type	Strae intensity	Subset input
TM_FLT_001	11	1	38	228	38	228	I	S	5	1	2	3.1
TM_FLT_002	11	1	55	243	49	213	I	P	5	1	2	3.1
TM_FLT_003	11	1	49	210	48	221	I	P	5	1	2	3.1
TM_FLT_004	11	1	63	266	5	352	I	P	5	1	2	3.1
TM_FLT_005	11	1	62	258	62	256	I	P	5	1	2	3.1
TM_FLT_006	11	1	52	246	49	271	I	P	5	1	2	3.1
TM_FLT_007	11	1	58	262	57	281	I	P	5	1	2	3.1
TM_FLT_008	11	1	68	205	18	288	I	P	3	1	2	3.1
TM_FLT_009	11	1	62	262	63	270	I	P	3	1	1	3.1
TM_FLT_010	11	1	85	205	16	294	I	P	3	1	1	3.1
TM_FLT_011	11	1	62	240	59	266	I	P	5	1	1	3.1
TM_FLT_012	11	1	45	213	28	271	I	P	2	2	2	3.1
TM_FLT_013	11	1	42	245	30	290	I	P	2	2	2	3.1
TM_FLT_014	11	1	32	242	21	287	I	P	2	2	2	3.1
TM_FLT_015	11	1	59	225	35	286	I	P	2	2	2	3.1
TM_FLT_016	11	1	83	223	57	144	X	X	2	2	2	3.1
TM_FLT_017	11	1	49	235	8	318	I	S	2	2	2	3.1
TM_FLT_018	11	1	48	183	39	226	I	S	7	2	2	3.1
TM_FLT_019	11	1	39	165	21	223	I	S	7	2	2	3.1
TM_FLT_020	11	1	60	44	60	30	N	S	5	1	2	3.1
TM_FLT_021	11	1	58	54	56	33	N	S	5	1	2	3.1
TM_FLT_022	11	1	50	36	49	20	N	S	5	1	2	3.1
TM_FLT_023	11	1	55	42	55	34	N	S	5	1	2	3.1
TM_FLT_024	11	1	65	52	63	28	N	S	1	1	1	3.1
TM_FLT_025	11	1	30	38	26	72	I	C	4	1	1	3.1
TM_FLT_026	11	1	55	28	52	1	I	C	5	1	1	3.1

Stat.ID	Format	Type	Dip	Dip Dir	Plunge	Azimuth	Slip sense	Conf. Level	Weigh factor	Activ. Type	Strae intensity	Subset input
TM_FLT_027	11	1	70	2	49	67	I	S	3	1	2	3.1
TM_FLT_028	11	1	65	50	50	354	I	C	2	1	1	3.1
TM_FLT_029	11	1	45	62	35	16	I	C	2	1	2	3.1
TM_FLT_030	11	1	25	350	25	356	I	C	2	1	2	3.1
TM_FLT_031	11	1	15	12	15	4	I	C	3	1	2	3.1
TM_FLT_032	11	1	55	290	44	242	I	C	5	2	2	3.1
TM_FLT_033	11	1	55	290	46	247	I	C	5	2	2	3.1
TM_FLT_034	11	1	55	290	38	233	I	C	5	1	2	3.1
TM_FLT_035	11	1	55	290	55	290	I	C	5	1	2	3.1
TM_FLT_036	11	1	55	290	55	293	I	C	5	1	2	3.1
TM_FLT_037	11	1	35	292	15	0	N	P	5	1	2	3.1
TM_FLT_038	11	1	45	294	45	290	I	C	2	1	2	3.1
TM_FLT_039	11	1	15	118	15	121	I	C	4	1	2	3.1
TM_FLT_040	11	1	45	128	36	86	I	C	3	1	1	3.1
TM_FLT_041	11	1	15	114	2	195	I	C	3	1	1	3.1
TM_FLT_042	11	1	45	110	35	155	N	S	3	1	1	3.1
TM_FLT_043	11	1	20	120	19	140	I	C	3	1	1	3.1
TM_FLT_044	11	1	45	182	35	138	I	C	3	1	2	3.1
TM_FLT_045	11	1	45	106	45	102	I	C	4	1	2	3.1
TM_FLT_046	11	1	52	243	24	313	D	S	5	2	2	3.1
TM_FLT_047	11	1	25	160	18	115	X	X	5	2	2	3.1
TM_FLT_048	11	1	42	182	11	105	X	X	5	2	2	3.1
TM_FLT_049	11	1	35	173	1	262	I	P	5	2	2	3.1
TM_FLT_050	11	1	25	155	15	105	X	X	5	2	2	3.1
TM_FLT_051	11	1	45	183	1	94	X	X	5	2	2	3.1
TM_FLT_052	11	1	38	175	2	266	I	P	5	2	2	3.1
TM_FLT_053	11	1	28	184	3	267	I	P	5	2	2	3.1

Stat.ID	Format	Type	Dip	Dip Dir	Plunge	Azimuth	Slip sense	Conf. Level	Weigh factor	Activ. Type	Strae intensity	Subset input
TM_FLT_054	11	1	40	238	41	240	I	S	5	2	2	3.1
TM_FLT_055	11	1	55	28	52	3	I	C	5	1	1	3.1
TM_FLT_056	11	1	55	28	54	11	I	C	5	1	2	3.1
TM_FLT_057	11	1	55	28	50	355	I	C	5	1	2	3.1
TM_FLT_058	11	1	68	10	61	328	I	C	2	1	1	3.1
TM_FLT_059	11	1	68	10	17	93	I	C	2	1	1	3.1
TM_FLT_060	11	1	45	60	30	6	I	C	2	1	1	3.1
TM_FLT_061	11	1	45	60	31	7	I	C	2	1	1	3.1
TM_FLT_062	11	1	65	264	43	199	I	P	3	1	2	3.1
TM_FLT_063	11	1	65	264	31	190	I	P	3	1	2	3.1
TM_FLT_064	11	1	60	110	1	199	D	C	2	2	1	3.1
TM_FLT_065	11	1	55	344	50	310	I	C	5	1	1	3.1
TM_FLT_066	11	1	50	108	49	90	I	C	4	1	2	3.1
TM_FLT_067	11	1	85	202	1	112	D	C	4	2	1	3.1
TM_FLT_068	11	1	40	222	38	201	I	P	4	1	1	3.1
TM_FLT_069	11	1	35	202	19	263	I	C	4	2	1	3.1
TM_FLT_070	11	1	35	202	23	255	I	C	4	2	1	3.1
TM_FLT_071	11	1	74	219	74	252	I	C	3	0	1	3.1
TM_FLT_072	11	1	70	208	64	256	I	S	3	0	1	3.1
TM_FLT_073	11	1	70	228	64	256	I	S	3	0	1	3.1
TM_FLT_074	11	1	70	8	22	90	D	C	4	1	2	3.1
TM_FLT_075	11	1	55	36	22	109	D	C	4	1	2	3.1
TM_FLT_076	11	1	55	36	30	102	D	C	4	1	2	3.1
TM_FLT_077	11	1	55	28	19	104	D	C	5	1	1	3.1
TM_FLT_078	11	1	70	354	38	67	D	C	3	2	1	3.1
TM_FLT_079	11	1	80	278	30	194	D	C	5	2	2	3.1
TM_FLT_080	11	1	80	278	75	231	D	C	5	2	2	3.1

Stat.ID	Format	Type	Dip	Dip Dir	Plunge	Azimuth	Slip sense	Conf. Level	Weigh factor	Activ. Type	Strae intensity	Subset input
TM_FLT_081	11	1	55	264	36	205	D	C	5	2	2	3.1
TM_FLT_082	11	1	40	236	33	196	D	C	3	2	2	3.1
TM_FLT_083	11	1	80	262	24	177	D	C	5	2	2	3.1
TM_FLT_084	11	1	80	262	19	348	D	C	5	1	2	3.1
TM_FLT_085	11	1	60	130	60	142	D	C	3	1	1	3.1
TM_FLT_086	11	1	85	212	81	157	D	C	4	1	0	3.1
TM_FLT_087	11	1	80	22	65	90	D	C	4	1	0	3.1
TM_FLT_088	11	1	65	144	64	160	D	C	4	1	0	3.1
TM_FLT_089	11	1	45	36	37	355	D	C	3	1	1	3.1
TM_FLT_090	11	1	70	124	4	35	D	C	3	1	2	3.1
TM_FLT_091	11	1	70	116	19	199	D	C	3	2	2	3.1
TM_FLT_092	11	1	40	90	8	10	D	C	3	2	2	3.1
TM_FLT_093	11	1	60	144	58	165	D	C	3	1	1	3.1
TM_FLT_094	11	1	30	34	29	22	D	C	3	1	1	3.1
TM_FLT_095	11	1	40	98	19	33	D	C	3	1	1	3.1
TM_FLT_096	11	1	35	10	35	358	D	C	3	1	1	3.1
TM_FLT_097	11	1	65	8	65	3	D	C	3	1	0	3.1
TM_FLT_098	11	1	45	40	16	327	D	C	3	1	0	3.1
TM_FLT_099	11	1	35	202	33	179	D	C	4	1	1	3.1

Table A.4: Dip and dip direction of the shear fractures filed data collected at Tshifufiamashi.

Stat.ID	Format	Type	Dip	Dip Dir	Slip sense	Conf. Level	Weigh factor	Activ. Type	Strae intensity	Subset input
TM_SF_01	11	4	30	40	I	P	4	1	0	3.2
TM_SF_02	11	4	65	264	I	P	3	2	0	3.2
TM_SF_03	11	4	70	280	I	P	2	2	0	3.2
TM_SF_04	11	4	30	310	X	x	2	2	0	3.2
TM_SF_05	11	4	75	192	X	x	3	1	0	3.2
TM_SF_06	11	4	30	142	X	x	5	1	0	3.2
TM_SF_07	11	4	65	116	X	x	5	2	0	3.2
TM_SF_08	11	4	60	354	X	x	5	2	0	3.2
TM_SF_09	11	4	75	340	X	x	5	2	0	3.2
TM_SF_10	11	4	70	114	X	x	5	1	0	3.2
TM_SF_11	11	4	20	26	X	x	5	1	0	3.2
TM_SF_12	11	4	35	194	X	x	3	1	0	3.2
TM_SF_13	11	4	50	258	X	x	5	1	0	3.2
TM_SF_14	11	4	85	208	D	C	3	2	0	3.2
TM_SF_15	11	4	60	42	D	C	5	1	0	3.2
TM_SF_16	11	4	45	10	D	C	3	1	0	3.2
TM_SF_17	11	4	75	26	D	C	3	1	0	3.2
TM_SF_18	11	4	70	224	D	C	4	1	0	3.2
TM_SF_19	11	4	89	262	D	C	4	1	0	3.2

Table A.5: Fold elements measurements (Dip, dip direction, strike and sense of bedding collected from the R2 fragment and the micro-folds observed at Tshifufiamashi; dip and dip direction of fold axial planes and plunge and azimuth of hinge lines collected from the small-scale folds observed in the CMN strata.

Bedding Planes-Tshifufiamashi Fragment				
Stat.ID	Dip	Dip/Dir	Sense	Str.
TM_BP_F01	75	204	SW	114
TM_BP_F02	78	228	SW	138
TM_BP_F03	74	234	SW	144
TM_BP_F04	76	230	SW	140
TM_BP_F05	52	243	SW	153
TM_BP_F06	70	242	SW	152
TM_BP_F07	60	250	WSW	160
TM_BP_F08	30	206	SW	116
TM_BP_F09	55	264	WSW	174
TM_BP_F10	50	240	SW	150
TM_BP_F11	54	244	SW	154
TM_BP_F12	64	250	WSW	160
TM_BP_F13	61	248	SW	158
TM_BP_F14	52	242	SW	152
TM_BP_F15	63	251	SW	161
TM_BP_F16	49	238	SW	148

Bedding Planes-Isoclinals fold (Tshifufiamashi)				
Stat.ID	Dip	Dip_Dir	Sense	Str.
TM_IBP_01	30	206	SW	116
TM_IBP_02	30	268	WSW	178
TM_IBP_03	20	216	SW	126
TM_IBP_04	20	224	SW	134
TM_IBP_05	40	238	SW	148
TM_IBP_06	20	202	SW	112
TM_IBP_07	38	230	SW	140
TM_IBP_08	30	228	SW	138
TM_IBP_09	20	36	NE	306
TM_IBP_10	20	44	NE	314
TM_IBP_11	40	58	NE	328
TM_IBP_12	20	22	NE	292
TM_IBP_13	38	50	NE	320
TM_IBP_14	23	48	NE	318
TM_IBP_15	54	64	NE	334
TM_IBP_16	20	216	SW	126
TM_IBP_17	60	70	ENE	340
TM_IBP_18	50	40	NE	310
TM_IBP_19	64	70	ENE	340
TM_IBP_20	20	224	SW	134
TM_IBP_21	40	58	NE	328
TM_IBP_22	80	58	NE	328
TM_IBP_23	38	50	NE	320
TM_IBP_24	23	228	SW	138
TM_IBP_25	86	224	SW	134
TM_IBP_26	60	216	SW	126
TM_IBP_27	58	204	SW	114
TM_IBP_28	61	214	SW	124

Fold Axial Plane		
Stat.ID	Dip	Dip Dir
TM_FAP_01	30	228
TM_FAP_02	20	224
TM_FAP_03	40	238
TM_FAP_04	20	202
TM_FAP_05	38	230
TM_FAP_06	28	218
TM_FAP_07	25	222
TM_FAP_08	24	218
TM_FAP_09	30	225
TM_FAP_10	32	228
TM_FAP_11	30	218
TM_FAP_12	32	222
TM_FAP_13	25	219
TM_FAP_14	26	224
TM_FAP_15	24	220
TM_FAP_16	30	230
TM_FAP_17	30	218
TM_FAP_18	32	217
TM_FAP_19	28	230
TM_FAP_20	28	228
TM_FAP_21	22	215
TM_FAP_22	42	200
TM_FAP_23	45	198
TM_FAP_24	50	196
TM_FAP_25	48	200

Hinge Line		
Stat.ID	Plun.	Azi.
TM_HL_01	10	138
TM_HL_02	20	150
TM_HL_03	5	110
TM_HL_04	5	120
TM_HL_05	10	130
TM_HL_06	12	130
TM_HL_07	20	135
TM_HL_08	0	120
TM_HL_09	40	140
TM_HL_10	25	125
TM_HL_11	28	115
TM_HL_12	18	122
TM_HL_13	15	130
TM_HL_14	20	148
TM_HL_15	20	140
TM_HL_16	5	122
TM_HL_17	6	121
TM_HL_18	20	138
TM_HL_19	15	128
TM_HL_20	16	121
TM_HL_21	16	120
TM_HL_22	5	112

Table A.6: Dip and dip direction of the mineralised joints collected at Tshifufia.

Stat ID	Format	Type	dip	dip-dir	slip sense	level confident	Weight factor	Activ type	Striae intens	Set input
TC-001	11	4	40	5	T	C	3	0	0	2.1
TC-002	11	4	38	32	T	C	3	0	0	2.1
TC-003	11	4	42	292	T	C	2	2	0	2.1
TC-004	11	4	25	350	T	C	2	2	0	2.1
TC-005	11	4	45	158	T	C	2	2	0	2.1
TC-006	11	4	62	50	T	C	2	2	0	2.1
TC-007	11	4	47	58	T	C	2	2	0	2.1
TC-008	11	4	50	54	T	C	2	2	0	2.1
TC-009	11	4	1	272	T	C	2	2	0	2.1
TC-010	11	4	68	80	T	C	2	2	0	2.1
TC-011	11	4	75	18	T	C	2	1	0	2.1
TC-012	11	4	35	110	T	C	5	1	0	2.1
TC-013	11	4	75	26	T	C	5	1	0	2.1
TC-014	11	4	75	18	T	C	3	1	0	2.1
TC-015	11	4	40	30	T	C	3	1	0	2.1
TC-016	11	4	70	32	T	C	3	1	0	2.1
TC-017	11	4	35	30	T	C	4	1	0	2.1
TC-018	11	4	85	38	T	C	4	1	0	2.1
TC-019	11	4	42	302	T	C	4	1	0	2.1
TC-020	11	4	65	70	T	C	3	1	0	2.1
TC-021	11	4	35	346	T	C	2	1	0	2.1
TC-022	11	4	85	204	T	C	2	1	0	2.1
TC-023	11	4	35	260	T	C	2	0	0	2.1
TC-024	11	4	40	286	T	C	2	0	0	2.1
TC-025	11	4	70	24	T	X	5	1	0	2.1
TC-026	11	4	40	78	T	X	5	1	0	2.1

Stat ID	Format	Type	dip	dip-dir	slip sense	level confident	Weight factor	Activ type	Striae intens	Set input
TC-027	11	4	73	84	T	C	3	1	0	2.1
TC-028	11	4	35	30	T	C	5	1	0	2.1
TC-029	11	4	35	186	T	C	2	1	0	2.1
TC-030	11	4	80	58	T	C	2	1	0	2.1
TC-031	11	4	45	340	T	C	2	1	0	2.1
TC-032	11	4	25	168	T	C	2	1	0	2.1
TC-033	11	4	60	344	T	C	2	1	0	2.1
TC-034	11	4	73	34	T	C	2	1	0	2.1
TC-035	11	4	25	28	T	C	2	1	0	2.1
TC-036	11	4	85	80	T	C	4	1	0	2.1
TC-037	11	4	45	178	T	C	4	1	0	2.1
TC-038	11	4	80	0	T	C	4	1	0	2.1
TC-039	11	4	80	130	T	C	4	1	0	2.1
TC-040	11	4	35	178	T	C	4	1	0	2.1
TC-041	11	4	85	260	T	C	4	1	0	2.1
TC-042	11	4	70	47	T	C	4	1	0	2.1
TC-043	11	4	60	50	T	C	4	1	0	2.1
TC-044	11	4	70	16	T	C	4	1	0	2.1
TC-045	11	4	20	180	T	C	4	1	0	2.1
TC-046	11	4	65	144	T	C	4	1	0	2.1
TC-047	11	4	62	14	T	C	4	1	0	2.1
TC-048	11	4	40	268	T	C	4	1	0	2.1
TC-049	11	4	55	128	T	C	4	1	0	2.1
TC-050	11	4	85	12	T	C	4	1	0	2.1
TC-051	11	4	62	136	T	C	4	1	0	2.1
TC-052	11	4	45	182	T	C	4	1	0	2.1
TC-053	11	4	75	186	T	C	4	1	0	2.1

Stat ID	Format	Type	dip	dip-dir	slip sense	level confident	Weight factor	Activ type	Striae intens	Set input
TC-054	11	4	50	0	T	C	4	1	0	2.1
TC-055	11	4	65	100	T	C	4	1	0	2.1
TC-056	11	4	30	114	T	C	4	1	0	2.1
TC-057	11	4	65	76	T	C	4	1	0	2.1
TC-058	11	4	25	190	T	C	4	1	0	2.1
TC-059	11	4	30	20	T	C	4	1	0	2.1
TC-060	11	4	80	198	T	C	4	1	0	2.1
TC-061	11	4	40	202	T	C	4	1	0	2.1
TC-062	11	4	72	288	T	C	5	0	0	2.1
TC-063	11	4	35	40	T	C	2	1	0	2.1
TC-064	11	4	60	24	T	C	2	1	0	2.1
TC-065	11	4	55	18	T	C	2	2	0	2.1
TC-066	11	4	44	60	T	C	2	0	0	2.1
TC-067	11	4	75	80	T	C	2	0	0	2.1
TC-068	11	4	45	58	T	C	2	0	0	2.1
TC-069	11	4	60	48	T	C	2	0	0	2.1
TC-070	11	4	80	70	T	C	2	0	0	2.1
TC-071	11	4	25	52	T	C	5	1	0	2.1
TC-072	11	4	70	90	T	C	4	1	0	2.1
TC-073	11	4	30	112	T	C	4	0	0	2.1
TC-074	11	4	50	98	T	C	4	2	0	2.1
TC-075	11	4	30	84	T	C	4	0	0	2.1
TC-076	11	4	45	256	T	C	5	1	0	2.1
TC-077	11	4	50	164	T	C	5	1	0	2.1
TC-078	11	4	70	274	T	C	5	1	0	2.1
TC-079	11	4	30	290	T	C	5	1	0	2.1
TC-080	11	4	85	300	T	C	5	1	0	2.1

Stat ID	Format	Type	dip	dip-dir	slip sense	level confident	Weight factor	Activ type	Striae intens	Set input
TC-081	11	4	60	162	T	C	5	1	0	2.1
TC-082	11	4	55	286	T	C	5	1	0	2.1
TC-083	11	4	20	230	T	C	5	1	0	2.1
TC-084	11	4	75	312	T	C	3	1	0	2.1
TC-085	11	4	89	122	T	C	3	0	0	2.1
TC-086	11	4	40	264	T	C	3	0	0	2.1
TC-087	11	4	25	352	T	C	3	0	0	2.1
TC-088	11	4	89	58	T	C	3	0	0	2.1
TC-089	11	4	45	170	T	C	3	0	0	2.1
TC-090	11	4	35	112	T	C	3	0	0	2.1
TC-091	11	4	40	260	T	C	3	0	0	2.1
TC-092	11	4	40	206	T	C	3	0	0	2.1
TC-093	11	4	76	22	T	C	3	0	0	2.1
TC-094	11	4	88	60	T	C	3	0	0	2.1
TC-095	11	4	89	130	T	C	2	0	0	2.1
TC-096	11	4	70	30	T	C	2	0	0	2.1
TC-097	11	4	72	32	T	C	2	0	0	2.1
TC-098	11	4	74	40	T	C	3	0	0	2.1
TC-099	11	4	74	36	T	C	4	0	0	2.1
TC-100	11	4	89	128	T	C	3	0	0	2.1
TC-101	11	4	88	127	T	C	2	0	0	2.1
TC-102	11	4	87	124	T	C	2	0	0	2.1
TC-103	11	4	70	308	T	C	3	0	0	2.1
TC-104	11	4	70	302	T	C	4	0	0	2.1
TC-105	11	4	78	40	T	C	4	0	0	2.1
TC-106	11	4	78	38	T	C	3	0	0	2.1
TC-107	11	4	70	37	T	C	3	0	0	2.1

Stat ID	Format	Type	dip	dip-dir	slip sense	level confident	Weight factor	Activ type	Striae intens	Set input
TC-108	11	4	75	312	T	C	2	0	0	2.1
TC-109	11	4	75	18	T	C	2	0	0	2.1
TC-110	11	4	75	310	T	C	3	0	0	2.1
TC-111	11	4	75	322	T	C	3	0	0	2.1
TC-112	11	4	70	310	T	C	3	0	0	2.1
TC-113	11	4	75	20	T	C	3	0	0	2.1
TC-114	11	4	74	24	T	C	3	0	0	2.1
TC-115	11	4	68	18	T	C	3	0	0	2.1
TC-116	11	4	68	312	T	C	3	0	0	2.1
TC-117	11	4	68	29	T	C	4	0	0	2.1
TC-118	11	4	68	30	T	C	4	0	0	2.1
TC-119	11	4	72	308	T	C	4	0	0	2.1
TC-120	11	4	74	306	T	C	3	0	0	2.1
TC-121	11	4	72	309	T	C	3	0	0	2.1
TC-122	11	4	89	120	T	C	3	0	0	2.1
TC-123	11	4	88	122	T	C	2	0	0	2.1
TC-124	11	4	88	118	T	C	1	0	0	2.1
TC-125	11	4	87	122	T	C	2	0	0	2.1
TC-126	11	4	87	128	T	C	3	0	0	2.1
TC-127	11	4	77	41	T	C	2	0	0	2.1
TC-128	11	4	75	42	T	C	3	0	0	2.1
TC-129	11	4	76	58	T	C	4	0	0	2.1
TC-130	11	4	89	62	T	C	2	0	0	2.1
TC-131	11	4	87	58	T	C	1	0	0	2.1
TC-132	11	4	86	54	T	C	1	0	0	2.1
TC-133	11	4	87	52	T	C	2	0	0	2.1
TC-134	11	4	76	50	T	C	3	0	0	2.1

Stat ID	Format	Type	dip	dip-dir	slip sense	level confident	Weight factor	Activ type	Striae intens	Set input
TC-135	11	4	74	51	T	C	2	0	0	2.1
TC-136	11	4	75	312	T	C	3	0	0	2.1
TC-137	11	4	68	20	T	C	3	0	0	2.1
TC-138	11	4	40	108	T	C	5	1	0	2.1
TC-139	11	4	70	94	T	C	5	1	0	2.1
TC-140	11	4	60	168	T	C	4	1	0	2.1
TC-141	11	4	75	48	T	C	4	1	0	2.1
TC-142	11	4	80	192	T	C	4	1	0	2.1

Table A.7: Dip and dip direction of the unmineralised joint field data collected at Tshifufia.

Stat ID	Format	type	dip	dip-dir	slip sense	level confident	Weight factor	Activ type	Striae intens	Set input
TC-001	11	4	28	356	T	C	3	0	0	2.2
TC-002	11	4	50	348	T	C	3	0	0	2.2
TC-003	11	4	70	92	T	C	3	0	0	2.2
TC-004	11	4	40	302	T	C	3	0	0	2.2
TC-005	11	4	40	142	T	C	3	0	0	2.2
TC-006	11	4	75	18	T	C	3	0	0	2.2
TC-007	11	4	65	78	T	C	3	0	0	2.2
TC-008	11	4	25	174	T	C	3	0	0	2.2
TC-009	11	4	30	100	T	C	3	0	0	2.2
TC-010	11	4	30	184	T	C	3	0	0	2.2
TC-011	11	4	35	100	T	C	3	0	0	2.2
TC-012	11	4	35	38	T	C	3	0	0	2.2
TC-013	11	4	55	24	T	C	3	0	0	2.2
TC-014	11	4	35	2	T	C	4	0	0	2.2

Stat ID	Format	type	dip	dip-dir	slip sense	level confident	Weight factor	Activ type	Striae intens	Set input
TC-015	11	4	35	74	T	C	2	0	0	2.2
TC-016	11	4	5	286	T	C	2	0	0	2.2
TC-017	11	4	40	116	T	C	4	0	0	2.2
TC-018	11	4	70	188	T	C	4	0	0	2.2
TC-019	11	4	50	152	T	C	4	0	0	2.2
TC-020	11	4	75	338	T	C	4	0	0	2.2
TC-021	11	4	70	110	T	C	4	0	0	2.2
TC-022	11	4	70	190	T	C	4	0	0	2.2
TC-023	11	4	60	158	T	C	4	0	0	2.2
TC-024	11	4	30	204	T	C	4	0	0	2.2
TC-028	11	4	68	312	T	C	3	0	0	2.2
TC-029	11	4	70	307	T	C	3	0	0	2.2
TC-030	11	4	74	305	T	C	3	0	0	2.2
TC-031	11	4	70	312	T	C	3	0	0	2.2
TC-032	11	4	80	58	T	C	2	0	0	2.2
TC-033	11	4	88	120	T	C	2	0	0	2.2
TC-034	11	4	80	122	T	C	2	0	0	2.2
TC-035	11	4	75	120	T	C	2	0	0	2.2
TC-036	11	4	74	124	T	C	1	0	0	2.2
TC-037	11	4	89	126	T	C	4	0	0	2.2
TC-038	11	4	75	310	T	C	3	0	0	2.2
TC-039	11	4	30	205	T	C	4	0	0	2.2
TC-040	11	4	45	221	T	C	4	0	0	2.2
TC-041	11	4	42	200	T	C	4	0	0	2.2
TC-042	11	4	38	45	T	C	4	0	0	2.2
TC-043	11	4	45	209	T	C	4	0	0	2.2

Stat ID	Format	type	dip	dip-dir	slip sense	level confident	Weight factor	Activ type	Striae intens	Set input
TC-044	11	4	45	210	T	C	4	0	0	2.2
TC-045	11	4	57	144	T	C	4	0	0	2.2
TC-046	11	4	38	169	T	C	4	0	0	2.2
TC-047	11	4	46	156	T	C	3	0	0	2.2
TC-048	11	4	50	144	T	C	3	0	0	2.2
TC-049	11	4	56	231	T	C	3	0	0	2.2
TC-050	11	4	66	234	T	C	3	0	0	2.2
TC-051	11	4	35	211	T	C	3	0	0	2.2
TC-052	11	4	40	45	T	C	3	0	0	2.2
TC-053	11	4	38	44	T	C	3	0	0	2.2
TC-054	11	4	34	56	T	C	3	0	0	2.2
TC-055	11	4	38	65	T	C	3	0	0	2.2
TC-056	11	4	42	47	T	C	3	0	0	2.2
TC-057	11	4	39	254	T	C	3	0	0	2.2
TC-058	11	4	65	56	T	C	3	0	0	2.2
TC-059	11	4	80	112	T	C	1	0	0	2.2
TC-060	11	4	28	356	T	C	2	0	0	2.2
TC-061	11	4	28	350	T	C	2	0	0	2.2
TC-062	11	4	30	349	T	C	3	0	0	2.2
TC-063	11	4	32	340	T	C	3	0	0	2.2
TC-064	11	4	40	342	T	C	3	0	0	2.2
TC-065	11	4	27	350	T	C	3	0	0	2.2
TC-066	11	4	35	2	T	C	3	0	0	2.2
TC-067	11	4	40	4	T	C	3	0	0	2.2
TC-068	11	4	40	10	T	C	3	0	0	2.2
TC-069	11	4	32	2	T	C	3	0	0	2.2

Stat ID	Format	type	dip	dip-dir	slip sense	level confident	Weight factor	Activ type	Striae intens	Set input
TC-070	11	4	10	286	T	C	3	0	0	2.2
TC-071	11	4	12	280	T	C	3	0	0	2.2
TC-072	11	4	11	284	T	C	3	0	0	2.2
TC-073	11	4	10	290	T	C	3	0	0	2.2
TC-074	11	4	35	64	T	C	3	0	0	2.2
TC-075	11	4	40	70	T	C	3	0	0	2.2
TC-076	11	4	45	72	T	C	3	0	0	2.2
TC-077	11	4	38	79	T	C	3	0	0	2.2
TC-078	11	4	34	70	T	C	3	0	0	2.2
TC-079	11	4	36	69	T	C	3	0	0	2.2
TC-080	11	4	41	58	T	C	3	0	0	2.2
TC-081	11	4	32	356	T	C	3	0	0	2.2

Table A.8: Dip/dip direction and plunge/azimuth of slickensided faults field data collected at Tshifufia.

Stat ID	Format	type	dip	dip-dir	plunge	Azimuth	slip sense	level confident	Weight factor	Activ type	Striae intens	Set input
TC_001	11	1	40	350	28	299	I	C	5	1	1	3.1
TC_002	11	1	35	360	22	305	I	C	5	1	2	3.1
TC_003	11	1	80	296	76	253	S	C	5	1	1	3.1
TC_004	11	1	30	328	29	343	S	C	5	1	2	3.1
TC_005	11	1	45	292	36	335	I	S	5	1	2	3.1
TC_006	11	1	20	286	11	343	I	S	4	1	2	3.1
TC_007	11	1	40	304	17	12	I	S	5	0	2	3.1
TC_008	11	1	85	342	85	342	I	C	5	2	2	3.1
TC_009	11	1	47	326	47	320	I	S	5	2	1	3.1
TC_010	11	1	50	348	46	318	I	S	5	2	1	3.1

Stat ID	Format	type	dip	dip-dir	plunge	Azimuth	slip sense	level confident	Weight factor	Activ type	Striae intens	Set input
TC_011	11	1	75	15	72	50	N	S	3	1	2	3.1
TC_012	11	1	45	332	45	329	N	S	5	2	2	3.1
TC_013	11	1	45	332	1	242	S	S	5	2	2	3.1
TC_014	11	1	30	334	30	334	N	S	5	1	2	3.1
TC_015	11	1	80	120	80	110	I	S	3	1	2	3.1
TC_016	11	1	80	300	80	298	I	S	4	2	1	3.1
TC_017	11	1	40	350	32	308	I	S	1	1	1	3.1
TC_018	11	1	30	154	29	177	N	S	5	2	1	3.1
TC_019	11	1	50	144	31	204	I	S	4	1	2	3.1
TC_020	11	1	40	284	29	235	I	S	5	1	2	3.1
TC_021	11	1	50	272	50	270	I	S	5	1	2	3.1
TC_022	11	1	40	350	33	310	I	C	5	2	2	3.1
TC_023	11	1	10	345	10	354	N	S	2	1	1	3.1
TC_024	11	1	75	322	75	320	I	S	4	1	0	3.1
TC_025	11	1	50	306	34	251	I	S	1	2	1	3.1
TC_026	11	1	15	120	14	136	D	P	1	1	1	3.1
TC_027	11	1	40	156	40	150	I	P	1	1	1	3.1
TC_028	11	1	15	160	15	151	I	S	2	1	1	3.1
TC_029	11	1	20	122	18	148	I	S	2	1	1	3.1
TC_030	11	1	60	146	58	168	I	S	2	1	1	3.1
TC_031	11	1	60	156	12	239	S	S	2	1	1	3.1
TC_032	11	1	50	164	17	239	S	P	2	1	1	3.1
TC_033	11	1	35	6	3	91	S	P	2	1	1	3.1
TC_034	11	1	60	165	33	97	S	P	2	1	1	3.1

Stat ID	Format	type	dip	dip-dir	plunge	Azimuth	slip sense	level confident	Weight factor	Activ type	Striae intens	Set input
TC_035	11	1	60	160	50	113	S	S	4	1	1	3.1
TC_036	11	1	85	160	44	75	S	S	5	1	1	3.1
TC_037	11	1	40	132	20	68	S	S	5	1	1	3.1
TC_038	11	1	30	148	3	233	I	P	4	1	1	3.1
TC_039	11	1	30	150	14	214	I	P	4	2	2	3.1
TC_040	11	1	35	6	1	95	I	P	4	1	1	3.1
TC_041	11	1	25	148	18	194	X	X	2	1	1	3.1
TC_042	11	1	62	160	55	202	I	S	4	1	1	3.1
TC_043	11	1	80	176	75	129	I	S	4	1	1	3.1
TC_044	11	1	89	145	80	229	I	S	4	1	1	3.1
TC_045	11	1	50	162	40	209	I	C	5	1	1	3.1
TC_046	11	1	60	165	44	222	D	C	5	1	1	3.1
TC_047	11	1	89	170	30	81	S	C	5	1	2	3.1
TC_048	11	1	89	163	13	73	S	C	5	1	2	3.1
TC_049	11	1	26	113	12	49	N	S	5	2	2	3.1
TC_050	11	1	18	180	18	182	X	X	5	2	2	3.1
TC_051	11	1	85	228	85	219	X	X	5	1	2	3.1
TC_052	11	1	42	112	28	58	X	X	2	2	1	3.1
TC_053	11	1	52	154	29	218	S	S	5	2	0	3.1
TC_054	11	1	25	148	13	88	X	X	5	2	1	3.1
TC_055	11	1	50	170	35	116	X	X	5	2	2	3.1
TC_056	11	1	40	176	22	115	X	X	5	1	0	3.1
TC_057	11	1	40	150	18	217	S	S	5	2	2	3.1
TC_058	11	1	50	156	35	102	S	S	4	2	2	3.1

Stat ID	Format	type	dip	dip-dir	plunge	Azimuth	slip sense	level confident	Weight factor	Activ type	Striae intens	Set input
TC_059	11	1	70	146	12	231	S	S	4	1	2	3.1
TC_060	11	1	50	340	46	312	X	X	4	2	2	3.1
TC_061	11	1	50	184	1	95	X	X	5	1	2	3.1
TC_062	11	1	45	128	37	86	X	X	5	2	2	3.1
TC_063	11	1	75	180	72	212	S	C	3	1	2	3.1
TC_064	11	1	70	108	9	195	S	C	3	1	2	3.1
TC_065	11	1	75	112	6	200	S	C	3	1	2	3.1
TC_066	11	1	60	334	32	43	S	C	4	1	2	3.1
TC_067	11	1	70	332	29	50	S	C	2	1	2	3.1

Table A.9: Dip and dip direction of shear fractures field data collected at Tshifufia

Stat ID	Format	type	dip	dip-dir	slip sense	level confident	Weight factor	Activ type	Striae intens	Set input
TC_001	11	4	53	208	M	C	3	0	0	3.2
TC_002	11	4	73	215	M	C	3	0	0	3.2
TC_003	11	4	40	78	M	X	5	1	0	3.2
TC_004	11	4	80	22	M	S	5	1	0	3.2
TC_005	11	4	40	92	M	S	5	1	0	3.2
TC_006	11	4	65	6	M	C	5	1	0	3.2
TC_007	11	4	75	60	M	X	5	1	0	3.2
TC_008	11	4	60	124	M	C	5	1	0	3.2
TC_009	11	4	35	80	M	C	4	1	0	3.2
TC_010	11	4	20	92	M	C	4	1	0	3.2
TC_011	11	4	25	84	M	C	4	1	0	3.2
TC_012	11	4	85	242	M	C	5	0	0	3.2

Stat ID	Format	type	dip	dip-dir	slip sense	level confident	Weight factor	Activ type	Striae intens	Set input
TC_013	11	4	75	250	M	C	5	0	0	3.2
TC_014	11	4	75	274	M	C	5	0	0	3.2
TC_015	11	4	85	64	M	C	5	1	0	3.2
TC_016	11	4	89	268	M	C	5	1	0	3.2
TC_017	11	4	85	102	M	C	5	1	0	3.2
TC_018	11	4	85	110	M	C	5	1	0	3.2
TC_019	11	4	85	108	M	C	5	1	0	3.2
TC_020	11	4	40	178	M	C	5	1	0	3.2
TC_021	11	4	30	144	M	C	3	1	0	3.2
TC_022	11	4	52	130	M	C	3	1	0	3.2
TC_023	11	4	45	260	M	X	4	1	0	3.2
TC_024	11	4	40	174	M	C	4	1	0	3.2
TC_025	11	4	38	152	M	C	4	1	0	3.2
TC_026	11	4	50	230	M	C	4	1	0	3.2
TC_027	11	4	10	214	M	C	2	1	0	3.2
TC_028	11	4	50	6	M	C	2	1	0	3.2
TC_029	11	4	40	174	M	C	3	1	0	3.2
TC_030	11	4	80	104	M	P	3	1	0	3.2
TC_031	11	4	25	142	M	P	5	1	0	3.2
TC_032	11	4	25	110	M	P	5	1	0	3.2
TC_033	11	4	45	130	M	P	5	1	0	3.2
TC_034	11	4	20	2	M	P	5	1	0	3.2
TC_035	11	4	35	14	M	X	2	1	0	3.2
TC_036	11	4	65	104	M	X	2	1	0	3.2
TC_037	11	4	75	108	M	X	5	1	0	3.2
TC_038	11	4	40	92	M	C	5	1	0	3.2

Stat ID	Format	type	dip	dip-dir	slip sense	level confident	Weight factor	Activ type	Striae intens	Set input
TC_039	11	4	40	108	M	C	5	1	0	3.2
TC_040	11	4	35	50	M	S	4	1	0	3.2
TC_041	11	4	65	174	M	S	4	1	0	3.2
TC_042	11	4	60	122	M	S	5	1	0	3.2
TC_043	11	4	55	152	M	S	5	1	0	3.2
TC_044	11	4	35	210	D	S	2	1	0	3.2
TC_045	11	4	40	216	D	S	2	1	0	3.2
TC_046	11	4	50	248	D	C	3	1	0	3.2
TC_047	11	4	40	258	D	C	3	1	0	3.2
TC_048	11	4	70	82	I	C	5	1	0	3.2
TC_049	11	4	40	28	I	C	5	1	0	3.2
TC_050	11	4	55	24	I	C	5	1	0	3.2
TC_051	11	4	55	100	I	C	3	1	0	3.2
TC_052	11	4	45	40	I	C	4	1	0	3.2
TC_053	11	4	60	140	D	X	2	1	0	3.2
TC_054	11	4	70	94	X	X	5	1	0	3.2
TC_055	11	4	85	48	D	S	5	1	0	3.2
TC_056	11	4	55	88	D	S	5	1	0	3.2

Table A.10: Folding elements measurements (Dip, dip direction, strike and sense of bedding collected from the R2 fragment and the micro-folds observed at Tshifufia; dip and dip direction of fold axial planes and plunge and azimuth of hinge lines collected from the small-scale folds observed in the CMN strata.

Bedding planes - Tshifufia Fragment				
Stat.ID	Dip	Dip_Dir	Sense	Str.
TC_BP_F01	52	153	SE	63
TC_BP_F02	70	152	SE	62
TC_BP_F03	60	160	SE	70

Bedding planes - Isoclinals fold (Tshifufia)				
Stat.ID	Dip	Dip_Dir	Sense	Str.
TC_IBP_01	73	332	NW	242
TC_IBP_02	66	150	SE	60
TC_IBP_03	30	229	NW	139

Fold Axial Planes		
Stat ID	dip	dip-dir
TC_001	20	320
TC_002	40	314
TC_003	40	330

Hinge Lines		
Stat ID	Plunge	Azi.
TC_001	0	220
TC_002	20	220
TC_003	5	215

Bedding planes-Tshifufia Fragment				
Stat.ID	Dip	Dip_Dir	Sense	Str.
TC_BP_F04	30	116	SE	26
TC_BP_F05	55	174	SE	84
TC_BP_F06	75	114	SE	24
TC_BP_F07	78	138	SE	48
TC_BP_F08	74	134	SE	44
TC_BP_F09	30	170	SE	80
TC_BP_F10	76	140	SE	50
TC_BP_F11	54	154	SE	64
TC_BP_F12	20	126	SE	36
TC_BP_F13	60	160	SE	70
TC_BP_F14	50	150	SE	60
TC_BP_F15	64	160	SE	70
TC_BP_F16	20	134	SE	44
TC_BP_F17	40	148	SE	58
TC_BP_F18	86	104	SE	14
TC_BP_F19	80	138	SE	48
TC_BP_F20	20	112	SE	22
TC_BP_F21	38	140	SE	50
TC_BP_F22	23	138	SE	48
TC_BP_F23	54	154	SE	64
TC_BP_F24	20	126	SE	36
TC_BP_F25	60	160	SE	70
TC_BP_F26	50	150	SE	60
TC_BP_F27	64	160	SE	70
TC_BP_F28	50	150	SE	60
TC_BP_F29	20	134	SE	44
TC_BP_F30	40	238	SW	148
TC_BP_F31	86	104	SE	14
TC_BP_F32	20	202	SW	112
TC_BP_F33	38	230	SW	140
TC_BP_F34	23	138	SE	48

Bedding planes-Isoclinals fold (Tshifufia)				
Stat.ID	Dip	Dip_Dir	Sense	Str.
TC_IBP_04	75	320	NW	230
TC_IBP_05	55	330	NW	240
TC_IBP_06	20	130	SE	40
TC_IBP_07	75	135	SE	45
TC_IBP_08	28	140	SE	50
TC_IBP_09	64	318	NW	228
TC_IBP_10	15	300	NW	210
TC_IBP_11	75	134	SE	44
TC_IBP_12	51	142	SE	52
TC_IBP_13	72	148	SE	58
TC_IBP_14	50	146	SE	56
TC_IBP_15	72	128	SE	38
TC_IBP_16	80	318	NW	228
TC_IBP_17	36	130	SE	40
TC_IBP_18	48	300	NW	210
TC_IBP_19	30	306	NW	216
TC_IBP_20	68	150	SE	60
TC_IBP_21	60	120	SE	30
TC_IBP_22	35	142	SE	52
TC_IBP_23	56	108	SE	18
TC_IBP_24	40	302	NW	212
TC_IBP_25	40	127	SE	37
TC_IBP_26	46	158	SE	68
TC_IBP_27	82	310	NW	220
TC_IBP_28	70	130	SE	40
TC_IBP_29	58	148	SE	58
TC_IBP_30	54	120	SE	30
TC_IBP_31	45	218	SW	128
TC_IBP_32	40	345	NW	255

Fold Axial Planes		
Stat ID	dip	dip-dir
TC_004	40	335
TC_005	50	324
TC_006	28	296
TC_007	28	304
TC_008	40	330
TC_009	70	220
TC_010	34	270
TC_011	30	292
TC_012	40	200
TC_013	50	180
TC_014	15	100
TC_015	25	315
TC_016	50	275
TC_017	74	250
TC_018	55	245
TC_019	38	280
TC_020	80	245
TC_021	10	80
TC_022	45	310
TC_023	25	320
TC_024	25	320
TC_025	25	320

Hinge Lines		
Stat ID	Plunge	Azi.
TC_004	20	235
TC_005	30	234
TC_006	20	194
TC_007	20	164
TC_008	30	180
TC_009	10	190
TC_010	21	205
TC_011	5	175
TC_012	40	180
TC_013	46	158
TC_014	20	280
TC_015	20	248
TC_016	20	240
TC_017	40	266
TC_018	40	250
TC_019	14	236
TC_020	5	234
TC_021	5	216
TC_022	20	50

Table A.11: Dip and dip direction of the mineralised and unmineralised joints collected at Kinsevere Hill

Stat ID	Format	type	Dip	Dip Dir	Slip sense	Level confidence	Weight factor	Activ type	Striae intens	Subset
KSV-1	11	4	70	100	T	C	3	0	0	1.1
KSV-2	11	4	65	92	T	C	4	0	0	1.1
KSV-3	11	4	55	45	T	C	3	0	0	1.1
KSV-4	11	4	45	42	T	C	3	0	0	1.1
KSV-5	11	4	43	43	T	C	3	0	0	1.1
KSV-6	11	4	30	102	T	C	4	0	0	1.1
KSV-7	11	4	28	98	T	C	3	0	0	1.1
KSV-8	11	4	85	356	T	C	4	0	0	1.1
KSV-9	11	4	85	268	T	C	3	0	0	1.1
KSV-10	11	4	75	330	T	C	3	0	0	1.1
KSV-11	11	4	60	335	T	C	3	0	0	1.1
KSV-12	11	4	62	330	T	C	3	0	0	1.1
KSV-13	11	4	58	328	T	C	3	0	0	1.1
KSV-14	11	4	45	325	T	C	3	0	0	1.1
KSV-15	11	4	40	38	T	C	3	0	0	1.1
KSV-16	11	4	30	58	T	C	3	0	0	1.1
KSV-17	11	4	42	348	T	C	3	0	0	1.1
KSV-18	11	4	60	320	T	C	3	0	0	1.1
KSV-19	11	4	75	352	T	C	3	0	0	1.1
KSV-20	11	4	35	315	T	C	3	0	0	1.1
KSV-21	11	4	30	305	T	C	3	0	0	1.1
KSV-22	11	4	45	302	T	C	3	0	0	1.1
KSV-23	11	4	38	298	T	C	3	0	0	1.1
KSV-24	11	4	42	182	T	C	5	0	0	1.1
KSV-25	11	4	35	173	T	C	5	0	0	1.1

Stat ID	Format	type	Dip	Dip Dir	Slip sense	Level confidence	Weight factor	Activ type	Striae intens	Subset
KSV-26	11	4	25	155	T	C	5	0	0	1.1
KSV-27	11	4	45	183	T	C	5	0	0	1.1
KSV-28	11	4	38	175	T	C	5	0	0	1.1
KSV-29	11	4	28	184	T	C	5	0	0	1.1
KSV-30	11	4	40	238	T	C	5	0	0	1.1
KSV-31	11	4	38	228	T	C	5	0	0	1.1
KSV-32	11	4	55	243	T	C	5	0	0	1.1
KSV-33	11	4	49	210	T	C	5	0	0	1.1
KSV-34	11	4	63	266	T	C	5	0	0	1.1
KSV-35	11	4	62	258	T	C	5	0	0	1.1
KSV-36	11	4	52	246	T	C	5	0	0	1.1
KSV-37	11	4	58	262	T	C	5	0	0	1.1
KSV-38	11	4	68	205	T	C	3	0	0	1.1
KSV-39	11	4	62	262	T	C	3	0	0	1.1
KSV-40	11	4	85	205	T	C	3	0	0	1.1
KSV-41	11	4	62	240	T	C	5	0	0	1.1
KSV-42	11	4	45	213	T	C	2	0	0	1.1
KSV-43	11	4	42	245	T	C	2	0	0	1.1
KSV-44	11	4	32	242	T	C	2	0	0	1.1
KSV-45	11	4	59	225	T	C	2	0	0	1.1
KSV-46	11	4	83	223	T	C	2	0	0	1.1
KSV-47	11	4	49	235	T	C	2	0	0	1.1
KSV-48	11	4	48	183	T	C	7	0	0	1.1
KSV-49	11	4	39	165	T	C	7	0	0	1.1
KSV-50	11	4	70	98	T	C	3	0	0	1.2
KSV-51	11	4	70	160	T	C	3	0	0	1.2

Stat ID	Format	type	Dip	Dip Dir	Slip sense	Level confidence	Weight factor	Activ type	Striae intens	Subset
KSV-52	11	4	38	158	T	C	3	0	0	1.2
KSV-53	11	4	40	45	T	C	3	0	0	1.2
KSV-54	11	4	60	358	T	C	3	0	0	1.2
KSV-55	11	4	80	340	T	C	3	0	0	1.2
KSV-56	11	4	30	305	T	C	3	0	0	1.2
KSV-57	11	4	85	235	T	C	3	0	0	1.2
KSV-58	11	4	42	238	T	C	3	0	0	1.2
KSV-59	11	4	68	228	T	C	3	0	0	1.2
KSV-60	11	4	50	225	T	C	3	0	0	1.2
KSV-61	11	4	49	226	T	C	3	0	0	1.2
KSV-62	11	4	50	227	T	C	3	0	0	1.2

Table A.12: Dip/dip direction and plunge/azimuth of slickensided faults field data collected at Kinsevere Hill.

Stat ID	Format	type	Dip	Dip Dir	Plunge	Azimuth	Slip sense	Level confidence	Weight factor	Activ type	Striae intens	Subset
KS-1	11	1	82	62	82	47	I	S	5	1	2	3
KS-2	11	1	80	60	80	55	I	S	5	1	2	3
KS-3	11	1	78	63	77	45	I	S	4	1	2	3
KS-4	11	1	81	64	81	57	I	S	4	1	2	3
KS-5	11	1	82	61	80	22	I	S	4	1	2	3
KS-6	11	1	45	230	44	243	D	S	3	1	3	3
KS-7	11	1	45	232	44	216	D	S	3	1	2	3
KS-8	11	1	45	231	45	230	I	S	2	1	2	3
KS-9	11	1	45	235	43	251	I	C	2	1	2	3

Stat ID	Format	type	Dip	Dip Dir	Plunge	Azimuth	Slip sense	Level confidence	Weight factor	Activ type	Striae intens	Subset
KS-10	11	1	42	66	34	24	I	C	5	1	2	3
KS-11	11	1	40	65	31	22	I	C	4	1	2	3
KS-12	11	1	38	69	28	22	I	C	3	1	2	3
KS-13	11	1	41	70	31	26	I	C	3	1	2	3
KS-14	11	1	70	270	13	355	I	C	3	1	2	3
KS-15	11	1	71	267	11	353	I	C	3	1	2	3
KS-16	11	1	68	285	11	10	I	C	3	1	2	3
KS-17	11	1	70	270	4	359	I	C	3	1	2	3

Table A.13: Folding elements measurements Dip, dip direction, strike and sense of bedding collected from the R2 fragment and the micro-folds observed at Tshifufia; dip and dip direction of fold axial planes and plunge and azimuth of hinge lines collected from the small-scale folds observed in the CMN strata

Bedding planes-KSV_Hill Fragment				
Stat.ID	Dip	Dip_Dir	Sense	Str.
KS_BP_01	70	252	SW	162
KS_BP_02	73	260	SW	170
KS_BP_03	74	258	SW	168
KS_BP_04	74	240	SW	150
KS_BP_05	70	258	SW	168
KS_BP_06	80	236	SW	146
KS_BP_07	64	225	SW	135
KS_BP_08	75	230	SW	140
KS_BP_09	80	235	SW	145
KS_BP_10	52	243	SW	153
KS_BP_11	70	242	SW	152
KS_BP_12	73	240	SW	150
KS_BP_13	50	248	SW	158

Bedding planes-Isoclinals KSV_Hill Fragment				
Stat.ID	Dip	Dip_Dir	Sense	Str.
KS_IBP_01	30	250	SW	160
KS_IBP_02	20	240	SW	150
KS_IBP_03	26	242	SW	152
KS_IBP_04	28	230	SW	140
KS_IBP_05	80	250	SW	160
KS_IBP_06	70	248	SW	158
KS_IBP_07	70	250	SW	160
KS_IBP_08	30	234	SW	144
KS_IBP_09	80	235	SW	145
KS_IBP_10	64	225	SW	135
KS_IBP_11	65	213	SW	123
KS_IBP_12	56	217	SW	127
KS_IBP_13	30	220	SW	130

Fold axial planes		
Stat ID	dip	dip-dir
KSV_001	40	220
KSV_002	45	240
KSV_003	50	190
KSV_004	20	210
KSV_005	17	217
KSV_006	10	200
KSV_007	20	218
KSV_008	30	220
KSV_009	20	228
KSV_010	15	200
KSV_011	15	198
KSV_012	15	210
KSV_013	20	200

Hinge lines		
Stat ID	Plun.	Azi.
KSV_001	15	120
KSV_002	10	130
KSV_003	12	140
KSV_004	5	90
KSV_005	10	117
KSV_006	10	100
KSV_007	10	118
KSV_008	5	120
KSV_009	10	118
KSV_010	3	100
KSV_011	5	98
KSV_012	10	110
KSV_013	3	130

Bedding planes-KSV_Hill Fragment				
Stat.ID	Dip	Dip_Dir	Sense	Str.
KS_BP_14	45	250	SW	160
KS_BP_15	60	250	SW	160
KS_BP_16	72	248	SW	158
KS_BP_17	73	245	SW	155
KS_BP_18	70	238	SW	148
KS_BP_19	80	248	SW	158
KS_BP_20	64	250	SW	160
KS_BP_21	58	224	SW	134
KS_BP_22	70	236	SW	146
KS_BP_23	68	246	SW	156
KS_BP_24	74	262	SW	172
KS_BP_25	68	258	SW	168

Bedding planes-Isoclinals KSV_Hill Fragment				
Stat.ID	Dip	Dip_Dir	Sense	Str.
KS_IBP_14	20	260	SW	170
KS_IBP_15	28	256	SW	166
KS_IBP_16	30	230	SW	140
KS_IBP_17	80	43	NE	313
KS_IBP_18	20	52	NE	322
KS_IBP_19	18	60	NE	330
KS_IBP_20	30	54	NE	324
KS_IBP_21	30	52	NE	322
KS_IBP_22	28	56	NE	326
KS_IBP_23	40	40	NE	310
KS_IBP_24	30	45	NE	315
KS_IBP_25	80	35	NE	305
KS_IBP_26	20	40	NE	310
KS_IBP_27	22	38	NE	308
KS_IBP_28	50	48	NE	318
KS_IBP_29	30	35	NE	305
KS_IBP_30	20	65	NE	335
KS_IBP_31	15	50	NE	320
KS_IBP_32	30	54	NE	324

Fold axial planes		
Stat ID	dip	dip-dir
KSV_014	20	221
KSV_015	18	250
KSV_016	15	214
KSV_017	30	240
KSV_018	20	235
KSV_019	35	230
KSV_020	40	220
KSV_021	30	210
KSV_022	32	240

Hinge lines		
Stat ID	Plun.	Azi.
KSV_014	8	140
KSV_015	12	120
KSV_016	20	115
KSV_017	15	115
KSV_018	5	112
KSV_019	3	120
KSV_020	13	103
KSV_021	8	138

APPENDIX 2

STRESS TENSOR LOCATION MAPS

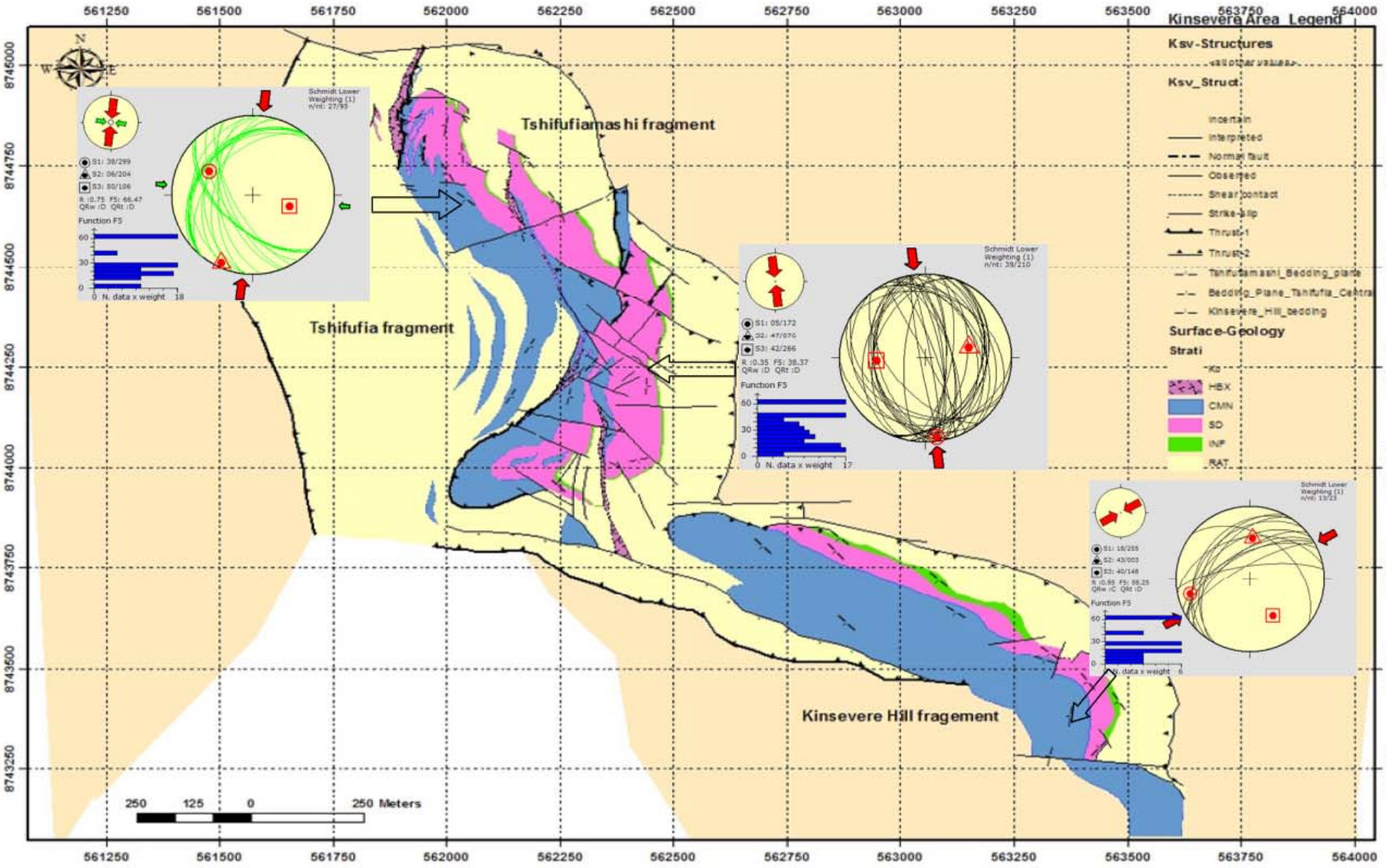

Figure 131: Location map of the stress tensor obtained from the mineralised joints in the Kinsevere area belonging to the stress compressive regime.

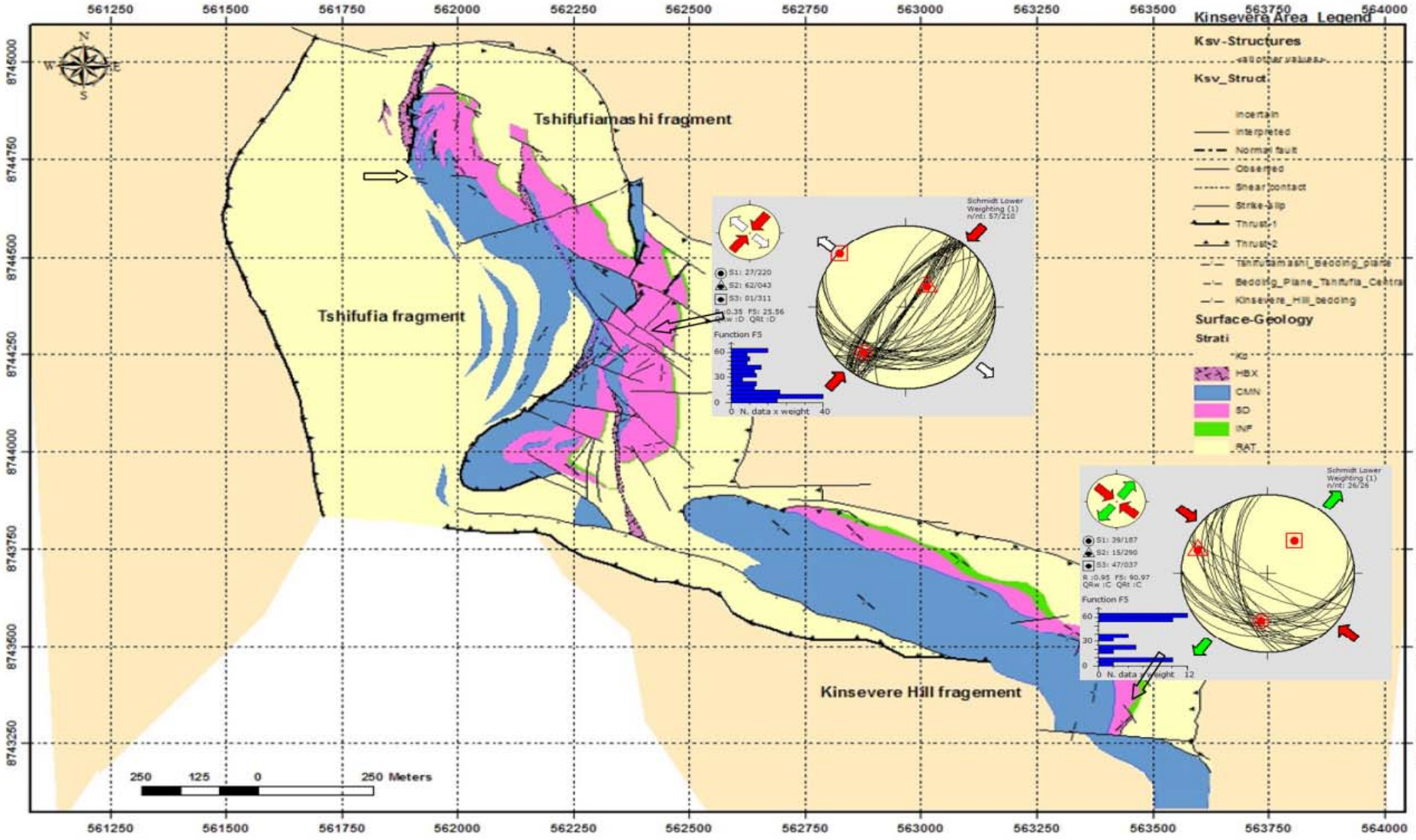

Figure 132: Location map of the stress tensor obtained from the mineralised joints in the Kinsevere area belonging to the strike-slip regime.

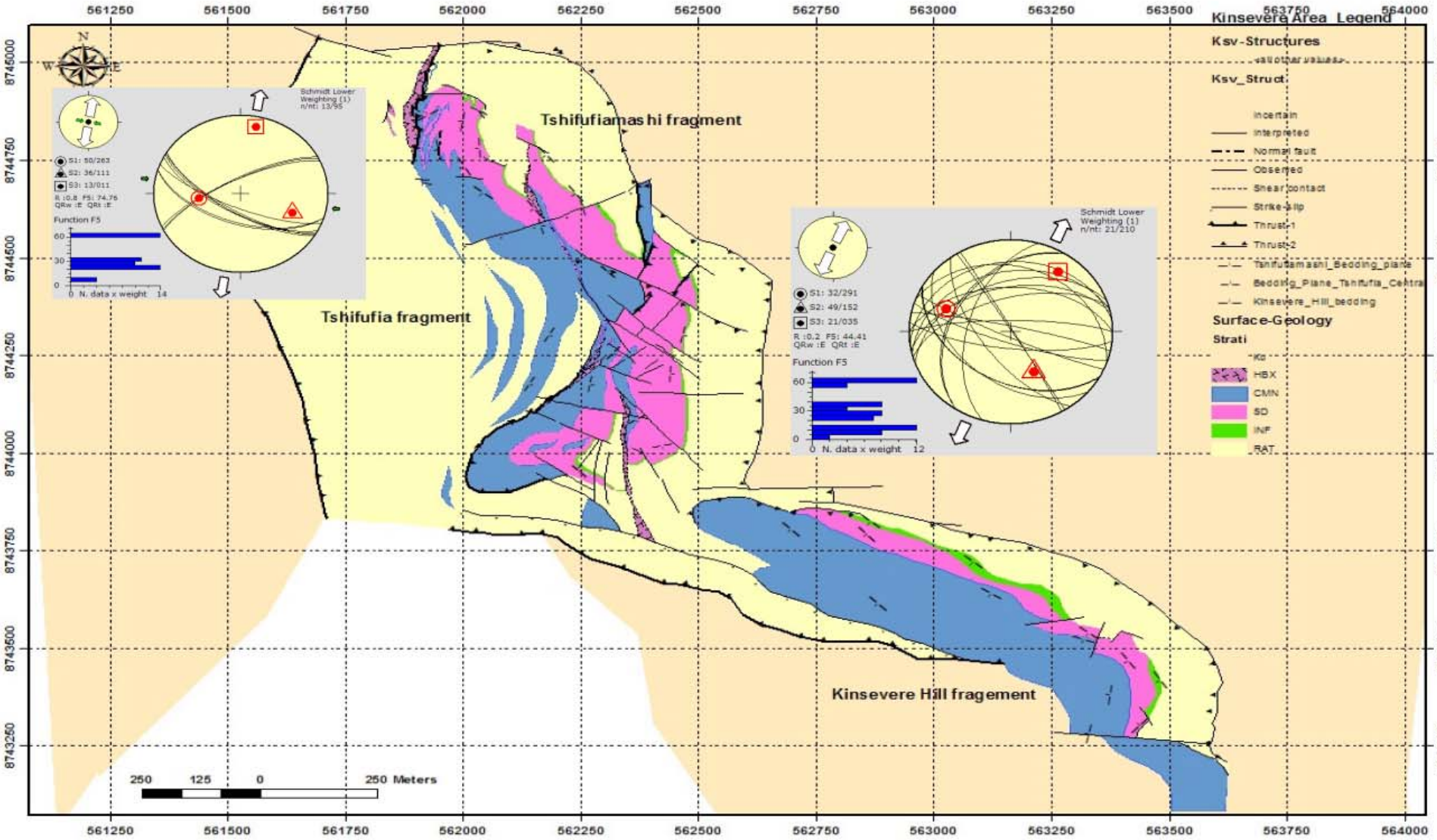

Figure 133: Location map of the stress tensor obtained from the mineralised joints in the Kinsevere area belonging to the extensive stress regime.

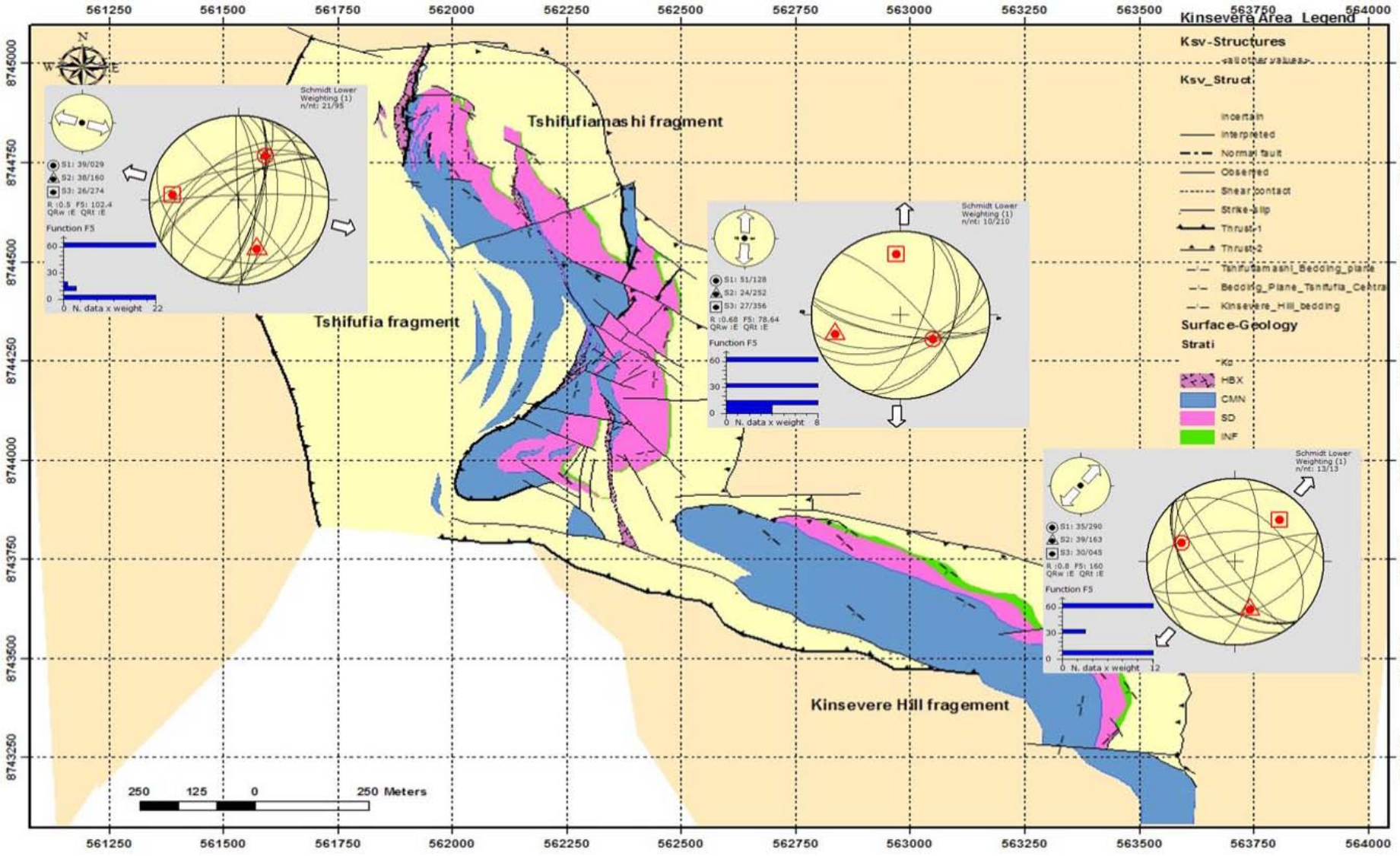

Figure 134: Location map of the stress tensor obtained from the unmineralised joints in the Kinsevere area belonging to the extensive stress regime.

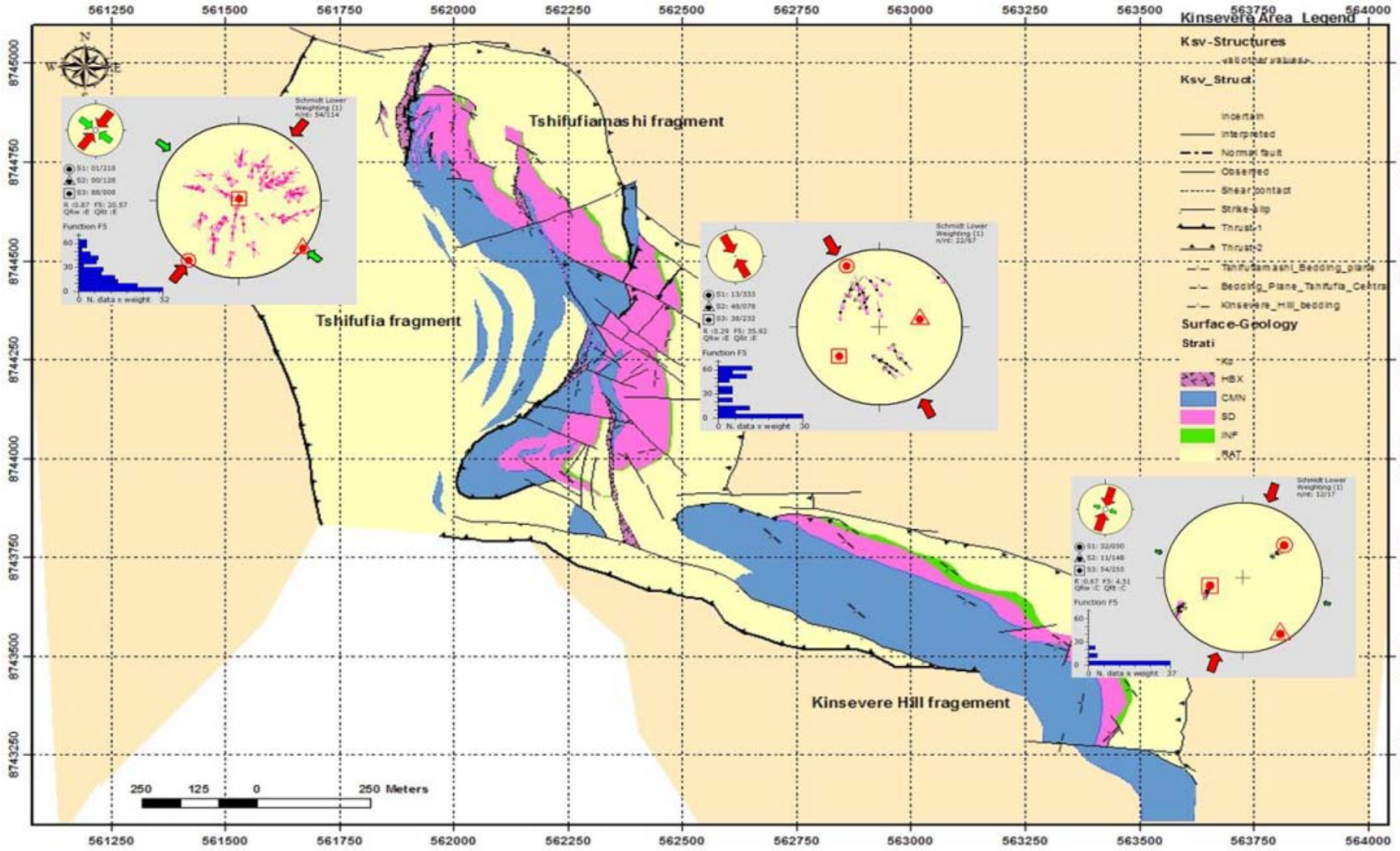

Figure 135: Location map of the stress tensor obtained from the slickensided faults (reverses) in the Kinsevere area belonging to the compressive stress regime.

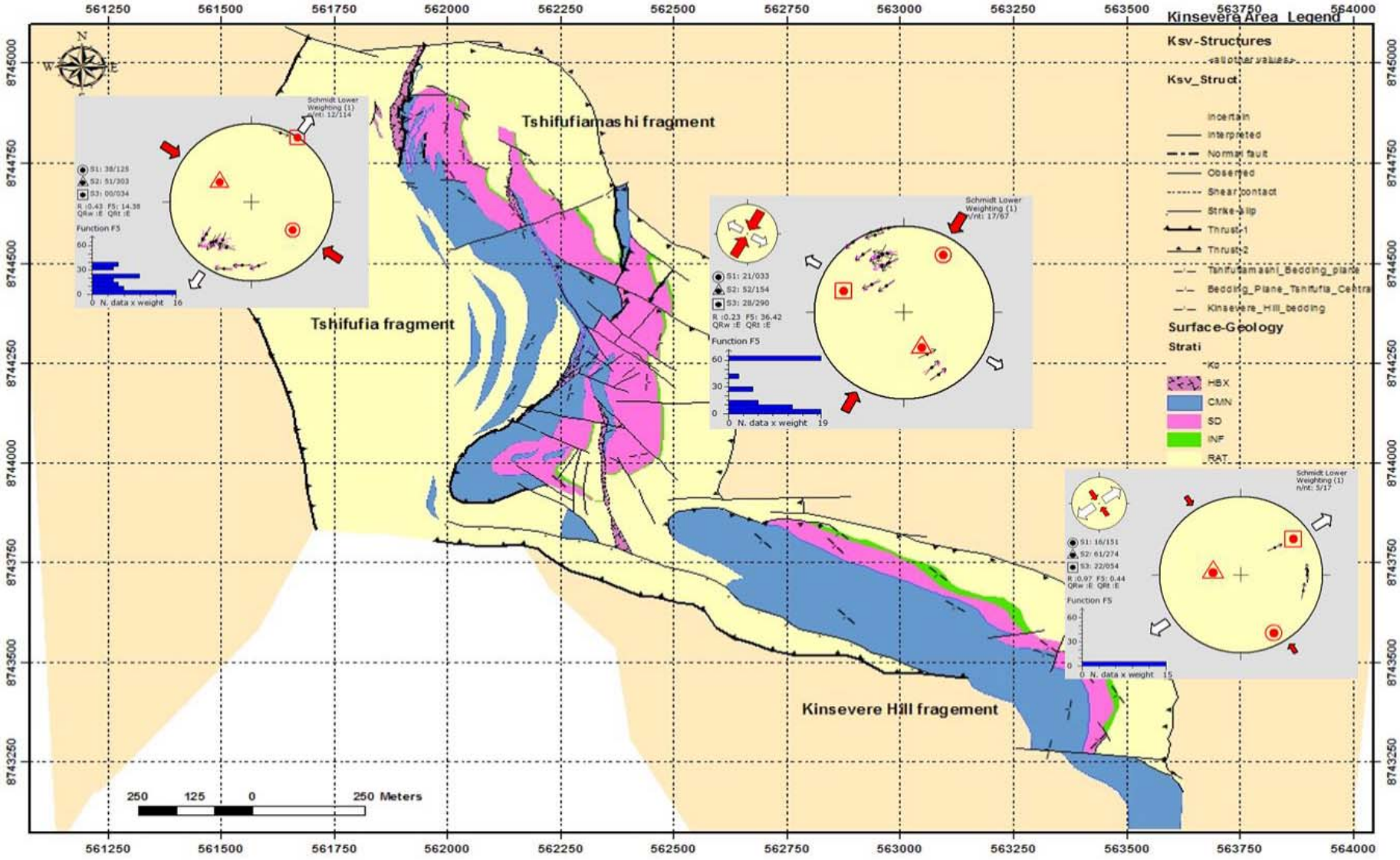

Figure 136: Location map of the stress tensor obtained from the strike-slip faults in the Kinsevere area belonging to the strike-slip stress regime.

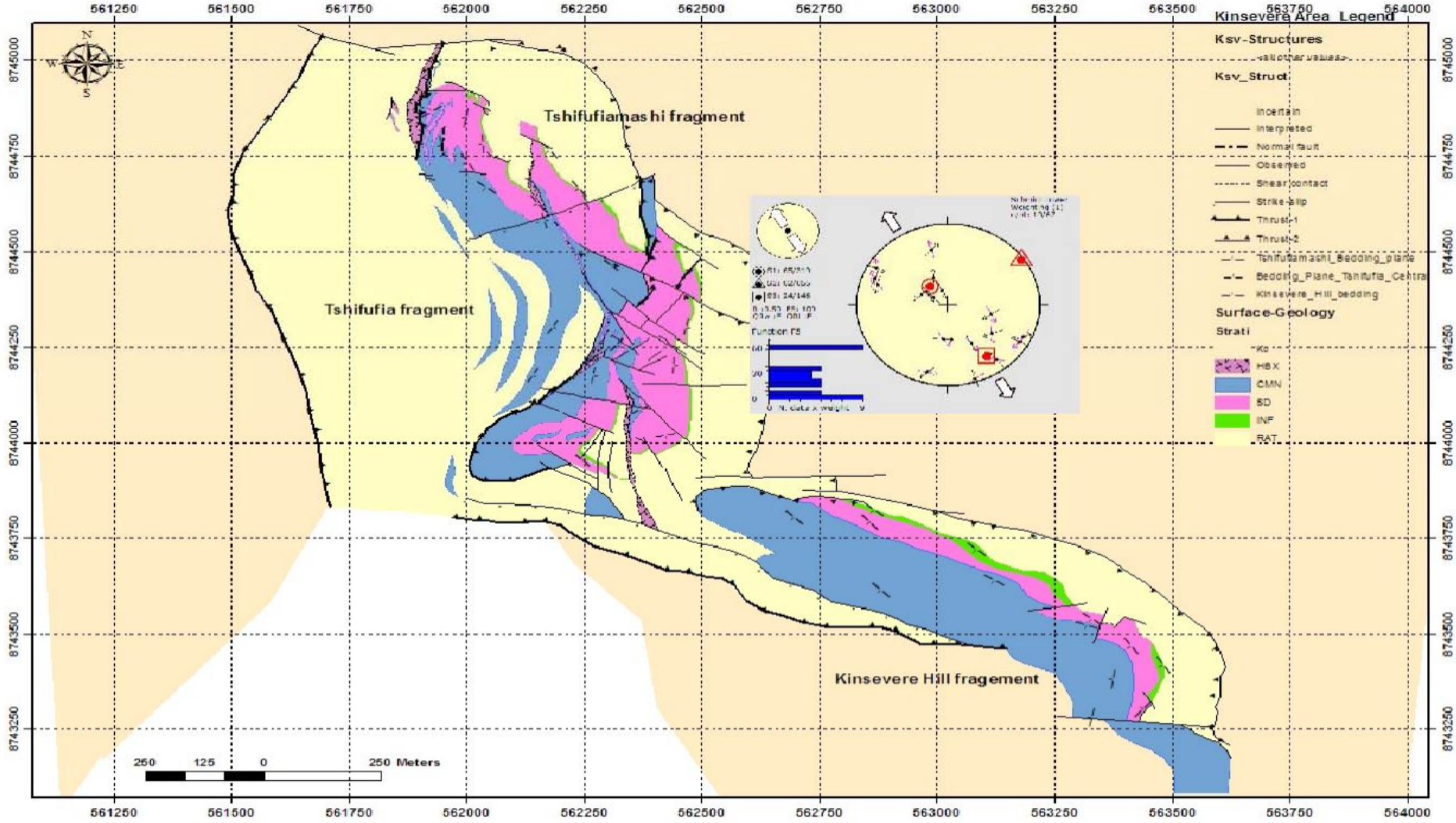

Figure 137: Location map of the stress tensor obtained from the slickensided faults in the Kinsevere area belonging to the extensive stress regime.

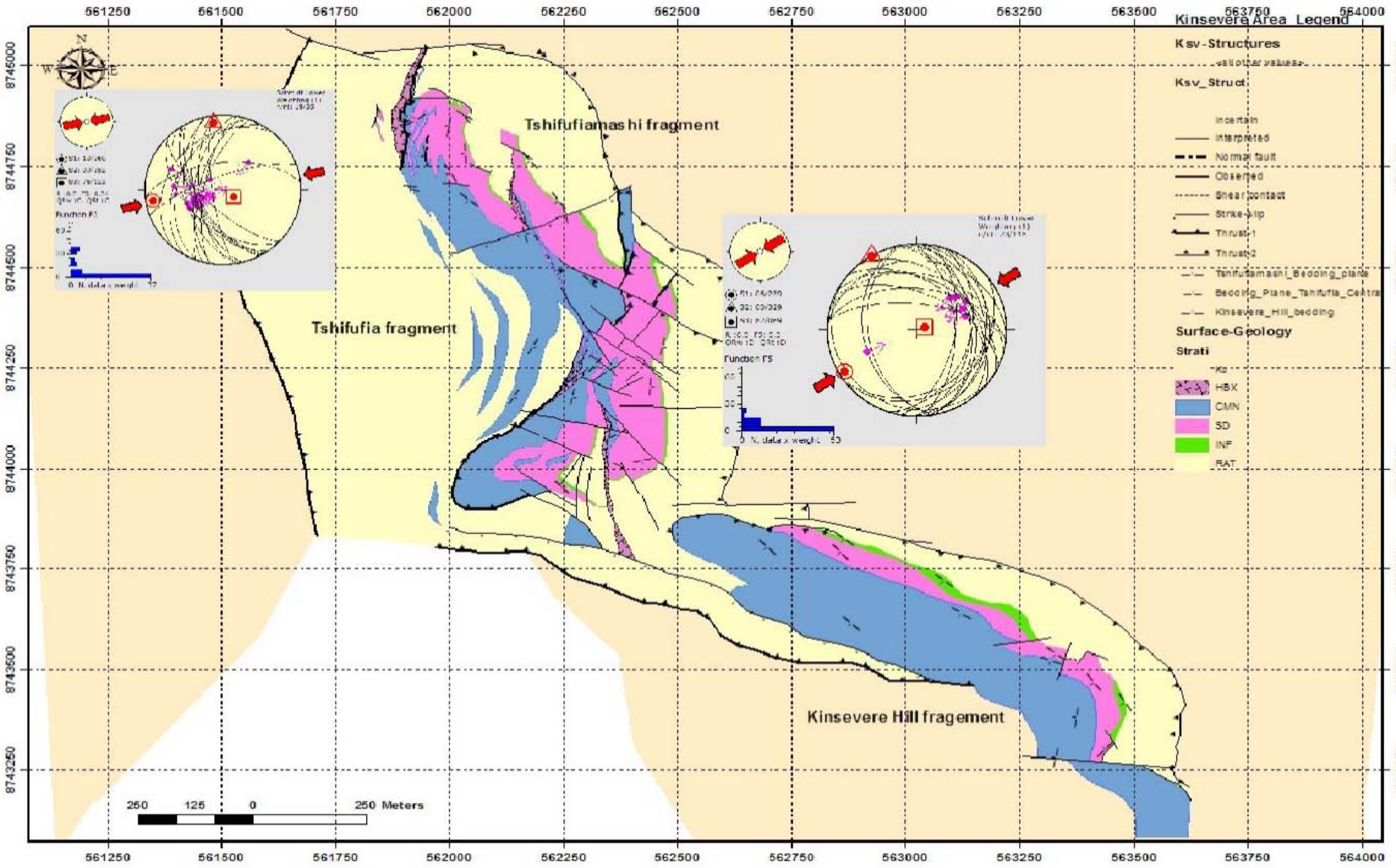

Figure 138: Location map of the stress tensor obtained from the shear fractures observed in the Kinsevere area belonging to the compressive stress regime.

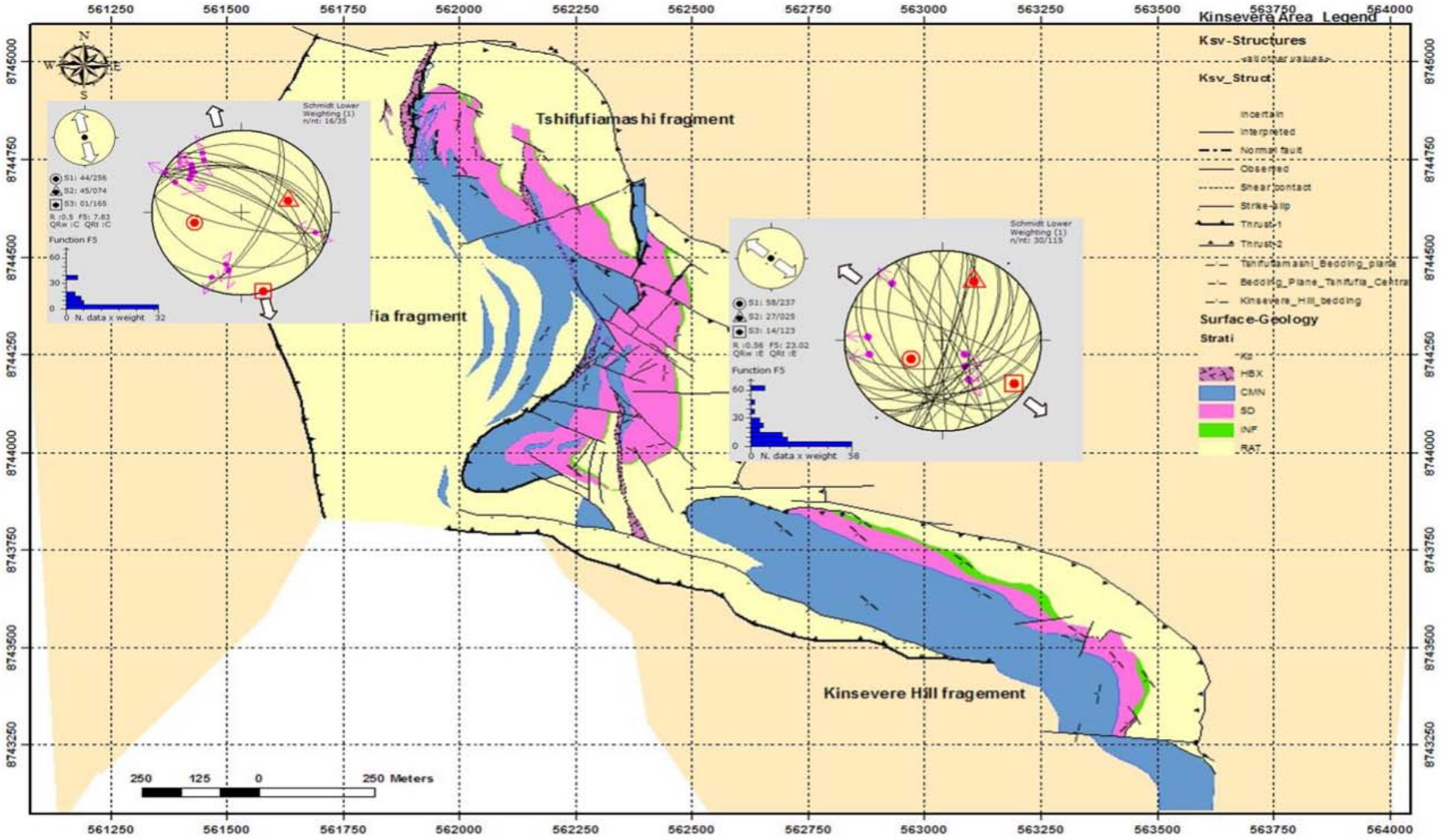

Figure 139: Location map of the stress tensor obtained from the shear fractures indicating normal faults observed in the Kinsevere area and belonging to the extensive stress regime.